



Rheology of concentrated suspensions and shear-induced migration

Talib Dbouk

► To cite this version:

Talib Dbouk. Rheology of concentrated suspensions and shear-induced migration. Other [cond-mat.other]. Université Nice Sophia Antipolis, 2011. English. NNT: . tel-00673964v2

HAL Id: tel-00673964

<https://theses.hal.science/tel-00673964v2>

Submitted on 21 Jan 2013

HAL is a multi-disciplinary open access archive for the deposit and dissemination of scientific research documents, whether they are published or not. The documents may come from teaching and research institutions in France or abroad, or from public or private research centers.

L'archive ouverte pluridisciplinaire **HAL**, est destinée au dépôt et à la diffusion de documents scientifiques de niveau recherche, publiés ou non, émanant des établissements d'enseignement et de recherche français ou étrangers, des laboratoires publics ou privés.



THÈSE

Présentée à

L'UNIVERSITÉ DE NICE - SOPHIA ANTIPOLIS

École Doctorale: Sciences Fondamentales et Appliquées

Pour obtenir le grade de

DOCTEUR EN SCIENCES

dans la spécialité: **PHYSIQUE**

par

Talib DBOUK

Rheology of concentrated suspensions and shear-induced migration

Thèse dirigée par Elisabeth LEMAIRE et

co-dirigée par Laurent LOBRY

préparée au Laboratoire de Physique de la Matière Condensée

soutenue le 14 décembre 2011

Jury:

Président: Georges BOSSIS - CNRS

Rapporteurs: Elisabeth GUAZZELLI - CNRS
Fadi MOUKALLED - American University of Beirut

Directeur: Elisabeth LEMAIRE - CNRS

Co-Directeur: Laurent LOBRY - UNS

Examineurs: Georges GAUTHIER - Université Paris-Sud 11

Resumé

Lorsqu'une suspension concentrée est en écoulement, il est fréquent d'observer que la concentration en particules ne reste pas homogène mais que les particules migrent vers des régions préférentielles de l'écoulement. Globalement, il existe deux types de modèles pour décrire cette interaction entre l'écoulement et la structure qui apparaît dans la suspension. Les premiers sont assez phénoménologiques et reposent sur l'étude des collisions qui surviennent entre les particules en écoulement. Ils donnent lieu à une description de la migration en terme de diffusion des particules. Le second modèle, appelé "**Suspension Balance Model**" (**SBM**), fait appel à l'action des contraintes normales d'origine particulaire engendrées par l'écoulement. Ce modèle semble très pertinent mais son utilisation souffre du manque de données sur les contraintes normales dans les suspensions.

Ce manuscrit rapporte une étude expérimentale et numérique de la rhéologie et de la migration induite par un écoulement dans des suspensions non-browniennes concentrées. La partie expérimentale consiste à mesurer, en géométrie torsionnelle plan-plan, la viscosité, les deux différences de contraintes normales et le tenseur des contraintes particulières.

Les contraintes particulières déterminées expérimentalement sont alors injectées dans le "**Suspension Balance Model**" qui relie le flux de particules à la divergence du tenseur des contraintes particulières, dans le cas d'un écoulement de cisaillement simple. Les équations couplées de la conservation de la masse, des particules et du moment d'inertie sont implémentées dans OpenFOAM® et résolues par la méthode des volumes finis. Les résultats numériques sont comparés à des résultats numériques et expérimentaux de la littérature.

Enfin, le **SBM** est généralisé pour être utilisé dans tout type d'écoulement à 2 dimensions ; les cas du cisaillement d'un nuage de particules et de l'effet de la gravité dans un écoulement de Couette horizontal sont traités.

Abstract

This thesis deals with an experimental and numerical investigation of the phenomenon of shear-induced particle migration in inhomogeneous shear flows of mono-dispersed non-colloidal suspensions at neglected inertia. Variety of diffusion flux models that predict the shear-induced migration were presented.

However, in this work, the **Suspension Balance Model** (**SBM**) is adopted. The latter describes the migration flux of particles as the divergence of the particle Stress tensor. According to the need for the different measurable parameters in this Model, a new experiment was developed for measuring the viscosity, the two Normal Stress Differences and the particle stress tensor of mono-dispersed non-Brownian suspensions of hard spheres flowing between rotating parallel disks over a wide range of concentrations (0.20 - 0.46).

The original **SBM** is modified based on the new measurements. The Finite Volume Method via the OpenFOAM® package is used as the technique to solve the problem numerically. Solutions are generated and results are compared to similar ones generated with the original model.

Finally, the **SBM** model is extended into two-dimensional situations within a general Frame-Invariant structure that takes into account the local kinematics of the suspension.

For my parents...

As good moments, during this thesis period i passed through very sad moments too.

First, it was a very sad moment when my father “A. DBOUK” passed away by the end of my first year, after a long struggling with disease.

Later, by the end of my third year, it was another sad moment for every one in our laboratory when two of our scientists “R. KOFMAN”, and “A. AUDOLY” passed away.

For their memory i intend to leave the next page blank.

Acknowledgements

I would like to express my sincere gratitude to my supervisors Professor Elisabeth LEMAIRE, and Doctor Laurent LOBRY for their continuous support, guidance, constructive criticism and patience.

Without their help and encouragement and really being as another family to me, this thesis would not have been possible.

My very special sincere gratitude too is to my collaborator supervisors Professor Francois PETERS, Professor Fadl MOUKALLED, and Professor Marwan DARWISH whose constant support, guidance and friendship were invaluable.

I would like also to thank the French gouvernement for the financial support which made this study possible, and who gave me the opportunity to continue my PhD studies in France.

I would like also to thank the French-Lebanese Project “CEDRE” for their financial aid which made the completeness of this study possible, and who opened a collaborative work between the French Laboratory LPMC in Nice, and the Lebanese one in the American University of Beirut.

I would also like to express my appreciation and my thanks to my two office mates Frédéric BLANC, and Guillaume HUILLARD for their greatful discussions and their invaluable friendship over the three years of the thesis.

My very special thanks too is for all the members of the LPMC laboratory whom i passed with unforgettable beautiful moments.

I would like to thank all my friends i have had through this period of study, with whom i spent very special nice times full of friendship and brotherhood.

Finally, I would like to thank my parents Ahmad & Loubna, my grandmother Samiha, my brother Bilal, my sisters Hoda & Nada, my cousins Hussein, Fadi, and Sami for their continuous support and encouragement, especially my mother Loubna for her great sacrifices and her patience over the last 27 years.

Nomenclature

J_f	Mass Flux at a face f
α_1	First Normal Stress Difference Coefficient
α_2	Second Normal Stress Difference Coefficient
α_p	Pressure Underrelaxation Coefficient
α_U	Velocity Underrelaxation Coefficient
δ_{ij}	Kronecker Delta
$\nabla \bullet$	Divergence Operator
Υ	Source Term Vector
ϵ	Strain (Deformation) Tensor
ς_{ij}	Deviatoric Stress Tensor
Δt	Time Step
$\dot{\epsilon}$	Strain Rate Tensor
$\dot{\gamma}$	Shear Rate
$\dot{\gamma}_{NL}$	Non-Local Shear Rate
η	Dynamic Viscosity
η_f	Suspending Fluid Viscosity

η_N	Particles Normal Stress Viscosity
η_P	Particles Shear Viscosity
Γ_Ψ	Diffusion Coefficient
Σ^f	Fluid Stress Tensor
Σ^p	Particle Stress Tensor
$\Sigma_{nn,2}^p$	The Modified Particle Normal Stress Diagonal Tensor
$\Sigma_{nn,3}^p$	The Modified Particle Normal Stress Anisotropic Tensor
Σ	Stress Tensor
$\Sigma_{nn,1}^p$	Particle Normal Stress Diagonal Tensor
\mathbf{A}	Sparse Matrix
\mathbf{E}	Local Rate of Strain Tensor
\mathbf{F}	Force
\mathbf{F}^H	Hydrodynamic Drag Force
\mathbf{n}	Unit Normal Vector
\mathbf{Q}	Parametric Symmetric Tensor
\mathbf{S}_f	Face-Area Vector
\mathbf{U}	Velocity Vector
\mathbf{X}	Position Vector In 3D Cartesian Coordinates
\mathbf{Z}	Flow Aligned Tensor
μ	Dynamic Viscosity
ν	Kinematic Viscosity
Ω	Angular Velocity

ω	Rotational Velocity
\vec{j}_l	Total Migration Flux Of Particles
\vec{j}_g	Difference-In-Densities Migration Flux
\vec{N}_η	Gradients In Viscosity Flux
\vec{N}_c	Collision Flux
\vec{N}_r	Curvature-Induced Flux
\vec{N}_t	Diffusive Migration Flux Of Particles
ϕ	Concentration (Volume Fraction) Of Particles
Π	Suspension Pressure
Ψ	Scalar Property
$\Re s_{\mathbf{P}}$	Residual
ρ	Medium Density
ρ_f	Fluid Density
ρ_p	Particles Density
τ	Shear Stress
\mathbf{g}	Gravitational Acceleration
Υ_t	Suspension Surface Tension
a_N	Matrix Off-Diagonal Coefficients
a_P	Matrix Diagonal Coefficients
$f(\phi)$	Sedimentation Hindrance Function
K_η	Empirical Parameter Of The Gradients In Viscosity Flux
K_c	Empirical Parameter Of The Collision Flux

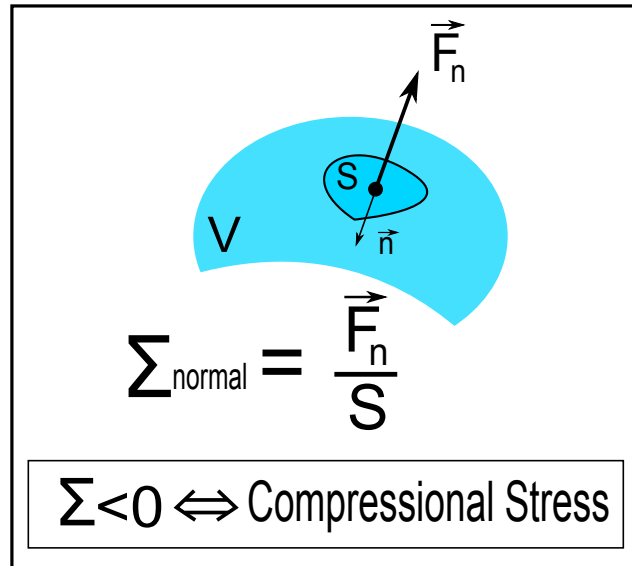
k_{oo}	Ordinates At The Origin
k_p	Slope
K_r	Empirical Parameter Of The Curvature-Induced Flux
kT	Thermal Energy
N_1	First Normal Stress Difference
N_2	Second Normal Stress Difference
$P\delta_{ij}$	Mean Normal Stress Tensor
P_a	Atmospheric Pressure
S_Ψ	Source Term
t_M	Migration Characteristic Time
$V_{\mathbf{P}}$	Volume Of A Control Volume Cell
a	Radius Of The Spherical Particles
Cr	Courant Number
Er	Numerical Error
h	Gap
L	Conduit Length
P	Pressure
p	Kinematic Pressure
Pe	Péclet Number
$r ; R$	Radius
Re	Reynolds Number
t	Time
tr	Trace Of A Tensor

ABBREVIATIONS

SBM	S uspension B alance M odel
FVM	F inite V olume M ethod
FCM	F orce C oupling M ethod
PIV	P articles I mage V elocimetry
LDV	L aser D oppler V elocimetry
NMR	N uclear M agnetic R esonance
SIMPLE	S emi- I mplicit M ethod for P ressure- L inked E quations
NS	N avier- S tokes
OO	O bject O riented
SD	S tokesian D ynamics
CV	C ontrol V olume

Stress Convention

Due to different Stress-sign conventions that exist in literature, we provide our convention used in this manuscript by following the most known convention, in suspensions rheology. The normal stresses are defined by directing the normals toward the interior side of a medium element (compressional stresses are negative) as you can see in the next drawing.



Contents

INTRODUCTION	25
1 STATE OF THE ART	30
1.1 OVERVIEW	30
1.2 AN INTRODUCTION TO RHEOLOGY	30
1.2.1 Run-up to rheology (before 1929)	30
1.2.2 Rheology birth (1929)	31
1.2.3 Rheology since its inception in 1929	31
1.2.4 Present rheology and the new face	32
1.3 SUSPENSIONS	32
1.3.1 Introduction	32
1.3.2 Inside a suspension	33
1.3.2.1 Suspension classification	33
1.3.2.2 Forces on particles	34
1.4 SUSPENSION RHEOPHYSICS	36
1.4.1 Material functions	36
1.4.2 Suspension viscometric functions (Viscosity & Normal Stress Differences)	36
1.4.2.1 Viscosity	36
1.4.2.2 Normal Stress Differences	41
1.5 RHEOMETRY	46
1.5.1 Stress, Strain, and the local Shear-rate	49

1.5.1.1	The Stress Tensor	49
1.5.1.2	The Strain (deformation) Tensor	50
1.5.1.3	The Shear Rate Scalar	52
1.5.2	Conservation Equations	52
1.5.2.1	Mass Conservation	53
1.5.2.2	Momentum Conservation	53
1.5.3	Measurements of η , N_1 , and N_2 in different flows	53
1.5.4	Measurements of material functions for a suspension in a torsional flow between two parallel-disks at low Reynolds Number	59
1.6	SHEAR-INDUCED MIGRATION	61
1.6.1	Migration in different geometries (Experimental Studies)	61
1.7	SHEAR-INDUCED MIGRATION MODELING	63
1.7.1	Overview	63
1.7.2	Constitutive modeling	63
1.7.3	Diffusion Models	65
1.7.3.1	Original Phillips Model	65
1.7.3.2	Modified Phillips Model	66
1.7.3.3	ϕ -Dependent K_c Model	67
1.7.3.4	Flow-aligned Tensor Model	67
1.7.3.5	Migration-Time Scaling	68
1.7.4	Suspension Balance Model	68
1.7.4.1	Overview	69
1.7.4.2	Mass and Momentum Conservation Equations	69
1.7.4.3	Migration-Time Scaling	71
1.7.4.4	The Non-Colloidal Suspension Stress	71
1.7.4.5	Model Parameters	73
2	THE NUMERICAL FINITE VOLUME METHOD	75
2.1	OVERVIEW	75

2.2	INTRODUCTION	75
2.3	DISCRETIZATION OF THE SOLUTION DOMAIN	77
2.4	DISCRETIZATION OF THE TRANSPORT EQUATION	79
2.4.1	Storage and Arrangement of variables	80
2.4.2	Discretization Of Spacial Terms	82
2.4.2.1	The Diffusion Term	82
2.4.2.2	The Convection Term	83
2.4.2.3	The Source Term	84
2.4.3	Temporal Discretization	85
2.4.4	Solution Techniques for Systems of Linear Algebraic Equations	87
2.4.5	Boundary Conditions	88
2.4.5.1	The Fixed Value BC	90
2.4.5.2	The Fixed Gradient BC	91
2.5	NUMERICAL ERRORS	91
2.5.1	The Residual Error Estimate	92
2.5.2	Convection and Diffusion Control	92
2.6	NAVIER-STOKES EQUATION DISCRETIZATION	93
2.6.1	Discretizing the equations	94
2.6.1.1	The Discretized Momentum Equation in a Matrix form	94
2.6.2	Pressure-Velocity Coupling Technique	94
2.6.2.1	The SIMPLE Algorithm	95
2.6.2.2	Under-relaxation	97
2.7	CLOSURE	99
3	THE Suspension Balance Model IN OpenFOAM®	100
3.1	OVERVIEW	100
3.2	MODEL GOVERNING EQUATIONS	101
3.3	NUMERICAL IMPLEMENTATION	102

3.3.1	Implementation of the “Suspension Balance Model” in “Open-FOAM®”	102
3.4	VALIDATION OF THE CODE IMPLEMENTATION IN Open-FOAM®	103
3.4.1	Suspension flow in channels	104
3.4.1.1	Suspension flow in a rectangular cross-section conduit	104
3.4.1.2	Suspension flow in a pipe (circular cross-section conduit)	110
3.4.2	Suspension flow in a Couette cell geometry	114
3.5	CLOSURE	120
4	MEASUREMENTS OF NORMAL STRESSES	121
4.1	OVERVIEW	121
4.2	INTRODUCTION	121
4.3	SUSPENSION MATERIAL FUNCTIONS IN A TORSIONAL FLOW BETWEEN TWO ROTATING PARALLEL PLATES	123
4.3.1	Torsional flow at small Reynolds Number	123
4.4	EXPERIMENTS	126
4.4.1	Experimental device	126
4.4.2	Suspensions	129
4.4.3	Experimental Procedure	131
4.4.4	Parallelism problem	132
4.4.5	Pressure Membranes (size and position)	134
4.4.6	Wall Slip Effects	136
4.4.7	Setup Validation	138
4.5	MATERIAL FUNCTIONS IN SUSPENSIONS, DETERMINATION OF η_s , α_1 , AND α_2	143
4.5.1	Suspension Viscosity	143
4.5.1.1	Shear-thinning	143

4.5.1.2	Variation with ϕ	145
4.5.1.3	Transient Response after shear reversal	146
4.5.2	Suspension Normal Stress Coefficients α_1 and α_2	149
4.5.3	Validity of α_1 and α_2 measurements	150
4.5.3.1	Influence of the suspended fluid viscosity	151
4.5.3.2	Influence of the capillary pressure	152
4.5.3.3	Comparison with the results of Singh and Nott 2003	153
4.5.3.4	Comparison with other results	157
4.5.4	Concluding remarks on the measurements of α_1 and α_2	160
4.6	PARTICLE NORMAL STRESSES	160
4.6.1	Results	160
4.6.2	Discussion	163
4.7	A TENTATIVE MEASUREMENT OF THE SUSPENSION MA- TERIAL FUNCTIONS AT HIGHER PARTICLE VOLUME FRAC- TIONS	167
4.8	SECONDARY FLOW IN ROTATING PARALLEL PLATE GE- OMETRY	170
4.8.1	Validation of the experimental procedure used to deter- mine α_1 and α_2	171
4.8.2	Visualization of the secondary flow	172
4.8.2.1	In a simple liquid	172
4.8.2.2	Secondary flow in a suspension	175
4.8.3	On the possible role of the secondary flow on the particle shear-induced migration in parallel plate geometry	178
4.9	CLOSURE	179
5	THE MODIFIED Suspension Balance Model	181
5.1	OVERVIEW	181
5.2	THE GOVERNING PARAMETERS	181

5.3	THE PARTICLE NORMAL STRESS TENSOR	182
5.4	THE MODIFIED SBM IMPLEMENTED IN OpenFOAM® . . .	183
5.4.1	Suspension Flow in a Large-gap Couette cell	183
5.4.2	Suspension Flow in a Small-gap Couette cell	186
5.5	THE SBM AND THE MODIFIED-SBM	191
5.6	CLOSURE	192
6	ADVANCED SUSPENSION MODELING	194
6.1	OVERVIEW	194
6.2	THE 2D FRAME-INVARIANT MODIFIED Suspension Balance Model	194
6.2.1	Introduction	194
6.2.2	Frame-Invariant Suspension Kinematics	195
6.2.2.1	Kinematic Ratio	196
6.2.2.2	Compression-Tension Coordinates and Transi- tion Matrix	197
6.2.3	Anisotropic Particle Stress in the SBM	198
6.2.4	Validation	201
6.2.4.1	2D Frame-Invariant Suspension Flow in a Chan- nel and in a Couette cell	201
6.2.4.2	Oscillating shear of a suspension cloud	203
6.3	THE SBM EXTENDED TO BUOYANCY	207
6.3.1	Validation	209
6.3.1.1	Viscous resuspension and 2D mixing	209
6.4	CLOSURE	213
7	SUMMARY, CONCLUSIONS & PERSPECTIVES	214
7.1	SUMMARY AND CONCLUSIONS	214
7.2	PERSPECTIVES	218
	APPENDICES	219

A	WEDGE TYPE MESH	220
A.1	Wedge type mesh description	220
B	NUMERICAL SCHEMES AND SOLUTION SOLVERS IN Open-FOAM®	222
B.1	Numerical Schemes & Solution Solvers	222
C	IN OpenFOAM®	224
C.1	The convection term (precisely in OpenFOAM®)	224
C.2	The flux term in OpenFOAM®	225
C.3	<i>Implementation of the SIMPLE algorithm in OpenFOAM®</i>	225
C.4	<i>References</i>	227
D	SCHEMES USED IN OpenFOAM® FOR THE DIFFERENT SIMULATION CASES	228
D.1	The schemes used in OPENFOAM® in this work for different simulation cases	228
D.2	Solvers settings used in OpenFOAM® in this work for different simulation cases	229

List of Figures

1.1	Classification of Suspensions.	33
1.2	Simple shearing of a material (fluid).	37
1.3	Normalized Suspension Viscosity	40
1.4	1.25 μm PVC particles in dioctyl phthalate [Hoffman 1972].	40
1.5	"Phase diagram" for suspension rheology, based on a dimensional analysis. Remade from [Stickel and Powell 2005].	41
1.6	HAAKE-Mars Thermo Scientific rotational Rheometer.	47
1.7	Common shear flow geometries taken from [Macosko 1994].	48
1.8	Stress Tensor.	49
1.9	Infinitesimal 1D strain	51
1.10	Rotating-Rod Instrument	54
1.11	Inclined-Plane Flow	55
1.12	Parallel-Cone-Plate Instrument	56
1.13	Cylindrical Couette cell Viscometer	57
1.14	Parallel-Disks Instrument	58
1.15	Diffusive Fluxes	66
1.16	Curvature Flux	67
1.17	Migration Flux \vec{j}_{\perp}	69
2.1	Control Volume "P"	78
2.2	Transport process in the CV	80
2.3	Arrangement of variables	81

2.4	Orthogonal Mesh Interface	82
2.5	Boundary Faces represented as Patches	89
2.6	Boundary Face b (patch)	90
3.1	Channel rectangular cross-section 2D Mesh	106
3.2	Channel 2D imposed boundary conditions	106
3.3	30% Suspension Steady State Concentration Profile	107
3.4	40% Suspension Steady State Concentration Profile	107
3.5	50% Suspension Steady State Concentration Profile	108
3.6	Centerline Steady State Concentration Profile	108
3.7	Residuals of the 30% Suspension case in Figure (3.3)	109
3.8	Circular cross-section pipe 2D Mesh	110
3.9	20% Suspension Steady State Concentration Profile	111
3.10	30% Suspension Steady State Concentration Profile	112
3.11	45% Suspension Steady State Concentration Profile	112
3.12	Centerline Steady State Concentration Profile	113
3.13	Couette cell	115
3.14	Couette cell Boundary Conditions	115
3.15	Transient Concentration Profiles at 200 revolutions	116
3.16	Transient Concentration Profiles at 12000 revolutions	117
3.17	Steady State Concentration Profiles in a Couette gap	119
4.1	Experimental Setup	126
4.2	STS Pressure Sensor	127
4.3	Experimental Setup	127
4.4	Paraffin Coating	128
4.5	Hydrostatic Pressure Test	128
4.6	Hydrostatic Pressure Test	129
4.7	The protocol of the applied torque Γ as function of time	132
4.8	Rotating Disk parallelism default	133
4.9	Stationary Disk parallelism default	133

4.10	Two parallel disks geometry of an error δh	134
4.11	$f(\xi)$	135
4.12	Correction of R_{real} to R_{eff}	136
4.13	Apparent Shear rate	137
4.14	Registered Signals by the sensors	139
4.15	The Shear Stress $\tau \equiv \Sigma_{12}$ Versus the Shear Rate $\dot{\gamma}_R$	140
4.16	The radial variation of the second normal stress Σ_{22}	141
4.17	The fluid pressure P_f	142
4.18	Resuspension in a Couette cell	143
4.19	Resuspension in a parallel plate geometry	144
4.20	The normalized suspension viscosity	145
4.21	Suspension Viscosity Response upon shear reversal	146
4.22	η_{min} and $\eta_{plateau}$ as function of ϕ	148
4.23	η_{ex} as function of ϕ	148
4.24	The ratios $\frac{\alpha_1}{\eta_s}$ and $\frac{\alpha_2}{\eta_s}$ as function of ϕ . $(1.8\phi - 0.356)$ is the fit for $2a = 140 \mu m$ & $(1.94\phi - 0.465)$ is the fit for $2a = 40 \mu m$	150
4.25	α_1/η_s (triangles) and α_2/η_s (squares) as function of h	152
4.26	$\Sigma_{zz}(r)/\eta\dot{\gamma}$ taken from Figure10 of [Singh and Nott 2003]	154
4.27	The ratios $\frac{\alpha_1}{\eta_s}$ and $\frac{\alpha_2}{\eta_s}$ as function of ϕ	156
4.28	$(\frac{\alpha_1}{2} + \alpha_2)$ as function of ϕ	157
4.29	Measured thrust force F as function of shear rate $\dot{\gamma}_R$	158
4.30	$(\alpha_2 - \alpha_1)$ as function of ϕ	159
4.31	Normalized pore pressure P_f as function of ϕ	161
4.32	$\frac{\Sigma_{22}^p(\dot{\gamma}_R)}{\Sigma_{12}}$ as function of ϕ	162
4.33	λ_2 and λ_3 as function of ϕ	163
4.34	$q(\phi)$	164
4.35	Σ_{33}^p as function of ϕ	165
4.36	The variation of (Π/Σ_{12}) with ϕ	166
4.37	Normalized pore pressure P_f as function of ϕ	167
4.38	$\Sigma_{22}(r)$ and $P_f(r)$ for a $\phi = 0.47$ suspension	168

4.39	Shear-banding zones. Remade from [Jarny et al. 2006].	169
4.40	Secondary Flow Radial Velocity	171
4.41	Inertial pressure p_i as function of r	172
4.42	Experimental Setup	173
4.43	Glycerine Injection	173
4.44	StreamLines	174
4.45	The Fronts	174
4.46	Front Displacement	175
4.47	Suspension Experimental Setup	176
4.48	Inward and Outward Migration. (Particles in White)	177
4.49	Suspension Outward Front displacement	178
5.1	Transient Concentration Profiles at 200 & 12000 revolutions	184
5.2	Transient Concentration Profiles $\omega t = 10^5$	186
5.3	Steady State Concentration Profiles of 30% initial suspension	188
5.4	Steady State Concentration Profiles of 40% initial suspension	189
5.5	Steady State Concentration Profiles of 50% initial suspension	190
5.6	Steady State Concentration Profiles of 40% initial suspension	191
5.7	Steady State Concentration Profiles of 40% initial suspension	192
6.1	Suspension flow between shearing and extending	196
6.2	compression-tension axes	198
6.3	B_t , B_c , and C as function of $\hat{\rho}_k$	200
6.4	Steady State Concentration Profiles of 40% initial suspension	202
6.5	The “Frame-Invariant” SBM 2D Steady State ϕ	202
6.6	Transient Concentration Profiles of 55% initial suspension	203
6.7	The “Frame-Invariant” SBM 2D concentration at 200 revolutions	203
6.8	Experimental [Metzger et al. 2011] initial 30% suspension cloud in an oscillatory shearing between two parallel plates.	204
6.9	Taken From [Metzger et al. 2011]	205
6.10	2D-Mesh of the 30% suspension cloud	205

6.11 30% suspension cloud extension in the flow direction at a strain amplitude $\gamma_0 = 8$.	206
6.12 30% suspension cloud extension in the flow direction	207
6.13 xy-2D mesh of the wide-gap Couette cell	210
6.14 Initial conditions on ϕ at $t = 0$	211
6.15 Concentration profile at 45 turns of the inner cylinder ($\phi \equiv c$), $\phi_m = 0.64$.	212
A.1 Wedge type Schematic	221

List of Tables

1.1	Dispersions Classification.	32
1.2	Forces present in a suspension.	34
1.3	Orders of magnitude of different force ratios	35
1.4	Numerical Simulations of 40% Suspension Normal Stress Differences. From [Sierou and Brady 2002]	45
4.1	Suspensions we used in our experiments	131
4.2	Correspondence between R_{real} & $R_{effective}$	136
4.3	Constitutive Laws of a ($2a = 140 \mu m$) suspension	144
4.4	α_1/η_s and α_2/η_s at different η_0 vlaues for $\phi = 45\%$	151
4.5	<i>From the values of α_1 and α_2 given in the paper of Singh & Nott (2003), the radial normal stress in the cylindrical Couette geometry is recalculated (4th column). The slopes of $[\Sigma_{zz}(\frac{r}{R})/\eta_0\dot{\gamma}_R]$ for the different volume fractions of particles are deduced from the Figure10 of the Singh and Nott paper (5th column). At last, the corrected values of α_1 and α_2 are deduced from their previous equations.</i>	154
4.6	Values of α_1/η_s and α_2/η_s at present measurements compared to the corrected ones obtained by [Singh and Nott 2003].	155
4.7	suspension Fronts Radial Velocities	178

INTRODUCTION

This thesis covers the rheology of concentrated non-Brownian suspensions and shear-induced migration of particles. The rheology of non-Brownian suspensions of solid spheres has been capturing many attentions widely, illustrated in numerous studies that have been done from about the 1970s. These suspensions are spreading quickly in our daily life in different forms such as paints, cosmetics, detergents, food stuffs, mud, fuel, rivers, etc... Thus, the knowledge and understanding of their mechanical behavior is very important and have motivated numerous theoretical, numerical, and experimental studies. The modelisation of concentrated suspensions is a hard task since the multibody-interactions have to be taken into account. An experimental characterization is also difficult because several complex phenomena such as wall slip or shear-induced migration can take place. This last phenomenon that leads to particle concentration inhomogeneities, and originates in size segregation in polydisperse systems, is observed in many flows and constitutes a crucial problem in many industrial processes.

Many experimental studies have been performed in order to characterize the shear-induced migration and to identify the mechanisms responsible for it.

Basically there exist two models which account for the particle migration. The first one is called “shear induced diffusion model” which explains the migration through the hydrodynamic collisions between particles in the shear flow. This model is phenomenological and does not allow a quantitative prediction of the migration since it introduces some diffusion coefficients which are not easily

reachable theoretically nor experimentally. The second model, named “Suspension Balance Model (**SBM**)”, is based on the action of the particle normal stresses which are present in a concentrated suspension subject to a shear flow. The predictions of this model could be quantitative. Nevertheless, there exist only few experimental data on the dependence of the particle normal stresses in a suspension on the shear rate value, or on the particle volume fraction.

The **SBM** was first formulated by [Nott and Brady 1994] to explain the particle migration toward the center-line in pressure-driven channel flow. This model has been refined by [Morris and Boulay 1999] to introduce the anisotropy of the particle stress tensor Σ^P . They proposed an expression for Σ^P such that the concentration profiles measured by other authors in various geometries ([Phillips et al. 1992] for a Couette flow, [Chapman 1990, Chow et al. 1994] for a parallel-plate torsional flow, and [Chow et al. 1995] for a cone and plate flow) fit the model. We propose here a direct determination of Σ^P and of the suspension material functions (the viscosity η_s and the normal stress differences N_1 and N_2) in a parallel-plate torsional flow. The direct determination of the normal stress differences and of the particle stress tensor are quite rare.

First [Gadala-Maria 1979] showed that the normal stress differences (more precisely $(N_1 - N_2)$) are proportional to the shear stress and are of the same order of magnitude.

[Zarraga et al. 2000] determined the Normal stress differences thanks to the anti-Weissenberg effect, and to the total force measurements exerted on a rotating cone or disk, on top of a stationary plane. They measured that N_1 & N_2 are both negative and that $N_1 \sim \frac{N_2}{4}$.

Later [Singh and Nott 2003] proposed a technique to measure both N_1 & N_2 by coupling data taken from two separate experiments, that’s by installing pressure transducers in a Couette cell geometry from one side, and in a two parallel disk cell from the other side. They obtained negative N_1 & N_2 , and $N_1 \approx N_2$.

Recently, [Boyer et al. 2011 a] have measured precisely $(N_1 + 2N_2)$ as a

function of the volume fraction of particles ϕ , using the anti-Weissenberg effect, in addition to, [Couturier et al. 2011] who have determined the second normal stress difference N_2 , by measuring the deformation of the free surface of a suspension flow in a narrow inclined channel. The latter two measurements show that N_1 is of the order of zero, and that N_2 is negative.

The numerical simulations of [Yeo and Maxey 2010a] using the Force Coupling Method (**FCM**) and the Stokesian Dynamics (**SD**) of [Sierou and Brady 2002] show that both N_1 and N_2 are negative, but with $N_1 \approx N_2$ in the **SD** simulations, and $N_1 \lesssim N_2$ in the **FCM**.

Concerning the measurement of the particle normal stress tensor, we can mention [Deboeuf 2008, Deboeuf et al. 2009] who were able to determine the third particle normal stress (in the vorticity direction), through the measurement of the pore pressure in a sheared suspension in a Couette cell. A so recent work of [Boyer et al. 2011 b] where the second particle normal stress has been measured is also to be mentioned. There exist also numerical estimations of the particle normal stresses both in Stokesian Dynamics [Sierou and Brady 2002] and in the **FCM** [Yeo and Maxey 2010a].

In this manuscript, we describe how the whole particle normal stress tensor is measured and the way the two normal stress differences are determined through, using a parallel-plate torsional flow device. For this purpose, we measure the radial profile of the second normal stress, $\Sigma_{22}(r)$ (in the velocity gradient direction) in the parallel-plate configuration. The first and the second normal stress differences are deduced from that profile [Bird et al. 1977]. Furthermore, we measure the pore pressure, P_f , in the suspension that allows one, when it is subtracted from the total normal stress, Σ_{22} , to evaluate the particle stress tensor.

Once Σ^p is determined, the **SBM** equations are implemented in the [Open-FOAM®] open source package. The stationary and transient concentration profiles are calculated for various simple shear flows (rectangular, circular channels and wide, narrow gap Couette cells) and compared to experimental and

numerical data found in the literature. Then following [Miller and Morris 2009], we extend our code to the 2D general case where the flow is no more restricted to be a simple shear. After a validation of the code with the flows of suspensions in channels and Couette cells, the general 2D solver is applied to the case of a 2D oscillating shear of a particle cloud between two parallel-plates [Metzger et al. 2011]. Finally, the last neutrally buoyant general 2D code is also re-extended to account for buoyancy and is validated through the case of resuspension and mixing of a suspension in a horizontal Couette cell [Rao et al. 2002 b].

Chapter 1

STATE OF THE ART

1.1 OVERVIEW

This chapter (1) includes the state of the art of the subject of this thesis. We present an introduction to Rheology in section (1.2), where we talk about its history. In section (1.3) an introduction to suspensions is made, where their rheophysics are covered in section (1.4). The Rheometry and its techniques are introduced in section (1.5), while the phenomenon of shear-induced migration of particles inside the suspensions is presented in section (1.6) with the experimental views in literature. Numerical modeling via different models for the latter phenomenon is shown in sections (1.7) and (1.7.4).

1.2 AN INTRODUCTION TO RHEOLOGY

1.2.1 Run-up to rheology (before 1929)

The period prior to the formal creation of the discipline of rheology, included tremendous efforts by numerous scientists at different key times [Deepak Doraiswamy]. The antiquity period shined out through Archimedes around 250 B.C., and [Newton 1687] who worked on Ideal Materials especially Perfect

1.2. AN INTRODUCTION TO RHEOLOGY

Rigid Bodies. Later, Ideal Elastic Solids have been born through out the work of Young (1807), and [Cauchy 1827] based on the efforts of [Boyle 1660] and [Hooke 1678]. By the 1700s, [Pascal 1663] eased out the way for [Bernoulli 1738] and [Euler 1755] to attack well what is known now under Inviscid Fluids¹. At the early 1800s, Newtonian-Liquids have been well named, and it was a celebration period because it was the birth of the [Navier 1823] - [Stokes 1845] equations which can describe the motion of a fluid in a given geometry such as a [Poiseuille 1841]. At the mid 1800s, Linear Viscoelasticity was defined and different Models were set up to describe this behavior of liquids, by different scientists like [Maxwell 1867], and [Boltzmann 1878]. By the early 1900s, more complex nonNewtonian-Liquids (suspensions, polymers..) behaviors have been observed experimentally, and have been well described through many mathematical Models by variety of physicists and mathematicians. We mention some of them like [Einstein 1906], [Bingham 1922], [Jeffrey 1922], and [Hershel and Bulkley 1926].

1.2.2 Rheology birth (1929)

The word “Rheology” was first named by the scientist “[Bingham 1944]” at Lafayette college in 1920, from a suggestion of his colleague, Markus Reiner [Wikipedia®]. During the 3rd decade of the 20th century, the science of Rheology has been born officially, and started to invade the family as the science of deformation and flow of matter.

1.2.3 Rheology since its inception in 1929

Since its inception in 1929, Rheology science has captured the attention of many scientists who have implemented their efforts in different wide areas of activities such as constituting theories and mathematical equations or Models, describing phenomena through experiments, studying advanced materials, and doing numerical computations.

¹Fluids which exhibit no resistance to flow.

1.3. SUSPENSIONS

1.2.4 Present rheology and the new face

As we have seen from the previous short historical excursion of the origins of rheology, we can say nowadays, Rheology is a middle-aged science after a century of previous works, continuing to evolve more and more. However the old face of this science that dealt with things from a nearly “macroscopic scale” has changed now to include the “microscopic scale” point of view of describing different phenomena in an attempt to connect the behavior of matter to its Microstructure [Tanner 2009].

At the moment it is obvious that Rheology is no more a single science discipline, but a one which is applied and well combined completely with other sciences like Physics and Chemistry to yield new disciplines such as Rheo-Physics, Rheo-Chemistry, and even Bio-Rheology.

1.3 SUSPENSIONS

1.3.1 Introduction

Industrial daily-life products like food, paints, cosmetics, detergents, fuel, and alloys, biological materials like milk and blood, in addition to natural ones such as clouds, muds, and rivers, are all examples of dispersions (Systems that are made of a combination of several gas, liquid, and solid phases). From now on, we will be dealing with dispersions systems of type “suspensions” more specifically, suspensions of mono-dispersed Solid particles ² in a continuous Liquid phase, as you can see in the following classification Table (1.1):

		Dispersed Phase		
		Gas	Liquid	<i>Solid</i>
Continuous Phase	Gas		vapors	aero-sol smokes
	<i>Liquid</i>	foams	emulsions	suspensions
	Solid	solid foams		alloys, polymers

Table 1.1: Dispersions Classification.

²All particles are of the same size and type.

1.3. SUSPENSIONS

For particles (solid phase) dispersed in a liquid phase, the two types of interactions that may occur are “particle-particle” and “particle-fluid” interactions. The final complex behavior of the suspension is determined through the dominance of one type of interaction over the other. Therefore, it is crucial to estimate the order of magnitude of the different forces acting on particles.

1.3.2 Inside a suspension

1.3.2.1 Suspension classification

Figure (1.1) shows a classification of suspensions according to the shape and size of the solid particles suspended in the liquid phase.

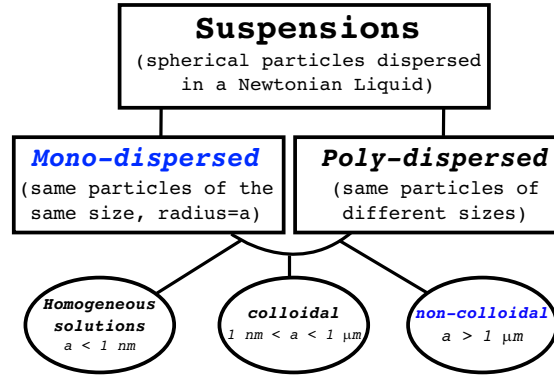


Figure 1.1: Classification of Suspensions.

There are two major parameters that define the state of a suspension:

1. The percentage of particles by volume in the liquid (ϕ), also known as the volume fraction of particles. The particle volume fraction of hard spheres in a suspension is given by

$$\phi = \frac{4}{3}\pi a^3 n \quad (1.1)$$

where n is the particle number density, and a the particle radius. The suspension is said to be dilute usually if ($\phi \leq 5\%$), and dense or concentrated when ($\phi \geq 30\%$).

1.3. SUSPENSIONS

2. The distribution of the particles the suspension. Thus, a well mixed suspension has a homogeneous distribution of particles, which an inhomogeneous suspension does not realize.

1.3.2.2 Forces on particles

Forces of different origins exist and act on the particles inside a suspension. The particle size is very important because it determines the type of particle-particle interactions that are dominant in the suspension, in addition to the significance of the shape of particles which determines the type of particle-fluid interactions. **Our work in this thesis is restricted only to solid spherical particles** of radius a . The following Table (1.2) provides an insight of the different forces that can be present in a suspension.

Forces	Mathematical Form	Parameters
Brownian	kT/a	k : Boltzmann's constant [$J \cdot K^{-1}$] T : Absolute Temperature [K]
Dispersion or Van der Waals	$\Theta_{effective}/a$	$\Theta_{effective}$: Hamaker constant [$N \cdot m$] $\Theta_{effective} = f(\Theta_{particles}, \Theta_{fluid})$
Electrostatic	$\xi \xi_0 \zeta^2$	ξ : dielectric constant of the fluid ξ_0 : permittivity of free space [$F \cdot m^{-1}$] ζ : electrostatic potential of the particles [V]
Hydrodynamic or viscous	$\eta a^2 \dot{\gamma}$	η : medium viscosity [$Pa \cdot s$] $\dot{\gamma}$: shear rate [s^{-1}]
Gravitational	$a^3 \Delta \rho g$	$\Delta \rho$: particle-fluid density difference [$kg \cdot m^{-3}$] g : gravitational constant [$m \cdot s^{-2}$]
Inertial	$\rho_f a^4 \dot{\gamma}^2$	ρ_f : fluid density [$kg \cdot m^{-3}$]

Table 1.2: Forces present in a suspension.

Moreover, in our study and as you will see in the coming chapter (4), we have always the following scalings for our monodispersed neutrally buoyant suspensions: shear rate $\dot{\gamma}$ is $O(1 s^{-1})$, suspension viscosity η is $O(1 Pa \cdot s)$, particle radius a is $O(50 \mu m)$, and fluid-particles-matched density ρ is $O(10^3 kg \cdot m^{-3})$ to the limit of $\frac{\Delta \rho}{\rho}$ which is $O(10^{-2})$. For an aqueous suspension, we have a typical value of $\Theta_{eff} \simeq 10^{-20} N \cdot m$ and $\zeta \simeq 30 \mu V$. All that provide one with a compar-

1.3. SUSPENSIONS

ison between the different forces (orders of magnitude) presented in our work as it is illustrated in the next table:

Different Force ratio	Order of magnitude in our work
$\frac{Brownian}{Viscous} \sim \frac{kT}{6\pi\eta a^3\dot{\gamma}}$	$\sim 10^{-09}$
$\frac{Electrical}{Viscous} \sim \frac{\xi\xi_0\zeta^2}{\eta a^2\dot{\gamma}}$	$\sim 10^{-02}$
$\frac{Dispersion}{Viscous} \sim \frac{\Theta_{eff}}{\eta a^3\dot{\gamma}}$	$\sim 10^{-10}$
$\frac{Gravitational}{Viscous} \sim \frac{a\cdot\Delta\rho\cdot g}{\eta\dot{\gamma}}$	$\sim 10^{-03}$
$\frac{Inertial}{Viscous} \sim \frac{\rho_f a^2\dot{\gamma}}{\eta}$	$\sim 10^{-06}$

Table 1.3: Orders of magnitude of different force ratios

According to table (1.3), the suspensions that will be considered in this study are non-colloidal, non-Brownian, and the flow is non-inertial.

To quantify these two last characteristics, it is usual to introduce two nondimensional numbers, which are the Particle Reynolds Number Re_p , and the Péclet Number Pe [Stickel and Powell 2005].

- The particle Reynolds Number is the ratio between inertial and viscous forces given by:

$$Re_p = \frac{\rho_f \dot{\gamma} a^2}{\eta_f} \quad (1.2)$$

where the subscript f stands for the fluid phase. Re_p is here of the order of $O(10^{-06})$.

- The Péclet Number is the ratio between Hydrodynamic and Brownian forces given by:

$$Pe = \frac{6\pi\eta_f a^3\dot{\gamma}}{kT} \quad (1.3)$$

Pe is here of the order of $O(10^{+09})$.

Moreover, it is good to note that the ratio of Péclet Number to the Reynolds Number is defined as the Schmidt Number given by:

$$Sc = \frac{Pe}{Re} \quad (1.4)$$

1.4 SUSPENSION RHEOPHYSICS

Understanding the behavior of a suspension is quite difficult due to the complexity of the physics which stands behind its Rheology. The behavior of any material is described, and its identity is given, through “material functions” that represent the relation between the applied forces (stress) on it and its response as deformation or shear rate. The **viscometric functions** are some of material functions which are the **viscosity** (1.4.2.1) and the **Normal Stress Differences** (1.4.2.2). The viscometric functions of a suspension will be described later through the methodology of taking firstly the Newtonian liquid alone, then observations on the changes will be done among adding the solid particle phase to the Newtonian matrix.

1.4.1 Material functions

The relations between various stress components, and various deformations, are the material functions, that can be derived from measurements on viscometric flows. The latter flows are generated in apparatus which are made in a way to have a well defined stress field to be applied, in order the kinematics to be measured, or viceversa. The material functions can be divided into both functions derived from shear flows and others derived from extensional flows. However, in this work we will be concerned with some material functions derived only from **shear flows**. The material functions and their methodology of determination are precisely described in [Bird et al. 1977, Bird et al. 1987, Barnes et al. 1989].

1.4.2 Suspension viscometric functions (Viscosity & Normal Stress Differences)

1.4.2.1 Viscosity

Let us consider in Figure (1.2) a shearing force which is generated in a medium (i.e. fluid) between the two surfaces, where one is stationary and the other surface is moving parallel to the fixed one.

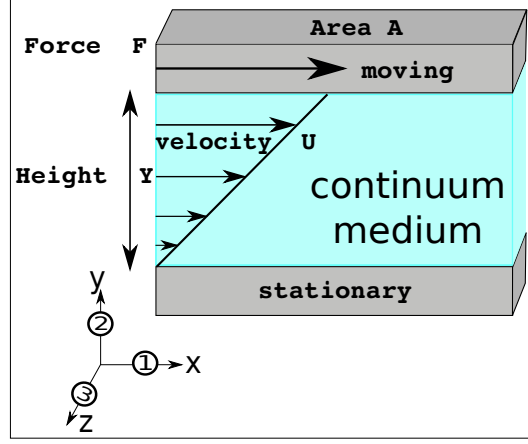


Figure 1.2: Simple shearing of a material (fluid).

An external force \mathbf{F} [N] must be applied to the moving surface to overcome the resistance of the medium. So, if we denote the magnitude of the shearing force by \mathbf{F} , then

$$\tau = \frac{\mathbf{F}}{A} \quad (1.5)$$

is defined as the shear stress (τ [Pa]), with A [m^2] being the area of the moving surface.

For a newtonian liquid, τ is proportional to the shear strain rate or simple shear rate $\dot{\gamma}$ defined as:

$$\dot{\gamma} = \frac{d\mathbf{U}}{dY} \text{ [s}^{-1}\text{]} \quad (1.6)$$

where Y [m] is the height variable and \mathbf{U} [$m \cdot s^{-1}$] is the medium velocity.

The proportionality term is what we call the dynamic viscosity (or the shear viscosity) and assigned the Greek letter eta (η) [Pa · s], where

$$\tau = \eta \frac{d\mathbf{U}}{dY} = \eta \cdot \dot{\gamma} \quad (1.7)$$

The kinematic viscosity coefficient ν in [$m^2 \cdot s^{-1}$], can be simply calculated from the dynamic one by dividing it by the density of the medium ρ .

- **Viscosity of a Suspension**

The “*suspension viscosity*” (η [Pa · s]) is an intrinsic property of the medium (a

1.4. SUSPENSION RHEOPHYSICS

material function) that represents the behavior between external applied forces (shear stress τ [Pa]), and the internal response through deformation rate (shear rate $\dot{\gamma}$ [s^{-1}]). This intrinsic property of the suspension $\eta(\phi)$ is an essential function of ϕ .

Experiments on suspensions of mono-dispersed solid spheres suspended in a Newtonian liquid captured the attention of many scientists. In the very dilute limit ($0 \leq \phi \leq 0.05$) the suspension viscosity obeys the Einstein law [Einstein 1906] given by:

$$\eta = \eta_0 (1 + 2.5\phi) . \quad (1.8)$$

where η_0 is the viscosity of the suspending Newtonian liquid.

Later, Batchelor extended the previous work of Einstein to a higher limit ($\phi \lesssim 0.15$) providing a new suspension viscosity law such that:

$$\eta = \eta_0 (1 + 2.5\phi + K\phi^2) \quad (1.9)$$

where the term in ϕ^2 accounts for hydrodynamic interactions between particle pairs that arise at higher volume fractions. K Values depend on the flow type and range from 4.375 [Roscoe 1952, Brinkman 1952] to 14.1 [Simha 1952]. The Batchelor's value $K = 6.2$ is obtained by taking into account the balance between Brownian diffusion and hydrodynamic interaction [Batchelor 1977].

To simplify a little, from now on, we will be denoting

$$\eta_s = \frac{\eta}{\eta_0} \quad (1.10)$$

as the normalized suspension viscosity (relative viscosity), where η_0 is the viscosity of the Newtonian suspending liquid, and η is the effective suspension viscosity.

The same previous relative suspension viscosity η_s was given later in different forms by many rheologists, who measured and modeled the experimental data

1.4. SUSPENSION RHEOPHYSICS

via various phenomenological equations that take into account the maximum possible packing volume fraction of particles (ϕ_m). We mention some of these models for the relative suspension viscosity presented in literature:

[Krieger and Dougherty 1959]:

$$\eta_s = \left(1 - \frac{\phi}{\phi_m}\right)^{-2.5\phi_m}, \quad (1.11)$$

[Maron and Pierce 1956] (Figure 1.3):

$$\eta_s = \left(1 - \frac{\phi}{\phi_m}\right)^{-2}, \quad (1.12)$$

[Leighton and Acrivos 1986]:

$$\eta_s = \left(1 + \frac{1.5\phi}{1 - \frac{\phi}{\phi_m}}\right)^2, \quad (1.13)$$

[Morris and Boulay 1999]:

$$\eta_s = 1 + 2.5\phi \left(1 - \frac{\phi}{\phi_m}\right)^{-1} + 0.1 \left(\frac{\phi}{\phi_m}\right)^2 \left(1 - \frac{\phi}{\phi_m}\right)^{-2}, \quad (1.14)$$

and [Zarraga et al. 2000]:

$$\eta_s = \frac{e^{-2.34\phi}}{\left(1 - \frac{\phi}{\phi_m}\right)^3} \quad (1.15)$$

Note, ϕ_m depends strongly on the particle shape and interaction, and is measured and found to be between 0.58 and 0.72 for monodispersed spheres. **In our manuscript here, we are only restricted to buoyancy free monodispersed hard spheres suspensions, where we measured in our experiments the viscosity law in equation (1.12) with $\phi_m = 0.58$ (see Figure 1.3).**

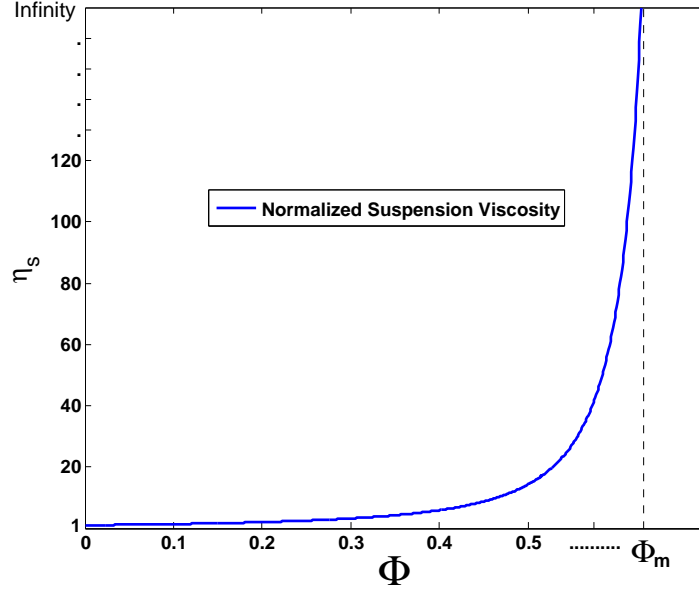
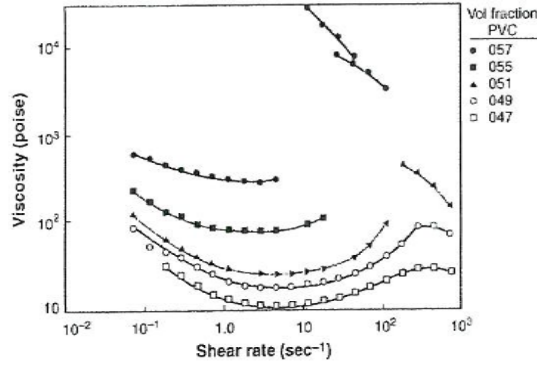


Figure 1.3: Normalized Suspension Viscosity

Figure 1.4: 1.25 μm PVC particles in dioctyl phthalate [Hoffman 1972].

Usually, non-Brownian suspensions are considered as viscous materials (i.e. whose viscosity does not depend on the shear rate $\left\{ \frac{\partial \eta_s}{\partial \dot{\gamma}} \sim 0 \right\}$ [Ovarlez et al. 2006]). But as indicated in Figure (1.4), this assumption is only valid for intermediate shear rate (or shear stress) values [Stickel and Powell 2005]. More different behaviors of the suspension may exist and which depend on the dimensionless numbers Re and Pe (1.3.2.2) as you can see in the phase diagram of Figure (1.5). In our study ($Re \sim 10^{-06}$) & ($Pe \sim 10^{+09}$) so that the

suspension viscosity will be considered as constant in shear rate.

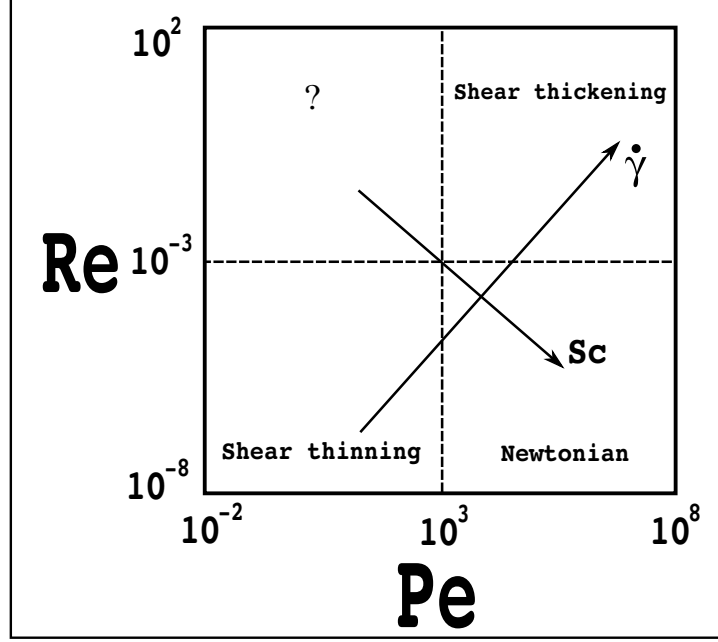


Figure 1.5: "Phase diagram" for suspension rheology, based on a dimensional analysis. Remade from [Stickel and Powell 2005].

1.4.2.2 Normal Stress Differences

1. Definitions

Normal stress differences $\{N_1 \text{ and } N_2\}$ constitute the second and third viscometric functions respectively in addition to viscosity, that characterize the properties of a material. These first & second normal stress differences in the 3D cartesian coordinate system $(x, y, z) \equiv (1, 2, 3)$ are defined as:

$$N_1 = \Sigma_{11} - \Sigma_{22} , \text{ and } N_2 = \Sigma_{22} - \Sigma_{33} , \text{ respectively.} \quad (1.16)$$

where Σ_{11} , Σ_{22} , and Σ_{33} are the three diagonal Normal components of the stress tensor (equation (1.19)). The normal stress differences of a material can be expressed as functions of the shear stress τ or the shear rate $\dot{\gamma}$. In

the following, we will adopt the formulation:

$$N_1 = -\alpha_1 (\dot{\gamma}) \cdot \eta_0 |\dot{\gamma}| ; N_2 = -\alpha_2 (\dot{\gamma}) \cdot \eta_0 |\dot{\gamma}| , \quad (1.17)$$

where α_1 and α_2 are the two measured parameters known as the normal stress coefficients.

2. Measurements Methods

The experimental setups and techniques used to measure α_1 and α_2 in a given material are still developing and under validation until now. A single experimental configuration can not give easily the access to both coefficients α_1 and α_2 separately, but gives usually a combination of them. So, let us go now to reveal some of the experimental setups reported in the literature. We mention first the rotating rod configuration experiment, known from the early works of [Weissenberg 1946], who tried to measure the normal stress differences in polymers. There exist also the rotating parallel cone-plate, parallel plate-plate and truncated-cone-plate configurations (known also as torsional rheometers) that allows one from the measurements of the radial pressure distribution, or from the total thrust force exerted on the plate while shearing, to measure the normal stress differences in steady or in oscillatory shear flows. We mention the early works in these geometries on polymers solutions of [Kotaka 1959, Lipson and Lodge 1968, Kaye et al. 1968, Marsh and Pearson 1968, Lodge and Hou 1980], and some of the recent works of [Jung et al. 2008, Aalcoutabli et al. 2009].

3. Suspension Normal Stress Differences

The studies in literature on suspensions for the measurements of N_1 and N_2 are rare compared to those on polymers. That's why recently different studies and experimental investigations were really interested in measuring the normal stress differences inside suspensions.

The latter studies on suspensions established that the normal stresses are

small at low concentrations, but rise rapidly when ϕ increases ($\phi \gtrsim 0.25$).

Experimentally, The early works started with [Gadala-Maria 1979] who showed that the normal stress differences, used to appear in concentrated suspensions of monodispersed hard spheres, are such that:

($[N_1 - N_2]$ is $O(\tau)$) and are both proportional to the shear stress $\tau = \eta\dot{\gamma}$ (N_1 & $N_2 \propto \tau$). Owing to this proportionality, the coefficients α_1 and α_2 defined in equation (1.17) do not depend on $\dot{\gamma}$ and equation (1.17) becomes:

$$N_1 = -\alpha_1 \cdot \eta_0 \cdot |\dot{\gamma}| ; N_2 = -\alpha_2 \cdot \eta_0 \cdot |\dot{\gamma}| , \quad (1.18)$$

One had to wait a lot till the millenium period when [Zarraga et al. 2000], and [Singh and Nott 2003] restudied the normal stress differences in sheared Stokesian suspensions.

In 2000 the Normal stress differences for monodispersed concentrated suspensions of hard spheres had been determined by [Zarraga et al. 2000] thanks to the anti-Weissenberg effect, and to the total force measurements exerted on a rotating cone or disk, on top of a stationary plane. [Zarraga et al. 2000] calculated both N_1 & N_2 by coupling two different systems where from the total force measurements they got the difference ($N_1 - N_2$), and from the anti-Weissenberg effect experiment they got ($N_2 + \frac{N_1}{2}$). They found that for $0.3 \leq \phi \leq 0.5$ ($N_1 < 0$; $N_2 < 0$ & $|N_1| < |N_2|$) with ($N_1 = (-0.15 \pm 0.05) \alpha \tau$; $N_2 = (-0.54 \pm 0.03) \alpha \tau$; $\alpha = 2.17 \phi^3 e^{2.34\phi}$).

Moreover, later [Singh and Nott 2003] proposed a technique to measure both N_1 & N_2 by coupling data taken too from two separate experimental systems, that's by installing pressure transducers in a Couette cell geometry from one side, and in a two-parallel-disks cell from the other side where the suspension was sheared in a pool of suspension. From

1.4. SUSPENSION RHEOPHYSICS

the axial suspension stress radial profile $\Sigma_{zz}(r)$, in the two-parallel-disks geometry [Singh and Nott 2003] got $(N_1 + N_2)$, and from the cylindrical Couette cell experiment obtained $(0.107 N_1 + 1.214 N_2)$. They showed that $(N_1 < 0 ; N_2 < 0 \ \& \ |N_1| \text{ is } O(|N_2|))$ but they do not depend in the same way on ϕ as it was found by [Zarraga et al. 2000].

Recently, [Boyer et al. 2011 a] have measured precisely $(N_2 + \frac{N_1}{2})$ as a function of the volume fraction of particles ϕ , using the anti-Weissenberg effect, in addition to, [Couturier et al. 2011] who have determined the second normal stress difference N_2 , by measuring the deformation of the free surface of a suspension flowing in a narrow inclined channel. The latter two measurements show that N_1 is of the order of zero, and that N_2 is negative (i.e. see their Figure 7 [Couturier et al. 2011]).

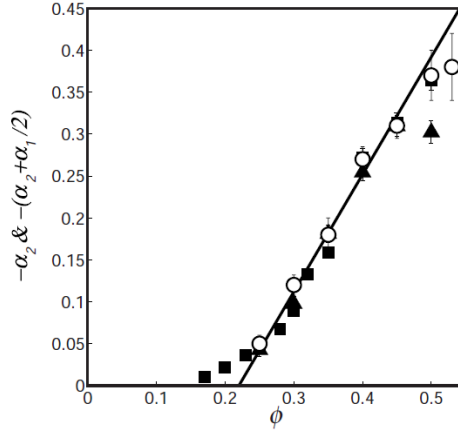


FIGURE 7. Second normal stress coefficient $-\alpha_2$ versus ϕ for present experiments: $a = 35 \pm 5 \mu\text{m}$ (■) and $a = 70 \pm 5 \mu\text{m}$ (▲). Normal stress coefficient combination $-(\alpha_2 + \alpha_1/2)$ versus ϕ for previous experiments of Boyer *et al.* (2011): $a = 70 \pm 5 \mu\text{m}$ (○). Linear fit of Boyer *et al.* (2011): $1.4(\phi - \phi_c)$ (solid line).

In chapter (4) we present in details the latest experimental set up, we developed, and reveal the study after measurements of the 3 material functions η , N_1 , and N_2 in monodispersed suspensions of hard spheres at different shear rates $\dot{\gamma}$, and at a wide zone of volume fraction of particles ϕ .

Numerically, the computations of normal stress differences for monodispersed concentrated suspensions of hard spheres are few. [Sierou and

1.4. SUSPENSION RHEOPHYSICS

[Brady 2002] via Stokesian Dynamics (**SD**) simulations (suspension as an infinite medium) showed that both N_1 and N_2 are negative, and N_1 is $O(N_2)$. They studied systems of number of particles N^* between 125 & 1000, for volume fractions ϕ between 0.10 & 0.50, and for an interparticle force $\mathcal{F} = \dot{\gamma}^* = 1000$ as you can see in the following Table 1.4.

N^*	η_s	$-N_1$	$-N_2$
125	6.2180 \pm 0.058	0.7830 \pm 0.038	0.8656 \pm 0.037
256	6.2286 \pm 0.072	0.8582 \pm 0.074	0.8536 \pm 0.150
512	6.2413 \pm 0.036	0.8301 \pm 0.047	0.8486 \pm 0.025
1000	6.2152 \pm 0.035	0.8396 \pm 0.025	0.8342 \pm 0.032

Table 1.4: Numerical Simulations of 40% Suspension Normal Stress Differences. From [Sierou and Brady 2002]

Recently, using the Force Coupling Method (**FCM**), [Yeo and Maxey 2010a, Yeo and Maxey 2010b] calculated the normal stress differences N_1 and N_2 for concentrated monodispersed suspensions of hard spheres. They did three-dimensional numerical simulations of concentrated suspensions of $O(1000)$ particles in a Couette flow at zero Reynolds number taking into account the wall effects on concentrated suspensions of non-colloidal particles [Yeo and Maxey 2010b]. Their simulations were performed for ϕ between 0.20 & 0.40 and their results are similar to those of [Sierou and Brady 2002] where they found negative N_1 and N_2 values, and N_1 is $O(N_2)$ as you can see in the following plot taken from their (Figure 11 on page 223 [Yeo and Maxey 2010b]):

1.5. RHEOMETRY

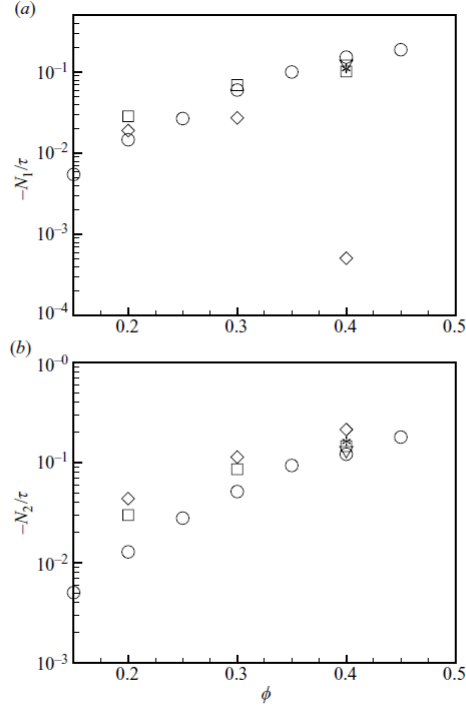


FIGURE 11. Normalized normal stress differences (a) $-N_1/\tau$ and (b) $-N_2/\tau$. \diamond , C2S, C3S and C4S; \square , C2L, C3L and C4La; ∇ , C4Lc; $*$, C4H; \circ , Sierou & Brady (2002).

1.5 RHEOMETRY

Rheometry generically refers to the experimental techniques used to determine the rheological properties of materials (i.e. measurements of η , N_1 , and N_2).

We distinguish two kinds of rheometers:

The shear rheometers such as that in (Figure1.6), and the extensional ones.

1.5. RHEOMETRY

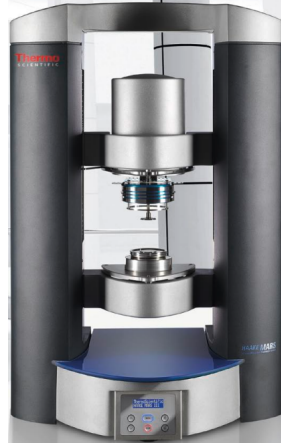


Figure 1.6: HAAKE-Mars Thermo Scientific rotational Rheometer.

Moreover, shear rheometers are divided into two groups: dragflows like the Couette cell apparatus, in which shear is produced between a moving and a fixed solid surface, and pressure-driven flows, in which shear is generated by a pressure difference over a closed channel. The important schematics of these types of shear rheometrical geometries with the coordinate systems used for analysis are shown in Figure (1.7). A detailed analysis on the calculations of the different rheological parameters and the experimental artifacts can be found in [Macosko 1994].





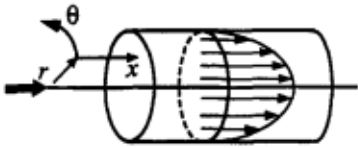
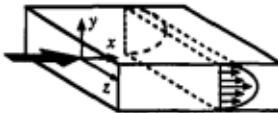
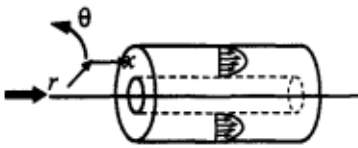
Drag Flows: Chapter 5 (section number)		Coordinates		
		x_1	x_2	x_3
Sliding plates (5.2)		x	y	z
Concentric cylinders (5.3) (Couette flow)		θ	r	z
Cone and plate (5.4)		ϕ	θ	r
Parallel disks (5.5) (torsional flow)		θ	z	r
Pressure Flows: Chapter 6 (section number)				
Capillary (6.2) (Poiseuille flow)		x	r	θ
Slit flow (6.3)		x	y	z
Axial annulus flow (6.4)		x	r	θ

Figure 1.7: Common shear flow geometries taken from [Macosko 1994].

In our manuscript where we measure the suspension material functions η , N_1 , and N_2 as you will see in chapter (4), we mainly used a two-parallel-disk geometry installed on a shear rheometer. Moreover

in a coming section, we will detail how to measure these material functions in such a geometry.

1.5.1 Stress, Strain, and the local Shear-rate

1.5.1.1 The Stress Tensor

The Stress is the quantity that represents applied forces on the surfaces of a volume, which will be the cause of any resulting deformation in that volume. In the 3D cartesian coordinate system $(x, y, z) \equiv (1, 2, 3)$ the Stress Σ is a 2^{nd} rank tensor (i.e. 3×3 Matrix) which has 9 components as you can see in the following Figure (1.8).

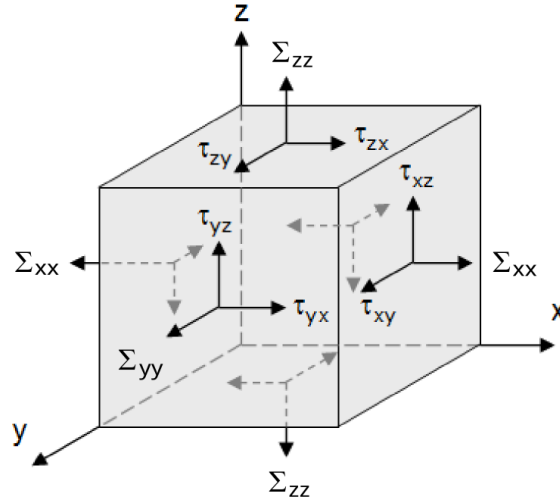


Figure 1.8: Stress Tensor.

$$\Sigma = \begin{bmatrix} \Sigma_{xx} & \tau_{yx} & \tau_{zx} \\ \tau_{xy} & \Sigma_{yy} & \tau_{zy} \\ \tau_{xz} & \tau_{yz} & \Sigma_{zz} \end{bmatrix} \quad (1.19)$$

The first subscript designates the axis perpendicular to the plane subjected to the force while the second subscript designates the direction in which the stress acts in that plane. Normal stresses Σ_{xx} , Σ_{yy} , and Σ_{zz} act on the planes normal to the axes x , y , and z respectively. For the static equilibrium, the shear

1.5. RHEOMETRY

stresses acting on mutually perpendicular planes must be equal:

$$\tau_{xy} = \tau_{yx} ; \tau_{xz} = \tau_{zx} ; \tau_{yz} = \tau_{zy} ; \quad (1.20)$$

Thus the stress tensor Σ is a symmetric tensor that can be completely defined by the only six components: Σ_{xx} , Σ_{yy} , Σ_{zz} , τ_{xy} , τ_{xz} , and τ_{yz} .

The stress tensor Σ can be expressed as the sum of two other stress tensors:

1. A volumetric stress tensor or mean normal stress tensor, $-P\delta_{ij}$, which tends to change the volume of the stressed body.
2. A deviatoric component known as the deviatoric stress tensor, ς_{ij} , which tends to distort it.

So, it can be written that:

$$\Sigma_{ij} = -P\delta_{ij} + \varsigma_{ij} , \quad (1.21)$$

where P is the mean stress or pressure given by:

$$P = -\frac{1}{3}\text{trace}(\Sigma_{ij}) = -\frac{(\Sigma_{11} + \Sigma_{22} + \Sigma_{33})}{3} , \quad (1.22)$$

and δ_{ij} is the kronecker delta defined as:

$$\delta_{ij} = \begin{cases} 1, & \text{if } i = j \\ 0, & \text{if } i \neq j \end{cases} . \quad (1.23)$$

1.5.1.2 The Strain (deformation) Tensor

The strain can be seen as the quantity that represents the amount of transformation (deformation) of a body from a reference configuration to a current configuration. In the 3D cartesian coordinate system $(x, y, z) \equiv (1, 2, 3)$ the strain ϵ is also a 2^{nd} rank tensor which has 9 components defined as following:

$$\boldsymbol{\varepsilon} = \begin{bmatrix} \varepsilon_{xx} & \varepsilon_{yx} & \varepsilon_{zx} \\ \varepsilon_{xy} & \varepsilon_{yy} & \varepsilon_{zy} \\ \varepsilon_{xz} & \varepsilon_{yz} & \varepsilon_{zz} \end{bmatrix} \quad (1.24)$$

Strains, like stresses, have normal strain and shear strain components (i.e. perpendicular to or along the face of an element respectively). Normal strain components are ε_{xx} , ε_{yy} , and ε_{zz} in the direction of the axes x , y , and z respectively, that can be represented as follows:

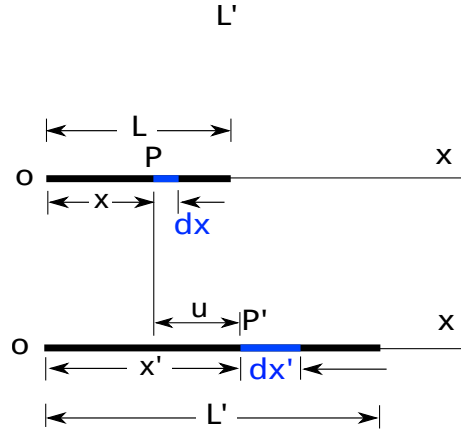


Figure 1.9: Infinitesimal 1D strain

If we consider an arbitrary point P in the bar of Figure (1.9), which has a position vector x , and its infinitesimal neighbor dx . Point P shifts to P' , which has a position vector x' , after the stretch. So, the small "step" dx is stretched to dx' .

The strain at point P can be defined as:

$$\varepsilon_{xx} = \frac{dx' - dx}{dx} \quad (1.25)$$

Since the displacement in the x -direction is $u = x' - x$, the strain can hence be rewritten as:

$$\varepsilon_{xx} = \frac{dx' - dx}{dx} = \frac{du}{dx} \quad (1.26)$$

1.5. RHEOMETRY

Thus, the strain is a 2^{nd} rank tensor that can be summarized as:

$$\epsilon_{ij} = \frac{1}{2} \left[\frac{\partial u_i}{\partial \chi_j} + \frac{\partial u_j}{\partial \chi_i} \right] \quad (1.27)$$

where u is the displacement vector, χ is coordinate, and the two indices i and j can range over the three coordinates $(1, 2, 3) \equiv (x, y, z)$ in three dimensional space.

γ_{ij} is the shear strain that acts in the (i, j) plane defined as:

$$\gamma_{ij} = \frac{\epsilon_{ij} + \epsilon_{ji}}{2} = \epsilon_{ij} \quad (i \neq j) \quad (1.28)$$

Strain rate tensor is the variation of the strain tensor with respect to time denoted as $\dot{\epsilon}$ and is equal to:

$$\dot{\epsilon} = \frac{d\epsilon}{dt} . \quad (1.29)$$

1.5.1.3 The Shear Rate Scalar

In our work the local shear rate will be a scalar quantity defined as:

$$\dot{\gamma} = \sqrt{2\mathbf{E} : \mathbf{E}} \quad (1.30)$$

where $\mathbf{E} = \frac{1}{2} [\nabla \mathbf{U} + (\nabla \mathbf{U})^T]$ is the local rate of strain tensor, and \mathbf{U} is the medium averaged velocity. **So from now on, wherever the words “shear stress” and “shear rate” are mentioned, it is clear that they correspond to the scalar quantities τ , and $\dot{\gamma}$ respectively.**

1.5.2 Conservation Equations

The material (Fluid) (i.e. Suspension) being under flow is considered as a continuum medium that obeys the conservation laws of both mass and momentum [Navier 1823, Stokes 1845].

1.5. RHEOMETRY

1.5.2.1 Mass Conservation

The mass conservation of the material under flow (i.e. suspension flow) is expressed through the continuity equation as follows:

$$\frac{\partial \rho}{\partial t} + \nabla \bullet (\rho \mathbf{U}) = 0 \quad (1.31)$$

where ρ is the material density, t is time, and \mathbf{U} is the flow mean velocity vector field.

1.5.2.2 Momentum Conservation

The momentum equation (or equation of motion) is given by:

$$\frac{\partial (\rho \mathbf{U})}{\partial t} + \nabla \bullet (\rho \mathbf{U} \mathbf{U}) = \nabla \bullet \Sigma + \rho \mathbf{g} \quad (1.32)$$

where Σ is material stress tensor (1.5.1.1), and $\rho \mathbf{g}$ are the gravitational body forces.

In our work, we are restricted to incompressible laminar Stokes flow types at very low Reynolds number ($Re \ll 1$) without external forces and at ($\rho = \text{constant} \ \& \ \frac{D\rho}{Dt} = 0$), where the previous mass continuity and momentum equations can be simplified to:

$$\nabla \bullet \mathbf{U} = 0 \quad (1.33)$$

and

$$\nabla \bullet \Sigma = 0. \quad (1.34)$$

1.5.3 Measurements of η , N_1 , and N_2 in different flows

In order to determine the material functions of a suspension from the measurable macroscopic quantities such as the torque, the force exerted on the flow geometry, or the surface deflection in a free surface flow, we will assume (as

presented in section 1.4.2) that both the shear and the normal stresses depend linearly on the shear rate (**Note** that it is not the case for polymeric liquids). The measurements of normal stress differences N_1 and N_2 through their coefficients α_1 and α_2 , respectively in different standard experimental arrangements can be summarized in the following enumeration:

1. **Rotating rod (material free surface deflection)**

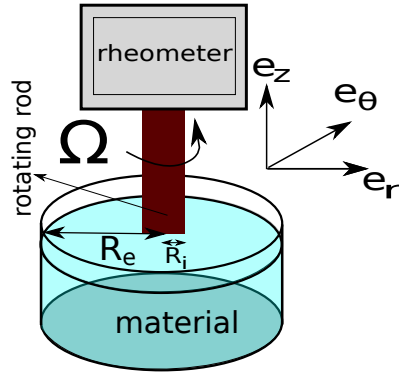


Figure 1.10: Rotating-Rod Instrument

[Zarraga et al. 2000, Boyer et al. 2011 a] used this type of geometry for suspension flows where N_1 and N_2 are responsible for the surface deflection.

In the absence of surface tension and inertia, the normal stress coefficients α_1 and α_2 in a rotating rod geometry of radius R_i and of angular velocity Ω inside a larger stationary cylinder of radius R_e , are given from N_1 and N_2 by:

$$\left(N_2 + \frac{1}{2}N_1\right) = -\rho g \left[(h(R_e) - h(r)) \cdot \frac{r^2 R_e^2}{R_i^2 (R_e^2 - r^2)} \right], \quad (1.35)$$

where h is height of the free surface of the material (i.e. suspension) being deflected.

2. Inclined trough of angle θ relatively to the horizontal direction

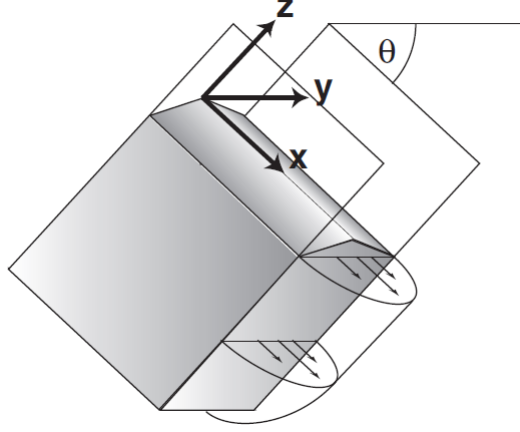


Figure 1.11: Inclined-Plane Flow

[Couturier et al. 2011] following [Tanner 1970] determined the value of α_2 upon analysing the free surface deflection of a suspension flowing through an inclined trough.

In the absence of surface tension and inertia, N_2 is given here (1.11) by:

$$\frac{N_2}{\tau} = - \left(\frac{h(y) - h(0)}{\tan \theta \cdot |y|} \right) \quad (1.36)$$

where $h(0)$ is a constant that can be determined by applying the mass conservation equation, i.e. $\int_{-W}^W [h(y) \cdot dy] \equiv 0$, and $2W$ is the width of the channel.

3. Parallel cone and plate

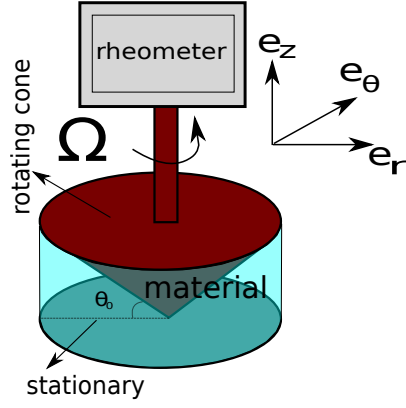


Figure 1.12: Parallel-Cone-Plate Instrument

In this configuration (1.12) N_1 is given by:

$$N_1 = \frac{2F}{\pi R^2 \dot{\gamma}}, \quad (1.37)$$

$$\dot{\gamma} = \frac{\Omega}{\theta_0} \quad (1.38)$$

where R is the radius of circular plate, θ_0 the angle between cone and plate (usually less than 4°), Ω the cone angular velocity, and F the magnitude of the force required to keep tip of cone in contact with the circular plate.

4. Cylindrical Couette cell

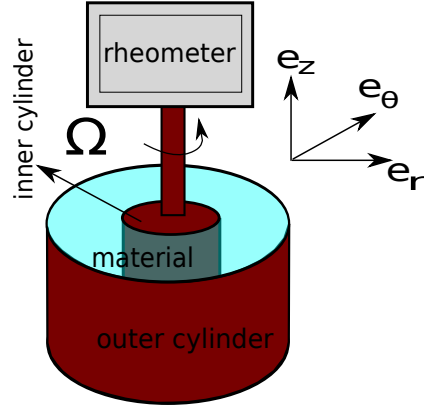


Figure 1.13: Cylindrical Couette cell Viscometer

Figure (1.13) shows a cylindrical Couette cell viscometer of a stationary outer cylinder of radius R_2 . The inner cylinder of radius R_1 is rotating at an angular velocity Ω . The viscometric functions in this geometry are given by:

$$\eta = \frac{\Gamma}{4\pi\Omega H} \cdot \frac{R_2^2 - R_1^2}{R_1^2 R_2^2}, \quad (1.39)$$

$$\beta \frac{N_1}{2} + (1 + \beta) N_2 = \Sigma_{rr}(R_2), \quad (1.40)$$

$$\dot{\gamma} = 2\Omega \frac{R_1^2 R_2^2}{R_2^2 - R_1^2} \cdot \frac{1}{r^2}, \quad (1.41)$$

where H is the height of the cylinders, Γ the torque on inner cylinder, $\Sigma_{rr}(R_2)$ is the measured normal pressures on the outer cylinder, and β a constant that depends on the cylinders radii. As an example, [Singh and Nott 2003] used this geometry for studying suspension flows.

5. Parallel disks

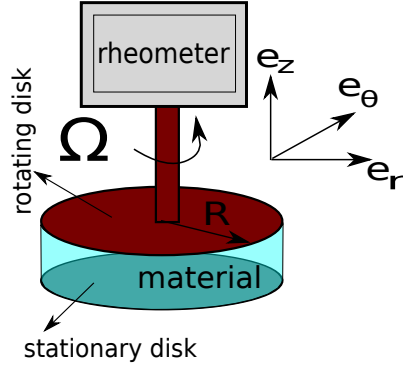


Figure 1.14: Parallel-Disks Instrument

This geometry that will be presented in detail in the following section allows measuring the difference of the first and the second normal stress differences from the total force exerted on one of the disks:

$$(N_1 - N_2) = \frac{F}{\pi R^2} \quad (1.42)$$

This geometry has been used by [Zarraga et al. 2000, Singh and Nott 2003] for the torsional flow of suspensions.

A detailed study on the calculation of the material functions in different geometries of the flow can be found in [Bird et al. 1977, Bird et al. 1987].

1.5.4 Measurements of material functions for a suspension in a torsional flow between two parallel-disks at low Reynolds Number

In our work, we worked on monodispersed suspensions in a torsional flow between two parallel-disks at low Reynolds Number to measure the suspension material functions η , N_1 , and N_2 . That's why it is good to detail here how to measure these material functions in such a geometry. The suspension is placed between two horizontal parallel disks of radius R , separated by a gap H . Then, a torque Γ is applied to the upper disk to rotate it with an angular velocity Ω , while the lower disk is always being stationary. Furthermore, the lower stationary plate is equipped with pressure transducers in such a way that the radial profile of the pressure is measurable. In the following we show that such an installation device allows one to measure the whole 3 material functions η , N_1 , and N_2 . Moreover, such a geometry presents the advantage of preserving a homogeneous concentration of particles in the suspension. Indeed, it is well known that shear-induced migration of particles is absent (or weak) in torsional shear flow between rotating disks, in contrast with other numerous flow geometries like cylindrical Couette cell or cone-plate geometry.

Here, in the torsional flow between two parallel-disks, the velocity is considered orthoradial given by:

$$v_\theta = r\Omega(z) . \quad (1.43)$$

After the projection of Stokes equation on the axes r , and θ one gets respectively:

$$\frac{\partial \Sigma_{33}}{\partial r} + \frac{\Sigma_{33} - \Sigma_{11}}{r} = 0, \quad (1.44)$$

and

$$\frac{\partial \Sigma_{12}}{\partial z} = 0 . \quad (1.45)$$

1.5. RHEOMETRY

The shear rate $\dot{\gamma} = r \frac{d\Omega(z)}{dz}$ is deduced from equations (1.43) and (1.45) on the form:

$$\dot{\gamma}(r) = \frac{\Omega r}{h}. \quad (1.46)$$

The suspension viscosity is related to the ratio of the applied torque on the upper disk, to its speed of rotation given by:

$$\eta = \frac{\Sigma_{12}}{\dot{\gamma}} = \frac{2h\Gamma}{\pi R^4 \Omega}. \quad (1.47)$$

The equation (1.44), using the definitions in (1.18) and upon expressing Σ_{11} and Σ_{33} as a function of Σ_{22} , gives the radial variation of the second component of the normal stress on the following form:

$$\frac{\partial \Sigma_{22}}{\partial r / R} = -\eta_0 \dot{\gamma}_R (\alpha_1 + 2\alpha_2), \quad (1.48)$$

where $\dot{\gamma}_R = \dot{\gamma}(r = R)$.

Equation (1.48) can be integrated now with the hypothesis that $\Sigma_{33}(R)$ is equal to the atmospheric pressure $-P_a$, in order to get $\Sigma_{22}(r)$:

$$\Sigma_{22}(r) = -\eta_0 \dot{\gamma}_R \left[(\alpha_1 + 2\alpha_2) \frac{r}{R} - (\alpha_1 + \alpha_2) \right] - P_a, \quad (1.49)$$

where P_a is the atmospheric pressure that can be simply chosen as the reference ($P_a = 0$).

If one measures the radial profile of Σ_{22} , equation (1.49) makes it possible to determine both α_1 and α_2 , since clearly the slope provides an access to $-(\alpha_1 + 2\alpha_2)$ and the ordinate at origin gives an access to $(\alpha_1 + \alpha_2)$.

Later, in chapter (4) we provide precisely our experimental procedure for the measurements of the material functions in monodispersed suspensions of hard spheres using such a device.

1.6 SHEAR-INDUCED MIGRATION

Here, we report on the particle migration, observed in several geometrical configurations. Numerous experiments of different configurations in the literature, have measured and reported that particles in initially homogeneous suspensions (noncolloidal, neutrally buoyant, rigid, monodispersed spheres suspended in viscous newtonian liquid) migrate usually to the lower-shear-rate regions in nonhomogeneous shear flows:

[Karnis et al. 1966, Arp and Mason 1977, Gadala-Maria 1979, Gadala-Maria and Acrivos 1980, Hookham 1986, Leighton and Acrivos 1987, Chapman 1990, Graham et al. 1991, Altobelli et al. 1991, Abbott et al. 1991, Phillips et al. 1992, Koh et al. 1994, Chow et al. 1994, Hampton et al. 1997, Breedveld et al. 1998, Lyon and Leal I 1998, Shapley et al. 2002, Shapley et al. 2004, Merhi et al. 2005, Ovarlez et al. 2006, Kim et al. 2008, Boyer et al. 2011 a, Deshpande and Shapley 2010]. The time scale of this migration of particles was observed to be completely different from one experimental configuration (e.g. Couette cylindrical cell) to another (e.g. torsional parallel-plate cell).

1.6.1 Migration in different geometries (Experimental Studies)

Most of suspension flow studies have been trying to measure and track the distribution of particles starting from a homogeneous suspension using different experimental techniques. Many of them have focused on the unidirectional simple shear flows such as the Couette cell of two concentric cylinders, the rotating parallel plates, the cone-plate geometry, the rectangular channels, and the circular pipes, while others were even interested in more complex flows. They tracked the concentration profile evolution (migration) of particles in the suspensions via numerous techniques. Some of them are direct like the (Nuclear Magnetic Resonance) **NMR** technique which provides directly the concentration profile $\phi(r)$, while others are indirect such as the (Particles Image Velocimetry) **PIV** and (Laser Doppler Velocimetry) **LDV** techniques that provide $\eta(r)$ from

1.6. SHEAR-INDUCED MIGRATION

which $\phi(r)$ is deduced indirectly according to the suspension viscosity law being adopted.

The Couette cell has captured the attentions of many, like [Abbott et al. 1991, Phillips et al. 1992, Chow et al. 1994, Breedveld et al. 1998, Shapley et al. 2002, Shapley et al. 2004].

In the Couette cell geometry, the measurements of the particle concentrations via numerous techniques showed the presence of radial migration from zones of high shear rate near the inner rotating cylinder toward lower shear rate regions near the outer stationary cylinder [Gadala-Maria 1979, Phillips et al. 1992, Shapley et al. 2002, Ovarlez et al. 2006].

The torsional flow between two rotating parallel disks is another configuration for suspension studies. The early measurements in the parallel plate geometry, reported mostly the absence of migration in semi-dilute and concentrated suspensions [Chan and Powell 1984, Chapman 1990, Chow et al. 1994], or a weak migration in dilute suspensions [Kim et al. 2008] or in concentrated ones [Merhi et al. 2005].

[Chapman 1990] conducted experiments on suspension flow in the parallel cone-plate geometry where an outward migration of particles was observed.

The circular pipes have been capturing the attentions of [Sinton et al. 1991, Hampton et al. 1997, Han et al. 1999]. And in the rectangular channels we mention [Koh et al. 1994, Lyon and Leal I 1998, Lyon and Leal II 1998]. The particles are shown to migrate toward the channel center-line where the shear rate is the lowest [Hampton et al. 1997, Lyon and Leal I 1998].

Even more, many researchers have been interested in suspension flow in complex geometries such as the (contraction \leftrightarrow expansion flows) [Iwamiya et al. 1994, Corbett and Phillips 1995, Altobelli et al. 1997, Rao et al. 2002 a, Rao

et al. 2007, Miller and Morris 2006, Moraczewski et al. 2005, Moraczewski and Shapley 2006, Moraczewski and Shapley 2007, Xi and Shapley 2008], and evolving flows [Miller and Morris 2006, Stickel et al. 2007, Ingber et al. 2009], in order to seek better and understand the particle dynamics at multiple stress components.

1.7 SHEAR-INDUCED MIGRATION MODELING

1.7.1 Overview

We describe briefly the different models that represent the migration with a diffusion flux that originates from the particle collisions in the suspension flow. We will describe more precisely another model, named “Suspension Balance Model” since the goal of this thesis is to determine experimentally (chapter 4) the parameters that intervene in this model. At the end of this manuscript we discuss the influence of these parameters on the predictions of the model.

These models in literature have been successful in predicting steady-state concentration profiles, but many of them have been less successful in predicting the transient concentration profiles over a range of parameters like the particle size a , the volume fraction of particles ϕ , and the geometry of the flow.

1.7.2 Constitutive modeling

As in paragraph (1.5.2), the suspension is considered here as a continuous medium and its behavior is governed by the continuity and the momentum equations, respectively as:

$$\frac{\partial \rho}{\partial t} + \nabla \bullet (\rho \mathbf{U}) = 0 \quad (1.50)$$

$$\frac{\partial (\rho \mathbf{U})}{\partial t} + \nabla \bullet (\rho \mathbf{U} \mathbf{U}) = \nabla \bullet \boldsymbol{\Sigma} + \rho \mathbf{g} \quad (1.51)$$

1.7. SHEAR-INDUCED MIGRATION MODELING

Moreover, we consider here in our study the steady flow of **neutrally buoyant incompressible monodispersed suspensions of hard spheres in a Newtonian Liquid at very low Reynolds Number** ($Re \ll 1$) and without external forces which transform the previous medium continuity equation in addition to the suspension momentum balance to:

$$\nabla \bullet \mathbf{U} = 0, \quad (1.52)$$

and

$$\nabla \bullet \Sigma = -\nabla P + \nabla \bullet \varsigma = \mathbf{0}, \quad (1.53)$$

respectively, where \mathbf{U} is the suspension mean velocity, ς is the deviatoric stress tensor, and P is the pressure ($\Sigma = -P\mathbf{I} + \varsigma$).

Moreover, an equation for the particle conservation can be written as:

$$\frac{\partial \phi}{\partial t} + \mathbf{U} \cdot \nabla \phi = -\nabla \bullet \vec{N}_t \quad (1.54)$$

where \vec{N}_t denotes the particle flux that accounts for different migration mechanisms such as sedimentation, Brownian motion, shear-induced, curvature-induced, or viscosity gradient-induced migrations. Equation (1.54) is solved in parallel with equations (1.52) & (1.53) to track the evolution of the particle concentration ϕ and of the flow field. **Here, we will be neglecting sedimentation and Brownian motion due to the neutrally buoyant non-colloidal suspensions we deal with.**

In the next section we describe briefly the different diffusive models in the literature that express \vec{N}_t as a diffusive flux. A detailed study on these different models can be found in the paper of [Kim et al. 2008].

1.7.3 Diffusion Models

1.7.3.1 Original Phillips Model

[Phillips et al. 1992] extended the works of [Leighton and Acrivos 1987, Leighton and Acrivos 1987] into the flux equation (1.54), where they explained the migration of particles from their net displacement during collisions, and proposed that this migration is the result of two fluxes induced by gradients of both viscosity and collision rate. They defined the collision flux as originating from the gradients in shear rate and in particle concentration:

$$\vec{N}_c = -K_c a^2 \phi \nabla (\phi \dot{\gamma}) \quad (1.55)$$

being explained physically as the migration of particles from zones where they experience high number of collisions (high shear rate zones) to regions of lower number of collisions among the particles (lower shear rate zones) (see Figure 1.15a). They defined the gradients in viscosity as the flux:

$$\vec{N}_\eta = -K_\eta \frac{a^2 \dot{\gamma} \phi^2}{\eta} \frac{d\eta}{d\phi} \nabla \phi \quad (1.56)$$

that accounts for the tendency of particles to migrate from the high to low viscous regions. Physically speaking, this flux exists (see Figure 1.15b) because during a collision the particle displacement is higher in the low viscous regions rather than in the high viscous ones. K_c and K_η are empirical parameters fitted experimentally. Thus the total flux \vec{N}_t responsible for migration, implemented in equation (1.54), had been given on the form of $\vec{N}_t = \vec{N}_c + \vec{N}_\eta$.

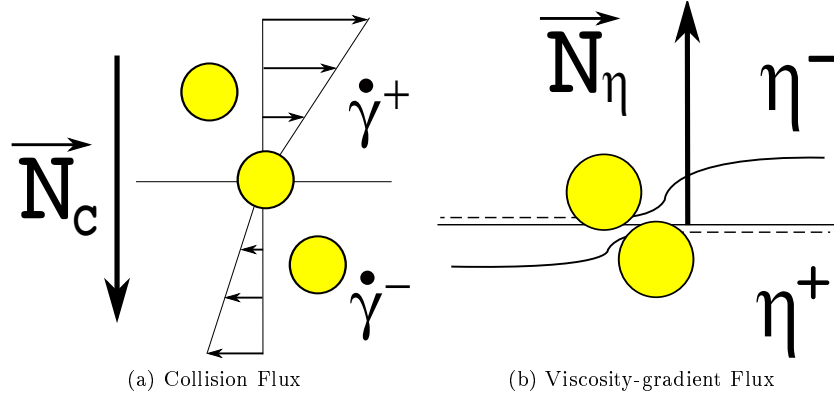


Figure 1.15: Diffusive Fluxes

Numerous experiments had and have been conducted to test the validity of the original Phillips' model. However, the failure of this model to predict well the migration of particles in a torsional flow between two parallel plates, had been reported through experimental evidences by [Chapman 1990, Chow et al. 1994]. They found that there is no, or very weak [Merhi et al. 2005], migration of particles in the torsional flow of a suspension between two parallel disks, which is in strong contrast with the original Phillips model that predicts an inward migration due to the linear radial dependence of the shear rate.

1.7.3.2 Modified Phillips Model

[Krishnan et al. 1996] proposed to introduce an additional migration flux originated from the flow curvature. They defined this additional curvature-induced flux as:

$$\vec{N}_r = K_r \mathbf{n} \kappa a^2 \dot{\gamma} \phi \quad (1.57)$$

being explained as the flux due to the different curved-streamlines in a shear flow (see Figure 1.16). The term \mathbf{n} is the unit normal vector in the radially outward direction in curved-streamline shear flow, κ is the curvature of the streamline, and K_r is an experimentally fitted parameter that must be re-adjusted with the other two previous parameters K_c and K_η . Finally, the total flux in the

modified Phillips model implemented in equation (1.54) had the form of $\vec{N}_t = \vec{N}_c + \vec{N}_\eta + \vec{N}_r$.

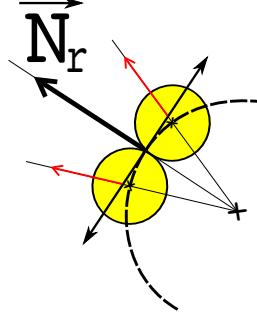


Figure 1.16: Curvature Flux

1.7.3.3 ϕ -Dependent K_c Model

[Graham et al. 1998] updated the last modified Phillips model by considering the parameter K_c as a function of the volume fraction of particles ϕ . Their argument was based on the works of [Brady and Morris 1997, Tetlow et al. 1998] such that when the original Phillips model (1.7.3.1) was employed in Couette cell experiments to predict the particle distribution, it was revealed that the outward migration happening near the inner cylinder wall was overestimated. Nevertheless this can be cured by introducing ϕ -dependent parameters.

1.7.3.4 Flow-aligned Tensor Model

This one here was based on the works of [Brady and Morris 1997] who introduced the idea of the non-isotropic nature of diffusion and migration processes, and employed it in their flow aligned tensor model in the velocity, velocity-gradient and vorticity directions. Later [Fang et al. 2002] incorporated the flow aligned tensor model concept into the diffusive flux model (original Phillips model (1.7.3.1)), and thus modified the two fluxes as the following:

$$\vec{N}_c = -K_c a^2 \phi \nabla (\phi \dot{\gamma} \mathbf{Z}) \quad (1.58)$$

$$\vec{N}_\eta = -K_\eta a^2 \phi^2 \dot{\gamma} \mathbf{Z} \nabla \ln \phi \quad (1.59)$$

1.7. SHEAR-INDUCED MIGRATION MODELING

where \mathbf{Z} is the flow aligned tensor that can be determined by imposing inhomogeneity in velocity, velocity-gradient, and vorticity directions.

Note that, in order to capture the experimental observations in various geometries with different particle volume fractions, authors had to introduce so many parameters that any quantitative prediction concerning the migration is not possible yet.

1.7.3.5 Migration-Time Scaling

The characteristic time τ_c for the migration in this modeling can be simply observed from equation (1.54) to scale as:

$$\tau_c \sim \left(\frac{H}{a}\right)^2 \frac{1}{\dot{\gamma}} \quad (1.60)$$

where a is the particle radius, $\dot{\gamma}$ the shear rate, and H is a lengthscale of the flow.

1.7.4 Suspension Balance Model

It was first proposed by [Nott and Brady 1994] and modified later by [Morris and Boulay 1999]. Its physical concept is that an inhomogeneous stress that exists due to the particle phase inside the suspension during flow, would be responsible for a migration phenomenon of the particles in order to balance that inhomogeneity (Figure (1.17)). The migration flux \vec{N}_t is defined as:

$$\vec{N}_t \equiv \vec{j}_\perp = \frac{2a^2}{9\eta_0} f(\phi) [\nabla \bullet \Sigma^p]. \quad (1.61)$$

where $f(\phi)$ is the sedimentation hindrance function that represents the mobility of the particle phase. Σ^p is the particle stress tensor that depends on both the concentration of particles ϕ and the shear rate $\dot{\gamma}$. The migration flux $\vec{N}_t \equiv \vec{j}_\perp$ in this model is directly proportional to the divergence of the particle stress tensor Σ^p . It can be seen as a result of concentration gradients in the suspension or shear rate gradients which induce gradients in the particle stress. In other

words, since $\Sigma^p = f(\phi, \dot{\gamma})$, if $\dot{\gamma} \neq \text{constant}$ or if $\phi \neq \text{constant}$ then a particle flux appears.

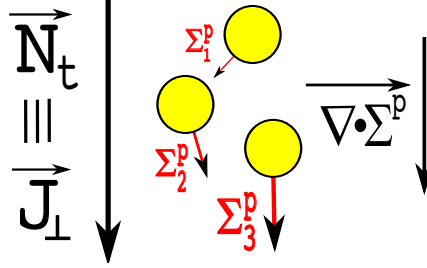


Figure 1.17: Migration Flux \vec{j}_\perp^p

We adopt this model in our work because it is the most quantitative and the least parametric among the previous ones mentioned above. Moreover, as you will see in chapter (4) that most (if not all) of the terms in this model can be measured experimentally.

1.7.4.1 Overview

The Suspension Balance Model is restricted to suspension flow of rigid monodispersed spherical particles of radius a immersed in a Newtonian fluid of density ρ_0 and viscosity η_0 . The flow of a suspension in this Model is assumed at viscous conditions where Reynolds number $Re = \frac{\rho_0 \dot{\gamma} a^2}{\eta_0}$ vanishes ($Re \rightarrow 0$), and where Brownian effects are neglected at infinite Péclet number $Pe = \frac{3\pi\eta_0 \dot{\gamma} a^3}{kT}$ ($Pe \rightarrow \infty$). The volume fraction of particles is in the range of $0 < \phi < \phi_m$, where ϕ_m is the maximum packing volume fraction of particles.

1.7.4.2 Mass and Momentum Conservation Equations

In this Suspension Balance Model the mixture of two phases (the particles and the fluid) is considered as a bulk suspension (continuous medium) that of course obeys the laws of conservation of mass and momentum. This approach was first developed by [Nott and Brady 1994] assuming that the particle phase can be taken as a continuum. Formally, [Drew and Lahey 1993] did an averaging procedure to get the mass conservation equation of the particle phase that is

$$\frac{\partial \phi}{\partial t} + \nabla \bullet (\mathbf{U}^p \phi) = 0, \quad (1.62)$$

where \mathbf{U}^p is the local velocity of the particle phase.

The particle momentum conservation at very small Reynolds number ($Re \rightarrow 0$) and at no external force is given by:

$$\nabla \bullet \Sigma^p + n \langle \mathbf{F}^H \rangle_p = \mathbf{0}, \quad (1.63)$$

where $\langle \rangle_p$ is the average on the particle phase, $n = \frac{3\phi}{4\pi a^3}$ is the number density of particles, and \mathbf{F}^H is the hydrodynamic drag force on a particle given by:

$$\mathbf{F}^H \cong -6\pi\eta_0 a f^{-1}(\phi) (\mathbf{U}^p - \mathbf{U}) \quad (1.64)$$

$f^{-1}(\phi)$ is the mean resistance since $f(\phi)$ is the sedimentation hindrance function that represents the mobility of the particle phase. [Richardson and Zaki 1954], and [Davis and Acrivos 1985] provided the form of $f(\phi)$ as

$$f(\phi) = \left(1 - \frac{\phi}{\phi_m}\right) (1 - \phi)^{\alpha-1}, \quad (1.65)$$

where $\alpha \in [2, 4]$ is a fitting parameter depending on the particles type. We adopted this form of $f(\phi)$ in our work, however there exist other forms of $f(\phi)$ such that used by [Morris and Boulay 1999]:

$$f(\phi) = (1 - \phi)^\alpha \quad (1.66)$$

The difference between both forms is the dependence of $f(\phi)$ on the maximum packing volume fraction of particles ϕ_m . We adopted a ϕ_m -dependent $f(\phi)$ based on the fact that the suspension has no settling velocity at $\phi = \phi_m$.

The migration flux in this modeling is defined as:

$$\vec{j}_I = \phi (\mathbf{U}^p - \mathbf{U}) \quad (1.67)$$

1.7. SHEAR-INDUCED MIGRATION MODELING

where the symbol \perp is used to denote the cross-stream direction of the migration.

Upon using this definition for \vec{j}_\perp , the flux $\vec{j}_\perp \equiv \vec{N}_t$ on its final form is obtained by substituting equation (1.64) in equation (1.63) such that:

$$\vec{j}_\perp = \phi (\mathbf{U}^p - \mathbf{U}) = \frac{2a^2}{9\eta_0} f(\phi) [\nabla \bullet \Sigma^p]. \quad (1.68)$$

The general final form of the particle mass conservation equation in (1.62) becomes:

$$\frac{\partial \phi}{\partial t} + \mathbf{U} \cdot \nabla \phi = -\nabla \bullet \left[\frac{2a^2}{9\eta_0} f(\phi) [\nabla \bullet \Sigma^p] \right]. \quad (1.69)$$

Thus, the knowledge of Σ^p and its variation in ϕ allows predicting the particles migration whatever the geometry is.

1.7.4.3 Migration-Time Scaling

Assuming that Σ_{ii}^p is $O(\eta\dot{\gamma})$, one can note that the migration time τ_m scaling provided by this Suspension Balance Model is consistent with that obtained in the diffusion models:

$$\tau_m = \left(\frac{H}{a} \right)^2 \frac{1}{\dot{\gamma}} \quad (1.70)$$

1.7.4.4 The Non-Colloidal Suspension Stress

In this model the total stress Σ is decomposed into a fluid phase stress Σ^f , and a particle phase stress Σ^p such that:

$$\Sigma = \Sigma^f + \Sigma^p. \quad (1.71)$$

The fluid phase stress Σ^f is defined as

$$\Sigma^f = -\hat{P}_f \mathbf{I} + 2\eta_0 \mathbf{E}, \quad (1.72)$$

1.7. SHEAR-INDUCED MIGRATION MODELING

where $\mathbf{E} = \frac{1}{2} [\nabla \mathbf{U} + (\nabla \mathbf{U})^T]$ is the local rate of strain tensor, and \hat{P}_f is the local fluid phase pressure. [Morris and Boulay 1999] suggested the constitutive law for the particle phase stress for shear flows as the following

$$\Sigma^p = -\Sigma_{nn,1}^p + 2\eta_0\eta_P(\phi)\mathbf{E} \quad (1.73)$$

where $\Sigma_{nn,1}^p = \eta_0\eta_N(\phi)\dot{\gamma}\mathbf{Q}$ is the particle normal stress diagonal tensor, $(2\eta_0\eta_P(\phi)\mathbf{E})$ is the particle shear stress tensor, $\eta_P(\phi) = (\eta_s(\phi) - 1)$ is the shear viscosity of the particle phase dimensionlessed by the viscosity of the suspending liquid η_0 , and $\eta_N(\phi)$ is “the normal stress viscosity” depending on ϕ . In their original paper, [Morris and Boulay 1999] proposed the following expression for $\eta_N(\phi)$:

$$\eta_N(\phi) = K_N \left(\frac{\phi}{\phi_m} \right)^2 \left(1 - \frac{\phi}{\phi_m} \right)^{-2} \quad (1.74)$$

where K_N is a fitting parameter that was set to 0.75 to match the experimental data of [Phillips et al. 1992].

\mathbf{Q} is a parametric symmetric tensor of the form

$$\mathbf{Q} = \begin{bmatrix} 1 & 0 & 0 \\ 0 & \lambda_2 & 0 \\ 0 & 0 & \lambda_3 \end{bmatrix} \quad (1.75)$$

that physically captures the anisotropy of the normal stress of the particle phase. Here, the principal directions of the tensor \mathbf{Q} in (1.75) are those of a viscometric shear flow as mentioned before with 1, 2, 3 denoting flow, velocity gradient, and vorticity directions, respectively. It is preferred to mention that the determination of the local principal directions for the flow becomes more complicated in general flow conditions. We will let this subject open to later discussion in chapter(6), where we developed a General Frame-Invariant 2D code.

The two normal stress differences and the suspension pressure Π are given in terms of this modeling by

$$N_1 = (\Sigma_{11} - \Sigma_{22}) = (\Sigma_{11}^p - \Sigma_{22}^p) = -\eta_0 \eta_N \dot{\gamma} (1 - \lambda_2), \quad (1.76)$$

$$N_2 = (\Sigma_{22} - \Sigma_{33}) = (\Sigma_{22}^p - \Sigma_{33}^p) = -\eta_0 \eta_N \dot{\gamma} (\lambda_2 - \lambda_3), \quad (1.77)$$

and

$$\Pi = -\frac{1}{3} \text{tr}(\Sigma^p) = -\Sigma_{11}^p \left(\frac{1 + \lambda_2 + \lambda_3}{3} \right) = -\left[\Sigma_{22}^p + \frac{1}{3}(\alpha_1 - \alpha_2) \right], \quad (1.78)$$

where $\text{tr}(\Sigma^p) = (\Sigma_{11}^p + \Sigma_{22}^p + \Sigma_{33}^p)$ with 1, 2 & 3 denoting flow, velocity gradient and vorticity directions, respectively.

The combination of the above definitions for both, the particle phase and fluid phase stress, Σ^f & Σ^p yields finally to a Bulk Suspension Stress Σ in the Suspension Balance Model of the form

$$\Sigma \equiv \Sigma^T = \Sigma^f + \Sigma^p = -P\mathbf{I} - \eta_0 \eta_N \dot{\gamma} \mathbf{Q} + 2\eta_0 \eta_s \mathbf{E}, \quad (1.79)$$

where P is the suspension pressure.

1.7.4.5 Model Parameters

There are only five parameters required in this Suspension Balance Model that are all measurable experimentally. These parameters are:

1. The sedimentation hindrance function $f(\phi)$ that represents the mobility of the particle phase.
2. The relative suspension viscosity η_s and its dependence on ϕ that can be measured experimentally as we have seen previously in section (1.4.2.1).
3. The normal stress viscosity $\eta_N(\phi)$ and its dependence on ϕ .
4. The ratio $\lambda_2 = \left(\frac{\Sigma_{22}^p}{\Sigma_{11}^p} \right)$.

5. And the ratio $\lambda_3 = \left(\frac{\Sigma_{33}^p}{\Sigma_{11}^p} \right)$.

So it is sufficient to provide these quantities $f(\phi)$, η_s , η_N , Σ_{11}^p , Σ_{22}^p , and Σ_{33}^p for a suspension to start predicting the migration of particles in it during the flow in any geometry.

Experimentally, the studies in literature for Σ_{11}^p , Σ_{22}^p , and Σ_{33}^p in suspensions are rare due to the experimental difficulties of their measurements. Until this date, all of the studies showed that Σ_{11}^p , Σ_{22}^p , and Σ_{33}^p (thus λ_2 , and λ_3) have not been measured completely in the flow of monodispersed suspensions of hard spheres. However, some studies in literature have measured a single one component of them such as [Deboeuf 2008, Deboeuf et al. 2009] who provided direct measurements of Σ_{33}^p for the shearing flow of these suspensions in a Couette cell geometry, or very recently [Boyer et al. 2011 b] who measured Σ_{22}^p (they know the whole stress tensor since they also measured α_1 and α_2). In addition to, [Zarraga et al. 2000] who provided indirect measurements of the Σ_{33}^p component by studying the resuspension of a settled suspension in a Couette flow.

Moreover, [Morris and Boulay 1999] adjusted numerically the Suspension Balance Model to fit well with experimental data on the migration of particles in a Couette cell, and got a value of λ_2 that varies between 0.6 and 0.85. For λ_3 , they explained how the weakness or the absence of migration observed for the flow of a suspension in a torsional flow between two parallel-disks, implies that the value of λ_3 must be equal to 0.5.

Numerically, the studies in literature for Σ_{11}^p , Σ_{22}^p , and Σ_{33}^p in suspensions are rare too. We can mention the works of [Sierou and Brady 2002] in Stokesian Dynamics, and [Yeo and Maxey 2010a] in Force Coupling Method.

So there is a lack of measurements of Σ_{11}^p , Σ_{22}^p , and Σ_{33}^p in the flow of suspensions. For that reason, **in our manuscript, we determine experimentally the values of Σ_{11}^p , Σ_{22}^p , and Σ_{33}^p and their dependence on ϕ for monodispersed suspensions as you will see in the experimental part of the thesis in chapter(4).**

Chapter 2

THE NUMERICAL FINITE VOLUME METHOD

2.1 OVERVIEW

This chapter (2) presents the essential body parts of the numerical technique “The Finite Volume Method” used in this work to discretize the different equations for incompressible flows of suspensions. In section (2.2) we start by introducing some of the numerous numerical methods used in the literature. Then, in the next following sections (2.3) & (2.4) we cover the procedures of discretizing both the solution domain, and the general transport equation. The Navier-Stokes equation discretization is presented in section (2.6). Finally, the closure of this chapter comes in section (2.7).

2.2 INTRODUCTION

Scientists, and especially physicists study different phenomena that occur in nature, and try to represent them via theoretical mathematical models. These models are sets of mathematical equations that describe well the physical phe-

2.2. INTRODUCTION

phenomena observed by the scientists. Heat transfer and fluid flow processes are so good example of these phenomena that occur usually in our real daily life in oceans, rivers, climate, volcanoes, etc... These processes are represented by different transport conservation equations.

Most of the time, mathematical equations are complex, and can't be solved analytically, but nowadays numerically can, due to the revolution in electronics and the presence of super computers. Some of those equations are the Partial Differential Equations (**PDEs**) which can be solved through different discretization techniques like the Finite Difference Method (**FDM**), the Finite Element Method (**FEM**), and the Finite Volume Method (**FVM**).

- *The Finite Difference Method* approximates the theoretical equations in differential form that's through substituting partial derivatives by Taylor series expansions or polynomial fitting to a certain order.
- *The Finite Element Method* or *Structural Analysis* is a method where the domain of interest can be sub-divided into a series of smaller regions in which the differential equations are approximately solved. Each region is referred to as an **element** and the process of subdividing a domain into a finite number of elements is referred to as discretization. Elements are connected at specific points, called **nodes**, and the assembly process requires that the solution be continuous along common boundaries of adjacent elements. The mathematical techniques used to approximate the equations are numerous such as [[Eulers Method](#)], [[Runge-Kutta Method](#)], [[Galerkin Method](#)] etc... At last, by assembling the set of equations for each region, the behavior over the entire problem domain is determined. This method is so well famous, and is the most widely used in solving solid structural analysis problems.
- *The Finite Volume Method* deals with the integral form of the conservation equations. The domain of interest here where calculations are done, is divided into finite number of control volumes (**CVs**) each has a barycen-

2.3. DISCRETIZATION OF THE SOLUTION DOMAIN

ter that represents the calculation node P . The domain has boundaries, and each \mathbf{CV} in it, is surrounded in between different \mathbf{CV} s via surfaces. Interpolation and variety of schemes are used to express variable values at the surface \mathbf{f} in terms of the nodal values. An advantage of this method is conservativeness, in contrast to the two previous methods, because here in this one, the surface integrals for volumes sharing the same face are equal for both of them. Thus, the **FVM** is a very good numerical approach to solve complicated **PDEs** systems, due to the physical approach in its background, not too hard to be understood and implemented, and it is the most widely used in solving fluid dynamics problems.

In this manuscript, we utilize the [OpenFOAM®] environment which uses the **FVM** to solve our **PDEs** system.

“The [OpenFOAM®] (Open Field Operation and Manipulation) **CFD**¹ Toolbox is a free, open source **CFD** software package produced by the “OpenCFD Ltd.” commercial company. [OpenFOAM®] uses the Finite Volume Method to solve systems of partial differential equations ascribed on any 3D unstructured mesh of polyhedral cells. The fluid flow solvers are developed within a robust, implicit, pressure-velocity, iterative solution framework. It has a large user base across most areas of engineering and science, from both commercial and academic organisations. [OpenFOAM®] has an extensive range of features to solve anything from complex fluid flows involving chemical reactions, turbulence and heat transfer, to solid dynamics and electromagnetics²”.

In the following sections, we explore the **FVM** in the spirit of [OpenFOAM®], where we present and explain most of its details.

2.3 DISCRETIZATION OF THE SOLUTION DOMAIN

The conservative equations in the **FVM** are solved over a certain domain (the solution domain) in space and time. This domain will be the domain where

¹Computational Fluid Dynamics

²From the webpage: <http://www.openfoam.com/>

2.3. DISCRETIZATION OF THE SOLUTION DOMAIN

calculations are done, and it is divided into a finite number of control volumes (or cells) as you can see in Figure (2.1). Each central control volume (central cell) has a central node “P” which is the calculation node, and has several neighbor control volumes (i.e. a neighbor to “P” is the control volume of central node “N”). Every control volume is also surrounded by different flat faces each defined by its surface vector \mathbf{S}_f that is normal to the face “f” ($\mathbf{S}_f = \mathbf{n}S_f$; $S_f = \text{Magnitude of Area}$; $\mathbf{n} = \text{unit normal vector}$), points outwards from the central cell, and has the magnitude of its surface area. Point “f” also represents the point in the middle of the face.

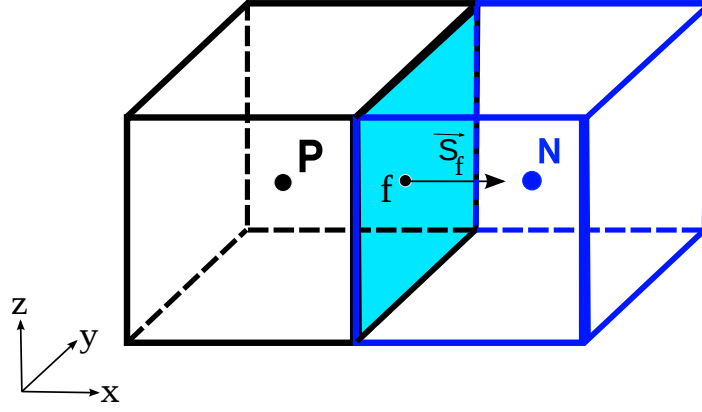


Figure 2.1: Control Volume “P”

The computational node “P” is located at the barycenter (centroid) of the control volumes, in a way such that:

$$\int_{V_P} (\mathbf{X} - \mathbf{X}_P) dV = 0, \quad (2.1)$$

where $\mathbf{X}(x, y, z)$ is the position vector in three dimensional cartesian coordinate system. The control volume faces in the mesh are also divided into two sets, boundary faces and internal faces.

It’s good to mention that the discretized domain is usually known as a Mesh. We are restricted here in this study to **orthogonal uniform Meshes** where all the **CVs** are cubic, do not overlap, and where the surface vector \mathbf{S}_f is parallel

2.4. DISCRETIZATION OF THE TRANSPORT EQUATION

to, and along, $\overline{\mathbf{PN}}$. However, there are many cases where the Mesh is non-orthogonal and a single control volume can be no more cubic and may thus have more than six surrounding faces, which is not the case here.

2.4 DISCRETIZATION OF THE TRANSPORT EQUATION

Most scalar properties when transported can be represented by the general transport equation of the following form

$$\underbrace{\frac{\partial \rho \Psi}{\partial t}}_{\text{Temporal term}} + \underbrace{\nabla \bullet (\rho \mathbf{U} \Psi)}_{\text{Convection term}} = \underbrace{\nabla \bullet (\rho \Gamma_{\Psi} \nabla \Psi)}_{\text{Diffusion term}} + \underbrace{S_{\Psi}(\Psi)}_{\text{Source term}}, \quad (2.2)$$

where Ψ is the scalar property, $\mathbf{U}(u, v, w)$ is the velocity vector, Γ_{Ψ} is the diffusion coefficient, ρ is the density, and S_{Ψ} the source term that is simply a good “dumping ground” [Moukalled and Darwish 2009] for everything that doesn’t fit into the other terms. An Example is the continuity equation:

$$\frac{\partial \rho}{\partial t} + \nabla \bullet (\rho \mathbf{U}) = 0, \quad (2.3)$$

where here $\Psi = 1$, $\Gamma_{\Psi} = 0$, and $S_{\Psi} = 0$. Another example is the x-Momentum equation

$$\frac{\partial \rho u}{\partial t} + \nabla \bullet (\rho u) = \nabla \bullet (\rho \nu \nabla u) - \frac{\partial P}{\partial x} + S_u, \quad (2.4)$$

where here $\Psi = u$, $\Gamma_{\Psi} = \nu$, and $S_{\Psi} = -\frac{\partial P}{\partial x} + S_u$.

The Finite Volume Method requires that equation (2.2) be satisfied over the control volume V_P around the point “P” in the integral form in both space and time such that:

$$\int_t^{t+\Delta t} \left[\int_{V_P} \frac{\partial \rho \Psi}{\partial t} dV + \int_{V_P} \nabla \bullet (\rho \mathbf{U} \Psi) dV \right] dt = \int_t^{t+\Delta t} \left[\int_{V_P} \nabla \bullet (\rho \Gamma_{\Psi} \nabla \Psi) dV + \int_{V_P} S_{\Psi}(\Psi) dV \right] dt. \quad (2.5)$$

2.4. DISCRETIZATION OF THE TRANSPORT EQUATION

In a physical sense of meaning, the term $\int_t^{t+\Delta t} \left(\int_{V_P} \frac{\partial \rho \Psi}{\partial t} dV \right) dt$ in the left hand side of equation (2.5) represents the rate of change of the property Ψ in the **CV**, and the second term $\int_t^{t+\Delta t} \left(\int_{V_P} \nabla \bullet (\rho \mathbf{U} \Psi) dV \right) dt$ is the net transport rate of the property Ψ into the volume due to convection. The term $\int_t^{t+\Delta t} \left(\int_{V_P} \nabla \bullet (\rho \Gamma_\Psi \nabla \Psi) dV \right) dt$ is the net transport rate of the property Ψ out of the control volume due to diffusion, and the last term $\int_t^{t+\Delta t} \left(\int_{V_P} S_\Psi(\Psi) dV \right) dt$ represents the net rate of augmentation of Ψ due to sources inside the control volume as it is shown in Figure (2.2).

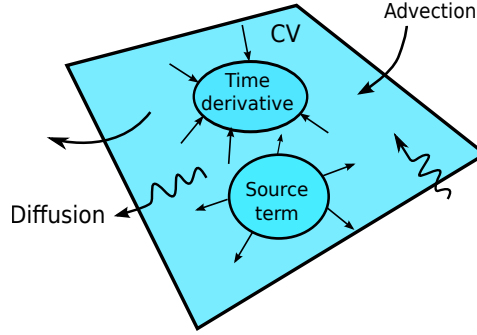


Figure 2.2: Transport process in the **CV**

The discretization of equation (2.5) will be examined now term by term in the coming sections, where the temporal discretization process is explained separately from the discretization process of the spatial terms.

2.4.1 Storage and Arrangement of variables

The first thing that comes to mind when discretizing the governing equations is to select the locations in the domain at which the values of the variables are to be stored. All dependent variables can be stored at the cell centers (i.e. in control volumes centers). This is called the “collocated-grid” arrangement [Versteeg and Malalasekera 1995]. However, in the “staggered-grid” arrangement [Patankar 1981] the velocities are stored at the cell faces (in a face center), separate from other variables as it is illustrated in the following Figure (2.3).

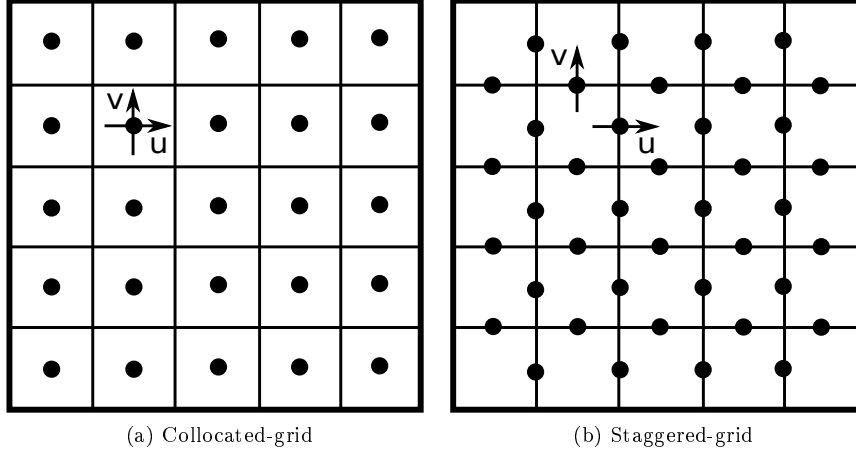


Figure 2.3: Arrangement of variables

The collocated-grid arrangement has significant advantages:

1. The number of coefficients that must be calculated is minimised because each of the governing equations is discretized using the same control volume.
2. It has significant advantages in complex solution domains, especially when the boundaries have slope discontinuities or the boundary conditions are discontinuous [Ferziger 1996].

However, the collocated arrangement was not used for a long time because of difficulties with pressure-velocity coupling and the occurrence of oscillations (checkerboarding) in the pressure field [Patankar 1981, Ferziger 1996]. A simple cure for this problem was proposed by [Rhie and Chow 1983] and since then the collocated arrangement has been adopted by most **CFD** (Computational Fluid Dynamics) codes including commercial ones. In our study here, the collocated-grid variable arrangement is adopted and the different terms discretization utilizing this arrangement are explained in the next sections.

2.4.2 Discretization Of Spacial Terms

2.4.2.1 The Diffusion Term

The diffusion term $\underbrace{\nabla \cdot (\rho \Gamma_\Psi \nabla \Psi)}_{\text{Diffusion term}}$ of equation (2.2), after using the Gauss Ostrogradsky divergence theorem, can be discretized over the central calculation control volume V_P of node “P” as the following:

$$\int_{V_P} \nabla \cdot (\rho \Gamma_\Psi \nabla \Psi) dV = \int_S d\mathbf{S}_f \cdot (\rho \Gamma_\Psi \nabla \Psi) = \sum_f \mathbf{S}_f \cdot (\rho \Gamma_\Psi \nabla \Psi)_f = \sum_f (\rho \Gamma_\Psi)_f \mathbf{n} S_f \cdot (\nabla \Psi)_f \quad (2.6)$$

where $\mathbf{S}_f = \mathbf{n} S_f$.

The term $(\nabla \Psi)_f$ can be calculated in different ways depending on the type of interpolation scheme being used. We use a scheme for the calculation of this term at the surface “f” as the following:

$$\mathbf{n} S_f \cdot (\nabla \Psi)_f = S_f \frac{\Psi_N - \Psi_P}{|\mathbf{d}|}, \quad (2.7)$$

where the vector \mathbf{d} between the center of the cell of interest “P” and the center of a neighbouring cell “N” is orthogonal to the face plane (i.e. \mathbf{d} is parallel to \mathbf{n}) (see Figure (2.4)).

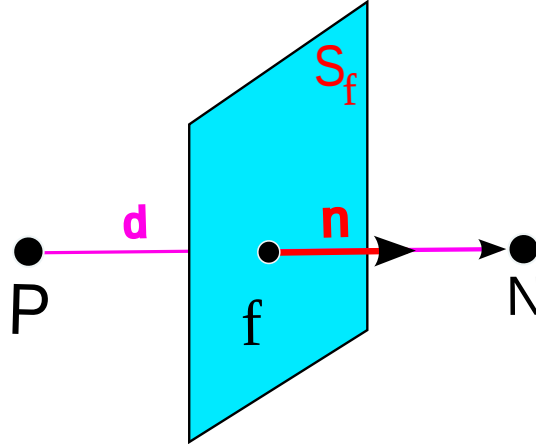


Figure 2.4: Orthogonal Mesh Interface

2.4.2.2 The Convection Term

The convection term $\underbrace{\nabla \bullet (\rho \mathbf{U} \Psi)}_{\text{Convection term}}$ in equation (2.2) and after using the Gauss Ostrogradsky divergence theorem, can be discretized over the central calculation control volume V_P of node “P” as the following:

$$\int_{V_P} \nabla \bullet (\rho \mathbf{U} \Psi) dV = \int_S d\mathbf{S} \cdot (\rho \mathbf{U} \Psi) = \sum_f \mathbf{S}_f \cdot (\rho \mathbf{U} \Psi)_f = \sum_f \mathbf{n} S_f \cdot (\rho \mathbf{U})_f \Psi_f = \sum_f J_f \Psi_f, \quad (2.8)$$

where J_f holds for the mass flux through the face “f”, defined as:

$$J_f = \mathbf{n} S_f \cdot (\rho \mathbf{U})_f \quad (2.9)$$

We define the kinematic flux Φ_f through the face “f” that will be used later as:

$$\Phi_f = \frac{J_f}{\rho}. \quad (2.10)$$

- Interpolation of the cell-centred values to the face centers is essential to the Finite Volume Method. The values of the different variables at the interface “f” are interpolated via many interpolation schemes that can be found in [Patankar 1981, Ferziger 1996, Jasak 1996]. We present some of them such as the upwind-difference and the central-difference schemes.

1. The Upwind-difference Scheme

This scheme is only a first-order accurate, but it guarantees boundedness³ of the solution. The boundedness of the solution is effectively ensured at the expense of accuracy. The convection term is calculated here according to the direction of the flow [Barakat and Clark 1966, Courant et al. 1952, Gentry et al. 1952]. The value of Ψ_f at the interface “f” is equal to the

³The physically realistic value of a property lies within proper bounds that should be guaranteed by the numerical scheme.

2.4. DISCRETIZATION OF THE TRANSPORT EQUATION

value of Ψ at grid point on the *upwind* side of the face such that:

$$\begin{cases} \Psi_f = \Psi_P & \text{for } \Phi_f \geq 0 \\ \Psi_f = \Psi_N & \text{for } \Phi_f < 0 \end{cases} \quad (2.11)$$

and it implies

$$J_f \Psi_f = \rho [\Psi_P \cdot \max(\Phi_f, 0) - \Psi_N \cdot \max(-\Phi_f, 0)] \quad (2.12)$$

2. The Central-difference Scheme

This scheme is second-order accurate, but the solution can be unbounded [Patankar 1978, Ferziger 1996].

$$\Psi_f = f_x \Psi_P + (1 - f_x) \cdot \Psi_N \quad (2.13)$$

where

$$f_x = \frac{|\mathbf{X}_f - \mathbf{X}_N|}{|\mathbf{X}_f - \mathbf{X}_N| + |\mathbf{X}_f - \mathbf{X}_P|} \quad (2.14)$$

For other existing schemes especially those that can be used in [OpenFOAM®], one can seek them down in Appendix B on page 222.

In our calculations in this manuscript we used the central difference scheme for interpolation.

2.4.2.3 The Source Term

The source term $\underbrace{S_\Psi(\Psi)}_{\text{Source term}}$ can be a constant or even a function of the property Ψ . For computational success, it must be linearised before discretization as described in [Patankar 1981] such that

$$S_\Psi(\Psi) = Su + Sp\Psi, \quad (2.15)$$

2.4. DISCRETIZATION OF THE TRANSPORT EQUATION

where Su and Sp can be also functions of the property Ψ with the condition on Sp for calculation-stability ($Sp < 0$) (see [Patankar 1981]). Thus, the discretization of the source term over the control volume after linearisation is going to be as the following:

$$\int_{V_P} S_\Psi(\Psi) dV = \int_{V_P} (Su + Sp\Psi) dV = SuV_P + SpV_P\Psi_P. \quad (2.16)$$

2.4.3 Temporal Discretization

If we denote all the spatial terms as $\lambda\Psi$ where λ is any spatial operator, then we can express a transient **PDE** in integral form as:

$$\int_t^{t+\Delta t} \left[\frac{\partial}{\partial t} \left(\int_{V_P} \rho\Psi dV \right) + \int_{V_P} \lambda\Psi dV \right] dt = 0 \quad (2.17)$$

After using the Implicit Euler Scheme (Explained in next section) for the time derivative, the first and second terms of equation (2.17) become:

$$\begin{aligned} \int_t^{t+\Delta t} \left[\frac{\partial}{\partial t} \left(\int_{V_P} \rho\Psi dV \right) \right] dt &= \int_t^{t+\Delta t} \frac{(\rho_P\Psi_P V_P)^{k+1} - (\rho_P\Psi_P V_P)^k}{\Delta t} dt \\ &= \frac{(\rho_P\Psi_P V_P)^{k+1} - (\rho_P\Psi_P V_P)^k}{\Delta t} \Delta t \end{aligned} \quad (2.18)$$

and

$$\int_t^{t+\Delta t} \left(\int_{V_P} \lambda\Psi dV \right) dt = \int_t^{t+\Delta t} (\lambda^*) \Psi dt \quad (2.19)$$

respectively, where (λ^*) represents the spatial discretization of λ . The current time values are represented by the superscript $(k+1)$, and the old time values by the superscript (k) .

The time integral can be discretized via different interpolation schemes such as the Implicit Euler, the Explicit Euler, and the Cranck-Nicolson schemes.

1. Euler Implicit Scheme

It uses implicit discretization of the spatial terms, thereby taking current

2.4. DISCRETIZATION OF THE TRANSPORT EQUATION

values Ψ^{k+1} such that:

$$\int_t^{t+\Delta t} (\lambda^*) \Psi dt = (\lambda^*) \Psi^{k+1} \Delta t \quad (2.20)$$

It is first-order accurate in time, guarantees boundedness and is unconditionally stable.

2. Euler Explicit Scheme

It uses explicit discretization of the spatial terms, thereby taking old values Ψ^k such that:

$$\int_t^{t+\Delta t} (\lambda^*) \Psi dt = (\lambda^*) \Psi^k \Delta t \quad (2.21)$$

It is first-order accurate in time and is unstable if the Courant number “Cr” is greater than 1. The Courant number is the ratio of the distance traveled by a disturbance in one time step to the length of a computational distance step.

$$Cr = \frac{\Delta t |\mathbf{U}|}{\Delta \mathbf{X}} \leq 1 \quad (2.22)$$

The Courant number must be less than or equal to unity ($0 < Cr \leq 1$) so as to ensure that the solution remains within the computational domain.

3. Crank–Nicolson Scheme

[Crank-Nicolson] uses the trapezoid rule to discretize the spatial terms, thereby taking a mean of current values Ψ^{k+1} and old values Ψ^k such that:

$$\int_t^{t+\Delta t} (\lambda^*) \Psi dt = (\lambda^*) \frac{\Psi^{k+1} + \Psi^k}{2} \Delta t \quad (2.23)$$

After finishing the discretization procedure of the spatial terms, and assuming no change of the \mathbf{CV} s in time (i.e. static mesh), the equation (2.5) is transformed into a “semi-discretized” [Hirsch 1991] equation of the form:

2.4. DISCRETIZATION OF THE TRANSPORT EQUATION

$$\int_t^{t+\Delta t} \left[\left(\frac{\partial \rho \Psi}{\partial t} \right)_P V_P + \sum_f J_f \Psi_f \right] dt = \int_t^{t+\Delta t} \left[\sum_f (\rho \Gamma_\Psi)_f \mathbf{n} S_f \cdot (\nabla \Psi)_f + (SuV_P + SpV_P \Psi_P) \right] dt. \quad (2.24)$$

The semi-discretized equation (2.24) can be transformed then, after we used the Crank-Nicolson scheme, into a discretized equation in space and time over the control volume “P” such that:

$$\frac{\rho_P^{k+1} \Psi_P^{k+1} - \rho_P^k \Psi_P^k}{\Delta t} V_P + \sum_f \left(\frac{J_f^{k+1} \Psi_f^{k+1} + J_f^k \Psi_f^k}{2} \right) = \sum_f \left(\frac{((\rho \Gamma_\Psi)_f \mathbf{n} S_f \cdot (\nabla \Psi)_f^{k+1}) + ((\rho \Gamma_\Psi)_f \mathbf{n} S_f \cdot (\nabla \Psi)_f^k)}{2} \right), \quad (2.25)$$

where the density ρ and the diffusivity Γ_Ψ are considered not changing with time. Equation (2.25) is solved for the current time values $(k+1)$.

In our work, we always respected that $Cr < 1$. Moreover, we used the [Crank-Nicolson] scheme for the temporal terms discretization.

2.4.4 Solution Techniques for Systems of Linear Algebraic Equations

Finally, the transport equation in its discretized shape (2.25), after assembly of the terms, gives an algebraic equation for each single **CV** of the form

$$a_P \Psi_P + \sum a_N \Psi_N = \Upsilon_P. \quad (2.26)$$

The value of Ψ_P depends on the values in the neighbouring **CV**s, thus creating a matrix system of algebraic equations:

$$\mathbf{A} \Psi = \Upsilon, \quad (2.27)$$

where $\mathbf{A} = a_P \Psi_P + \sum a_N \Psi_N$, with \mathbf{A} being a sparse matrix of coefficients a_P on the diagonal and coefficients a_N out off the diagonal, Ψ is the vector of Ψ -s for all control volumes and Υ is the source term vector. **Note** that \mathbf{A} and Υ contain the assembled terms of equation (2.26) from both the current and the

2.4. DISCRETIZATION OF THE TRANSPORT EQUATION

previous time steps, $(k + 1)$ and (k) , respectively. There are two main methods, **direct** and **iterative**, in order to solve the algebraic system of equations (2.27). Some examples of the **direct methods** used are the [Gaussian elimination] and the Cramer's rule matrix inversion [Cramers Rule] methods.

Iterative methods are the Jacobi and Gauss Siedel methods, in addition to the Thomas or Tri-diagonal Matrix Algorithm (TDMA) (see [Versteeg 1995]), Conjugate Gradient method (CG) [Hestens and Steifel 1952], Incomplete Cholesky preconditioned Conjugate Gradient (ICCG) [Jacobs 1980], and the Bi-CGSTAB method by [Van Der Vorst 1992].

Iterative methods have a main advantage over the direct methods which is the calculation speed where less space for the computer memory is needed during calculations, especially when dealing with large systems at four dimensional situations [Muzaferija 1994].

In our work we use both Preconditioned conjugate gradient (PCG) and Preconditioned bi-conjugate gradient (PBiCG) iterative methods that are implemented in [OpenFOAM®] during the solution procedure.

2.4.5 Boundary Conditions

The control volumes of the mesh like in Figure (2.1) may have internal faces but also faces that coincide with the boundary faces of the mesh. These faces may have **numerical** boundary conditions (**BCs**), where they will be denoted as patches, thus separating them from the internal faces as you can observe in Figure (2.5).

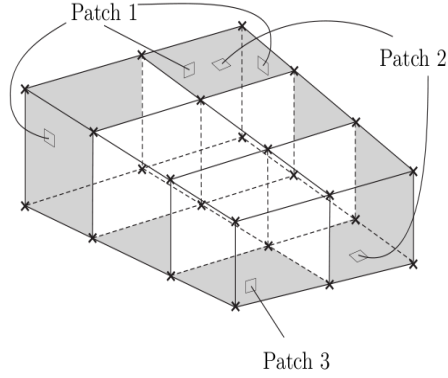


Figure 2.5: Boundary Faces represented as Patches

The **numerical** boundary conditions are divided into two types:

1. ***Dirichlet*** boundary conditions that prescribe the value of the variable on the boundary;
2. ***Neumann*** boundary conditions that prescribe the gradient of the variable normal to the boundary.

It is good to note that the boundary conditions for any problem are built in the algebraic equations system in (2.26) before solving it.

When we perform discretization of terms that include the sum over faces, \sum_f , we need to consider what happens when one of the faces is a boundary face.

2.4.5.1 The Fixed Value BC

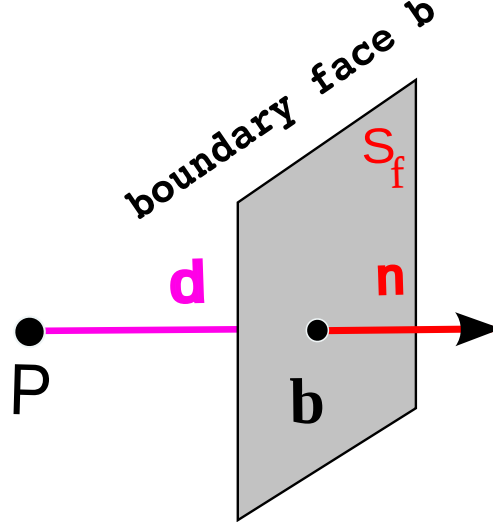


Figure 2.6: Boundary Face b (patch)

The fixed value boundary condition forces the value of Ψ at the boundary face \mathbf{b} to be equal to $\Psi_{\mathbf{b}}$. Thus, this has to be taken into account in the discretization procedure of the convection and diffusion terms on the boundary face as you will see next.

- **Diffusion Term:** According to the equation (2.6): $\int_{V_P} \nabla \bullet (\rho \Gamma_{\Psi} \nabla \Psi) dV = \sum_f (\rho \Gamma_{\Psi})_f \mathbf{n} S_f \cdot (\nabla \Psi)_f$ the diffusion term will be discretized on the **CV** of a boundary face \mathbf{b} with the face gradient calculated as the following:

$$\mathbf{n} S_f \cdot (\nabla \Psi)_f = S_f \frac{\Psi_{\mathbf{b}} - \Psi_P}{|\mathbf{d}|}, \quad (2.28)$$

where \mathbf{n} and \mathbf{d} are parallel as you can see in Figure (2.6). Moreover, the term $(\rho \Gamma_{\Psi})_f$ on the boundary will be simply equal to $(\rho \Gamma_{\Psi})_{\mathbf{b}}$.

- **Convection Term:** The convection term is discretized as

$$\int_{V_P} \nabla \bullet (\rho \mathbf{U} \Psi) dV = \sum_f J_f \Psi_f, \quad (2.29)$$

where the term, in the summation, at the boundary face \mathbf{b} will be equal to $J_{\mathbf{b}} \Psi_{\mathbf{b}}$.

2.5. NUMERICAL ERRORS

2.4.5.2 The Fixed Gradient BC

Here, the dot product of the outward pointing unit normal and the gradient can be defined on the boundary as the following:

$$(\mathbf{n} \cdot \nabla \Psi)_{\mathbf{b}} = g_{\mathbf{b}}. \quad (2.30)$$

- **Diffusion Term:** The diffusion term then will be discretized here as in equation (2.6): $\int_{V_P} \nabla \cdot (\rho \Gamma_{\Psi} \nabla \Psi) dV = \sum_f (\rho \Gamma_{\Psi})_f \mathbf{n} S_f \cdot (\nabla \Psi)_f$, where the term inside the summation, according to the definition in (2.30) will be on the boundary face \mathbf{b} equal to $(\rho \Gamma_{\Psi})_{\mathbf{b}} S_f g_{\mathbf{b}}$.
- **Convection Term:** The value of Ψ here at the boundary face \mathbf{b} will be calculated from the value in the control volume center “ P ” and the prescribed gradient $(\nabla \Psi)_{\mathbf{b}}$ (see Figure 2.6) such that:

$$\Psi_{\mathbf{b}} = \Psi_P + \mathbf{d} \cdot (\nabla \Psi)_{\mathbf{b}} = \Psi_P + |\mathbf{d}| g_{\mathbf{b}}. \quad (2.31)$$

2.5 NUMERICAL ERRORS

After solving the linear algebraic system of equations (2.27) for the property $\Psi(\mathbf{X}, t)$, the resulting numerical solution Ψ on the cell centers of the mesh on the calculation domain is an approximate solution to the exact solution ψ . The Numerical Error “Er” can be simply defined as

$$Er = \psi - \Psi. \quad (2.32)$$

Different methods of Error estimation exist such as those based on Taylor Series Expansion like “Richardson Extrapolation”, and “Direct Taylor Series Error estimate”, in addition to others like “the Moment Error Estimate”, and “the Residual Error Estimate” methods. All these methods for Error estimation, well analysed in the **FVM**, can be found in [Jasak 1996].

In our work where we use the [OpenFOAM®] package, we use the “Residual Error Estimate” method that will be discussed briefly in the coming section.

2.5.1 The Residual Error Estimate

Here the spirit of the “Residual Error Estimate” in the Finite Volume Method comes from the Errors Estimation technique in the Finite Element Method [Zienkiewicz et al. 1989]. Taking equation (2.2) in a steady-state the residual of the control volume “P” can be calculated as the following

$$\begin{aligned} \Re_{es_P}(\Psi) &= \int_{V_P} [\nabla \bullet (\rho \mathbf{U} \Psi) - \nabla \bullet (\rho \Gamma_{\Psi} \nabla \Psi) - Su - Sp\Psi_P] dV \\ &= \sum_f \mathbf{n} S_f \cdot [(\rho \mathbf{U})_f \Psi_f - (\rho \Gamma_{\Psi})_f (\nabla \Psi)_f] - Su V_P - Sp \Psi_P V_P, \end{aligned} \quad (2.33)$$

At last for convergence check during the iterations, the maximum of all the residuals at the control volumes must obey the following:

$$\text{Max}(\Re_{es_P}(\Psi)) \ll \epsilon \quad (2.34)$$

where ϵ is $O(10^{-4})$.

2.5.2 Convection and Diffusion Control

- **Convection Control**

Most of the calculation schemes are sensitive to the computational time and space intervals $(\Delta t, \Delta \mathbf{X})$ used. The sensitivities for variety of problems are usually discussed in terms of the **Courant number** Cr that was previously defined in equation (2.22) ($0 < Cr \leq 1$).

- **Diffusion Control**

The Numerical diffusion is controlled to be within the physical realistic one through the following imposed condition:

$$\frac{\Gamma \Delta t}{(\Delta \mathbf{X})^2} < 1 \quad (2.35)$$

So in our simulations we choose a mesh that has a $\Delta \mathbf{X}$, and then we calculate its corresponding Δt that satisfies both conditions of (2.22) and (2.35).

2.6 NAVIER-STOKES EQUATION DISCRETIZATION

Any fluid motion is described under the Navier-Stokes (NS) equations. The latter equations require here special treatments for the discretisation procedure on the control volume through the Finite Volume Method, especially the way it is developed inside the [OpenFOAM®] tool we use.

The transient continuity and momentum equations in the NS system are

$$\frac{\partial \rho}{\partial t} + \nabla \bullet (\rho \mathbf{U}) = 0, \quad (2.36)$$

and

$$\frac{\partial (\rho \mathbf{U})}{\partial t} + \nabla \bullet (\rho \mathbf{U} \mathbf{U}) - \nabla \bullet (\eta \nabla \mathbf{U}) = -\nabla P, \quad (2.37)$$

respectively, where \mathbf{U} is the average velocity, ρ is the fluid density, P is the pressure, and η is the dynamic viscosity.

For an incompressible neutrally buoyant system $\left(\frac{D\rho}{Dt} = \frac{\partial \rho}{\partial t} + \nabla \rho \cdot \mathbf{U} = 0 \right)$ and dividing all by ρ , equations (2.36) and (2.37) can be rewritten as:

$$\nabla \bullet \mathbf{U} = 0, \quad (2.38)$$

and

$$\frac{\partial \mathbf{U}}{\partial t} + \nabla \bullet (\mathbf{U} \mathbf{U}) - \nabla \bullet (\nu \nabla \mathbf{U}) = -\nabla p, \quad (2.39)$$

where $\left(\nu = \frac{\eta}{\rho} \right)$ is the kinematic viscosity, and $\left(p = \frac{P}{\rho} \right)$ is the kinematic pressure. While solving these two equations, there exist two major difficulties:

1. The convection term $\nabla \bullet (\mathbf{U} \mathbf{U})$ is nonlinear, since the velocity \mathbf{U} is multiplied by itself.
2. The equations are strongly coupled in \mathbf{U} and p .

2.6. NAVIER-STOKES EQUATION DISCRETIZATION

This precludes to solve out simultaneously the velocity and pressure without great difficulty, and requires iterative algorithms while solving for the different variables (i.e. \mathbf{U} , p). In our work here, we use the “**SIMPLE**” algorithm (defined later) to solve that difficulty.

2.6.1 Discretizing the equations

Both equations (2.38) and (2.39) are discretized and written for each cell in the grid, which will result in a huge set of equations. According to [Auvinen et al. 2010] (as in [OpenFOAM®]), the discrete forms of equations (2.38) (continuity) and (2.39) (momentum) are written, respectively, as:

$$\sum_f (\mathbf{U}_f \cdot \mathbf{n}S_f) = 0 \quad (2.40)$$

$$\frac{\Delta \mathbf{U}}{\Delta t} V_P + \sum_f \mathbf{U}_f \Phi_f - \sum_f (\nu \nabla \mathbf{U})_f \mathbf{n}S_f = - \sum_f p_f \mathbf{n}S_f \quad (2.41)$$

2.6.1.1 The Discretized Momentum Equation in a Matrix form

The final form of the matrix equation which results from the momentum equation (2.41) discretization can be written in the following form:

$$a_P \mathbf{U}_P + \sum a_N \mathbf{U}_N = \mathbf{src} - \nabla p, \quad (2.42)$$

where \mathbf{src} is a source vector, and ∇p is left out of the source vector in its original form.

2.6.2 Pressure-Velocity Coupling Technique

The differential equations system is strongly coupled in $(p \ \& \ \mathbf{U})$ and cannot be solved directly. Iterative solution methods (approach) are the only choice [Ferziger 1996, Patankar 1981]. There are different iterative solution methods that can be used to solve the inter-coupling $(p \ \& \ \mathbf{U})$ system of equations

(2.36), and (2.37). In this manuscript, we use the “SIMPLE” algorithm [Ferziger 1996, Patankar 1981, Versteeg and Malalasekera 1995] implemented in [OpenFOAM®] to solve the inter-coupling (p & \mathbf{U}) system of equations.

2.6.2.1 The SIMPLE Algorithm

The **SIMPLE** (Semi-Implicit Method for Pressure-Linked Equations) algorithm is a technique that allows to couple the Navier-Stokes equations with an iterative procedure to seek p and \mathbf{U} fields such that the obtained fields satisfy well both the continuity and the momentum equations [Patankar 1981]. We will try to explain this method in the spirit of equation (2.42).

Let “ i ” be a time index that constitutes the outer iterations for time. Then the discretized momentum equation (2.42) at this time “ i ” becomes on the following form:

$$a_P \mathbf{U}_P^i + \sum a_N \mathbf{U}_N^i = \mathbf{src}^i - (\nabla p)^i \quad (2.43)$$

In order for the solution of equation (2.43) for the fields \mathbf{U}_P^i and p^i to satisfy continuity and momentum, equation (2.43) must be solved iteratively. This is done in the **SIMPLE** algorithm through a technique by adding internal iterations of an index “ j ” to the outer iteration “ i ” of time.

Thus, equation (2.43) can be written now in both “ i ” and “ j ” iteration indices on the following form:

$$a_P \mathbf{U}_P^{i,j} + \sum a_N \mathbf{U}_N^{i,j} = \mathbf{src}^{i,j-1} - \nabla p^{i,j} \quad (2.44)$$

with

$$\mathbf{U}_P^{i,j} = \left[\frac{-\sum a_N \mathbf{U}_N^{i,j} + \mathbf{src}^{i,j-1}}{a_P} \right] - \frac{\nabla p^{i,j}}{a_P} \quad (2.45)$$

The source \mathbf{src} contains all the terms that are explicitly computed (i.e. body forces, linearized terms, etc...). At the end of iterations on “ j ”, the final $\mathbf{U}_P^{i,j}$ & $p^{i,j}$ fulfill well the continuity and momentum equations. In the following,

2.6. NAVIER-STOKES EQUATION DISCRETIZATION

sometimes the time index “ i ” will be dropped out from the equations, just to simplify the formulation.

The steps of the **SIMPLE** algorithm (1 to 4) are inside the single time step “ i ” as follows:

1. **Momentum Predictor:** First, we start from \mathbf{U}^{j-1} & p^{j-1} (for the first iteration “ $j = 1$ ” & one takes $\mathbf{U}^{i,0} = \mathbf{U}^{i-1}$; $p^{i,0} = p^{i-1}$). Then assemble and solve the discretized momentum equation (2.45) from the previous iteration step “ $j - 1$ ” to compute an intermediate (momentum-predictor) new velocity field $\mathbf{U}_P^{*,j}$ on the form:

$$\mathbf{U}_P^{*,j} = \frac{-\sum a_N \mathbf{U}_N^{*,j} + \mathbf{src}^{j-1}}{a_P} - \frac{\nabla p^{j-1}}{a_P} \quad (2.46)$$

[Note $\mathbf{U}_P^{*,j}$ is a first approximation of \mathbf{U}_P^j at the iteration “ j ”] that do not satisfy the following discrete continuity equation:

$$\{\nabla \bullet \mathbf{U}_P^j\} = \sum_f (\mathbf{U}_f^j \cdot \mathbf{n}_{S_f}) = 0 \quad (2.47)$$

In order for the velocities to fulfill this latter equation, the velocity and the pressure fields should be corrected by introducing two correction terms \mathbf{U}' and p' such that:

$$\mathbf{U}_P^j = \mathbf{U}_P^{*,j} + \mathbf{U}'_P \quad (2.48)$$

$$p^j = p^{j-1} + p' \quad (2.49)$$

2. **Pressure solution:** Upon using the definition in (2.45) \mathbf{U}' can be written as:

$$\mathbf{U}'_P = \left[\frac{-\sum a_N \mathbf{U}'_N}{a_P} \right] - \frac{\nabla p'}{a_P} \quad (2.50)$$

Introducing the latter \mathbf{U}'_P of equation (2.50) in the discrete continuity equation (2.47) one gets:

$$\nabla \bullet \mathbf{U}_P^{*,j} = -\nabla \bullet \mathbf{U}'_P \quad (2.51)$$

2.6. NAVIER-STOKES EQUATION DISCRETIZATION

that implies a discrete Poisson pressure equation on the form:

$$\sum_f (\mathbf{U}_f^{*j} \cdot \mathbf{n}) S_f = - \sum_f \left(\frac{-\sum a_N \mathbf{U}'_N}{a_P} - \frac{\nabla p'}{a_P} \right) \cdot \mathbf{n} S_f \quad (2.52)$$

In the **SIMPLE** algorithm, the term $\left[\frac{-\sum a_N \mathbf{U}'_N}{a_P} \right]$ is neglected, and equation (2.52) becomes:

$$\sum_f (\mathbf{U}_f^{*j} \cdot \mathbf{n}) S_f = \sum_f \left(\frac{\nabla p'}{a_P} \right) \cdot \mathbf{n} S_f \quad (2.53)$$

The solution of this last discrete pressure equation gives the correction term p' of the new pressure field p^j .

3. **Explicit Velocity Correction:** Correct the velocities according to equation (2.48) to obtain the new \mathbf{U}_P^j that satisfies continuity and correct the pressure according to equation (2.49) to get the new p^j .
4. Go back to step 1 and repeat, using \mathbf{U}_P^j and p^j as improved estimates for \mathbf{U}_P^{j+1} and p^{j+1} , untill all corrections are negligibly small.
5. Advance to the next time step “ $i + 1$ ”.

2.6.2.2 Under-relaxation

In the iterative algorithms (i.e. **SIMPLE**) that seeks the solution of the algebraic equations, it is often desirable to speed up or to slow down the changes, from iteration to iteration, in the values of the dependent variables. This process is well known as overrelaxation or underrelaxation. Consequently, in the “**SIMPLE**” algorithm (loop) both velocity and pressure are under-relaxed in order to prevent divergence problems and control the speed up of the calculations [Patankar 1981]. Moreover, the performance of the “**SIMPLE**” algorithm does not converge rapidly and depends greatly on the size of **time step**, or -for steady flows- on the value of the underrelaxation parameter used in the momentum equations.

- **Concerning velocity**, the underrelaxation of the momentum equation is done by a coefficient α_U that is applied during the iteration “ j ” in the following way:

$$\mathbf{U}_P^j = \mathbf{U}_P^{j-1} + \alpha_U \left(\mathbf{U}_P^j - \mathbf{U}_P^{j-1} \right) \quad (2.54)$$

or can be written on the following form after using equation (2.42):

$$\frac{a_P}{\alpha_U} \mathbf{U}_P^j + \sum_f a_N \mathbf{U}_N^j = \mathbf{src}^j - \nabla p^j + \frac{(1 - \alpha_U)}{\alpha_U} a_P \mathbf{U}_P^{j-1} \quad (2.55)$$

where the underrelaxation parameter ($0 \leq \alpha_U \leq 1$).

- **Concerning pressure**, it has been found by trial and error that convergence can be improved if one adds only a portion of p' to p^{j-1} in the following way:

$$p^j = p^{j-1} + \alpha_p p' \quad (2.56)$$

after the pressure equation is solved, where ($0 \leq \alpha_p \leq 1$). Thus, only some part of the new pressure is used, and the rest is taken from the previous iteration round (**Note:** this also increases computation stability [Patankar 1981, Ferziger 1996]). An optimum can be found in literature [Ferziger 1996] for the choice of α_U & α_p according to the following:

$$\alpha_p = (1 - \alpha_U) \quad (2.57)$$

Note: For the implementation of the “SIMPLE” algorithm in [Open-FOAM®] environment, see Appendix C on page 224.

2.7 CLOSURE

The conservative Finite Volume Method for incompressible flows had been described globally in this chapter (2) in a simplified clear manner. However, an extension of this method for compressible flows can be found in literature well explained by [[Moukalled and Darwish 2009](#)].

Chapter 3

THE Suspension Balance Model IN OpenFOAM®

3.1 OVERVIEW

This chapter (3) tackles the process of developing a computational open-source code used to solve the simple shear flow problems of concentrated suspensions. The technique used here is based on considering the suspension (the liquid and the particle phases) as a continuum medium to solve the flow equations. The Suspension Balance Model (SBM) [Nott and Brady 1994, Morris and Boulay 1999] described in chapter (1) is used to model the shear-induced migration of particles in various geometries.

The Model is implemented in the [OpenFOAM®] [C++] Object-Oriented (OO) source code in [OpenFOAM®] package which uses the Finite Volume Method (FVM) for the spatial discretization of the transport equations. In this chapter (3) we aim to provide an overview of the original SBM and its numerical implementation in [OpenFOAM®].

3.2. MODEL GOVERNING EQUATIONS

In section (3.2), Governing Equations of the SBM development are presented. In section (3.3), the technique of implementation of the SBM utilizing the Finite Volume Method is presented. In section (3.4), validation of the implemented-code for the flow of suspensions at various concentrations in different geometries are discussed, and compared with the previous studies in literature.

3.2 MODEL GOVERNING EQUATIONS

The **SBM**, that was presented and explained previously in chapter (1) for the incompressible Stokes flow of monodispersed neutrally buoyant non-Brownian suspensions of hard spheres, can be summarized by the following system of three coupled equations:

$$\nabla \bullet \mathbf{U} = 0, \quad (3.1)$$

$$\left\{ \begin{array}{c} \nabla \bullet \Sigma = \nabla \bullet \Sigma^f + \nabla \bullet \Sigma^p = \mathbf{0} \\ \Updownarrow \\ -\nabla P + \nabla \bullet (2\eta_0\eta_s \mathbf{E}) - \nabla \bullet (\eta_0\eta_N \dot{\gamma} \mathbf{Q}) = \mathbf{0} \end{array} \right\} \quad (3.2)$$

$$\frac{\partial \phi}{\partial t} + \mathbf{U} \cdot \nabla \phi = -\nabla \bullet \vec{j}_\perp. \quad (3.3)$$

where \mathbf{U} is the suspension mean velocity field vector, Σ the suspension stress tensor, and \vec{j}_\perp the shear-induced migration flux of particles relative to the mean motion of the suspension that were all defined precisely in chapter (1). We recall that:

$$\vec{j}_\perp = \frac{2a^2}{9\eta_0} f(\phi) [\nabla \bullet \Sigma^p]. \quad (3.4)$$

3.3 NUMERICAL IMPLEMENTATION

3.3.1 Implementation of the “Suspension Balance Model” in “OpenFOAM®”

The [OpenFOAM®] [C++] library is a pack of applications divided into two different categories which are “solvers” and “utilities”. The “solvers” are those where all the actual calculations are performed while the “utilities” provide a wide range of functionalities for pre- and post-processing. The user can implement his own Model as a “ new solver” and pass it to the already existing library thus creating a new implemented Model describing a certain new physical phenomenon, as we will do with the implementation of the **SBM**.

The system of equations (3.1), (3.2), and (3.3) is implemented by modifying the “transientSimpleFoam Solver” in the open source code [OpenFOAM®] to a new solver which represents the SBM.

Precisely, equations (3.1) and (3.2) which describe the flow behavior have been solved iteratively via the **SIMPLE** algorithm technique described previously in chapter (2). The convective term is absent here, and the $\nabla \bullet \Sigma^p$ term that corresponds to the particle normal stresses is simply added to the source term **src**. The transport equation (3.3) is solved following the detailed procedures in chapter (2) where we used the Crank-Nicholson scheme in the discretization of the $\frac{\partial \phi}{\partial t}$ term.

3.4. VALIDATION OF THE CODE IMPLEMENTATION IN OPENFOAM®

The following shows briefly the Implementation procedure inside the transientSimpleFoam Solver:

```
int main(int argc, char *argv[])
{
    Info<< " \nStarting time loop\n" << endl;
    for (runTime++; !runTime.end(); runTime++)
    {
        # include "readPISOControls.H" # include "CourantNo.H"

        Calculating parameters:  $\eta_0, \eta_S, \eta_N, \eta_P, \mathbf{E}, \dot{\gamma}, \Sigma^f, \Sigma^p, \Sigma, \vec{j}_\perp$ , etc...
        // Pressure-velocity SIMPLE corrector
        for (int corr=0; corr<nCorr; corr++) (SIPMLE iteration)
        {
            solve steady Stokes momentum:  $\nabla \bullet \Sigma = \mathbf{0}$ ;
            velocity-pressure correction to satisfy continuity  $\nabla \bullet \mathbf{U} = 0$ ;
        }
        At each time step solve transport equation
             $\frac{\partial \phi}{\partial t} + \mathbf{U} \cdot \nabla \phi = -\nabla \bullet \vec{j}_\perp$  to get new  $\phi$ 
        runTime.write();
    }
}
```

The validity of the Model implementation in [OpenFOAM®] is presented and discussed in the following section(3.4).

3.4 VALIDATION OF THE CODE IMPLEMENTATION IN Open-FOAM®

Any new implemented written code must be tested for its validation. That's usually done by tackling different examples which already exist on another different softwares or codes, and compare the results of the new written code with them and with the existing experiments in literature. In section (3.4.1), we will present the suspension flow in both rectangular and circular cross-sectional

3.4. VALIDATION OF THE CODE IMPLEMENTATION IN OPENFOAM®

channels, while in section (3.4.2) an example of the suspension flow in a Couette cell geometry will be presented.

3.4.1 Suspension flow in channels

3.4.1.1 Suspension flow in a rectangular cross-section conduit

Our numerical simulations for the pressure-driven flow of a suspension in a 2D rectangular cross-section (**CS**) conduit are compared with the numerical code written by [Miller 2004, Miller and Morris 2006]. All the numerical data are also compared with the experimental ones presented by [Lyon and Leal I 1998] who measured the concentration profile distribution of the particles ϕ using laser-Doppler velocimetry (**LDV**) method. Their experiments used monodispersed spherical PMMA¹ particles, large enough to neglect Brownian effects, and of diameters between 50 and 100 μm . Moreover, the particles were immersed in a Newtonian liquid (Triton X-100 + UCON 75-H) of dynamic viscosity $\eta_0 = 0.48 Pa \cdot s$ at 20 °C, and of density $\rho_f = 1.19 g \cdot cm^{-3}$ which was equal to that of the PMMA particles ($\rho_p = \rho_f = \rho$) in order to prevent sedimentation problems.

The rectangular **CS** conduit was of length L , and of width $2H$. Consequently, different experimental parameters were chosen in a way to neglect inertia, i.e. $Re_p \ll 1$ where Re_p is the particles Reynolds number [Goldsmith et al. 1967] defined as:

$$Re_p = \frac{4}{3} \frac{\rho}{\eta} \frac{a^3}{H^2} \mathbf{U}_{max} \quad (3.5)$$

\mathbf{U}_{max} is the maximum suspension velocity and a the particle radius.

Another parameter is the ratio $\left[\frac{L}{H}\right]_{ss}$ that was chosen in a way to ensure that, the measured profiles were at fully developed state. [Nott and Brady 1994] have shown that the profiles are fully developed if:

$$\left[\frac{L}{H}\right]_{ss} \gtrsim \frac{1}{12g(\phi)} \left(\frac{H}{a}\right)^2 \quad (3.6)$$

where $g(\phi)$ stands for the bulk particle concentration dependence of the shear-

¹Polymethyl methacrylate

3.4. VALIDATION OF THE CODE IMPLEMENTATION IN OPENFOAM®

induced diffusion coefficient. After a good fitting to their experimentally measured diffusion coefficients, [Leighton and Acrivos 1987], and later [Chapman 1990] have found $g(\phi)$ on the following form

$$g(\phi) = \frac{1}{3}\phi^2 \left(1 + \frac{1}{2}e^{8.8\phi} \right). \quad (3.7)$$

Some zones during the flow may be experiencing a zero shear rate such as at the channel centerline. In this latter situation, the model predicts concentration profiles with a cusp representing a singularity ($\phi = \phi_m$). This singularity is localised in a narrow zone whose size is of the order of magnitude of the particle size, where the description of the suspension as a continuum medium makes no sense any more. In order to eliminate this singularity at the channel centerline, a non-local shear rate $\dot{\gamma}_{NL}$ [Nott and Brady 1994, Miller and Morris 2006] is defined and added to the local shear rate $\dot{\gamma}$ in equation (1.73) such that

$$\dot{\gamma}_{NL} = a_s \frac{\mathbf{U}_{max}}{H}, \quad (3.8)$$

where a_s is equal to 0, ϵ , or ϵ^2 and $\epsilon = \frac{a}{H}$.

To solve the concentration distribution profile of particles, during the flow inside the conduit of a rectangular **CS** (cross-sectional) area, the two-dimensional domain of the conduit, as you can see in Figure (3.1), is meshed using the already installed “blockMesh” utility in [OpenFOAM®]. The 2D Mesh is uniform in the y-direction (velocity gradient direction) of width $W = 2H = 20\delta y$, but nonuniform in the velocity direction: $L = 100\delta x$ with an expansion ratio equal to $\left(\frac{1}{50}\right)$ in the direction of flow, in order to better capture the different properties at the inlet of the conduit.

3.4. VALIDATION OF THE CODE IMPLEMENTATION IN OPENFOAM®

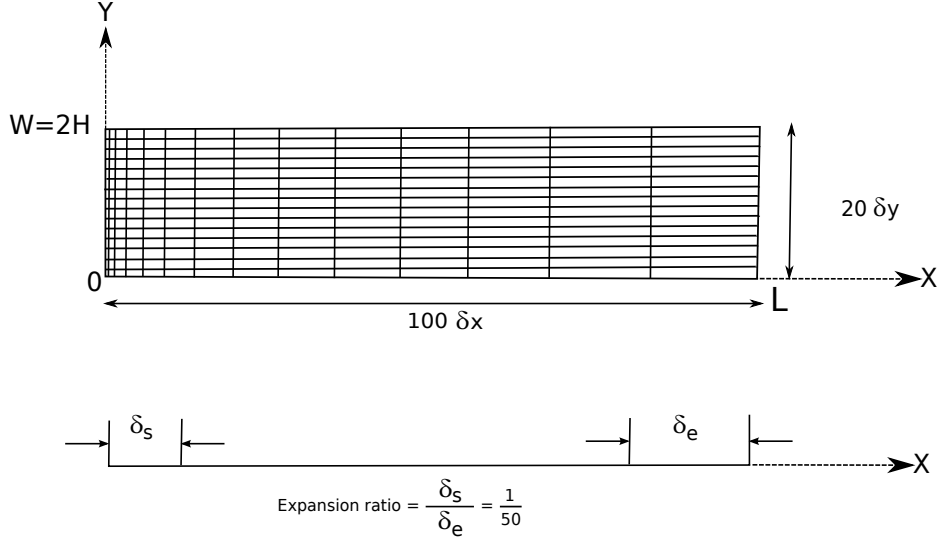


Figure 3.1: Channel rectangular cross-section 2D Mesh

The imposed boundary conditions of the problem of a suspension flow in a channel, to be used in the system of equations (3.1), (3.2), and (3.3), are represented in Figure (3.2).

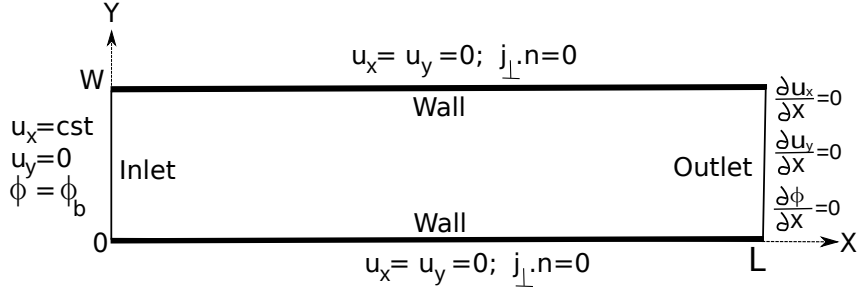


Figure 3.2: Channel 2D imposed boundary conditions

Results for the fully-developed steady state profiles of the concentration ϕ of bulk suspension values ϕ_b of 0.30, 0.40, and 0.50, and at parameters of $\frac{H}{a} = 18$, $\eta_s = \left(1 - \frac{\phi}{\phi_m}\right)^{-2}$, $\phi_m = 0.68$, $\alpha = 4$, $\lambda_2 = 0.8$, $\lambda_3 = 0.5$, and $a_s = \epsilon$ are shown in the following Figures (3.3), (3.4), (3.5), and (3.6).

3.4. VALIDATION OF THE CODE IMPLEMENTATION IN OPENFOAM®

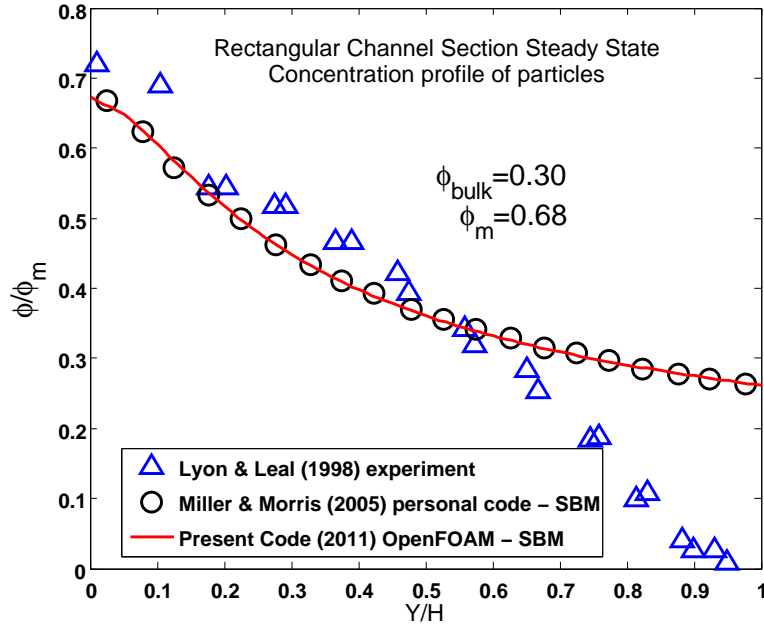


Figure 3.3: 30% Suspension Steady State Concentration Profile

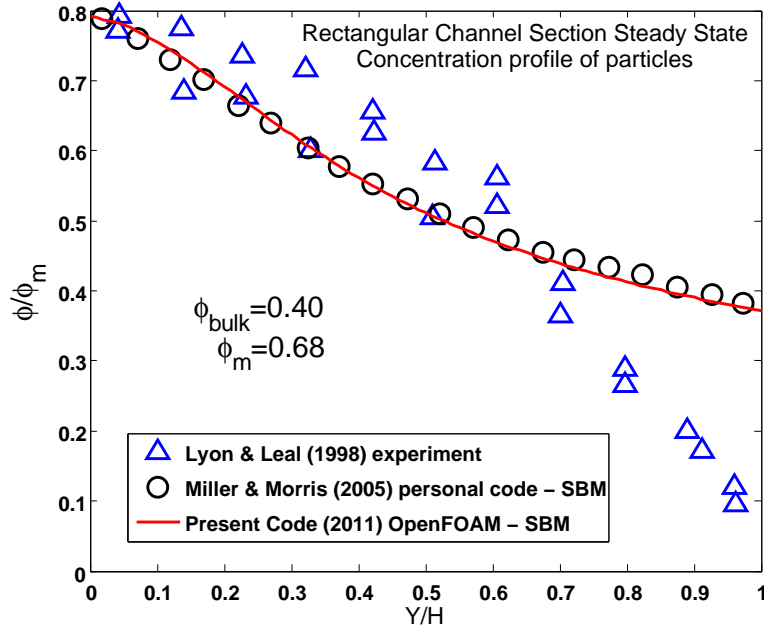


Figure 3.4: 40% Suspension Steady State Concentration Profile

3.4. VALIDATION OF THE CODE IMPLEMENTATION IN OPENFOAM®

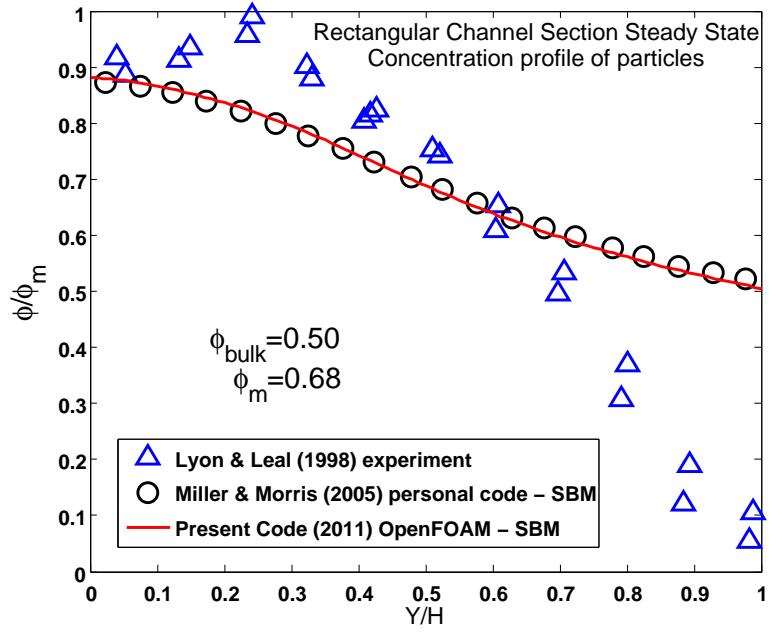


Figure 3.5: 50% Suspension Steady State Concentration Profile

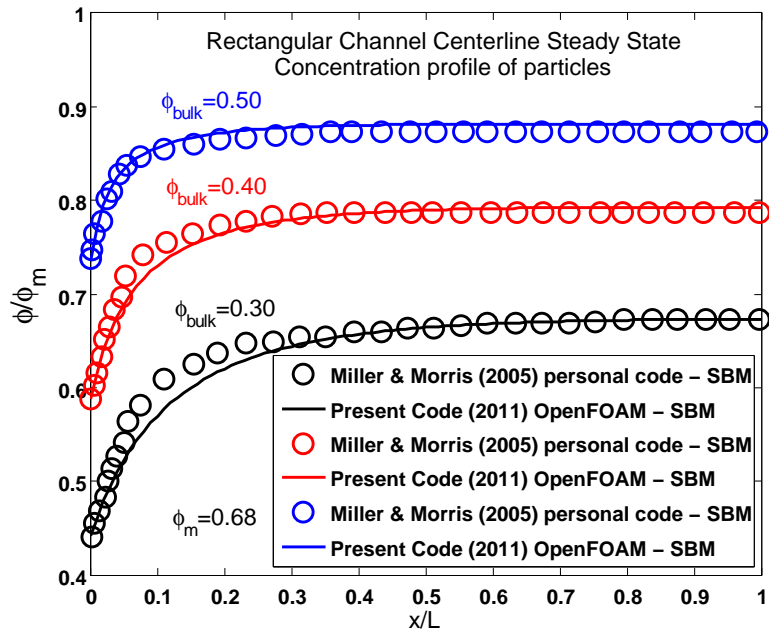


Figure 3.6: Centerline Steady State Concentration Profile

The Numerical profiles of our implemented code in [OpenFOAM®] in the

3.4. VALIDATION OF THE CODE IMPLEMENTATION IN OPENFOAM®

present study, were in good agreement with those of the 2D code given by [Miller and Morris 2006] along the cross section of the rectangular channel as you can see in Figures (3.3), (3.4), and (3.5). However, we observe a slight difference between the data along the centerline of the channel especially at the first quarter of the conduit length in (3.6).

Figure (3.7) shows an example of the evolution of *Residuals* (see section (2.5.1)) with the number of iterations of the different calculated variables (“c” stands for the concentration ϕ , \mathbf{U} the velocity, and p the pressure), from start untill the steady state in concentration is reached.

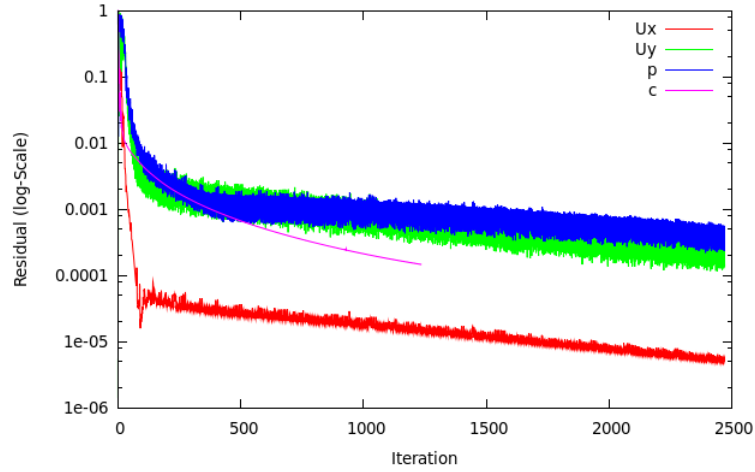


Figure 3.7: Residuals of the 30% Suspension case in Figure (3.3)

The number of iterations necessary to calculate the concentration “c” ($c \equiv \phi$) is half of that needed by the velocity and the pressure fields. That’s due to the fact that “c” was calculated at each time step outside the “SIMPLE” loop, where we did 2 pressure-velocity “SIMPLE” corrections (see the code in section 3.3.1) and look at the Appendix D on page 228 for the different settings we used in simulations for the [Numerical Schemes] and the [Solution Solvers].

As a conclusion for the previous section (3.4.1.1), the implementation in [OpenFOAM®] of the **SBM** for the shear flows of monodispersed suspensions was successful, and well tested for a 2D flow of a suspension inside a rectangular **CS** conduit. We will move now to the next following section (3.4.1.2), where

3.4. VALIDATION OF THE CODE IMPLEMENTATION IN OPENFOAM®

the validity of our implemented code in [OpenFOAM®] will be studied for a suspension flow inside a pipe.

3.4.1.2 Suspension flow in a pipe (circular cross-section conduit)

Similarly, the flow of suspensions in pipes is simulated, but as an axisymmetry problem. Axisymmetric geometries are implemented in [OpenFOAM®] in a 2D manner via what's known as "Wedge-type-geometry", that is explained in the Appendix A on page 220.

[Hampton et al. 1997] made their experiments on suspensions undergoing pressure driven flow in a circular conduit. They used the **NMR** imaging technique to capture the spatial particle distribution in the cross-section of the pipe. Their experiments included monodispersed suspensions of PMMA spherical particles of mean diameter $2a = 650\mu m$, and of density $\rho_p = 1180.7 Kg \cdot m^{-3}$ matched to that of the suspended liquid ρ_f . Their latter suspended liquid was of dynamic viscosity $\eta_0 = 2.1 Pa \cdot s$ at $28^\circ C$.

The two-dimensional domain of the pipe, as you can see in Figure (3.8), is meshed uniformly in both the r -axis and z -axis directions, of diameter $R = 20\delta r$ and of length $L = 100\delta z$. The boundary conditions for the problem are similar to those in Figure (3.2).

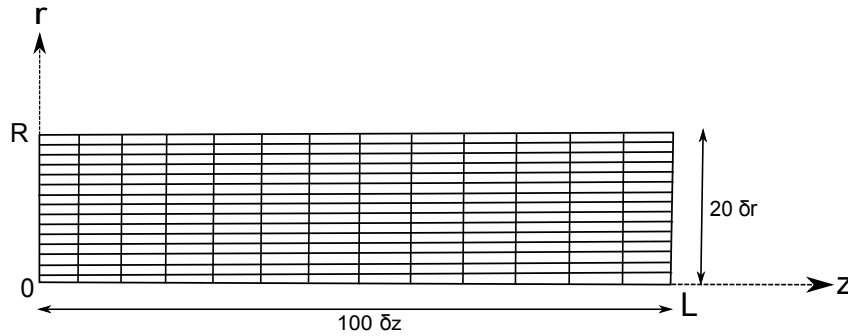


Figure 3.8: Circular cross-section pipe 2D Mesh

The results of the numerical simulations, by using our code, for the suspen-

3.4. VALIDATION OF THE CODE IMPLEMENTATION IN OPENFOAM®

sion flow inside a pipe of concentrations 0.20, 0.30, and 0.45, and at parameters $\frac{R}{a} = 16$, $\eta_s = \left(1 - \frac{\phi}{\phi_m}\right)^{-2}$, $\phi_m = 0.68$, $\alpha = 2$, $\lambda_2 = 0.8$, $\lambda_3 = 0.5$, and $a_s = \epsilon$ are viewed out in the following Figures (3.9), (3.10), (3.11), and (3.12).

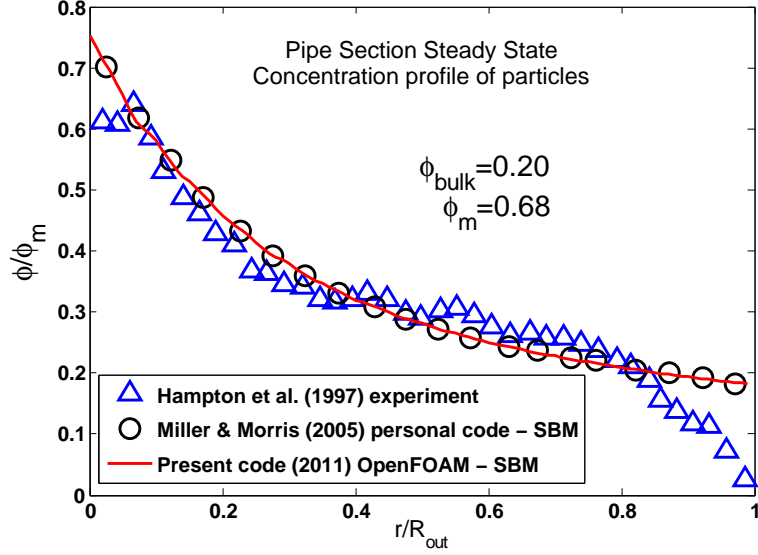


Figure 3.9: 20% Suspension Steady State Concentration Profile

3.4. VALIDATION OF THE CODE IMPLEMENTATION IN OPENFOAM®

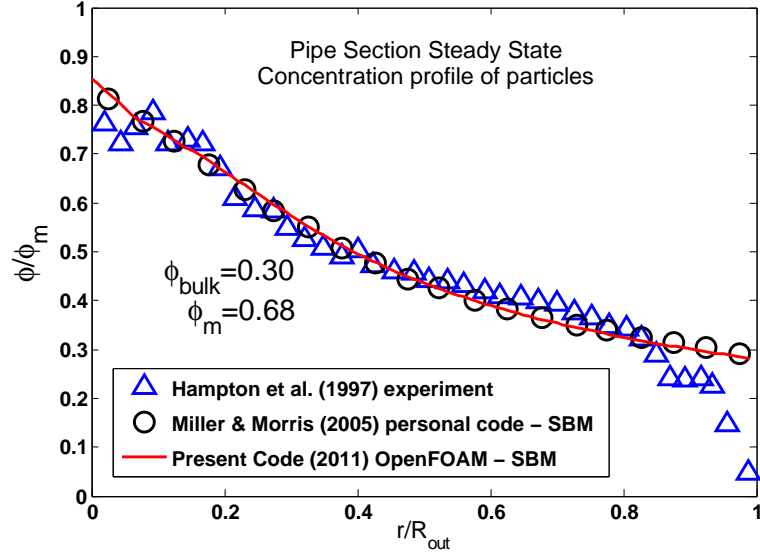


Figure 3.10: 30% Suspension Steady State Concentration Profile

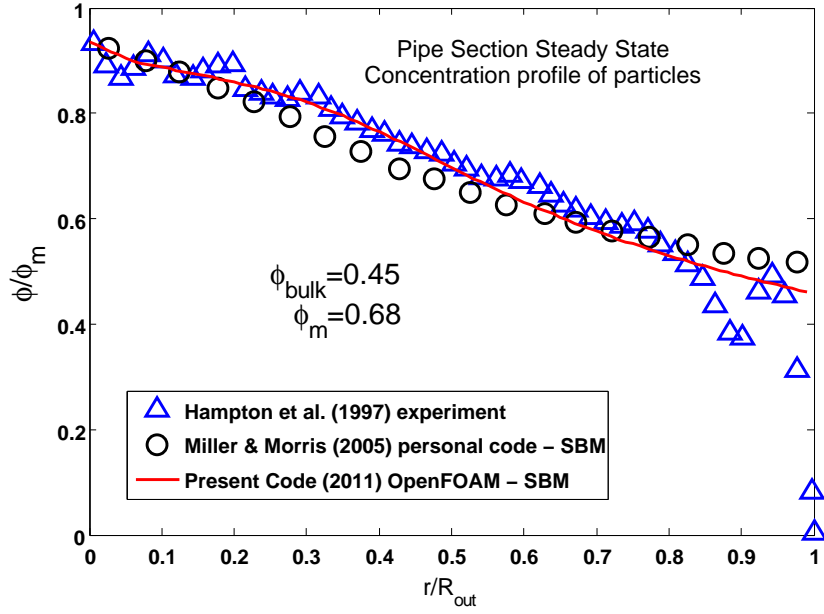


Figure 3.11: 45% Suspension Steady State Concentration Profile

3.4. VALIDATION OF THE CODE IMPLEMENTATION IN OPENFOAM®

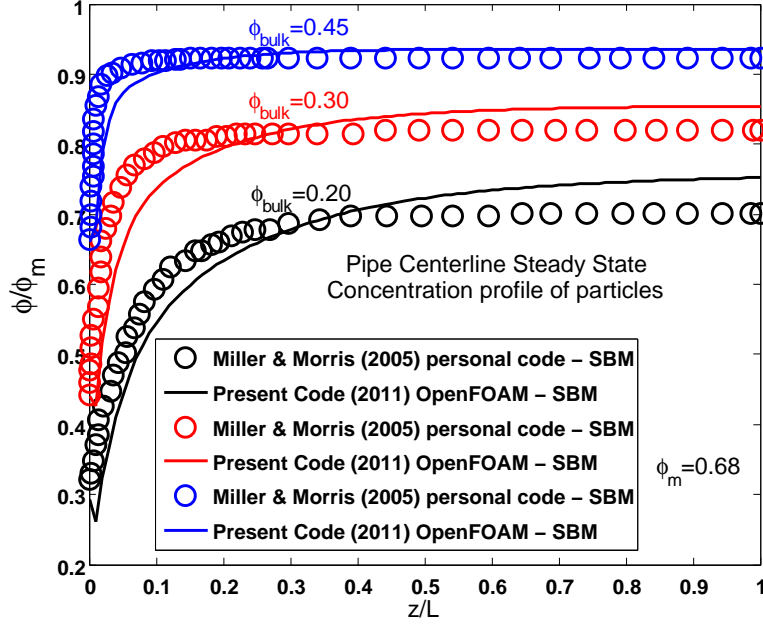


Figure 3.12: Centerline Steady State Concentration Profile

Good closeness is observed between our numerical data results, and those provided by [Miller and Morris 2006] which can emphasize the well implementation of the original **SBM** inside the [OpenFOAM®] environment. This closeness is especially good for the 20% and 30% concentration profiles across the section of the pipe. For the 45% one can see an observable deviation between our numerical profile and that obtained by [Miller and Morris 2006]. This slight difference may be due to some interpolation scheme types that have been taken differently in the two codes. Furthermore, in Figure (3.12), we observe that the concentration profiles along the pipe centerline that we calculated are not the same as those presented by [Miller and Morris 2006].

Looking more carefully at the results of [Miller and Morris 2006], we realized that the profiles they present as obtained at the centerline were actually at $(\frac{r}{R}) \sim 0.02$ (first points in Figures (3.9), (3.10) & (3.11)). This leads to a difference which is the more important the lower the volume fraction is.

3.4.2 Suspension flow in a Couette cell geometry

The suspension flow in a Couette cell is here a flow between two concentric cylinders, the inner cylinder is rotating with an angular velocity Ω , and the other is stationary. The suspension, before the flow occurs, has a uniform distribution of particles in the geometrical space. During the flow, it is observed that the particles migrate toward the outer cylinder.

The Suspension Balance Model, implemented through equations (3.1), (3.2) and (3.3) in the [OpenFOAM®] environment, is used and tested for the monodisperse suspension flow in a Couette cell geometry. Our numerical data are compared with the experimental ones of [Phillips et al. 1992] and most of all with the numerical profiles provided by [Morris and Boulay 1999].

In their experiment, [Phillips et al. 1992] used a monodispersed suspension of PMMA spheres of mean diameter $2a = 675\mu m$, suspended in a Newtonian liquid mixture of dynamic viscosity $\eta_0 = 4.95 Pa \cdot s$ at $23.15^\circ C$, and of density $\rho_f \simeq \rho_p = \rho = 1182 Kg \cdot m^{-3}$.

The inner and outer radii of the Couette cell were $0.64 cm$ and $2.38 cm$, respectively. The cavity length was $25 cm$. They measured the profile concentration using the **NMR** technique.

We consider here the Couette cell as infinite cylinders, and with no gravitational effects in the vertical axial direction, which reduces the problem to be simulated in 1D in the radial direction. We use a Wedge-type geometry defined in Appendix A on page 220 due to the axi-symmetry of the problem. The 1D domain of calculation and the boundary conditions are shown in Figures (3.13) and (3.14) respectively. It is good to mention that the tensor \mathbf{Q} defined in equation (1.75) will have here (for the flow in a Couette cell geometry) the following form:

$$\mathbf{Q} = \begin{bmatrix} \lambda_2 & 0 & 0 \\ 0 & 1 & 0 \\ 0 & 0 & \lambda_3 \end{bmatrix}.$$

That's due to the respect of its previous definition for the principal directions

3.4. VALIDATION OF THE CODE IMPLEMENTATION IN OPENFOAM®

1, 2 & 3 which stand for the flow, velocity-gradient and vorticity directions, respectively.

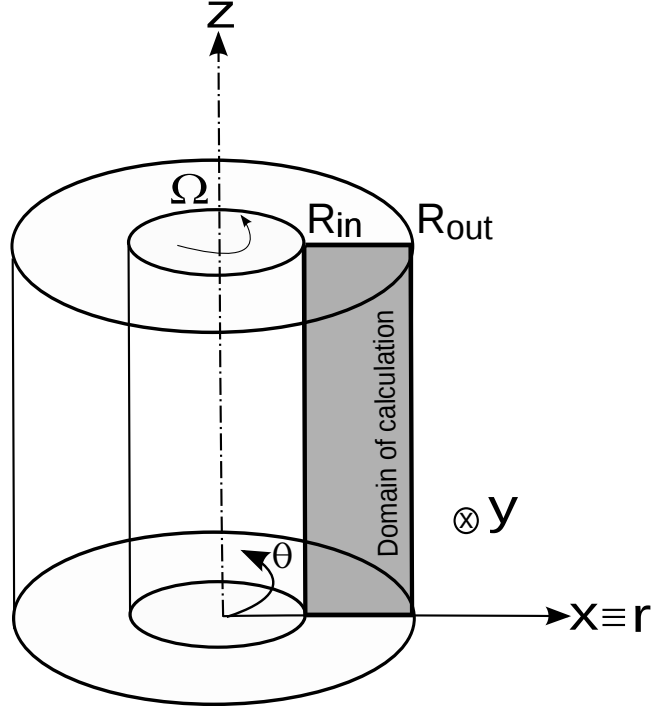


Figure 3.13: Couette cell

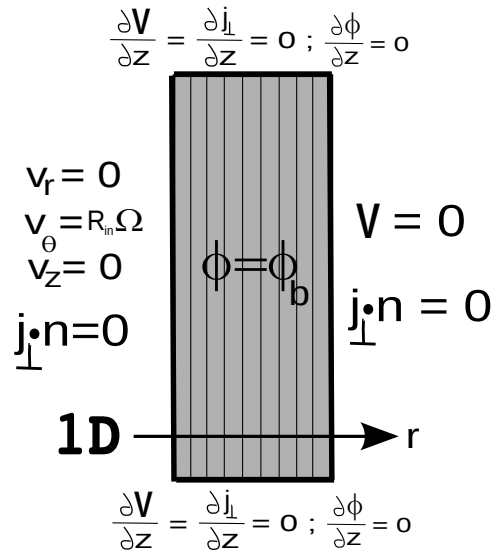


Figure 3.14: Couette cell Boundary Conditions

3.4. VALIDATION OF THE CODE IMPLEMENTATION IN OPENFOAM®

Our 1D numerical results for the transient concentration profiles evolution were at the following model variables:

$$K_n = 0.75, \frac{a}{R_{out}} = 0.0143, \phi_{bulk} = 0.55, \alpha = 4, \phi_m = 0.68, \lambda_2 = 0.8, \lambda_3 = 0.5, a_s = 0, f(\phi) = (1 - \phi)^\alpha, \eta_s = 1 + 2.5\phi \left(1 - \frac{\phi}{\phi_m}\right)^{-1} + 0.1 \left(\frac{\phi}{\phi_m}\right)^2 \left(1 - \frac{\phi}{\phi_m}\right)^{-2},$$

and $\eta_N = K_n \left(\frac{\phi}{\phi_m}\right)^2 \left(1 - \frac{\phi}{\phi_m}\right)^{-2}$.

The evolution of the particles distribution in the suspension sheared between the two cylinders is shown in the following Figures (3.15) and (3.16). The **SBM** predicts well the direction of the migration of particles toward the outer cylinder, and it quantifies well the particles distribution in the gap. We have more closeness to the experimental data by using [OpenFOAM®] compared to the 1D numerical simulations of [Morris and Boulay 1999]. However, the small difference between our numerical profiles and those obtained by [Morris and Boulay 1999] code may be due to different interpolation schemes they used during their numerical resolutions for the problem.

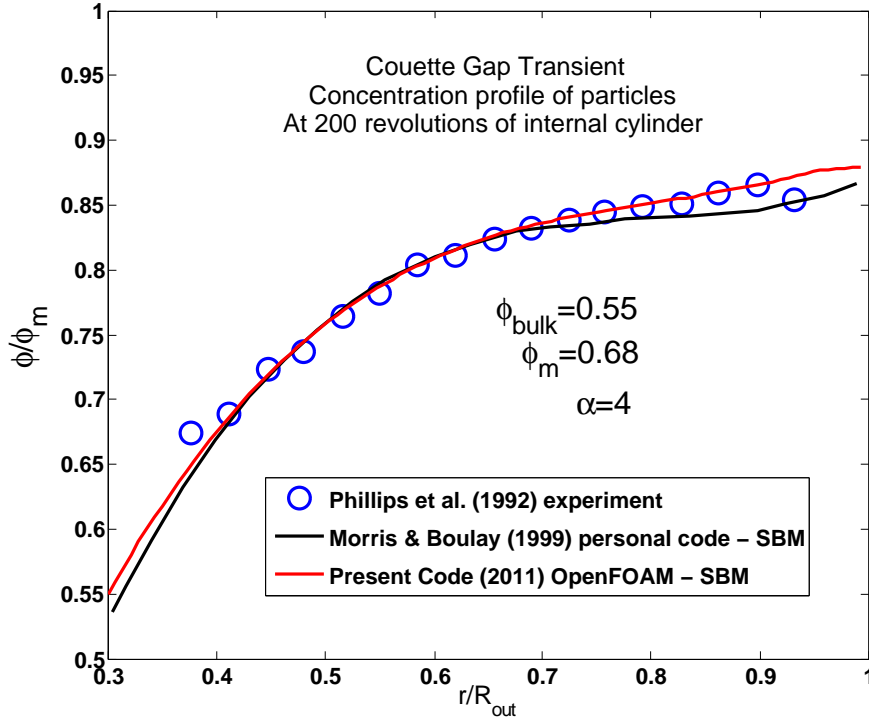


Figure 3.15: Transient Concentration Profiles at 200 revolutions

3.4. VALIDATION OF THE CODE IMPLEMENTATION IN OPENFOAM®

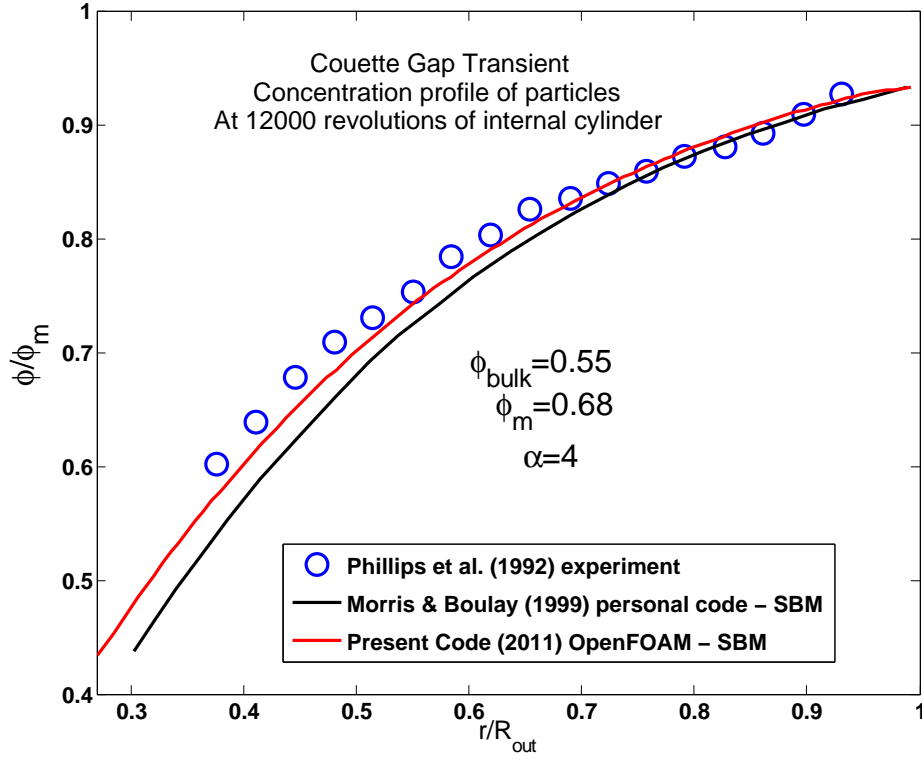


Figure 3.16: Transient Concentration Profiles at 12000 revolutions

It is good to remention the importance of the maximum volume fraction packaging value ϕ_m in affecting well the numerical results. Here ϕ_m was taken to be 0.68 by [Morris and Boulay 1999] just to fit their steady concentration profiles experimental data with the numerical obtained ones by the **SBM**, and with the viscosity form they adopted as $\eta_s = 1 + 2.5\phi \left(1 - \frac{\phi}{\phi_m}\right)^{-1} + 0.1 \left(\frac{\phi}{\phi_m}\right)^2 \left(1 - \frac{\phi}{\phi_m}\right)^{-2}$. We took their same ϕ_m value 0.68 here just to test the validity of implementation of the Suspension Balance Model in [OpenFOAM®] for the Couette cell flow. However, we will see later in chapter 4 that for a suspension of $2a = 140 \mu m$ we measure a ϕ_m of 0.58 .

Analytically, at steady state and in the cylindrical coordinate system, the radial momentum balance is represented by the following equation:

3.4. VALIDATION OF THE CODE IMPLEMENTATION IN OPENFOAM®

$$\frac{1}{r} \frac{\partial}{\partial r} (r \Sigma_{rr}) = \frac{\Sigma_{\theta\theta}}{r}. \quad (3.9)$$

According to the definition of N_1 and N_2 in equation (1.76), equation (3.9) can be rewritten as:

$$\frac{\partial \Sigma_{rr}}{\partial r} = \frac{\Sigma_{\theta\theta} - \Sigma_{rr}}{r} = \frac{N_1}{r}, \quad (3.10)$$

where θ , and r denote the flow and velocity gradient directions, respectively.

Using equations (1.73) & (1.76) in expression (3.10), and replacing N_1 by its form yields

$$\lambda_2 \frac{d(\eta_N \dot{\gamma})}{dr} = \frac{\eta_N \dot{\gamma} (1 - \lambda_2)}{r}, \quad (3.11)$$

which is solved in conjunction with the shear stress balance

$$\frac{1}{r^2} \frac{\partial}{\partial r} (r^2 \Sigma_{r\theta}) = 0, \quad \Sigma_{r\theta} \equiv \tau = \eta_0 \eta_s(\phi) \dot{\gamma}, \quad (3.12)$$

and

$$\dot{\gamma} = r \frac{\partial}{\partial r} \left(\frac{u_\theta}{r} \right). \quad (3.13)$$

The balance in shear stress yields

$$\dot{\gamma} = \frac{C}{r^2 \eta_s(\phi)}, \quad (3.14)$$

which is substituted in equation (3.11) to give

$$q(\phi) \equiv \frac{\eta_N(\phi)}{\eta_s(\phi)} = A_c r^{\frac{1+\lambda_2}{\lambda_2}}, \quad (3.15)$$

where A_c represents a constant determined by requiring $\phi(r)$ to average to

3.4. VALIDATION OF THE CODE IMPLEMENTATION IN OPENFOAM®

the imposed bulk concentration $\phi_{bulk} \equiv \phi_b$ such that

$$\phi_b \pi (R_{out}^2 - R_{in}^2) = \int_{R_{in}}^{R_{out}} \phi(r) \cdot 2\pi r dr \quad (3.16)$$

The analytical predicted steady state concentration profiles using equations (3.15) and (3.16) for a bulk suspension of $\phi_b = 0.55$, and at $\lambda_2 = 0.8$, are compared with the experimental results of [Phillips et al. 1992] as you can see in Figure (3.17). Our steady numerical profile using the **SBM** in [OpenFOAM®] (line in Figure (3.17)) matches exactly the analytic profile solution of equations (3.15) and (3.16) (circles in Figure (3.17)).

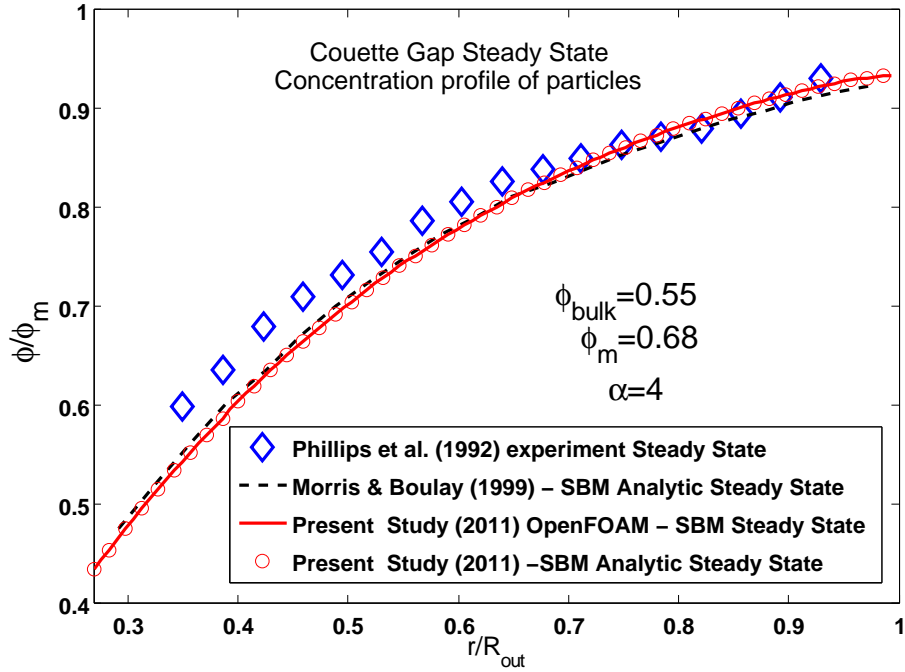


Figure 3.17: Steady State Concentration Profiles in a Couette gap

Note that it is not the case for the stationary profile obtained numerically by [Morris and Boulay 1999] that calculated the values of ϕ near the inner cylinder slightly underestimated.

3.5 CLOSURE

In this chapter (3) we have seen the implementation of the original Frame-Dependent Suspension Balance Model in the [OpenFOAM®] environment, and its validity for suspension flows inside channels of two different cross-sectional areas, and for suspension flows inside Couette cell geometry. Note that here all the simulations have been done using the “original SBM” as it was presented previously in Literature by [Nott and Brady 1994, Morris and Boulay 1999]. The next coming two chapters (4) and (5) will be a revisit on the “SBM”, where the chapter (4) describes the experiments that have been done to determine well its different important parameters $\eta_s(\phi)$, $\eta_N(\phi)$, λ_2 and λ_3 . Another chapter (5) will present different simulations examples using the modified version of the “SBM”, according to our present determination for its latter parameters.

Chapter 4

MEASUREMENTS OF NORMAL STRESSES

4.1 OVERVIEW

In this chapter (4) we present a developed experimental technique for the measurements of Normal stresses in non-Brownian suspensions. We start by an Introduction in section (4.2), and the theoretical background of the Suspension material functions in a torsional flow between two rotating parallel plates in section (4.3). Our experiments are shown and discussed in section (4.4). Later, the determination of the three material functions η_s , α_1 , and α_2 in the suspensions are explained in section (4.5), and the particle normal stresses are presented in section (4.6). Finally, it is the closure of this chapter (4) in section (4.9).

4.2 INTRODUCTION

Despite of some existing differences among the results in literature, the suspension viscosity as a function of the volume fraction of particles is quite well

known. However, it is a different situation for normal stress differences that are still mysterious in the suspensions with very few things known about them. It is well established that whenever the concentration of particles is large enough, normal stress differences used to appear in the suspensions. The early works of [Gadala-Maria 1979] have shown that the normal stress differences (actually the difference $N_1 - N_2$) were proportional to the shear stress, and of the same order of magnitude. Then, one had to wait until the year 2000, where the Normal stress differences had been determined thanks to the anti-Weissenberg effect, and to the total force measurements exerted on a rotating cone or disk, on top of a stationary plane [Zarraga et al. 2000]. Later [Singh and Nott 2003] proposed a technique to measure both N_1 & N_2 by coupling data taken from two separated experiments, that's by installing pressure transducers in a Couette cell geometry from one side, and in a two parallel disks cell from the other side. Recently, [Boyer et al. 2011 a] have measured precisely $(N_1 + 2N_2)$ as a function of the volume fraction of particles ϕ , using the anti-Weissenberg effect, in addition to, [Couturier et al. 2011] who have determined the second normal stress difference N_2 , by measuring the deformation of the free surface of a suspension flow in a narrow inclined channel. The latter two measurements show that N_1 is of the order of zero, and that N_2 is negative. We present here the direct determination of both Normal stress differences N_1 & N_2 by a technique of measuring the Normal stress radial profile Σ_{22}^T (in the direction of velocity-gradient) in a torsional suspension flow between rotating parallel plates [Bird et al. 1977]. Concurrently, the pore pressure¹ P_f was measured via circular grids that separate the solid particles phase from the liquid one, which allowed us to deduce the particle normal stress Σ_{22}^p given by: $\Sigma_{22}^p = \Sigma_{22}^T - \Sigma^f$, that's by subtracting the isotropic fluid stress, Σ^f , from the total normal stress $\Sigma_{22}^T \equiv \Sigma_{22}$. The knowledge of the three normal components of the particle stress $2^{nd} - rank$ tensor Σ_{11}^p , Σ_{22}^p , and Σ_{33}^p is of great importance, due to the significant role they play in predicting the phenomenon of shear-induced migration of parti-

¹The pressure of the fluid in the pore space is just the pressure exerted by the overlying fluids between the solid spheres.

4.3. SUSPENSION MATERIAL FUNCTIONS IN A TORSIONAL FLOW BETWEEN TWO ROTATING PARALLEL PLATES

cles in non-Brownian suspensions. That's according to the "Suspension Balance Model" of [Nott and Brady 1994, Morris and Boulay 1999]. [Deboeuf et al. 2009] have proposed direct determination of the third component in the latter tensor, Σ_{33}^p , by measuring the pressure in a sheared suspension through grids attached to the walls of a Couette cell geometry. They found [GISEC06 2010] that the particle normal stresses vary quadratically with ϕ . Moreover, [Zarraga et al. 2000], and [Acrivos et al. 1993] measured indirectly the component Σ_{33}^p by regarding the resuspension of a sedimented bed of particles. Whenever, the bed of particles is sheared, its height changes till reaching a stationary value which represents in the vertical direction, the balance between the gravitational volumetric force on a particle, and the gradient of the particle normal stress. The next sections expose that, our results [Dbouk et al. 2011] are in good agreement with the different previous measurements found in literature.

4.3 SUSPENSION MATERIAL FUNCTIONS IN A TORSIONAL FLOW BETWEEN TWO ROTATING PARALLEL PLATES

First of all, it's necessary to mention the argument of choosing this type of geometry, where the normal stresses are measured in a torsional flow of a suspension sheared between two rotating parallel disks. Our choice was made, after taking into account the previous observations presented in the literature, which showed that the shear-induced migration of particles has no existence, or it is so weak, in such a flow [Chow et al. 1994, Chapman 1990, Merhi et al. 2005, Bricker and Butler 2006]. So, the concentration remains homogeneous enough during the experiment, and we can determine the following material functions α_1 , α_2 , and η_s ($\eta_s = \frac{\eta}{\eta_0}$) at a well controlled volume fraction of particles ϕ .

4.3.1 Torsional flow at small Reynolds Number

Our work here is restricted to the flow of non-Brownian monodispersed suspensions of hard spheres. We are at neglected inertial effects, and where the

4.3. SUSPENSION MATERIAL FUNCTIONS IN A TORSIONAL FLOW BETWEEN TWO ROTATING PARALLEL PLATES

hydrodynamic forces dominate over the brownian ones ($Re \ll 1$ & $Pe \gg 1$) as we have mentioned previously in section (1.3.2.2) of chapter (1).

The viscosity of the suspension sheared in the torsional flow between two parallel disks is given by:

$$\eta = \frac{\Gamma}{2\pi R^3 \dot{\gamma}_R} \left(3 + \frac{d \ln(\Gamma/2\pi R^3)}{d \ln \dot{\gamma}_R} \right), \quad (4.1)$$

$$\dot{\gamma}_R = \frac{\Omega R}{h} \quad (4.2)$$

where R is the disks radius, Γ the torque on the upper rotating disk of angular velocity Ω , $\dot{\gamma}_R$ the shear rate at edge of the system, and h is the gap.

If the suspension viscosity η is independent of $\dot{\gamma}$ [*i.e.* $\left(\frac{d \ln(\Gamma/2\pi R^3)}{d \ln \dot{\gamma}_R} \right) \approx 1$], then it will be such that:

$$\eta = \frac{2\Gamma}{\pi R^3 \dot{\gamma}_R} = \frac{2\Gamma h}{\pi R^4 \Omega} \quad (4.3)$$

Before showing the normal stress coefficients α_1 and α_2 , it is good to note that in this manuscript the normal stresses are defined by directing the normals toward the interior side of a medium element (compressional stresses are negative) as we have shown previously in the stress convention on page 12.

The normal stress coefficients α_1 and α_2 are defined as:

$$\alpha_1 = -\frac{N_1}{\eta_0 \cdot |\dot{\gamma}|} \text{ \& } \alpha_2 = -\frac{N_2}{\eta_0 \cdot |\dot{\gamma}|}. \quad (4.4)$$

The radial variation of the second component of the normal stresses is defined as (see section 1.5.4):

$$\Sigma_{22}(r) = -\eta_0 \dot{\gamma}_R \left[(\alpha_1 + 2\alpha_2) \frac{r}{R} - (\alpha_1 + \alpha_2) \right] - P_a, \quad (4.5)$$

where P_a is the atmospheric pressure we choose as the reference ($P_a = 0$).

Thus, equation (4.5) makes it possible to determine both α_1 and α_2 if one measures the radial profile of Σ_{22} . In our experiment, we then expect to have a

4.3. SUSPENSION MATERIAL FUNCTIONS IN A TORSIONAL FLOW BETWEEN TWO ROTATING PARALLEL PLATES

linear profile of Σ_{22} in the radial direction, where the slope k_p gives an access to $-(\alpha_1 + 2\alpha_2)$ and the ordinate at origin k_{oo} gives an access to $(\alpha_1 + \alpha_2)$. In addition to the direct transducers that allow the measurements of $\Sigma_{22}(r)$, four indirect transducers were placed behind four respective holes. The holes were covered with grids to retain the particles in the rheometer gap such that the transducers attached to them measure the pore pressure P_f in the suspension. Upon subtracting $\Sigma_{22}^f = -P_f$ from the measured normal stress on the flush mounted transducers Σ_{22} , we can get what we call “the second particle normal stress Σ_{22}^p ” such that:

$$\Sigma_{22}^p = \Sigma_{22} - \Sigma_{22}^f . \quad (4.6)$$

This idea is based on and emphasized in the existing bi-phase Models in the literature, where the total stresses in the suspension are defined as the sum of both, the fluid stresses and the particle stresses [Nott and Brady 1994, Morris and Brady 1998]. Moreover, the idea of measuring the fluid interstitial pressure by separating the suspension from direct contact with the sensors via grids, comes from the previous works of [Deboeuf et al. 2009] who measured the pore pressure in a sheared suspension in a cylindrical Couette cell.

As a short summary, the radial profile of Σ_{22} gives us an access to both α_1 and α_2 , and the measurements of the pore pressure P_f allow us to get and extract Σ_{22}^p using equation (4.6), where from these terms α_1 , α_2 and Σ_{22}^p we can deduce the other two particle normal stresses Σ_{11}^p , and Σ_{33}^p utilising both, the isotropy of the fluid stress, and the definitions in equation (1.16):

$$\Sigma_{11}^p = \Sigma_{22}^p + N_1 ; \Sigma_{33}^p = \Sigma_{22}^p - N_2 . \quad (4.7)$$

Thus we have seen now the methodology of getting the three particle normal stresses Σ_{11}^p , Σ_{22}^p and Σ_{33}^p , where we will show you soon that their knowledge is of a huge significance.

4.4 EXPERIMENTS

4.4.1 Experimental device

The suspension was placed between two parallel disks of radius $R = 5.5\text{cm}$, and gap $h = 2\text{ mm}$, inside a controlled Mars II Rheometer (Haake, Thermofisher) as you can see in Figure (4.1).



Figure 4.1: Experimental Setup

Four flush mounted pressure transducers (sensors) (STS ATM $\pm 25\text{ mbar}$; Figure (4.2)) had been installed directly in the stationary lower disk at different

4.4. EXPERIMENTS

positions ($R_i = 1.1, 3, 3.3, \text{ and } 3.9 \text{ cm}$) as it is illustrated in the Figure (4.3):



Figure 4.2: STS Pressure Sensor

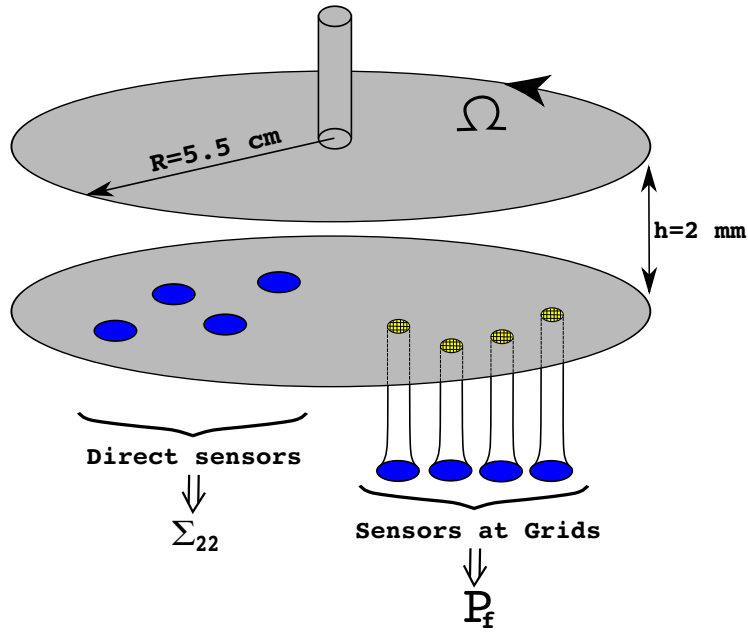


Figure 4.3: Experimental Setup

The pressure transducer membranes have to be exactly at the surface (if not, a hole pressure is to be accounted for). To solve this problem we coated the membranes at the surface via RTV elastomer. But, we discovered quickly that this elastomer is too fragile which obliged us to remove it and seek another solution. The final good decision was to coat the membranes surface with paraffin as you can see in the following Figure (4.4).

4.4. EXPERIMENTS

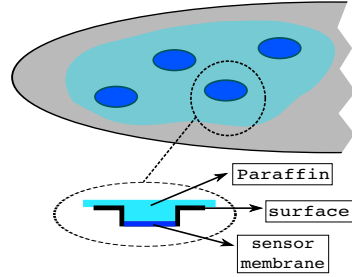


Figure 4.4: Paraffin Coating

After the coating process the pressure sensors were tested by measuring the hydrostatic pressure of a column of Glycerine in water solution of height h . It is shown in Figures (4.5) & (4.6) that all the pressure transducers work very well after coating the surface with paraffin, and all measure fine the hydrostatic pressure with a maximum deviation of around 2% only.

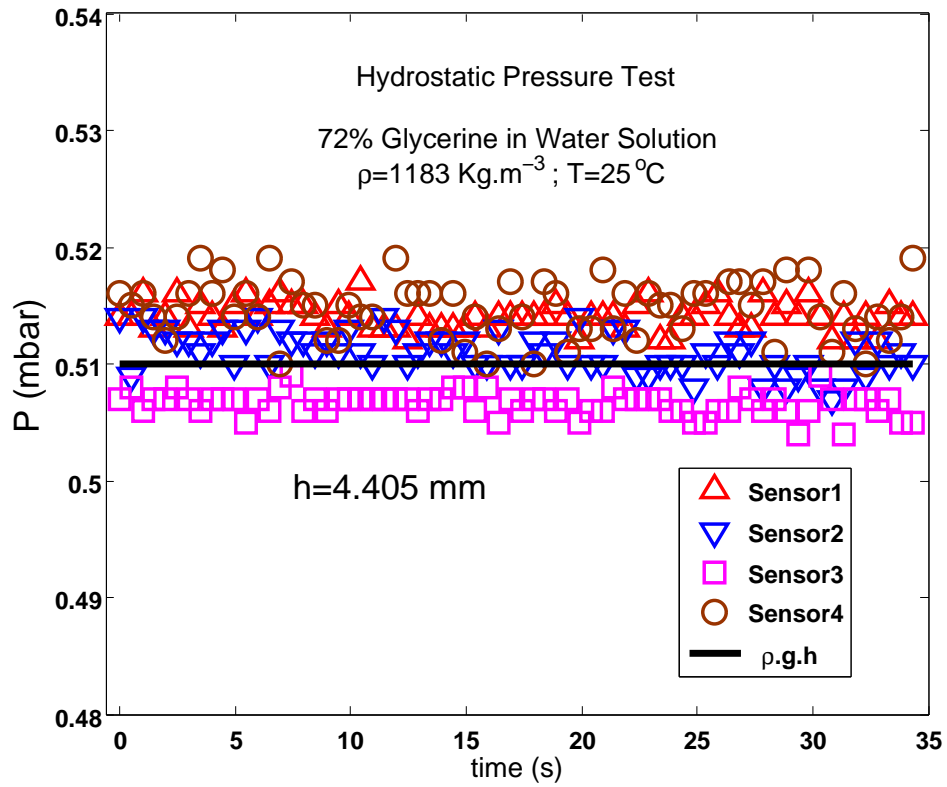


Figure 4.5: Hydrostatic Pressure Test

4.4. EXPERIMENTS

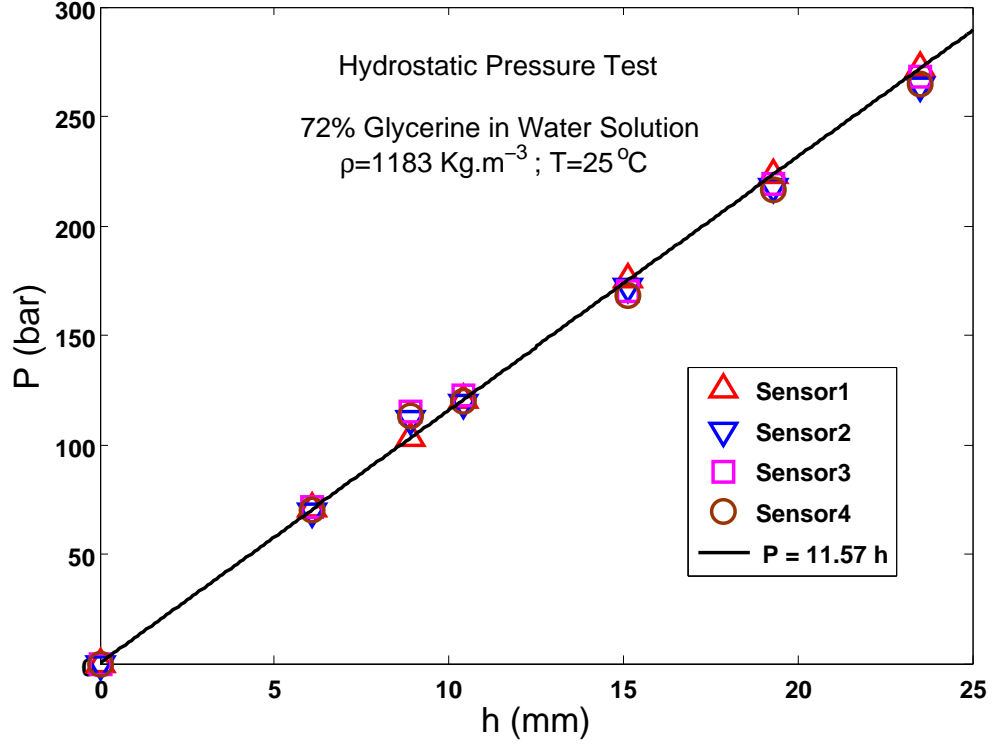


Figure 4.6: Hydrostatic Pressure Test

Furthermore, four holes 2 mm in diameter have been made in the lower stationary disk (see Figure 4.3). They were covered with grids (square-meshed) that are well fitted inside the holes ($50 \mu\text{m}$ space at the edge). That's to retain the spherical particles between the two disks in a way such that the transducers attached to them can measure well the pore pressure P_f in the suspension.

4.4.2 Suspensions

We have studied the suspensions of monodispersed spherical particles of polystyrene (Dyno seeds TS, Microbeads) of diameters $40 \text{ \& } 140 \mu\text{m}$ ($\pm 5\%$) dispersed in a newtonian liquid which is a mixture of water, Ucon Oil 75H90000 (Dow) ($\rho_{ucon} = 1.09 \text{ kg} \cdot \text{m}^{-3}$, $\eta_{ucon} = 30 \text{ Pa} \cdot \text{s}$), and zinc bromide. The newtonian liquid mixture was prepared in such a way that its density matched enough that of the particles ($\rho_f = \rho_p = \rho = 1.05 \text{ kg} \cdot \text{m}^{-3}$) in order to prevent any sedi-

4.4. EXPERIMENTS

mentation problem, and also that its viscosity η_0 may vary up to several tens of the centipoise². We used suspensions of volume fraction of particles ϕ between 20% and 50%. The suspending fluid viscosity η_0 has been chosen and modified by diluting the Ucon Oil with water in a way such that the suspension viscosity η is always of the order of $1 \text{ Pa} \cdot \text{s}$, whatever the volume fraction of particles ϕ is. This order of magnitude of the suspension viscosity permits one of getting measurable normal stresses, throwing away the problems of Edge Fracture. Indeed, the normal stresses in a suspension at a given volume fraction of particles are proportional to the shear stress, and it is well known that the second normal stress difference, if negative, is the motor of the Edge Fracture which appears whenever $|N_2|$ passes a critical value [Keentok and Xue 1999] of the order of $|N_{2c}| = 5\Upsilon_t/h$, where Υ_t is the surface tension of the suspension.

Taking $70 \text{ mPa} \cdot \text{m}$ for Υ_t , then $|N_{2c}| \approx 150 \text{ Pa}$. We will see later that our measured second normal stress difference N_2 is of the order of the shear stress Σ_{12} ($|N_2| \sim (0.5 \leftrightarrow 0.8) \cdot \Sigma_{12}$). So, whenever the volume fraction of particles increases, we decrease the fluid viscosity in a way where we can register a shear rate of some tens of s^{-1} without that the shear stress passes 50 Pa .

Moreover, we use large disks ($R = 5.5 \text{ cm}$) and such a large dimension makes it difficult to fill the cell, and it is easier to manipulate a suspension whose viscosity is not too large. In addition to all that, the use of a low viscous suspending fluid facilitates the removing of bubbles that appear when the particles are mixed with the fluid.

The following Table (4.1) of data shows the characteristics of the different suspensions we studied in our experiments. It is good to mention that whatever the viscosity of the suspending fluid is, the particles are large enough so that the Colloidal and Brownian forces are negligible near the Hydrodynamic ones. That is illustrated through the Péclet Number that was much larger than 1, even at small values of shear rate of order of 10 s^{-1} : $Pe = \frac{3\pi\eta_0 a^3 \dot{\gamma}}{\kappa T} \geq (10^6 \dot{\gamma})$.

² 1 centipoise = 0.001 pascal second.

4.4. EXPERIMENTS

Particle diameter 140 μm												
ϕ	0.2	0.245	0.28	0.28	0.3	0.34	0.36	0.38	0.42	0.44	0.45	0.46
η_0 (Pa.s.)	0.36	0.36	0.142	0.93	0.36	0.24	0.24	0.24	0.151	0.151	0.151	0.130

Particle diameter 140 μm							Particle diameter 40 μm				
ϕ	0.46	0.47	0.48	0.49	0.5	0.5	0.3	0.35	0.4	0.45	0.47
η_0 (Pa.s.)	0.143	0.143	0.143	0.17	0.07	0.07	1	0.235	0.235	0.173	0.083

Table 4.1: Suspensions we used in our experiments

4.4.3 Experimental Procedure

For each volume fraction of particles, a suspension of 30 grams was prepared and placed in a closed flask (The suspension mass introduced between the two the disks was about 25 grams). After mixing the particles within the fluid, the suspension was put under ultrasound for a period of 2 hours, then the flask was placed inside an oven at 50 °C for 12 hours in order to decrease the suspending fluid viscosity and to facilitate the removing of the bubbles. After taking the samples out from the oven, they were reweighted to verify nothing was evaporized. When it is cooled down to the standard room temperature, the suspension is placed on the bottom stationary disk with huge attention, in order to avoid any air bubbles that may arise during the filling process. The process of moving down the upper disk to diminish the gap, was slow enough to retain a conservative stable air/suspension interface, and to prevent any air bags from being trapped by the suspension. The upper disk is moved 50 μm below its measurement position so that the distance h between the disks is decreased to the value $(h - 50)$, and the excess in the suspension is cleaned with attention. Then the upper disk is removed up by +50 μm so that the gap became again equal to h $[(h - 50) + 50]$. In the experiments presented here $h = 2.5 \text{ mm}$.

At this stage, the pressure sensors are set to zero as a reference. Then a staircase torque Γ in two opposite directions (clockwise & anti-clockwise), including rest periods, is applied to the suspension on the upper disk causing its rotation. The followed protocol of applying the latter torque is presented in Figure (4.7).

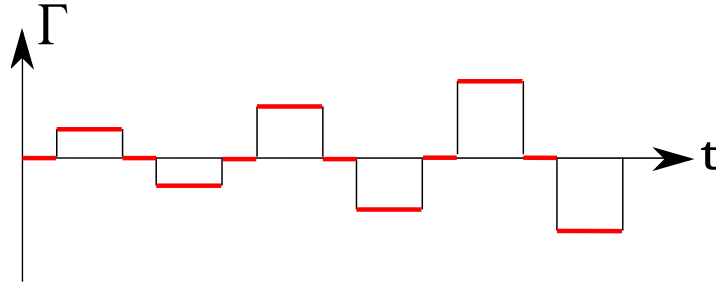


Figure 4.7: The protocol of the applied torque Γ as function of time

The period, at which the torque was applied, was equal to the period being needed by the rotating upper disk to complete at least 3 rotations. The reason of applying this protocol of torque on the upper disk is explained in the next section.

4.4.4 Parallelism problem

There are two possible errors that may arise due to defaults in parallelism in the experimental setup:

1. The axis of rotation is perpendicular to the stationary disk but not to the rotating one as you can see in the following Figure (4.8). During half a period of rotation, the flow above a given transducer is compressional and the pressure exerted on the transducer is increased, while during the other one, the flow is extensional and the pressure is lessened. To correct this parallelism default, the pressure measured at the different transducers is averaged over few revolutions.

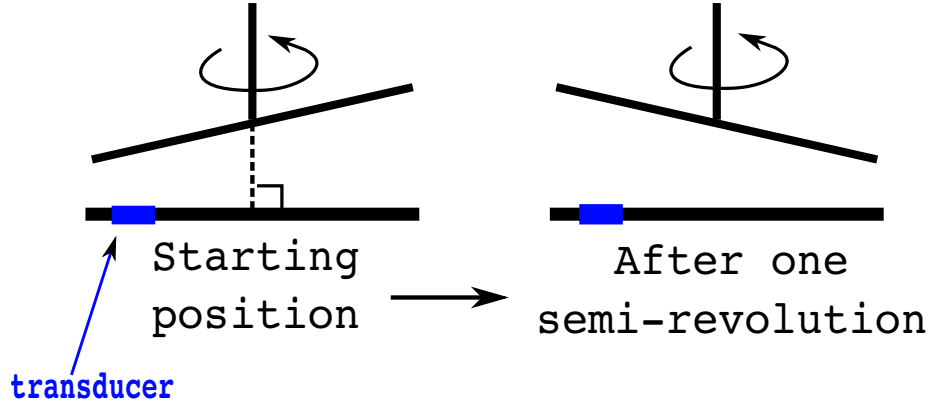


Figure 4.8: Rotating Disk parallelism default

2. The axis of rotation is perpendicular to the rotating disk but not to the stationary one as you can see in Figure (4.9). This problem is avoided too by taking an average on changing the direction of rotation.

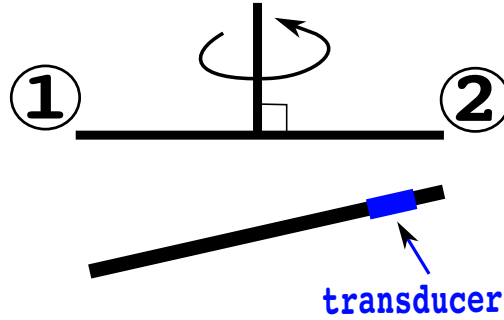


Figure 4.9: Stationary Disk parallelism default

Indeed, if the rotor turns in an anti-clockwise direction from point 1 to point 2 the flow is contractional, while in the clockwise direction (from 2 to 1) the flow is elongational. Thus, averaging the clockwise and anti-clockwise rotations cancel the pressure induced by this kind of parallelism default. These effects if not taken into account can be important and of the same order of magnitude as the signals that are going to be measured.

In lubrication approximation for a stationary viscous flow between two planes forming a small angle θ , [Guyon et al. 2001] give the difference in the pressure δp in their equation (4.159) of page (230) such that:

4.4. EXPERIMENTS

$$\delta p = \frac{6\eta V}{\theta} \cdot \frac{(e_2 - e_x)(e_x - e_1)}{e_x^2(e_1 + e_2)}. \quad (4.8)$$

In Figure (4.10) we represent our two parallel disks configuration with an error δh in parallelism, where it is clear that $e_1 = h - \delta h$, $e_2 = h + \delta h$, $e_x = h$, $V = \Omega R$, and for small angles $\theta \approx \frac{\delta h}{R}$. Upon substituting all these parameters in equation (4.8), one gets the difference in pressure as:

$$\delta p = 2\eta\Omega R^2 \frac{\delta h}{h^3} = 2\Sigma_{12} \frac{\delta h \cdot R}{h^2} \quad (4.9)$$

where

$$\Sigma_{12} \equiv \tau = \eta\dot{\gamma}_R \quad (4.10)$$

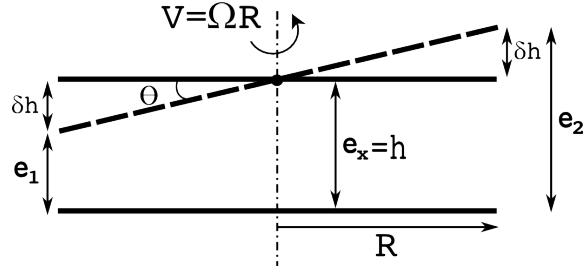


Figure 4.10: Two parallel disks geometry of an error δh

In our experiments, $R = 5.5 \text{ cm}$, and $h = 2.5 \text{ mm}$, and we have measured $\delta h \lesssim 50 \text{ } \mu\text{m}$ that implies a $\delta p \lesssim \frac{\Sigma_{12}}{2}$. Consequently, in order to eliminate this default in pressure δp , we measure Σ_{22} by rotating the upper disk in both clockwise and anti-clockwise directions, and then we average all the registered data from both.

4.4.5 Pressure Membranes (size and position)

Because of the large membrane surface of the pressure sensors we used (membrane radius = 10 mm), the imposed pressure by the flow of the suspension is not the same on all positions of the surface of the membrane. To take that into account, it required us to do a certain correction in the sensor positions so

4.4. EXPERIMENTS

that to be more accurate in our measurements. So, we started by determining a response function $f(\xi)$ of the sensor by applying a punctual force on different radial positions r of the sensor membrane. Experimentally, that punctual force was applied via placing a steel sphere of $2mm$ in diameter on different radii of the sensor, where its responses were registered. The response function is well represented in Figure (4.11). Then, the variation of the pressure on the sensor surface during the flow was approximated by a linear variation: $p = p_0 + p_1 \cdot r$, where r is the distance taken from the center of the disk, as you can see in Figure (4.12).

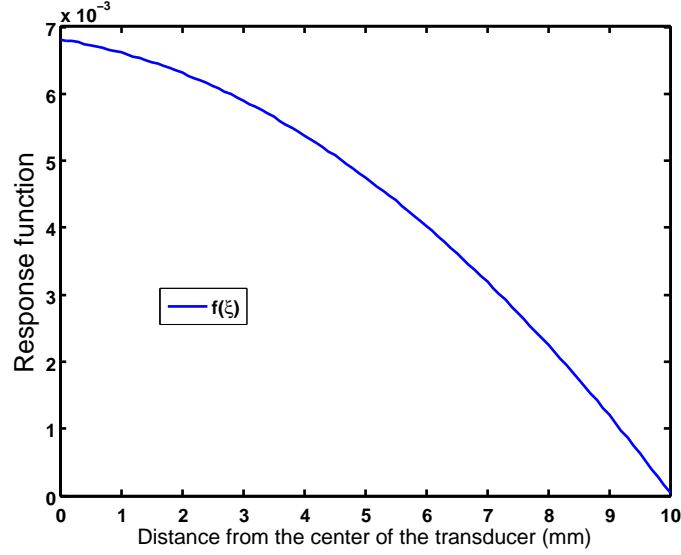


Figure 4.11: $f(\xi)$

Then, the effective radius R_{eff} where the sensor was virtually resituated at, was calculated as the following: $p_1 R_{eff} = \int_{S_{sensor}} (f(\xi) \cdot p_1 \cdot r) dS_{sensor}$, where S_{sensor} is the surface area of the sensor. The integral was calculated numerically, and Table (4.2) below gives the correspondance between the actual radii where the sensors were placed, and the effective corrected ones. We mention that only the smallest radius value was corrected.

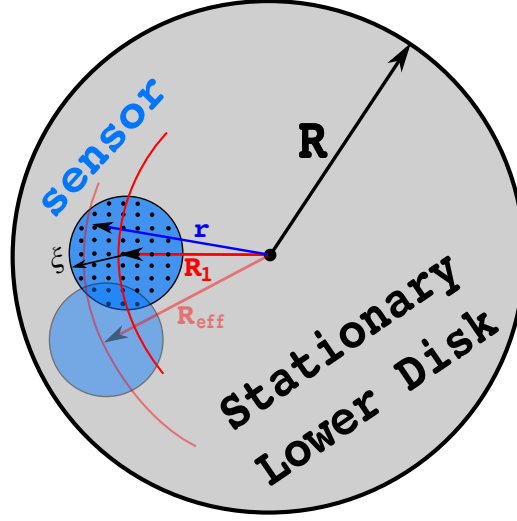


Figure 4.12: Correction of R_{real} to R_{eff}

R_{real} (cm)	1.1	3	3.3	3.9
$R_{effective}$ (cm)	1.1774	3.0276	3.3251	3.9212

Table 4.2: Correspondence between R_{real} & $R_{effective}$

4.4.6 Wall Slip Effects

Even if its origin is not absolutely clear, it is well known that wall slip is present when concentrated suspensions are sheared. [Jana et al. 1995] performed local measurements, using Laser Doppler Velocimetry, in narrow-gap Couette geometry to determine the slip length at the wall. They characterize the wall slip by an apparent slip velocity, i.e. the difference between the velocity of the walls and the velocity of the suspension at the same position. They showed that the slip velocity, u_s , was related to the local shear rate $\dot{\gamma}$ and the local volume fraction ϕ by:

$$u_s = \frac{\eta_s}{q} \cdot a \cdot \dot{\gamma} \quad (4.11)$$

where q is a constant that is determined experimentally ($q = 8$ in their study). Following [Jana et al. 1995], we introduce a slip velocity, both at the stationary

4.4. EXPERIMENTS

and rotating disks, that is proportional to the shear rate such that:

$$u_s(r) = \frac{\eta_s}{q} \cdot a \cdot \dot{\gamma}(r) . \quad (4.12)$$

Thus the apparent shear rate as shown in Figure (4.13) is given by:

$$\dot{\gamma}_{app}(r) = \frac{2u_s + \dot{\gamma}h}{h} = \frac{\Omega r}{h} \quad (4.13)$$

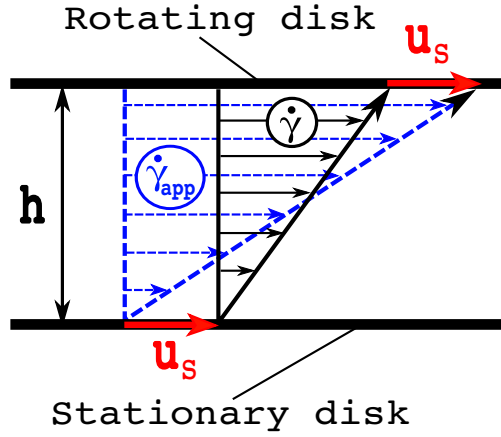


Figure 4.13: Apparent Shear rate

Since the stress τ is controlled such that:

$$\frac{\tau}{\eta_0} = \eta_s \cdot \dot{\gamma} = \eta_{app} \cdot \dot{\gamma}_{app} \quad (4.14)$$

We deduce that:

$$\eta_s = \frac{\eta_{app}}{1 - \frac{2a}{qh}\eta_{app}} \quad (4.15)$$

Moreover, since the normal stress differences N_1 and N_2 scale linearly with $\dot{\gamma}$ [$N_{1,2} = \alpha_{1,2} \cdot (\eta_0 \dot{\gamma})$], then the same previous correction applies for α_1 and α_2 such that:

$$(\alpha_{1,2}) = \frac{(\alpha_{1,2})_{app}}{1 - \frac{2a}{qh}\eta_{app}} \quad (4.16)$$

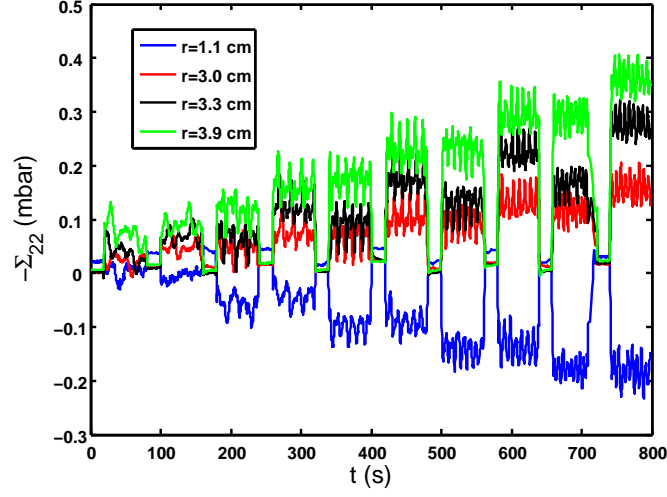
4.4. EXPERIMENTS

Orders of magnitude speaking, for a $\phi = 40\%$ monodispersed suspension of hard spheres of ($2a = 140 \mu m$) and at $h = 2.5 mm$, we have $\eta_s \sim 10$ which implies $\left[\left(\frac{\eta_s}{\eta_{app}}\right) = \left(1 + \frac{2a}{qh}\eta_s\right)\right] \sim [1 + (7 \cdot 10^{-03} \cdot 10)] \sim 1.07$. **Consequently, it means that the effect of wall slip in our experiments is not too important. Furthermore, in the following, we will speak about the ratios of α_1 and α_2 over η_s (or α_{1app} and α_{2app} over η_{app}), quantities that are not affected by the wall slip.**

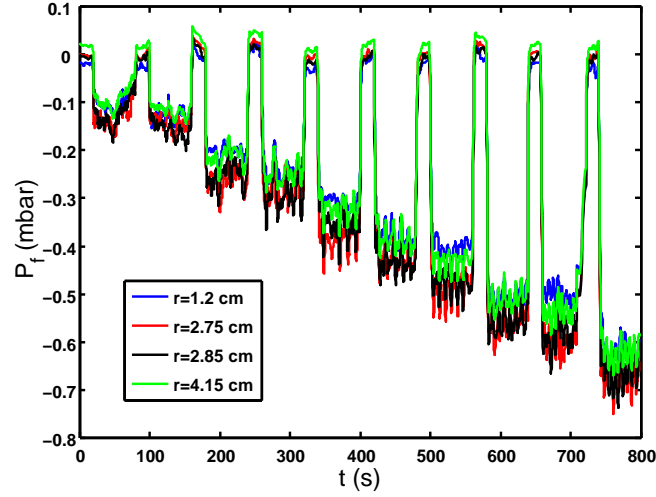
4.4.7 Setup Validation

Figure (4.14) provides an example of the registered signals by both, the direct sensors (Figure (4.14a)), and those attached to the grids (Figure (4.14b)) for a suspension of 46% of particles $140 \mu m$ in diameter.

4.4. EXPERIMENTS



(a) Registered Signals at the direct sensors



(b) Registered Signals at sensors at the grids

Figure 4.14: Registered Signals by the sensors

The curve in Figure (4.15) shows the variation of the shear stress as a function of the shear rate (shear rate at $r = R$), for a suspension of 46% of particles. As expected, the viscosity of the suspension is almost independent of the shear rate, despite of a weak shear-thinning that can be observed if one looks very carefully.

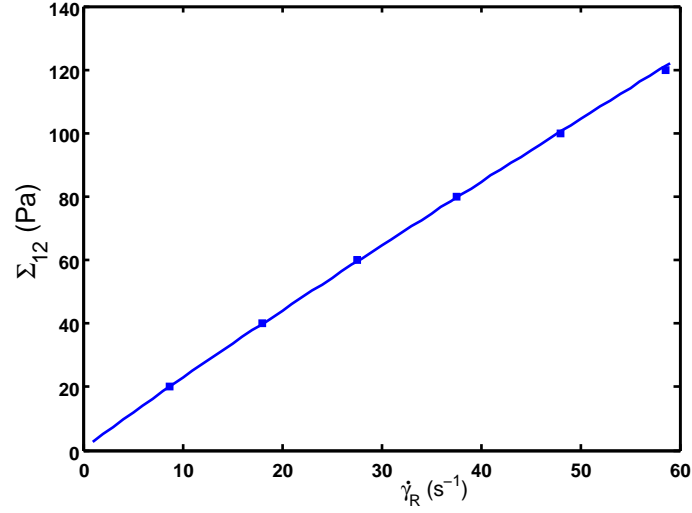
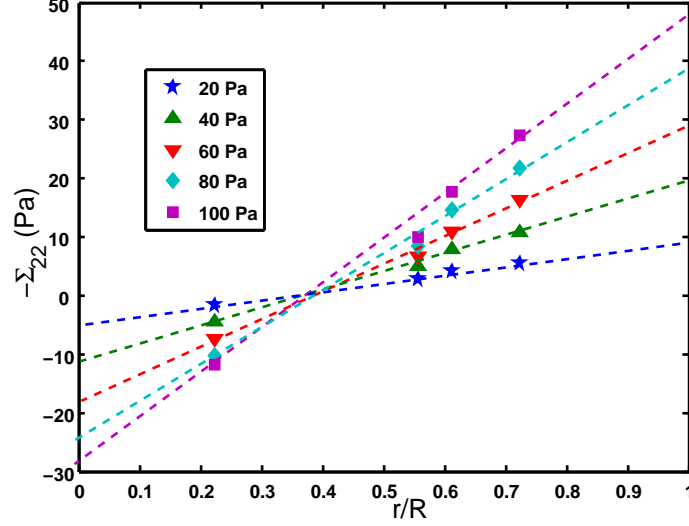


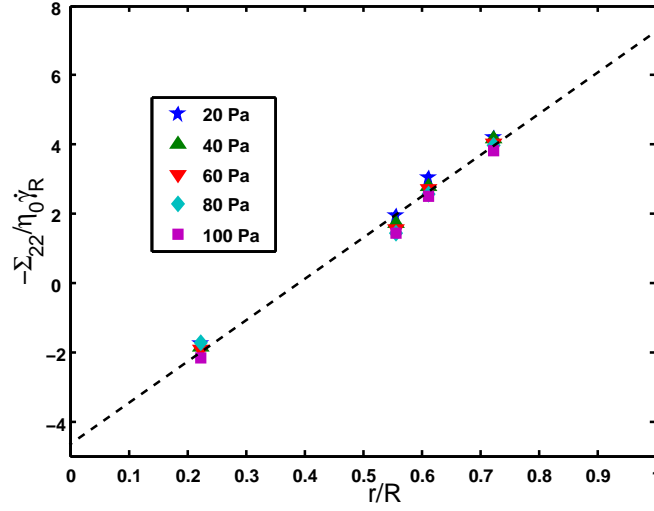
Figure 4.15: The Shear Stress $\tau \equiv \Sigma_{12}$ Versus the Shear Rate $\dot{\gamma}_R$

The rheological behavior of the suspension was well represented by a power law ($\tau = 2.62\dot{\gamma}^{0.942}$) but can also be represented by a linear one, as we did. Figure (4.16a) shows the mean radial variation of $(-\Sigma_{22})$, averaged over several revolutions in the two clockwise and anti-clockwise directions, obtained for different applied shear stresses to a suspension of 46% of particles ($2a = 140 \mu m$).

4.4. EXPERIMENTS



(a) The radial variation of $(-\Sigma_{22})$



(b) The radial variation of $(-\Sigma_{22}/\eta_0\dot{\gamma}_R)$

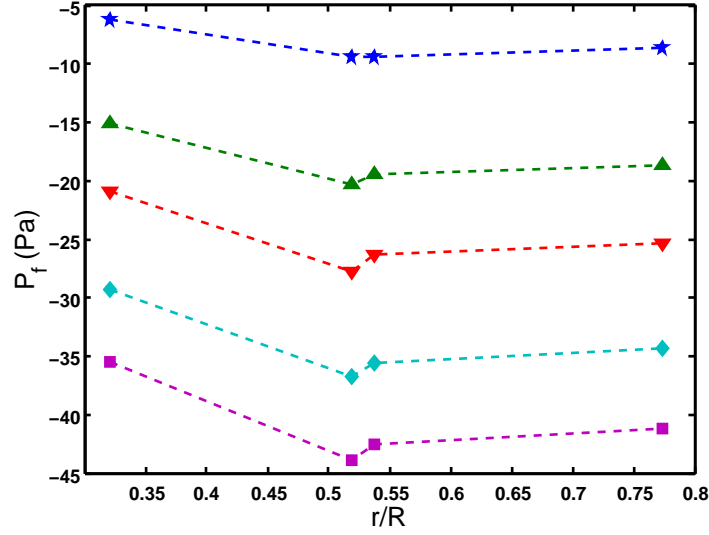
Figure 4.16: The radial variation of the second normal stress Σ_{22}

As it was predicted by equation (4.5), the suspension normal stress (Σ_{22}) varies linearly in $(\frac{r}{R})$, and Figure (4.16b) that represents the different points gathered at the same radial positions, reveals that the ratio $(\Sigma_{22}/\eta_0\dot{\gamma}_R)$ is well independent of $\dot{\gamma}_R$.

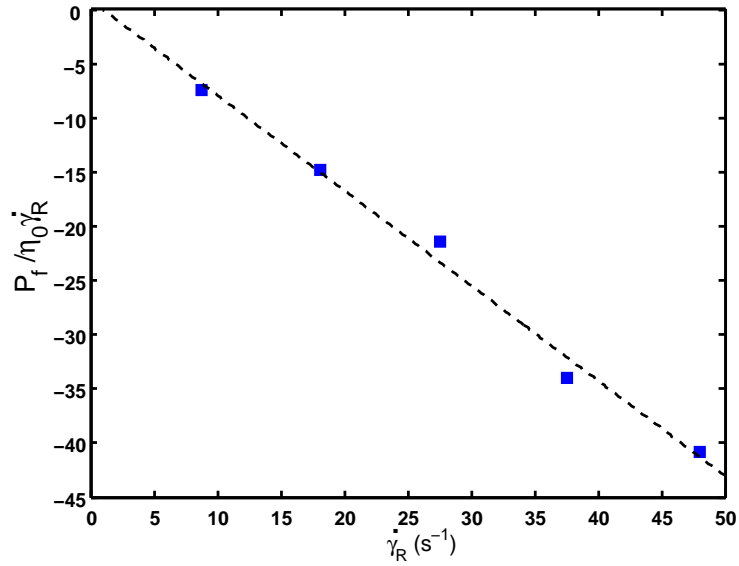
The Figure (4.17a) indicates that the pore pressure P_f is almost constant in

4.4. EXPERIMENTS

$(\frac{r}{R})$, which is consistent with the absence or weakness of the migration of particles in the torsional flow of a suspension between two parallel plates [Chapman 1990, Chow et al. 1994].



(a) The radial profile of the fluid pressure P_f



(b) The fluid pressure P_f versus the Shear Rate

Figure 4.17: The fluid pressure P_f

Hereafter, P_f will be representing the mean fluid pressure on the four sensors

4.5. MATERIAL FUNCTIONS IN SUSPENSIONS, DETERMINATION OF η_S , α_1 , AND α_2

at the grids, where we verified as you can see in Figure (4.17b) that this pressure P_f varies almost linearly with $\dot{\gamma}_R$.

4.5 MATERIAL FUNCTIONS IN SUSPENSIONS, DETERMINATION OF η_S , α_1 , AND α_2

4.5.1 Suspension Viscosity

4.5.1.1 Shear-thinning

The viscosity of a suspension is almost independent of $\dot{\gamma}$ but a slight shear-thinning is often observed [Zarraga et al. 2000, Stickel and Powell 2005]. There is no clear explanation for this behavior. The only interpretation available in the literature has been given by [Acrivos et al. 1994] who measured the shear-thinning of a suspension sheared in a cylindrical Couette cell. He shows that the shear-thinning behavior, he observed, can be explained by the resuspension of the particles that have not exactly the same density as that of the fluid. The particles are supposed to settle in the gap between the two cylinders. When the shear flow is applied they are resuspended over a height that increases with an increasing shear rate. The particle volume fraction in the settled layer decreases and thus, the torque on the rotating cylinder decreases too (see Figure (4.18)).

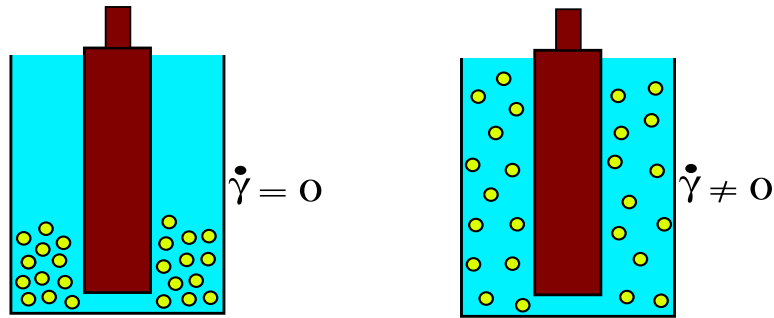


Figure 4.18: Resuspension in a Couette cell

We think that the resuspension can not explain the shear-thinning behavior we observed in the parallel-plates geometry since in such a configuration, the

4.5. MATERIAL FUNCTIONS IN SUSPENSIONS, DETERMINATION OF η_S , α_1 , AND α_2

particles sedimentation would lead to a decrease of the torque on the upper rotating plate and their resuspension should be responsible for an increase of the torque (i.e shear-thickening behavior) (see Figure (4.19)).

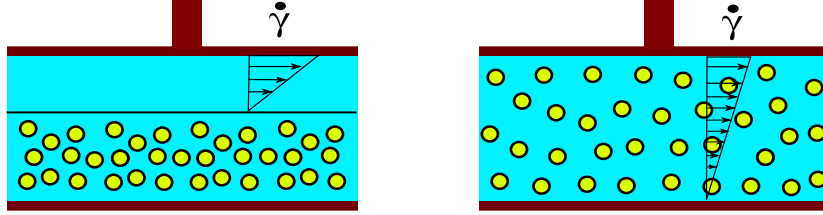


Figure 4.19: Resuspension in a parallel plate geometry

Nevertheless, our measurements show that the shear thinning behavior is weak but increases as the particle volume fraction increases. The Table (4.3) gives the constitutive laws that we have measured for different particle volume fractions ranging from 0.2 to 0.49.

ϕ	$\frac{\tau}{\eta_0}$
0.2	$1.95 \dot{\gamma}^1$
0.24	$2.48 \dot{\gamma}^1$
0.3	$4.6 \dot{\gamma}^{0.996}$
0.34	$5.68 \dot{\gamma}^{0.996}$
0.36	$7.25 \dot{\gamma}^{0.992}$
0.38	$8.33 \dot{\gamma}^{0.989}$
0.42	$14.3 \dot{\gamma}^{0.968}$
0.44	$18.7 \dot{\gamma}^{0.941}$
0.45	$25.2 \dot{\gamma}^{0.946}$
0.48	$37.4 \dot{\gamma}^{0.933}$
0.49	$50.6 \dot{\gamma}^{0.925}$

Table 4.3: Constitutive Laws of a ($2a = 140 \mu m$) suspension

It's worth listing that these measurements have been carried out over a limited range of shear rates that typically varies from 10 to $50 s^{-1}$. So it is no use attaching too much importance to these results, and in the following the suspensions will be considered viscous (i.e. with a viscosity independent of the shear rate). Moreover, the values of the viscosity that will be given, will be the averaged values of the viscosity measured for different shear rates in the range

$10 \rightarrow 50 \text{ s}^{-1}$.

4.5.1.2 Variation with ϕ

The variation of the reduced viscosity with the particle volume fraction is represented in Figure (4.20) for two different monodispersed particle-size suspensions.

The experimental data fit well the Krieger-Dougherty Law of the form:

$$\eta_s = \frac{1}{\left(1 - \frac{\phi}{\phi_m}\right)^2}, \text{ with } \phi_m = 0.58. \quad (4.17)$$

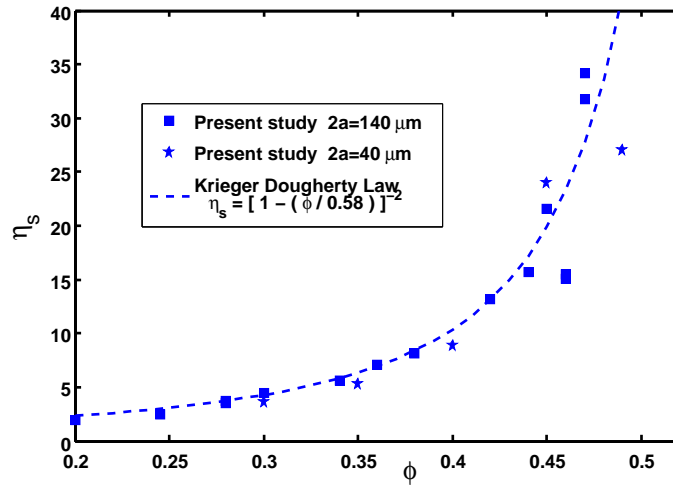


Figure 4.20: The normalized suspension viscosity

However, one can clearly observe some dispersion in the results, that's probably due to variations in temperature, since the only controlled one was that of the room with a variation of $\pm 1^\circ\text{C}$. We measured that a 2°C variation, modifies the suspending fluid viscosity about 8%. One must also keep in mind that the suspending fluid is a mixture of water & Ucon Oil 75H90000, where the viscosity is very sensitive to the mixture composition. Thus, a possible evaporation of water in the mixture during the suspension placement process between the

4.5. MATERIAL FUNCTIONS IN SUSPENSIONS, DETERMINATION OF η_S , α_1 , AND α_2

two disks inside the rheometer and even during the experiment, may change the suspending fluid viscosity.

4.5.1.3 Transient Response after shear reversal

Following [Gadala-Maria and Acrivos 1980], we have measured the shear viscosity response of a suspension placed in a cylindrical Couette cell when the flow direction is inverted. The experiments are carried out with a controlled-stress rheometer “CARRI MED CSL 100”. The Couette cell consists of two cylinders whose radii are 13.5 and 15 mm and length 40 mm. The inner cylinder rotates in a direction till a deformation of about 5 is attained. Then, the torque direction is reversed and the viscosity response is recorded. A typical signal obtained with a $\phi = 0.44$ suspension is presented on Figure (4.21).

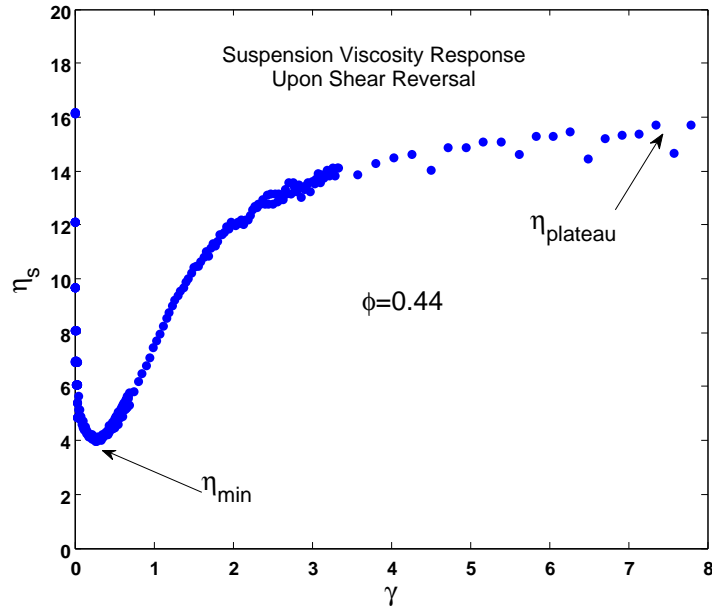


Figure 4.21: Suspension Viscosity Response upon shear reversal

This kind of transient behavior has been explained by both the destruction and the reformation of shear induced structure in the suspension [Gadala-Maria and Acrivos 1980], and by the relaxation of the contact forces between particles when the shear is reversed [Narumi et al. 2002, Kolli et al. 2002]. Thus,

4.5. MATERIAL FUNCTIONS IN SUSPENSIONS, DETERMINATION OF η_S , α_1 , AND α_2

the minimum of the viscosity (η_{min}) corresponds to a suspension where the particles are distributed almost isotropically. If indeed η_{min} is reached when the suspension structure is almost isotropic, then η_{min} can be compared to the so called “high frequency dynamic viscosity” that according to [Sierou and Brady 2002] is obtained when the system microstructure has not been affected by the flow and is purely hydrodynamic in origin.

Then, subtracting η_{min} from $\eta_{plateau}$, we will be able to obtain the excess viscosity η_{ex} that arises from particle interactions in the structure induced by the flow [Sierou and Brady 2002]. Before doing that, we have to make some remarks:

- It is necessary to use a Couette cell rather than a parallel plate geometry, because the key parameter of the response is the deformation γ (and not the time) and in a parallel plate geometry the deformation is not constant spatially (i.e. zero at $r = 0$, and maximum at $r = R$).
- The measurements are very rough due to different facts such as:
 - Slipping.
 - Migration that can be very quick when ϕ is high [Ovarlez et al. 2006].
 - The gap between the cylinders is a little bit small $h = 1.5 \text{ mm}$ (i.e. $\frac{h}{2a} = 11$), while a gap equal to 15 particle diameters is usually considered necessary for measuring the bulk viscosity [Zarraga et al. 2000].
 - The rheometer inertia is not corrected.
 - The temperature is not well controlled.

Nevertheless, and having in mind these limitations, we can perform the measurements for different particle volume fractions. The variation of η_{min} and $\eta_{plateau}$ with ϕ are represented in Figure (4.22).

4.5. MATERIAL FUNCTIONS IN SUSPENSIONS, DETERMINATION OF η_S , α_1 , AND α_2

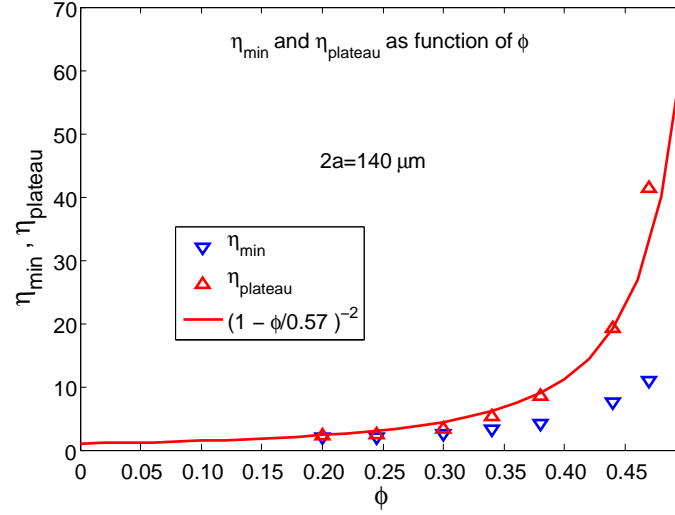


Figure 4.22: η_{\min} and η_{plateau} as function of ϕ

As expected from the poor accuracy of the measurements, there is a noticeable dispersion in the reported values. The normalized excess viscosity η_{ex} is reported in Figure (4.23).

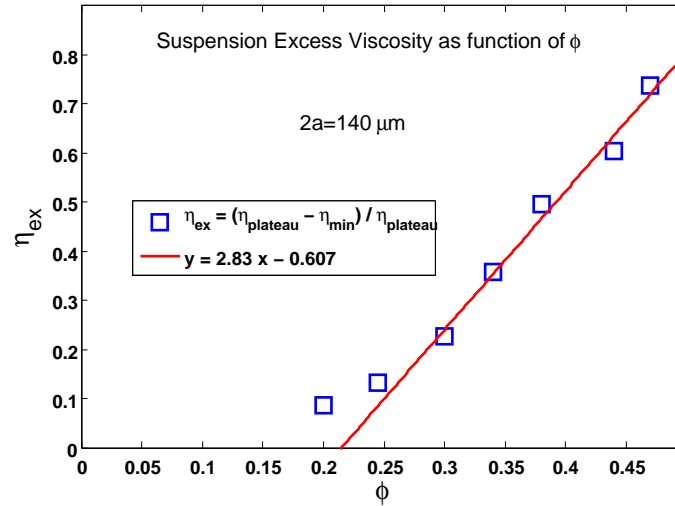


Figure 4.23: η_{ex} as function of ϕ

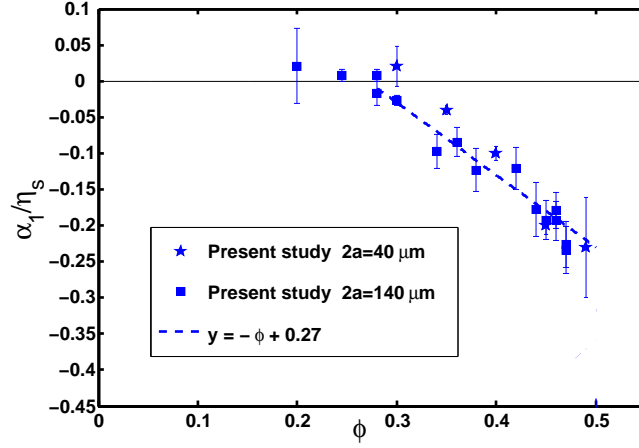
We note that above a threshold-like value of the particle volume fraction, the excess viscosity increases almost linearly with ϕ . In the following we will show that this behavior is to be related to the behavior of the normal stresses.

4.5.2 Suspension Normal Stress Coefficients α_1 and α_2

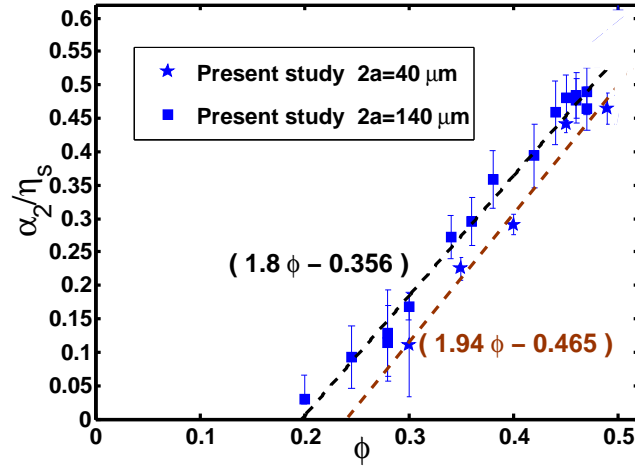
As mentioned in (4.3.1), the slope and the origin at ordinate of the second normal stress are measured for different values of particle volume fractions from where the values of α_1 and α_2 are deduced. As explained in (4.4.6), a wall slip is probably present. Rather than to correct it, we chose to present in the following the ratios of the normal stress coefficients to the suspension viscosity rather than the normal stress coefficients. Indeed, these ratios are supposed not to depend on the wall slip since, according to (4.4.6), the correction is the same for the viscosity as for the normal stress coefficients (see equation (4.16))

α_1 and α_2 are presented in Figures (4.24a) and (4.24b), respectively. It is observed that above a threshold value α_1 and α_2 vary linearly with the particle volume fraction. α_1 and α_2 are measured to be of opposite signs. This last significant point of observation (sign opposition) is in contrast with all the previous measurements presented in the literature, and thus it will be well discussed in the next section.

4.5. MATERIAL FUNCTIONS IN SUSPENSIONS, DETERMINATION OF η_s , α_1 , AND α_2



(a) The ratios $\frac{\alpha_1}{\eta_s}$ as function of ϕ



(b) The ratios $\frac{\alpha_2}{\eta_s}$ as function of ϕ

Figure 4.24: The ratios $\frac{\alpha_1}{\eta_s}$ and $\frac{\alpha_2}{\eta_s}$ as function of ϕ . $(1.8\phi - 0.356)$ is the fit for $2a = 140 \mu\text{m}$ & $(1.94\phi - 0.465)$ is the fit for $2a = 40 \mu\text{m}$.

4.5.3 Validity of α_1 and α_2 measurements

Both, the negative sign of α_1 and the elevated values it has at increasing volume fraction of particles ($|\alpha_1| \approx \frac{\alpha_2}{2}$ for $\phi \approx 0.45$), are surprising, because they are in contrast with many previous results in the literature [Zarraga et al. 2000, Singh

4.5. MATERIAL FUNCTIONS IN SUSPENSIONS, DETERMINATION OF η_s , α_1 , AND α_2

and Nott 2003, Couturier et al. 2011]. So, when we obtained these novel results, we attempted to seek experimental artifacts which may led to those strange values of α_1 . Our different proceeded tests are coming soon in the section, where we will visit also the results of [Singh and Nott 2003] to show that an adequate treatment for their measurements leads to α_1 and α_2 values that are close to our measured ones. At the end of this section, we will compare our obtained experimental data to other results in the literature, where we will try to review the similarities and disagreements between them.

4.5.3.1 Influence of the suspended fluid viscosity

All previous studies used suspending fluids which are more viscous than the ones we used. $1 \text{ Pa} \cdot \text{s} \lesssim \eta_0 \lesssim 5 \text{ Pa} \cdot \text{s}$ for [Zarraga et al. 2000], $\eta_0 = 2.15 \text{ Pa} \cdot \text{s}$ for [Couturier et al. 2011], and $\eta_0 = 2.19 \text{ Pa} \cdot \text{s}$ for [Singh and Nott 2003], but in the present study, we have $0.05 \text{ Pa} \cdot \text{s} \lesssim \eta_0 \lesssim 0.5 \text{ Pa} \cdot \text{s}$. So, we wanted to know if the suspending fluid viscosity η_0 has an influence on the values of the coefficients α_1 and α_2 . For that reason, we measured the radial profile of Σ_{22} in a suspension of 45% of PMMA particles ($2a = 140 \mu\text{m}$) in suspending fluids of different viscosities. Table (4.4) shows the measured values of α_1 and α_2 in suspensions of 45% of particles dispersed in fluids of different η_0 viscosities.

Fluid viscosity $\eta_0 \text{ (Pa} \cdot \text{s)}$	Slope $\frac{k_p}{\eta_s} = \frac{\alpha_1 + 2\alpha_2}{\eta_s}$	Ordinate at origin $\frac{k_{00}}{\eta_s} = -\frac{\alpha_1 + \alpha_2}{\eta_s}$	α_1/η_s	α_2/η_s
0.09	0.74	-0.28	-0.18	0.46
0.15	0.77	-0.26	-0.25	0.51
0.185	0.70	-0.22	-0.18	0.48
0.36	0.71	-0.25	-0.21	0.46
0.72	0.72	-0.23	-0.26	0.49

Table 4.4: α_1/η_s and α_2/η_s at different η_0 vlaues for $\phi = 45\%$

Despite a dispersion among the numbers, we observe no significant influence of the suspending fluid viscosity on the values of α_1 and α_2 .

4.5.3.2 Influence of the capillary pressure

Here we stopped and asked ourselves the question: Is it OK to use the boundary condition $\Sigma_{33}(r=R) = -P_a$. Practically, during the flow, the air/suspension interface may deform and the change in its curvature may induce a capillary pressure. Indeed, the order of magnitude of the capillary pressure is the same as the normal stresses that are expected to arise in the sheared suspension: $P_c = \frac{\Upsilon_t}{r_c} \sim 50 \text{ Pa}$, where $\Upsilon_t \sim 50 \mu\text{N} \cdot \text{m}$ is the order of magnitude of the suspension surface tension, and $\frac{1}{r_c} \sim \frac{2}{h} = 10^3 \text{ m}^{-1}$ is the interface curvature. This order of magnitude of the capillary pressure is well comparable to the values of Σ_{22} we measure. So, if the capillary pressure really plays a role during the measurements of Σ_{22} profile, we should measure different profiles upon changing the value of the gap h . It is not the case, as it is well shown in Figure (4.25), the values of α_1 and α_2 are independent of h .

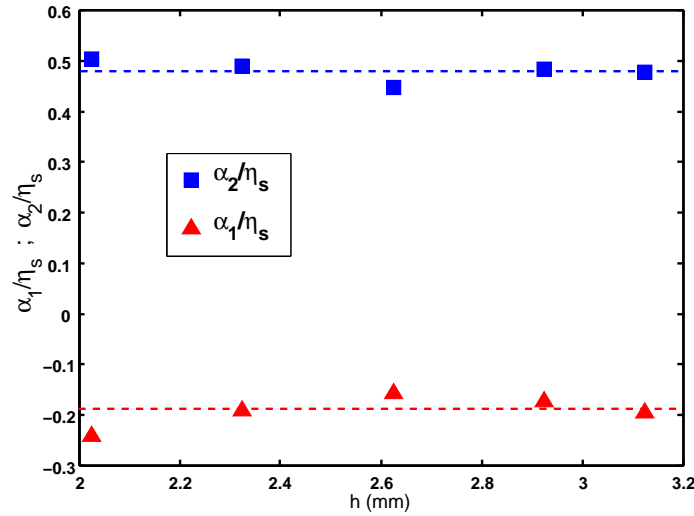


Figure 4.25: α_1/η_s (triangles) and α_2/η_s (squares) as function of h

One must note that it was not possible to vary the gap (h) in an important manner. Indeed, the liquid must be held between the two parallel disks by capillarity. That's what prevented us from separating more the two disks. On the other hand, narrowing the gap too much will increase the error in parallelism.

Moreover, the capillary pressure with respect to the inter-particle distance

4.5. MATERIAL FUNCTIONS IN SUSPENSIONS, DETERMINATION OF η_S , α_1 , AND α_2

$P_{cp} = \frac{\tau_t}{a}$ did not have any influence on the measurements of α_1 and α_2 , as it is indicated in the Figures (4.24a) & (4.24b), where we find almost identical results for suspensions of different particle sizes ($2a = 40$ & $140 \mu m$).

Thus, the capillary effects both at macroscopic and at the particle scales seem not to play any role.

4.5.3.3 Comparison with the results of Singh and Nott 2003

[Singh and Nott 2003] proposed to determine α_1 and α_2 by measuring the radial normal stress, Σ_{rr} , in a cylindrical Couette geometry and the axial stress profile, $\Sigma_{zz}(r)$, in a parallel plate geometry. The former, is related to $\frac{\alpha_1}{\eta_s}$ and $\frac{\alpha_2}{\eta_s}$ by

$$\frac{\Sigma_{rr}(R_0)}{\eta_0|\dot{\gamma}_0|} = -(1 + \beta)\alpha_2 - \frac{\beta}{2}\alpha_1, \quad (4.18)$$

where $\dot{\gamma}_0$ is the shear rate at the outer cylinder, where Σ_{rr} is measured, and $\beta = 0.214$ is a geometrical coefficient that depends only on the cylinders radii ratio. They obtain a second equation for the determination of α_1 and α_2 from the measurement of the axial stress at the rotation axis, $\Sigma_{zz}(0)$ in parallel plate torsional flow. Actually, the value of $\Sigma_{zz}(0)$ is extrapolated from the measurement of $\Sigma_{zz}(r)$ at three radial positions (Figure10 in [Singh and Nott 2003]). The relation they use is (eq.5.6 in their paper):

$$\frac{d}{d\dot{\gamma}_R} [\Sigma_{zz}(r=0)] = \eta_0(\alpha_1 + \alpha_2). \quad (4.19)$$

This relation is equivalent to the equation (4.5) at $r = 0$ and is valid only if the condition $\Sigma_{33}(r = R) = -P_a$ is applicable whereas it is not the case in the Singh and Nott's experiment, since they used a rotating top plate over a pool of suspension (Figure 3b, in their paper). In such a geometrical configuration, the boundary condition $\Sigma_{33}(r = R) = -P_a$ is no more satisfied and equations (4.5) or (4.19) cannot be used. On the other hand, the slopes of $\Sigma_{zz}(r)$ can be used, independently of the boundary conditions, to determine $(\alpha_1 + 2\alpha_2)$. [Singh and Nott 2003] show in their paper the variation of $\Sigma_{zz}(r)$ in the parallel plate

4.5. MATERIAL FUNCTIONS IN SUSPENSIONS, DETERMINATION OF η_S , α_1 , AND α_2

geometry as you can see from the following Figure (4.26).

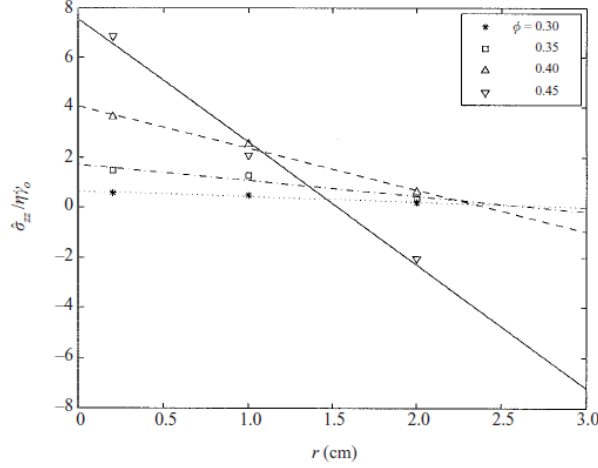


FIGURE 10. The axial normal stress $\hat{\sigma}_{zz}$ at different radial positions in the parallel-plate device. Here $\dot{\gamma}_o$ is the shear rate at the rim.

Figure 4.26: $\Sigma_{zz}(r)/\eta\dot{\gamma}$ taken from Figure10 of [Singh and Nott 2003]

From the values of α_1 and α_2 that they give, we recalculate $\Sigma_{rr}(r = R_0)$ they should have obtained in the Couette cell and consequently using equation (4.18) the combination $\left[(1 + \beta)\alpha_2 + \frac{\beta}{2}\alpha_1\right]$. Then, from the slope of $\Sigma_{zz}(r)$ determined with Figure (4.26), we deduce $(\alpha_1 + 2\alpha_2)$. And, at last, from these two combinations of α_1 and α_2 , we calculate α_1 and α_2 as it is illustrated in Table (4.5).

Singh & Nott results						Modified values	
ϕ	α_1	α_2	\Rightarrow	$\left[\frac{\Sigma_{rr}(R_0)}{\eta_0 \dot{\gamma}_0 }\right] =$ $-(1+\beta)\alpha_2 - \frac{\beta}{2}\alpha_1$	$\frac{\partial\left(\frac{\Sigma_{rr}(R_0)}{\eta_0 \dot{\gamma}_0 }\right)}{\partial\frac{r}{R}} =$ $-(\alpha_1+2\alpha_2)$	deduced from columns 4 & 5	
0.30	0.314	0.314		-0.415	-0.56	-0.15	0.36
0.35	0.475	1.23		-1.54	-2	-0.65	1.33
0.40	0.9	3.14		-3.91	-5	-1.75	3.38
0.45	1.54	5.98		-7.42	-14.6	2.88	5.86

Table 4.5: From the values of α_1 and α_2 given in the paper of Singh & Nott (2003), the radial normal stress in the cylindrical Couette geometry is recalculated (4th column). The slopes of $[\Sigma_{zz}(\frac{r}{R})/\eta_0\dot{\gamma}_R]$ for the different volume fractions of particles are deduced from the Figure10 of the Singh and Nott paper (5th column). At last, the corrected values of α_1 and α_2 are deduced from their previous equations.

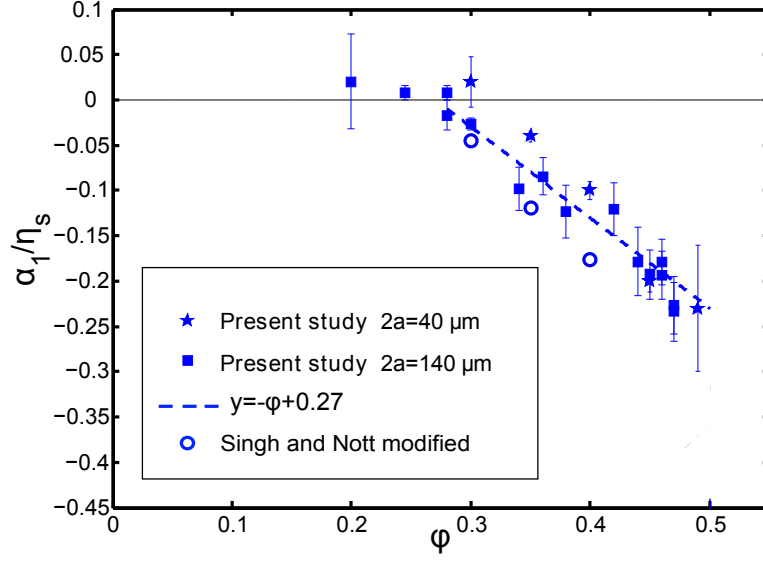
4.5. MATERIAL FUNCTIONS IN SUSPENSIONS, DETERMINATION OF η_S , α_1 , AND α_2

ϕ	Singh & Nott Modified		Present Measurement	
	α_1/η_s	α_2/η_s	α_1/η_s	α_2/η_s
0.30	-0.0350	0.110	-0.0290	0.1689
0.35	-0.119	0.244	-0.080	0.2839
0.40	-0.176	0.340	-0.130	0.37595
0.45	0.1447	0.325	-0.1925	0.4806

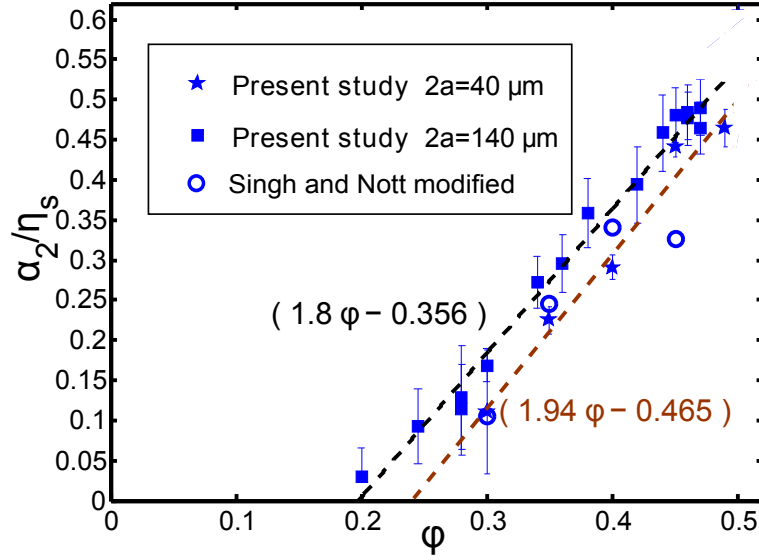
Table 4.6: Values of α_1/η_s and α_2/η_s at present measurements compared to the corrected ones obtained by [Singh and Nott 2003].

We note that, for the 3 lowest particles volume fractions, α_1 is negative. These values, divided by the suspension viscosity given by [Singh and Nott 2003] and referred as "Singh & Nott modified" are plotted together with our results on Figures (4.27a) and (4.27b) (open circles). The agreement is very good for the different values of α_1 and α_2 for $\phi = 0.3, 0.35$ and 0.4 . For $\phi = 0.45$, the [Singh and Nott 2003] modified value of α_1 is positive and we have no explanation for that. But, one can note that the $\Sigma_{zz}(r)$ profile registered in the parallel plate geometry for this particle volume fraction ($\phi = 0.45$) looks strange when compared with the profiles obtained for the other values of ϕ (i.e. see Figure 4.26). The line at ($\phi = 0.45$) does not intersect with the other lines at the same point, as these other lines do intersect each other.

4.5. MATERIAL FUNCTIONS IN SUSPENSIONS, DETERMINATION OF η_s , α_1 , AND α_2



(a) The ratios $\frac{\alpha_1}{\eta_s}$ as function of ϕ



(b) The ratios $\frac{\alpha_2}{\eta_s}$ as function of ϕ

Figure 4.27: The ratios $\frac{\alpha_1}{\eta_s}$ and $\frac{\alpha_2}{\eta_s}$ as function of ϕ

4.5.3.4 Comparison with other results

Following [Zarraga et al. 2000], [Boyer et al. 2011 a] have used a rotating rod geometry to measure the combination of normal stress coefficients $(\alpha_2 + \frac{\alpha_1}{2})$, which is half the slope k_p (equation (4.5)) that we measure in our two parallel disk geometry. They show that $(\alpha_2 + \frac{\alpha_1}{2})$ remains as small as immeasurable for $\phi < 0.2$. However, above $\phi \approx 0.22$, it increases linearly with increasing the concentration. Their results together with ours are plotted in Figure (4.28), and are in good agreement.

Moreover, we have also to compare our results with those of [Zarraga et al. 2000]. The first experiment reported by [Zarraga et al. 2000] consists of measuring the net thrust force F on one of the two disks in a torsional flow. This Force is directly proportional to the difference $(N_1 - N_2)$ given by:

$$(N_1 - N_2) = \frac{2F}{\pi R^2} \left(1 + \frac{1}{2} \frac{d \ln F}{d \ln \dot{\gamma}_R} \right). \quad (4.20)$$

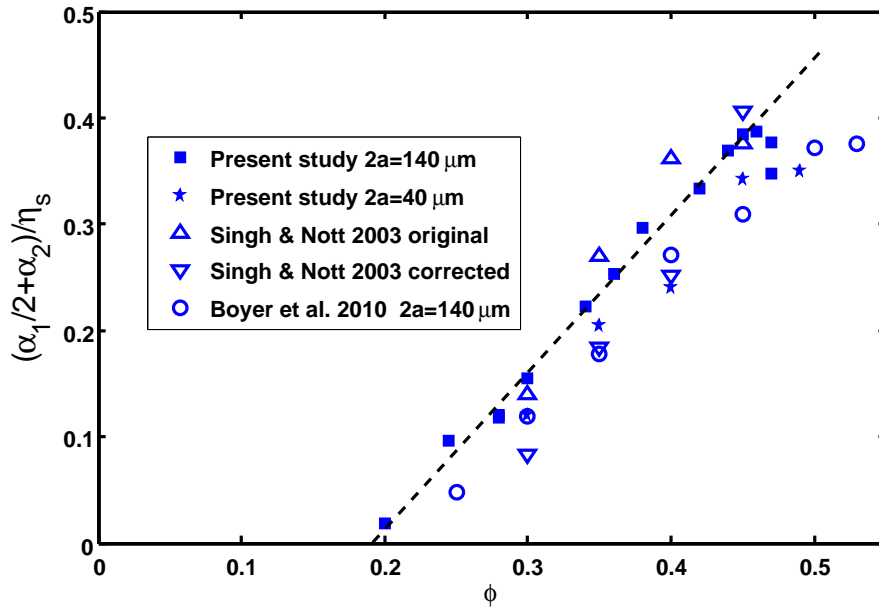


Figure 4.28: $(\frac{\alpha_1}{2} + \alpha_2)$ as function of ϕ

First we have measured directly the force exerted on the upper plate when

4.5. MATERIAL FUNCTIONS IN SUSPENSIONS, DETERMINATION OF η_S , α_1 , AND α_2

the suspension is sheared, in order to verify that the integral of the measured $\Sigma_{22}(r)$ over the disk surface give the same value as the thrust force measured by the rheometer. An example of result, obtained at a $\phi = 0.42$ suspension is presented in Figure (4.29), where one can clearly observe that the direct measurement of the Force (stars) and its calculation from the Σ_{22} profile (squares) give almost the same result.

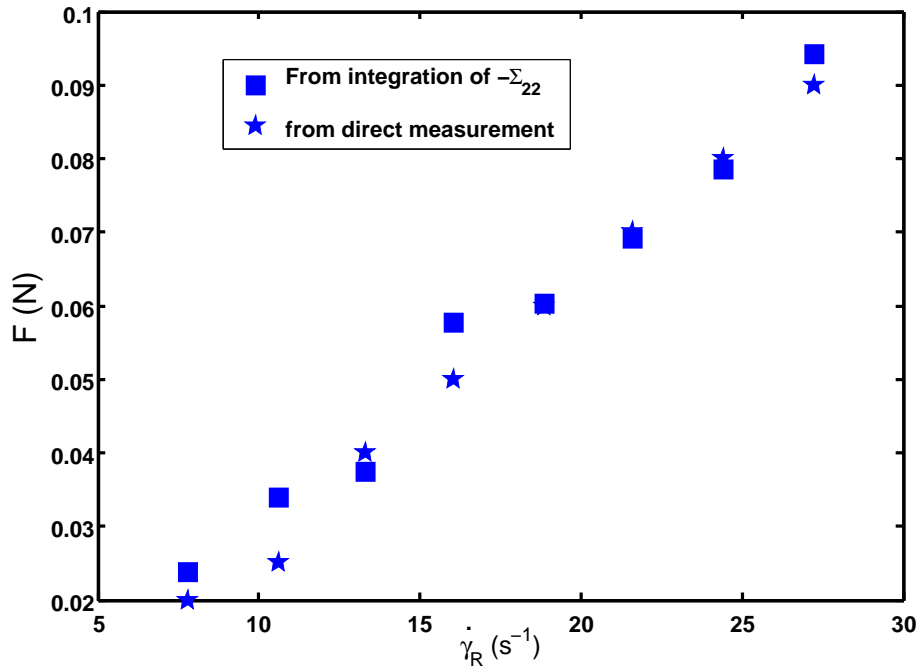


Figure 4.29: Measured thrust force F as function of shear rate $\dot{\gamma}_R$

Figure (4.30) shows the difference $(\alpha_2 - \alpha_1)$ together with the correlation proposed by [Zarraga et al. 2000] to fit their data in the range $\phi = 0.35 \leftrightarrow 0.5$. The normal Force we measured is approximately two times larger than that reported by [Zarraga et al. 2000]. This difference is not so surprising because, the shear stress behavior already reported by [Zarraga et al. 2000] is quite different from that we observed. Indeed, they measure a significant shear-thinning behavior that is not observable in the present study.

Otherwise, the magnitude of α_1 that we measured is inconsistent with the results obtained by [Couturier et al. 2011], who show that α_2 which has been

4.5. MATERIAL FUNCTIONS IN SUSPENSIONS, DETERMINATION OF η_s , α_1 , AND α_2

measured upon observing the shape of the suspension free-surface in a tilted trough flow, is equal to the combination $(\alpha_2 + \frac{\alpha_1}{2})$, measured previously by [Boyer et al. 2011 a] with the same suspensions. In this way, [Couturier et al. 2011] estimate that $\frac{|\alpha_1|}{\eta_s}$ is less than 0.06.

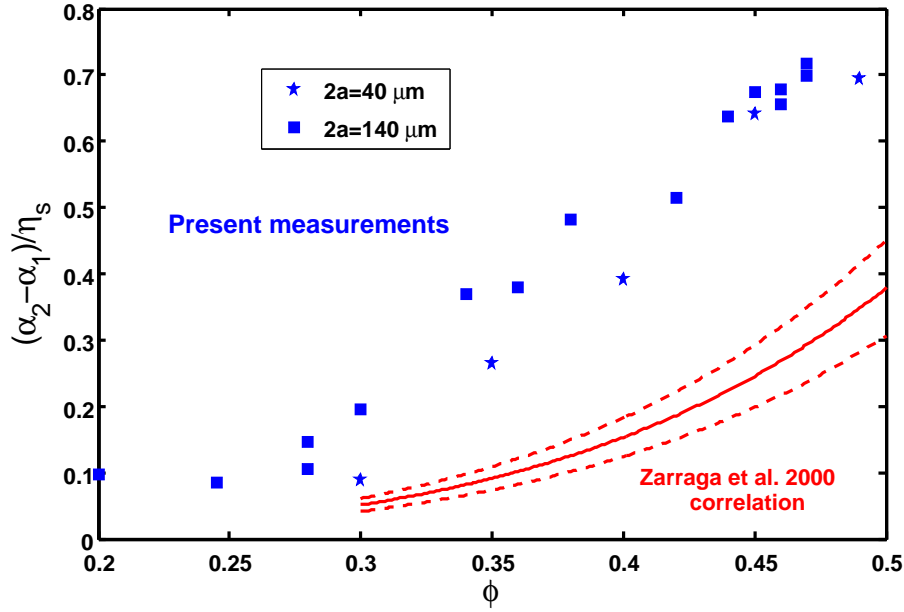


Figure 4.30: $(\alpha_2 - \alpha_1)$ as function of ϕ

At last, we have to mention that the numerical simulations using either Force Coupling Method (**FCM**) [Yeo and Maxey 2010a] or Stokesian Dynamics (**SD**) [Sierou and Brady 2002] show that both N_1 and N_2 are negative, and $N_1 \approx N_2$ in **SD** simulation, and $N_1 < N_2$ in **FCM** calculations. However, [Sierou and Brady 2002] investigated the effect of sliding friction on the rheological behavior of a suspension and showed that an increase in the friction coefficient gave rise to an increase of the viscosity, to an increase of the second normal stress difference, but to a decrease of the first normal stress difference (in magnitude). They explain this result by the change in the suspension microstructure induced by the particle friction. The microstructure is shifted in such a way that the density of particles that would give rise to a positive N_1 , is increased, while the density of particles that would give rise to a negative N_1 , is lessened, and vice versa for

4.6. PARTICLE NORMAL STRESSES

N_2 . Consequently, the friction results in a decrease of $|N_1|$ and in an increase of $|N_2|$. The question is whether the friction effect on the microstructure can be so large that N_1 even becomes positive?

4.5.4 Concluding remarks on the measurements of α_1 and α_2

We are aware that the negative sign of α_1 (N_1 positive) can appear surprising. However, we have conducted several tests that have been unable to invalidate our measurements. The size of the particles, the gap width and the viscosity of the suspending liquid have been shown not to influence the results. We have revisited the results of [Singh and Nott 2003] and have shown that for $0.3 \leq \phi \leq 0.4$ they were consistent with ours. However, there remain some significant discrepancies with other results of the literature that are still to be explained.

4.6 PARTICLE NORMAL STRESSES

4.6.1 Results

As described in section (4.3.1), the pore pressure is measured and when the fluid stress is subtracted from the total stress, the particle contribution to the bulk stress is deduced (equation (4.6)). In Figure (4.31), the square symbols denote the variation of the normalized pore pressure with the volume fraction of particles. These measurements have been performed with the ($2a = 140 \mu m$) suspensions. We have not been able to measure the pore pressure in the suspensions of small particles since the grid screen openings ($50 \mu m$) were larger than the particles ($2a = 40 \mu m$). As expected and reported by [Deboeuf et al. 2009], the flow generates a suction pressure in the liquid whose magnitude increases with the particle volume fraction. The value of the total stress $-\Sigma_{22}(0)/\Sigma_{12}(R) = -(\alpha_1 + \alpha_2)/\eta_s$ at $r = 0$ is also plotted in Figure (4.31) (triangles). We observe that, $-\Sigma_{22}(0)/\Sigma_{12}(R) \approx P_f/\Sigma_{12}(R)$. This result was expected, since at $r = 0$, $\dot{\gamma}(r = 0) = 0$, the particle stress as well as the

4.6. PARTICLE NORMAL STRESSES

normal stress differences N_1 and N_2 should be equal to zero, and thus the total stress should be equal to the fluid stress. In a coming section, we will show that this is not true anymore when $\phi > 0.46$.

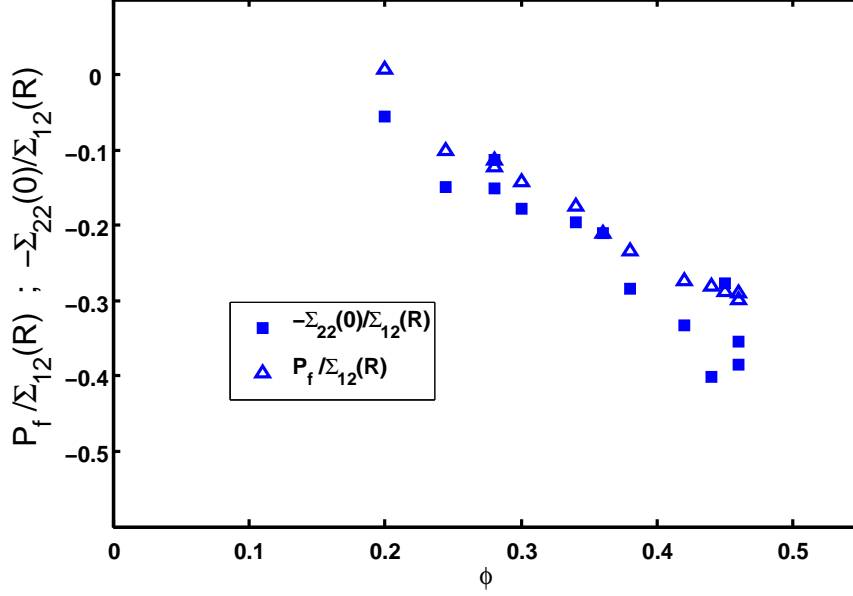


Figure 4.31: Normalized pore pressure P_f as function of ϕ

Coming back to the determination of the particle stress, we can write:

$$\frac{\Sigma_{22}^p(\dot{\gamma}_R)}{\eta_0 \dot{\gamma}_R} = \frac{\Sigma_{22}(\dot{\gamma}_R)}{\eta_0 \dot{\gamma}_R} + \frac{P_f}{\eta_0 \dot{\gamma}_R}. \quad (4.21)$$

The second particle normal stress, normalized by the tangential stress is presented in Figure (4.32). The experimental results can be fitted either with a quadratic law: $\left[-\frac{\Sigma_{22}^p}{\Sigma_{12}} = 4.1\phi^2\right]$, or with a linear law above a threshold value, ϕ_c , of the volume fraction ϕ : $\left[-\frac{\Sigma_{22}^p}{\Sigma_{12}} = 3.15(\phi - \phi_c)\right]$ with $\phi_c \sim 0.19$. This result looks like that of [Boyer et al. 2011 a] who showed a sudden change in the behavior of $(\alpha_2 + \frac{\alpha_1}{2})$ that appears at the threshold of 20%.

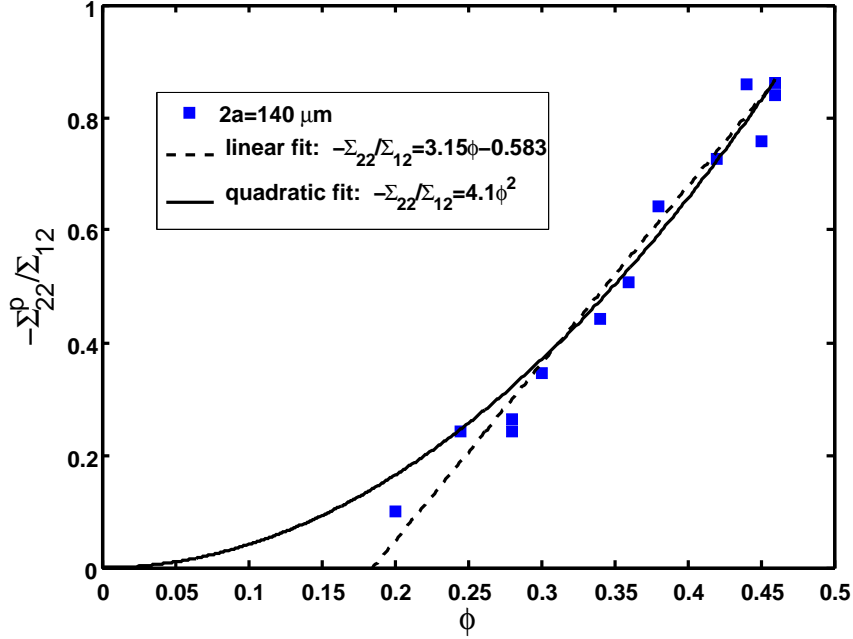


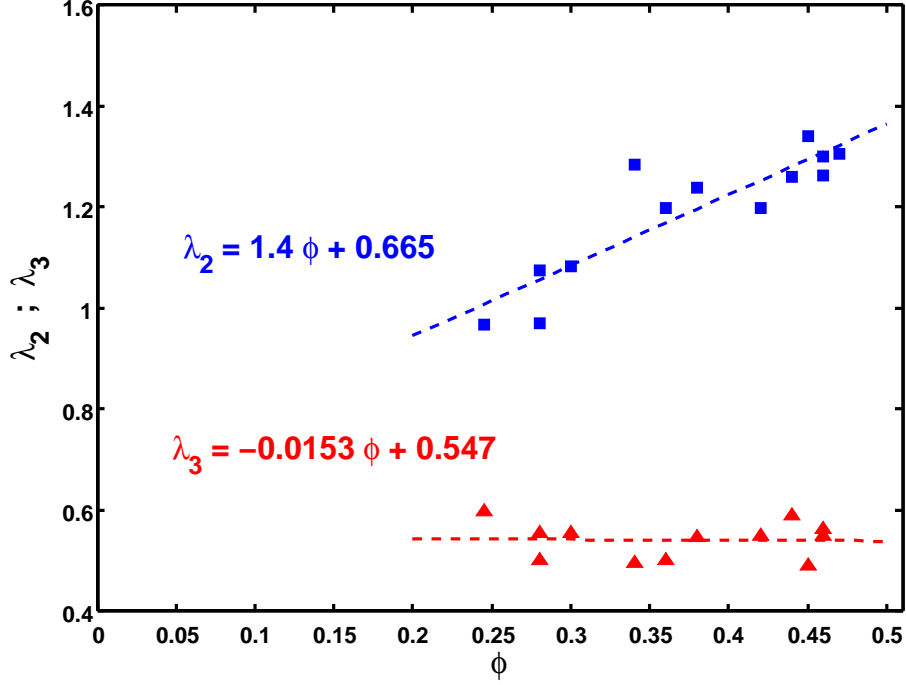
Figure 4.32: $\frac{\Sigma_{22}^p(\dot{\gamma}_R)}{\Sigma_{12}}$ as function of ϕ

This threshold-like behavior also recalls of the excess viscosity shown in Figure (4.23). It is comforting that these two quantities behave in the same manner because, both normal stresses and excess viscosity, originate from the nonhydrodynamic forces between particles in a suspension that has been structured by the shear flow.

The existence of a threshold particle volume fraction, ϕ_c , is still under discussion and we plan to make efforts trying to measure normal stresses for lower concentrations $\phi < 0.2$.

Finally, supposing that the fluid pressure is isotropic (that is intuitive but maybe inexact [Nott, Guazelli, and Pouliquen 2011]), we can deduce from the values of α_1 , α_2 and Σ_{22}^p the other two particle normal stresses Σ_{11}^p and Σ_{33}^p such that:

$$\frac{\Sigma_{11}^p(\dot{\gamma})}{\eta_0 \dot{\gamma}} = \frac{\Sigma_{22}^p(\dot{\gamma})}{\eta_0 \dot{\gamma}} - \alpha_1 ; \quad \frac{\Sigma_{33}^p(\dot{\gamma})}{\eta_0 \dot{\gamma}} = \frac{\Sigma_{22}^p(\dot{\gamma})}{\eta_0 \dot{\gamma}} + \alpha_2 . \quad (4.22)$$

Figure 4.33: λ_2 and λ_3 as function of ϕ

Then, the ratios $\lambda_2 = \frac{\Sigma_{22}^p}{\Sigma_{11}^p}$ (squares) and $\lambda_3 = \frac{\Sigma_{33}^p}{\Sigma_{11}^p}$ (triangles) that appear in the Suspension Balance Model can be obtained. They are plotted in Figure (4.33).

4.6.2 Discussion

First, all particle normal stress components are compressive (negative). A result that is consistent with the microstructure that appear in a sheared suspension with an excess of particle pairs in the compressional quadrant [Phung et al. 1996, Brady and Morris 1997, Parsi and Gadala Maria 1987]. Second, we measure that the particle normal stresses are of the same order of magnitude as the second normal stress difference N_2 . Furthermore, we have measured the 3 variables involved in the Suspension Balance Model proposed by [Morris and Boulay 1999] to explain the shear-induced migration, which are: $q(\phi) \doteq \frac{\eta_N(\phi)}{\eta_s(\phi)} = \frac{-\Sigma_{11}^p(\phi)/\eta_0\dot{\gamma}}{\eta_s(\phi)}$, λ_2 and λ_3 .

Figure (4.34) represents the variation of $q(\phi)$ with ϕ^2 , where one observes

4.6. PARTICLE NORMAL STRESSES

clearly that up to $\phi \approx 0.47$, $q(\phi)$ varies quadratically and the experimental data are very well represented by the dashed line:

$$q(\phi) = \frac{\eta_N(\phi)}{\eta_s(\phi)} = \frac{-\Sigma_{11}^p(\phi)/\eta_0\dot{\gamma}}{\eta_s(\phi)} = 3.2\phi^2; \phi \leq 0.47. \quad (4.23)$$

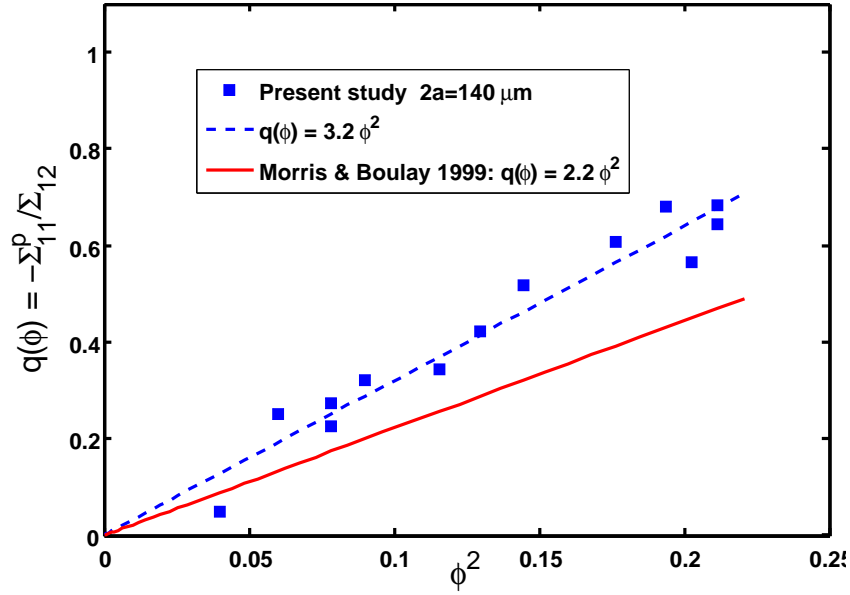


Figure 4.34: $q(\phi)$

The solid line represents the function $q(\phi) = \frac{\eta_N(\phi)}{\eta_s(\phi)} = 2.2\phi^2$ as the ratio of $\eta_N(\phi)$ proposed by [Morris and Boulay 1999] to the normalized suspension viscosity $\eta_s(\phi)$ we measured in equation (4.15). Despite we measure a $q(\phi)$ nearly 1.4 times larger than that used in the model of [Morris and Boulay 1999], we capture well the expected quadratic behavior.

On the other side, in the model of [Morris and Boulay 1999], the coefficients λ_2 and λ_3 were supposed, due to the lack of experimental data, to be independent of the volume fraction of particles ϕ . As you can see from the ratios $\lambda_2 = \frac{\Sigma_{22}^p}{\Sigma_{11}^p}$ (squares) and $\lambda_3 = \frac{\Sigma_{33}^p}{\Sigma_{11}^p}$ (triangles) in Figure (4.33), this hypothesis is under suspicion for $0.2 < \phi < 0.46$. λ_3 is almost constant and equal to 0.5

4.6. PARTICLE NORMAL STRESSES

as the model of [Morris and Boulay 1999] predicts, based on the absence of migration in a torsional flow between two parallel disks. But, λ_2 slightly increases with ϕ , and its values are some how greater than those proposed by [Morris and Boulay 1999], who gave a value of $\lambda_2 = 0.8$ extracted from comparisons between their model predictions of the concentration profiles, and the measured data of [Phillips et al. 1992] of a flow in large gap Couette cell. Thereby, our obtained results at $\phi = 0.2 \leftrightarrow 0.46$ are well close to those used in the proposed model of [Morris and Boulay 1999], and not even far away from those obtained by [Yeo and Maxey 2010a] in FCM. The latter obtained λ_2 and λ_3 that vary linearly with ϕ , in the zone $\phi = 0.2 \leftrightarrow 0.4$ such that $0.46 \lesssim \lambda_2 \lesssim 0.61$ and $0.45 \lesssim \lambda_3 \lesssim 0.77$.

Moreover, as you can see in Figure (4.35) our measured results for Σ_{33}^p are close to those reported by [Deboeuf 2008, Deboeuf et al. 2009], who measured the pore pressure in a suspension flow in a Couette cylindrical cell.

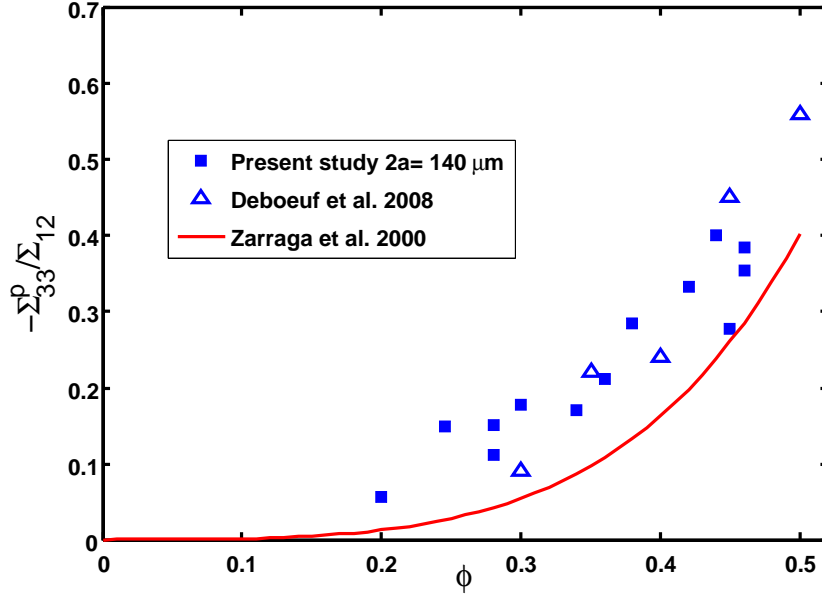


Figure 4.35: Σ_{33}^p as function of ϕ

Our results are also in rather good agreement with those of [Acrivos et al.

4.6. PARTICLE NORMAL STRESSES

1993, Zarraga et al. 2000], while we measure slightly greater values for $-\Sigma_{33}^p$.

Finally, the mean particle normal stress is equal to the particle pressure Π^p :

$$\Pi^p = -\frac{\text{tr}(\Sigma^p)}{3} = -\left[\frac{\Sigma_{11}^p + \Sigma_{22}^p + \Sigma_{33}^p}{3}\right] = -\left[\Sigma_{22}^p + \frac{1}{3}(\alpha_1 - \alpha_2)\right]. \quad (4.24)$$

Figure (4.36) represents the variation of (Π^p/Σ_{12}) with ϕ , which permits the comparison of our results with those obtained by [Sierou and Brady 2002] in Stokesian Dynamics (triangles up). The solid line is the fit of our results for $\phi = 0.2 \leftrightarrow 0.46$ with the law proposed by [Mills and Snabre 2009] given by:

$$\Pi = \beta \eta_0 \dot{\gamma} \frac{\phi^{\frac{7}{3}}}{(\phi - \phi_m)^2}, \text{ with } \beta \approx 1.3. \quad (4.25)$$

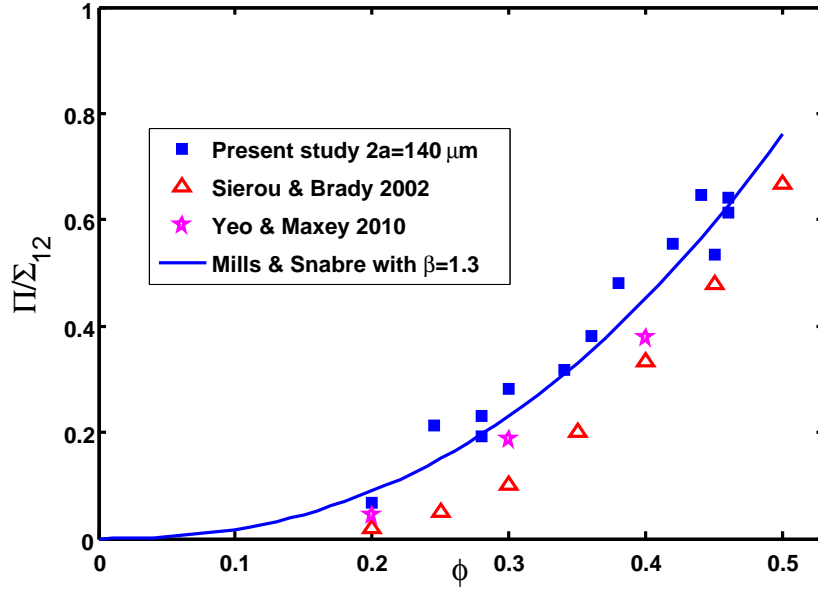


Figure 4.36: The variation of (Π/Σ_{12}) with ϕ

On the same Figure (4.36) we show also the particle pressure obtained by [Yeo and Maxey 2010a] in FCM (equation 4.26), with a note that the agreement

4.7. A TENTATIVE MEASUREMENT OF THE SUSPENSION MATERIAL FUNCTIONS AT HIGHER PARTICLE VOLUME FRACTIONS

with our results is very well satisfactory:

$$\Pi^p = -\Sigma_{11}^p \cdot \frac{(1 + \lambda_2 + \lambda_3)}{3}. \quad (4.26)$$

4.7 A TENTATIVE MEASUREMENT OF THE SUSPENSION MATERIAL FUNCTIONS AT HIGHER PARTICLE VOLUME FRACTIONS

We tried to measure α_1 , α_2 , η_s and P_f for particle volume fractions higher than 0.46. We noticed that for these high concentrations, the value of $\Sigma_{22}(0)$, extrapolated from the measurement of Σ_{22} at four radial positions, was not equal to the pore pressure (averaged over the 4 at-grid-transducers) (see Figure (4.37)).

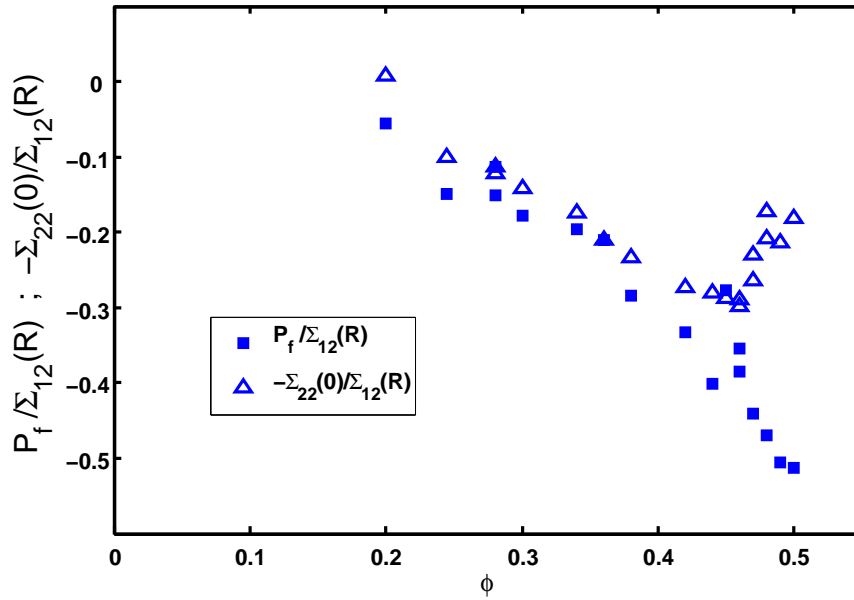


Figure 4.37: Normalized pore pressure P_f as function of ϕ

This result was difficult to understand since the particle normal stresses are expected to vary *linearly* with shear rate and especially to be zero at a zero-shear

4.7. A TENTATIVE MEASUREMENT OF THE SUSPENSION MATERIAL FUNCTIONS AT HIGHER PARTICLE VOLUME FRACTIONS

rate. Thus, the only contribution to the normal stress at the center of the disks should be the fluid stress, i.e. $\Sigma_{22}(0) = \Sigma^f = -P_f$. Looking more carefully at the $\Sigma_{22}(r)$ profile, we observe that for high particle volume fraction, it is no more linear. See for instance the profile obtained for a $\phi = 0.47$ suspension and represented on Figure (4.38).

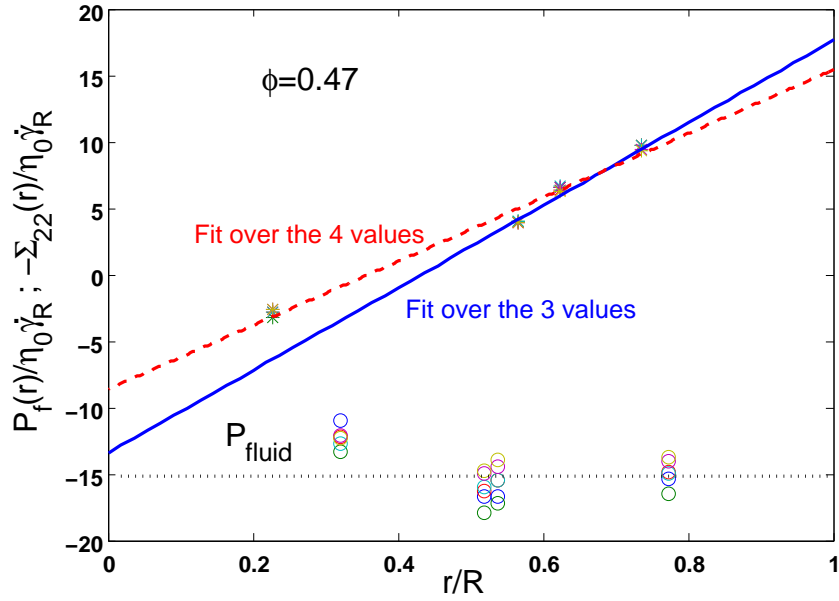


Figure 4.38: $\Sigma_{22}(r)$ and $P_f(r)$ for a $\phi = 0.47$ suspension

The dotted line represents the average pore pressure $\left(\frac{P_f}{\eta_0 \dot{\gamma}_R}\right)$ and the dashed line is the linear fit of $-\Sigma_{22}(r)$ over the four direct transducers that gives $\left(\frac{-\Sigma_{22}(r)}{\eta_0 \dot{\gamma}_R} = -8.6\right)$. If rather than fitting over the four values of $-\Sigma_{22}(r)$, we just consider the three outermost sensors, the linear fit of $-\Sigma_{22}(r)$ gives $\left(\frac{-\Sigma_{22}(r)}{\eta_0 \dot{\gamma}_R} = -13\right)$, a value which is close to $\left(\frac{P_f}{\eta_0 \dot{\gamma}_R}\right)$.

This would be interpreted by the presence of a central zone in the gap between the disks where the flow is not a simple shear one. This could occur if the suspension behavior is not newtonian and in particular if the suspension is a viscoplastic material that behaves as a rigid body at low stresses.

An image of what happens in such a case can be found in [Jarny et al. 2006] who measured the velocity profile in a clay suspension that has a yield stress and

4.7. A TENTATIVE MEASUREMENT OF THE SUSPENSION MATERIAL FUNCTIONS AT HIGHER PARTICLE VOLUME FRACTIONS

that is sheared between two rotating disks. They show that the clay suspension is separated into two zones, one where the flow is a simple shear flow and a zone where the material moves as a block with no internal shearing (see Figure 4.39).

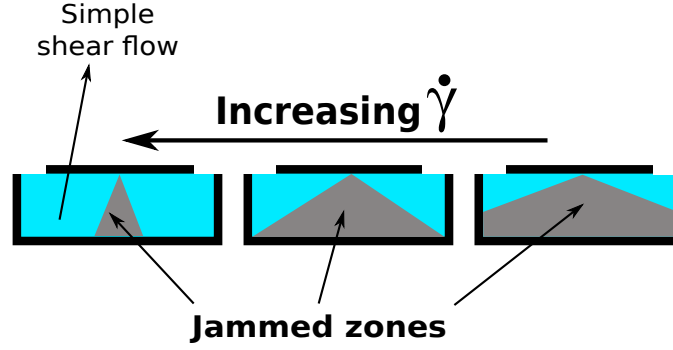


Figure 4.39: Shear-banding zones. Remade from [Jarny et al. 2006].

This kind of shear-banding could explain why the $\Sigma_{22}(r)$ profile is not linear anymore. Furthermore, if an unsheared zone exists in the gap, the measurements of the viscosity that are deduced from the ratio of the applied torque on the measured angular velocity are invalid. Thus, we are unable to determine the ratios $\frac{\alpha_1}{\eta_s}$ and $\frac{\alpha_2}{\eta_s}$ even if we could determine α_1 and α_2 from the fit of $\Sigma_{22}(r)$ obtained with the three outermost transducers.

At last, this interpretation of the non-linearity of $\Sigma_{22}(r)$ deserves some remarks. In the section (4.5.1.1), we have shown that the suspensions were slightly shear-thinning and that this behavior increased with the increase of the volume fraction of particles ϕ . In the same section (4.5.1.1), we have represented the rheological behavior of the suspensions with a power law but it is also possible to do that with a Bingham law:

$$\tau = \eta_B (\dot{\gamma}) + \tau_s . \quad (4.27)$$

For example, for the $\phi = 0.47$ suspension, we obtain $\tau (Pa) = 4.3\dot{\gamma} (s^{-1}) + 2.8 (Pa)$ with $\eta_0 = 0.143 Pa \cdot s$.

4.8 SECONDARY FLOW IN ROTATING PARALLEL PLATE GEOMETRY

The torsional steady shear flow of a Newtonian fluid between two rotating parallel plates witnesses a large-scale secondary flow due to inertia which appears as a toroidal motion with inflow near the stationary plate, and outflow near the moving one. We use the equation [18] of [McCoy and Denn 1971], for the “infinite disk” solution ($\frac{R}{h} \rightarrow \infty$) at low Reynolds number, where the radial velocity due to secondary flow (to 2^{2d} order in pseudo-Reynolds number N_{Re}) is given by:

$$u = -\left(\frac{r}{R}\right) \left(\frac{N_{Re}}{60}\right) \left[4\left(1 - \frac{z}{h}\right) - 9\left(1 - \frac{z}{h}\right)^2 + 5\left(1 - \frac{z}{h}\right)^4\right] R\omega, \quad (4.28)$$

where

$$N_{Re} = \frac{\rho h^2 \omega}{\eta} \quad (4.29)$$

and ω is angular velocity of the rotating disk.

The variation of the velocity $\left(\frac{u}{\omega r N_{Re}/60}\right)$ over the gap is well represented in Figure (4.40).

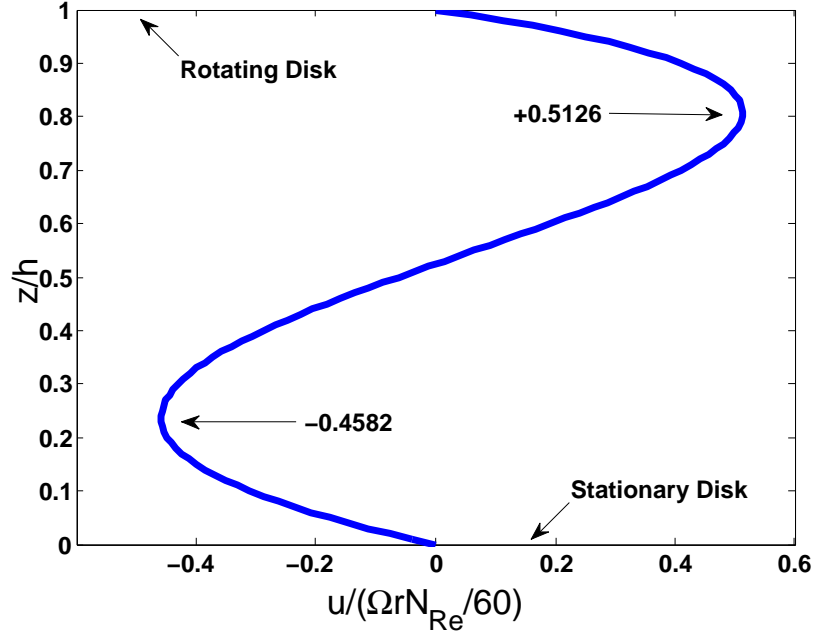


Figure 4.40: Secondary Flow Radial Velocity

The variation of the inertial pressure p_i of a simple fluid sheared between two parallel disks is given by:

$$p_i(z=0) = 0.15\rho\omega^2(r^2 - R^2), \quad (4.30)$$

where ρ is the fluid density.

4.8.1 Validation of the experimental procedure used to determine α_1 and

α_2

We have made use of the previous inertial pressure of equation (4.30) to validate the experimental procedure described in section (4.4.3).

The gap between the disks is filled with a mixture of water and ucon oil ($\eta \sim 1 \text{ Pa} \cdot \text{s}$, $\rho = 1.05 \cdot 10^3 \text{ kg} \cdot \text{m}^{-3}$). Figure (4.41) shows the pressure profile we measured for different angular velocities using both the direct sensors (in triangles) and the grid transducers (in squares). **Note** that expression (4.30)

4.8. SECONDARY FLOW IN ROTATING PARALLEL PLATE GEOMETRY

is valid only if the Reynolds number is low (typically not greater than few unities). In these measurements that we have conducted, the Reynolds number was between 0.3 (*for* $\Omega = 2 \text{ rad} \cdot \text{s}^{-1}$) and 1.4 (*for* $\Omega = 9.7 \text{ rad} \cdot \text{s}^{-1}$) so that expression (4.30) was valid. Figure (4.41) shows a good agreement between our measured pressure profiles and those predicted by equation (4.30).

Note that the inertial pressure was completely negligible in the experiments carried out to measure α_1 and α_2 . Indeed in these experiments, the maximum shear rate was about 50 s^{-1} that corresponds to an angular velocity $\Omega = \frac{\dot{\gamma}h}{R} \approx 2 \text{ rad} \cdot \text{s}^{-1}$ and to an inertial pressure $p_i \approx 2 \text{ Pa}$.

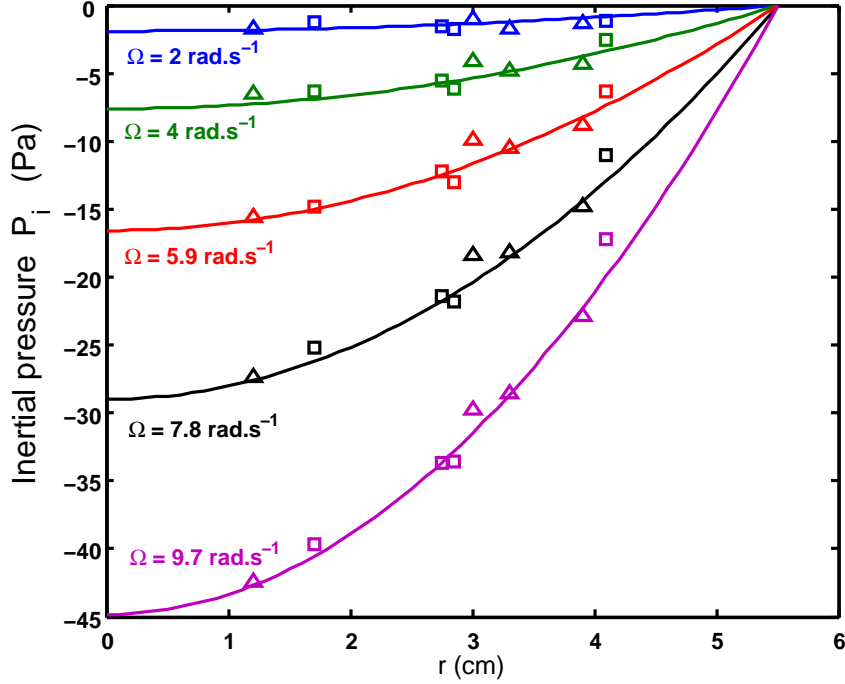


Figure 4.41: Inertial pressure p_i as function of r .

4.8.2 Visualization of the secondary flow

4.8.2.1 In a simple liquid

A Glycerine sample is sheared between two parallel disks of dimensions, $h = \text{gap} \in [2.5 ; 35.0] \text{ mm}$; $r_1 = 50,10 \pm 0,02 \text{ mm}$; $R = 58,09 \pm 0,01 \text{ mm}$. The upper disk is stationary, while the lower one rotates by means of a motor at a

4.8. SECONDARY FLOW IN ROTATING PARALLEL PLATE GEOMETRY

certain rotational velocity ω (Figure 4.42).

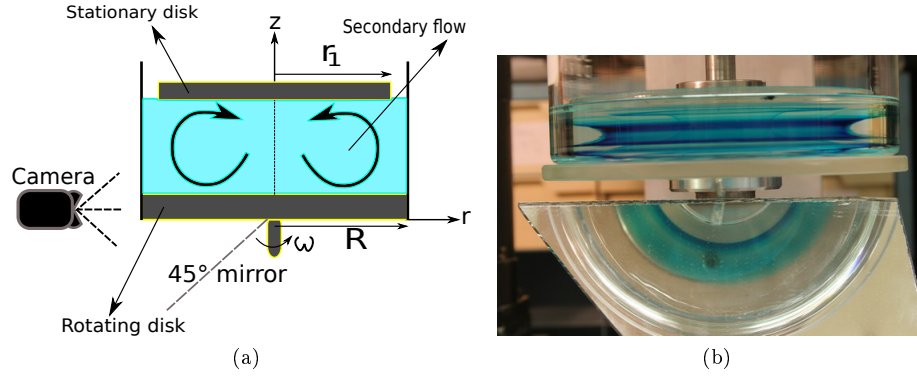


Figure 4.42: Experimental Setup

A mirror, making 45° with the horizontal, is placed under the lower disk so that the digital camera can catch straight clear planar images. A droplet of colored glycerine is injected from top by means of a syringe, before lowering down the upper disk to make contact with the surface of the sample (Figure 4.43).

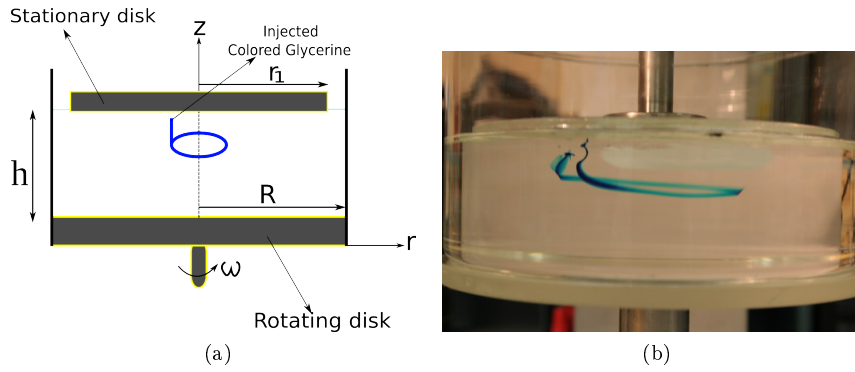


Figure 4.43: Glycerine Injection

It was observed that, at large gaps, a recirculation existed clearly caused by the secondary flow, where the streamlines are shown on Figure (4.44).

4.8. SECONDARY FLOW IN ROTATING PARALLEL PLATE GEOMETRY

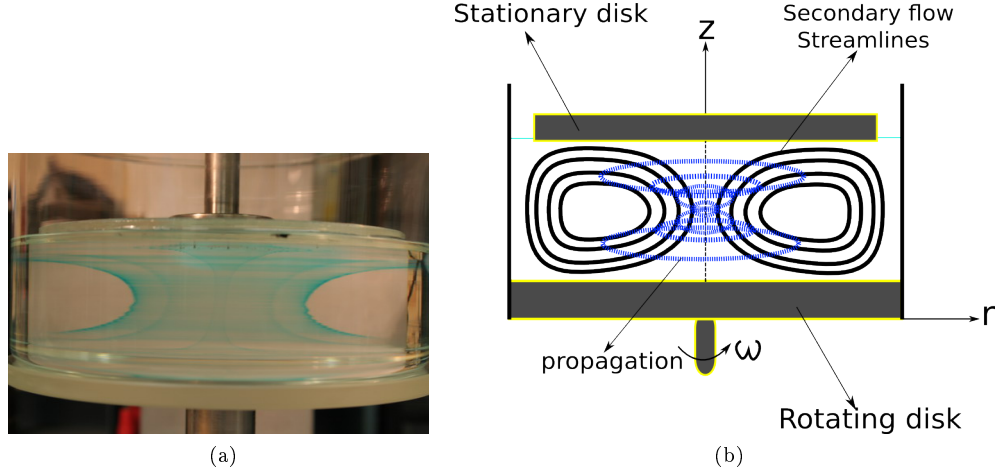


Figure 4.44: StreamLines

At smaller gaps, the recirculation appears like fronts that propagate in opposite directions. After taking different photos of the fronts (Figure 4.45), we did images tracking in order to measure their velocities.

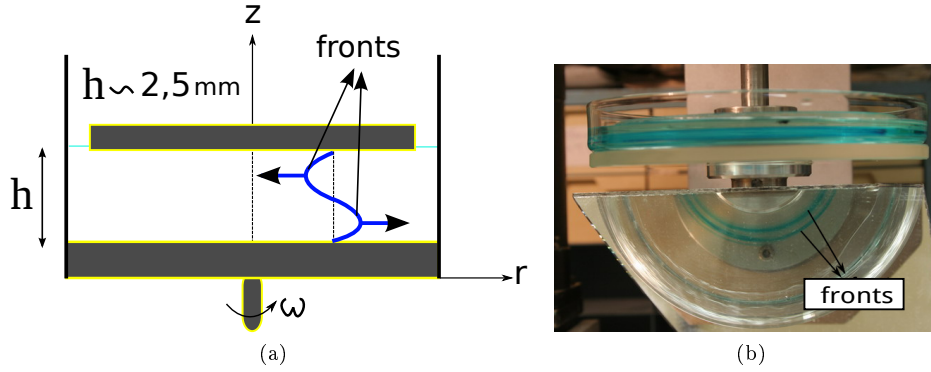


Figure 4.45: The Fronts

The experimental results obtained with $\omega = 1.32 \text{ rad}\cdot\text{s}^{-1}$, $\nu = \frac{\eta}{\rho} = 873.34 \text{ mm}^2\cdot\text{s}^{-1}$ and $h = 2.5 \text{ mm}$ are presented in Figure (4.46) together with the theoretical ones calculated from (4.28): $r_{front}(t) = r_0 e^{A^\pm t}$ with $A^+ = 0.5126 \left(\frac{\omega N_{Re}}{60} \right)$ & $A^- = 0.4582 \left(\frac{\omega N_{Re}}{60} \right)$. The signs + and - stand for the outward and inward fronts, respectively. The agreement is good and especially better for the inward front displacement.

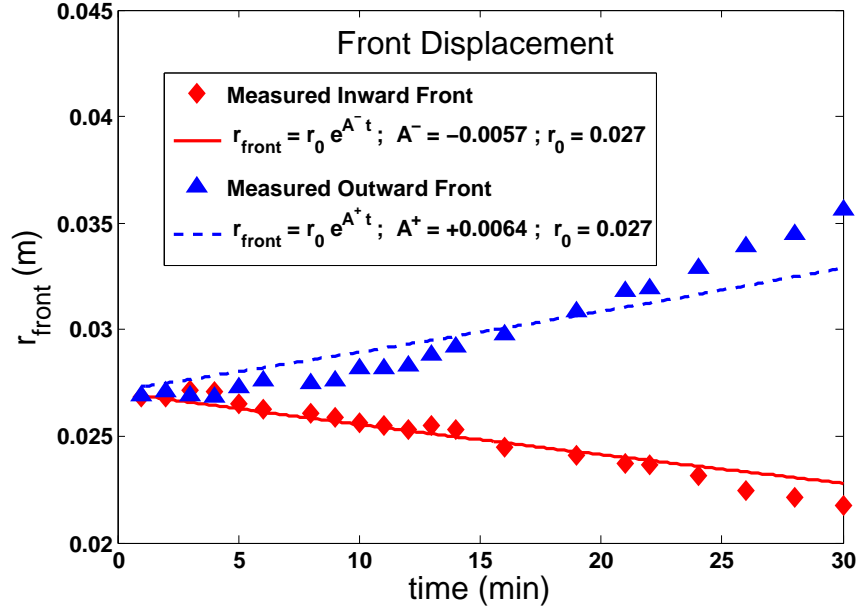


Figure 4.46: Front Displacement

4.8.2.2 Secondary flow in a suspension

The secondary flow has also been studied in a 10% suspension of PMMA particles ($2a = 80 \mu m$) dispersed in a mixture of Transformer oil and Ugilec (Elf Atochem) such that the density of the fluid is equal to that of the particles. The suspension is sheared between two parallel disks mounted on a controlled stress rheometer (CARRI-MED CSL 100). The upper rotating disk is transparent and covered with a conducting material ITO (Indium Tin Oxide) and then grounded to the earth. The lower disk is connected to a high voltage source that supplies a DC voltage between -1500 V and +1500 V. The gap between the disks is $h = 800 \mu m$. The experimental setup is presented in Figure (4.47).

4.8. SECONDARY FLOW IN ROTATING PARALLEL PLATE GEOMETRY

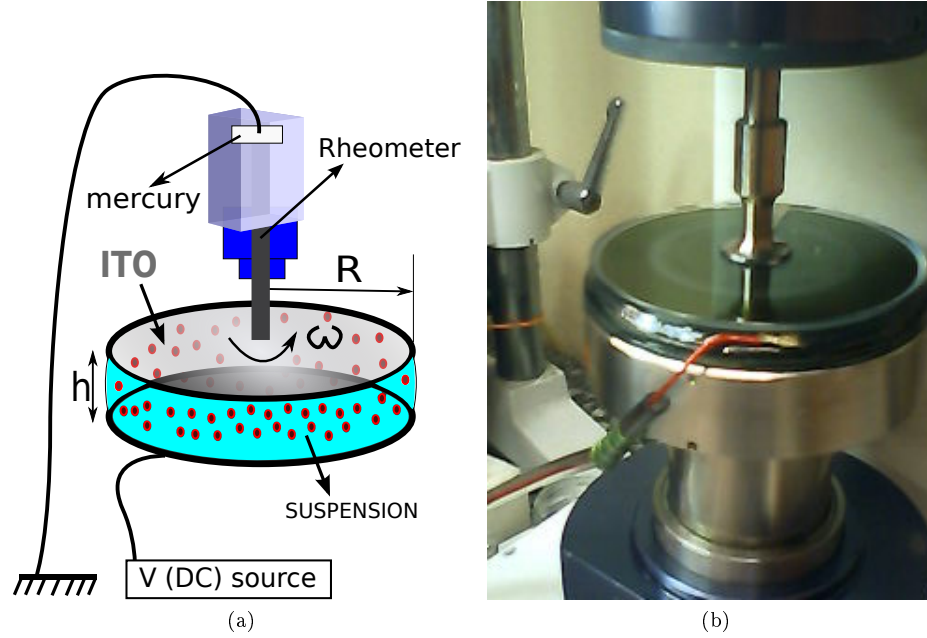
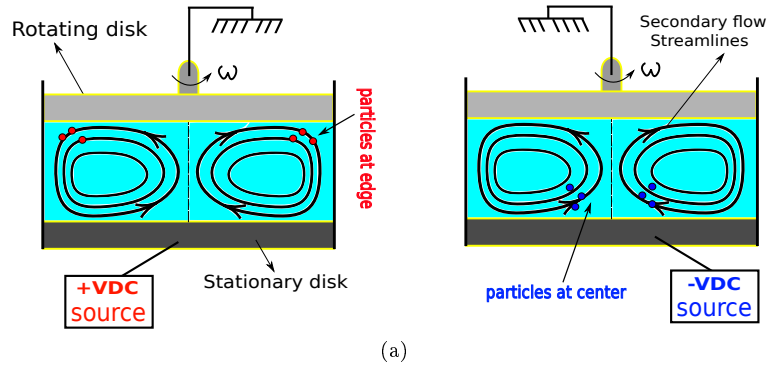


Figure 4.47: Suspension Experimental Setup

Whenever the voltage is applied on the stationary disk, the particles that carry a positive electrical charge are attracted by either the upper or the lower plate according to the sign (+Ve DC or -Ve DC) of the applied source electric field. If the particles are being attracted by the upper plate rotating, they move outward under the effect of the secondary flow and stay at the edge. But, if the lower stationary plate attracted the particles, they move inward and accumulate at the center due to the fact that the secondary flow at the stationary plate (disk) is an inflow (see Figure 4.48).

4.8. SECONDARY FLOW IN ROTATING PARALLEL PLATE GEOMETRY



(b) Positive voltage +500 VDC. The particles migrated toward the edge

(c) Negative voltage -500 V DC. The particles migrated toward the center

Figure 4.48: Inward and Outward Migration. (Particles in White)

So, we observe a particle front that moves inward in the negative voltage case, and outward in the positive voltage case. The front velocity is measured (Figure 4.49) for different applied torques (or different angular velocities).

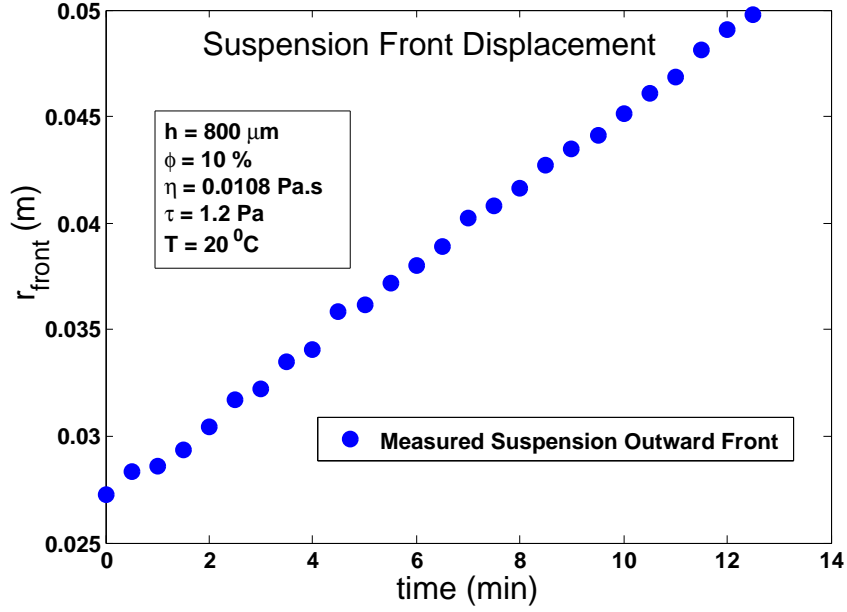


Figure 4.49: Suspension Outward Front displacement

These results are presented and compared to the theoretical values of the secondary flow radial velocities deduced from equation (4.28) in Table (4.7).

τ (Pa)	1.2	2.4	3.6
ω ($\text{rad} \cdot \text{s}^{-1}$)	1.62	3.3	6.08
$V_r(\text{experimental})$ ($\mu\text{m} \cdot \text{s}^{-1}$)	34.7	138.8	500
$V_r(\text{theoretical})$ ($\mu\text{m} \cdot \text{s}^{-1}$)	35.6	148	502

Table 4.7: suspension Fronts Radial Velocities

A very good agreement is observed among the results.

4.8.3 On the possible role of the secondary flow on the particle shear-induced migration in parallel plate geometry

As we have seen in the section (1.7.3.5), the shear-induced migration characteristic time t_M scales as $d^2 / (\dot{\gamma} a^2 D(\phi))$, with $D(\phi) \sim K_c \phi$. Thus, in the torsional flow of a suspension between two parallel disks, this time will be scaling as $t_M \sim \frac{1}{K_c \phi \dot{\gamma}} \frac{R^2}{a^2}$. Moreover, the characteristic time for the secondary flow scales as $t_S \approx \frac{R}{u} = \frac{60}{\omega N_{Re}}$. So, comparing both times, for the suspension of

$\phi = 10\%$, where $K_c \sim 0.1$ [Chapman 1990, Merhi et al. 2005], one gets a criterion for the sheared-induced migration in parallel plates geometry to be measurable as $\text{Re} \ll 60K_c\phi\frac{a^2}{h^2}$ that is $\text{Re} \ll \frac{a^2}{h^2}$.

4.9 CLOSURE

Using a single experiment, this chapter (4) have proposed a determination methodology of the three material functions (the viscosity, and the two normal stress differences) in non-Brownian suspensions of hard spheres for a wide zone of concentrations $\phi = 0.2 \leftrightarrow 0.46$. The measurement of the radial profile of Σ_{22} in a torsional flow between two parallel disks, provides us with the two linear combinations of α_1 and α_2 : The slope of Σ_{22} gives $-(\alpha_1 + 2\alpha_2)$, and the ordinate at the origin returns $(\alpha_1 + \alpha_2)$. Simultaneously, we measure the viscosity of the suspension. It is so well surprising, we measure a positive N_1 . For that reason, we did a chain of tests to show that the sign of N_1 does not depend neither on the particles size, nor on the gap size between the two disks. The behavior of $[(\alpha_1 + 2\alpha_2)/\eta_s]$ as a function of the volume fraction of particles ϕ is very close to that measured recently by [Boyer et al. 2011 a] in a rotating rod experiment. When ϕ is less than 0.47, α_1/η_s and α_2/η_s seemed to vary linearly with the volume fraction with threshold of orders 0.25 for α_1/η_s , and 0.2 for α_2/η_s .

The pore pressure measurements permit us to have an access to the values of the particle normal stress in the direction of velocity-gradient ($\Sigma_{22}^p = \Sigma_{22} + P_f$), and to deduce from Σ_{22}^p , α_1 and α_2 the two other particle normal stresses Σ_{11}^p and Σ_{33}^p . The particle normal stresses are of the same order of magnitude of N_2 . Generally, our obtained results for the particle normal stresses are in good agreements with those presented in the literature, which were obtained numerically [Sierou and Brady 2002, Yeo and Maxey 2010a], theoretically

[Mills and Snabre 2009], and experimentally [Deboeuf 2008, Deboeuf et al. 2009, Zarraga et al. 2000]. We observe, as [Sierou and Brady 2002] showed numerically, that the three particle normal stresses (Σ_{11}^p , Σ_{22}^p , and Σ_{33}^p) do not vary exactly in the same manner with the variation of the volume fraction of particles ϕ . This is in a difference with the particle normal stresses used by [Morris and Boulay 1999] in the Suspension Balance Model that explains and predicts the shear-induced migration of particles. Nevertheless, the values of Σ_{11}^p , Σ_{22}^p and Σ_{33}^p that we have measured are not very different from that proposed by [Morris and Boulay 1999]. As they found, we obtain $\lambda_3 = \frac{\Sigma_{33}^p}{\Sigma_{11}^p} \approx 0.5$, and a quadratic variation of $q(\phi) = \frac{\eta_N(\phi)}{\eta_s(\phi)} = \frac{-\Sigma_{11}^p}{\Sigma_{12}}$ such that ($q(\phi) = 3.2\phi^2$) for us, and ($q(\phi) = 2.2\phi^2$) for them. At last, while they suppose that $\lambda_2 = \frac{\Sigma_{22}^p}{\Sigma_{11}^p}$ is independent of ϕ , we measured a slight increase of λ_2 when ϕ increases from 0.2 ($\lambda_2 \approx 1$) to 0.46 ($\lambda_2 \approx 1.3$).

Above $\phi = 0.47$, we have not been able to measure neither the material functions (η_s , α_1 and α_2) nor the particle normal stresses (Σ_{11}^p , Σ_{22}^p , and Σ_{33}^p). In particular we have observed that the Σ_{22} profile deviated from its predicted expression. We suppose that for high ϕ , the flow between the disks is no more a simple shear flow in the central region. Further rheo-optics experiments should be performed to measure the velocity profile between the disks and to verify that a jammed zone is present.

At last we have studied the secondary flow that is present in the torsional between two parallel plates. It has been used to validate the pressure measurements. The secondary flow velocity has been measured both in a simple liquid and in a suspension, and its influence on the shear induced particles migration has been estimated.

Chapter 5

THE MODIFIED Suspension Balance Model

5.1 OVERVIEW

Here we present the *modification* of the original SBM of [Nott and Brady 1994, Morris and Boulay 1999] according to our experimental results obtained in chapter (4). In section (5.2), we summarise the parameters that intervene in this SBM, then in section (5.3), the modified particle normal stress tensor is presented according to our measurements. Later, the validation of the modified SBM in Couette cell and in rectangular channel flows via [OpenFOAM®] are tackled in section (5.4), and the closure of this chapter (5) comes in section (5.6).

5.2 THE GOVERNING PARAMETERS

The central modification in the SBM, defined in section (1.7.4) of chapter (1), lies in its Σ^p tensor that plays a significant role in the migration flux \vec{j}_\perp of particles (equation 1.61). That's because, the latter is driven by the

5.3. THE PARTICLE NORMAL STRESS TENSOR

divergence of the particle stress tensor which can be written now, according to our experimental measurements, in its new form as:

$$\mathbf{\Sigma}^p = -\mathbf{\Sigma}_{nn,2}^p + 2\eta_0\eta_p(\phi) \mathbf{E}, \quad (5.1)$$

where $\mathbf{\Sigma}_{nn,2}^p$ will be the modified particle stress diagonal tensor defined as:

$$\mathbf{\Sigma}_{nn,2}^p = - \begin{bmatrix} \mathbf{\Sigma}_{11}^p & 0 & 0 \\ 0 & \mathbf{\Sigma}_{22}^p & 0 \\ 0 & 0 & \mathbf{\Sigma}_{33}^p \end{bmatrix} = \eta_0\eta_N(\phi) \dot{\gamma} \begin{bmatrix} 1 & 0 & 0 \\ 0 & \lambda_2(\phi) & 0 \\ 0 & 0 & \lambda_3(\phi) \end{bmatrix} \quad (5.2)$$

with the measured parameters η_N , η_s , λ_2 , and λ_3 . We recall that $\lambda_2 = \frac{\Sigma_{22}^p}{\Sigma_{11}^p}$, $\lambda_3 = \frac{\Sigma_{33}^p}{\Sigma_{11}^p}$, and $\eta_p = (\eta_s - 1)$.

5.3 THE PARTICLE NORMAL STRESS TENSOR

We got experimentally, as [Sierou and Brady 2002] showed numerically, that the 3 particle normal stresses ($\mathbf{\Sigma}_{11}^p$, $\mathbf{\Sigma}_{22}^p$, and $\mathbf{\Sigma}_{33}^p$) do not vary exactly in the same manner with the variation of the volume fraction of particles ϕ . That is inconsistent with the hypothesis in the original **SBM** model proposed by [Morris and Boulay 1999], which consists of supposing that the 3 particle normal stresses ($\mathbf{\Sigma}_{11}^p$, $\mathbf{\Sigma}_{22}^p$, and $\mathbf{\Sigma}_{33}^p$) vary in the same way with the variation of the volume fraction of particles ϕ . From our experimental measurements of ($\mathbf{\Sigma}_{22}^p$, α_1 , and α_2) in chapter (4), we measured, thus modified, the particle stress tensor $\mathbf{\Sigma}^p$ in the **SBM** according to the following parameters η_N , η_s , λ_2 , and λ_3 :

$$\eta_s(\phi) = \left(1 - \frac{\phi}{\phi_m}\right)^{-2} \text{ with } \phi_m = 0.58 \quad (5.3)$$

$$\eta_N(\phi) = 3.2\phi^2\eta_s(\phi) \quad (5.4)$$

5.4. THE MODIFIED SBM IMPLEMENTED IN OPENFOAM®

Note that in the latter equation (5.4), we made the implicit hypothesis that the normal particle viscosity η_N is proportional to the suspension shear viscosity η_s .

$$\lambda_2(\phi) = 1.4\phi + 0.665 \quad (5.5)$$

$$\lambda_3(\phi) = -0.015\phi + 0.547 \quad (5.6)$$

It is important to keep in mind that these variations of η_s , η_N , λ_2 , and λ_3 have been obtained for particle volume fractions in the range of $[0.20 \leq \phi \leq 0.47]$. In the following we will allow ourselves to generalise and use these expressions even if ϕ doesn't belong to the latter range, when it is outside of $0.20 \leftrightarrow 0.47$. Of course, this would deserve further experimental confirmation.

5.4 THE MODIFIED SBM IMPLEMENTED IN OpenFOAM®

We present here different simulations using the “Modified-SBM” implemented in [OpenFOAM®]. We study the suspension flow in Couette cells of both large and small gaps, trying to validate the modified model through the comparisons with the experimental data found in literature.

5.4.1 Suspension Flow in a Large-gap Couette cell

Let us now go back and take the experiments of [Phillips et al. 1992] of a suspension flow in a large gap $\left(\frac{R_{out}}{R_{in}} \approx 3.7\right)$ of a Couette cell. Figure (5.1) shows the transient concentration profiles at $n = 200$ and $n = 12000$ revolutions of the internal cylinder at variables $\frac{a}{R_{out}} = 0.0143$, $\phi_{bulk} = 0.55$, $\alpha = 3.5$ & 4 , $\phi_m = 0.68$, $f(\phi) = \left(1 - \frac{\phi}{\phi_m}\right)(1 - \phi)^{\alpha-1}$, and $\frac{\eta_s}{\eta_0} = \left(1 - \frac{\phi}{\phi_m}\right)^{-2}$.

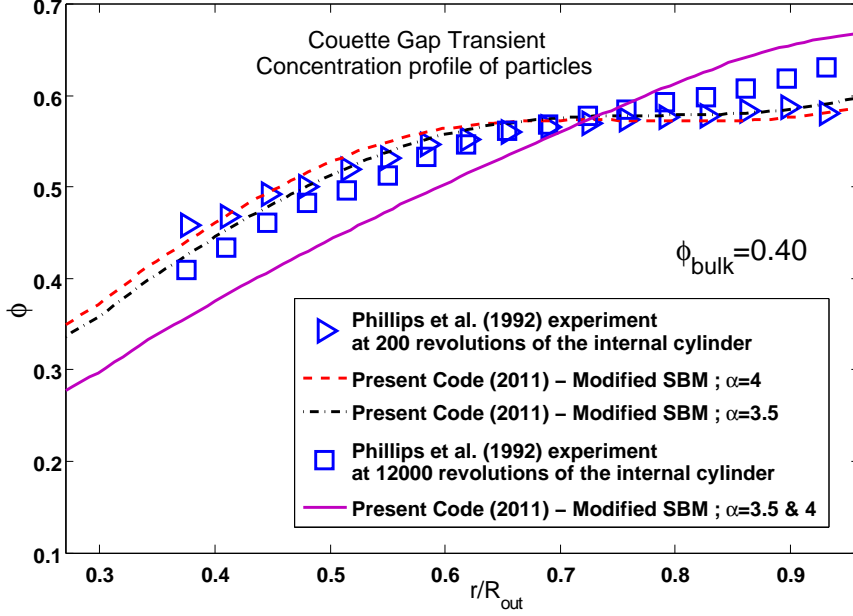


Figure 5.1: Transient Concentration Profiles at 200 & 12000 revolutions

We observe good matching between the “Modified **SBM**” predicted concentrations and the experimental data obtained by [Phillips et al. 1992] via the direct measuring method “**NMR**”, specifically at $n = 200$ revolutions of the inner cylinder (Figure 5.1). However, the Model predictions deviates away from the experimental profile at $n = 12000$ revolutions. The discrepancy between the experimental results of [Phillips et al. 1992] and our numerical ones is not surprising since, according to [Phillips et al. 1992] the maximum packing volume fraction ϕ_m of the suspension they studied is 0.68, while for our suspension $\phi_m = 0.58$. This means that, for a reason that we ignore here, the material functions are not the same for the two suspensions.

Moreover, it is then good to recall that the form of $f(\phi) = \left(1 - \frac{\phi}{\phi_m}\right) (1 - \phi)^{\alpha-1}$ we adopted, is phenomenological and has been borrowed from the sedimentation modeling [Richardson and Zaki 1954]. The term $\left(1 - \frac{\phi}{\phi_m}\right)$ is introduced in such a way that the particle velocity would be zero when $\phi = \phi_m$. The value of the exponent α is not well controlled and can be taken in the range from 3

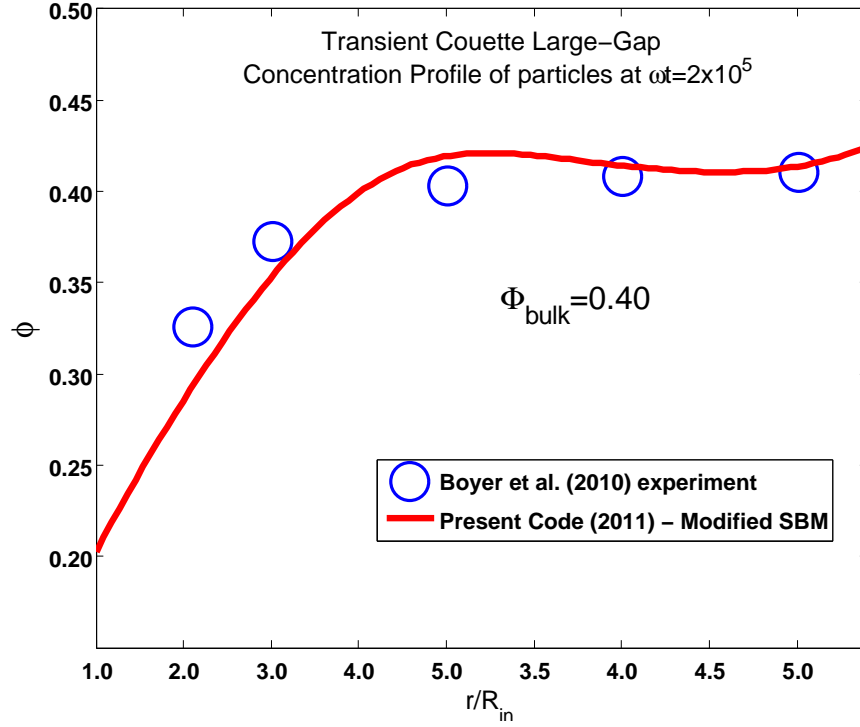
5.4. THE MODIFIED SBM IMPLEMENTED IN OPENFOAM®

to 5 which also may affect the results.

Fortunately, we have been able to compare our numerical results to experimental ones obtained by [Boyer et al. 2011 a] with the same suspension as that we have used to measure Σ^P . They present results on the particle migration in a suspension sheared in a large-gap Couette cell $\left(\left(\frac{R_{out}}{R_{in}}\right)_{max} = 11\right)$. Their experimental setup consisted of a rotating rod of $R_{in} = 5, 10 \& 12.5 \text{ mm}$ and of length $L = 50 \text{ mm}$ immersed in a suspension in a cylindrical container having a radius of $R_{out} = 55 \text{ mm}$. They used in their experiments a suspension made of the same polystyrene spherical beads as we used ($2a = 140 \mu\text{m}$), dispersed in a Newtonian liquid of viscosity $\eta_0 = 2.15 \text{ Pa} \cdot \text{s}$ at 25° C .

During the experiment they did transient measurements of the concentration profiles of particles in the sheared suspension by taking samples using a pipette at different radial distances in the large gap. Each sample was then weighted then immersed into a large quantity of water, filtered and dried. Volume fractions were obtained as the ratio of the mass of the particles to the mass of the sample. They noted that this basic method proved to be fairly accurate as the spatially averaged volume fraction gives the initial volume fraction with less than 5 % discrepancy.

The numerical simulations of the [Boyer et al. 2011 a] experiment of a 0.40 suspension using the “Modified **SBM**” with $\frac{a}{R_{out}} = 0.001272$, $\alpha = 4$, $\phi_m = 0.58$, $f(\phi) = \left(1 - \frac{\phi}{\phi_m}\right)(1 - \phi)^{\alpha-1}$, and $\frac{\eta_s}{\eta_0} = \left(1 - \frac{\phi}{\phi_m}\right)^{-2}$ are presented in the following Figure (5.2).

Figure 5.2: Transient Concentration Profiles $\omega t = 10^5$

The “Modified SBM” as you can see in Figure (5.2) predicts quite well the transient volume fraction of particles ϕ in the large gap at $\omega t = 10^5$ of a suspension of initial bulk concentration of 40%, where ω is the speed of rotation of the inner rod and t is time.

5.4.2 Suspension Flow in a Small-gap Couette cell

[Shapley et al. 2002, Shapley et al. 2004] conducted **LDV** experiments on suspension flow in a small-gap Couette cell. The setup consisted of an inner cylinder of radius $R_{in} = 5.715\text{ cm}$ and an outer one of $R_{out} = 6.31\text{ cm}$, resulting in a gap width of $h = 0.595\text{ cm}$, which is 10.4% of the inner cylinder radius and about 30 particle diameters wide.

They used PMMA particles ($2a \approx 200\text{ }\mu\text{m}$) dispersed in a Newtonian liquid of viscosity $\eta_0 = 0.84\text{ Pa}\cdot\text{s}$ at 22°C .

5.4. THE MODIFIED SBM IMPLEMENTED IN OPENFOAM®

They used the **LDV** technique to measure the suspension velocity profile $v(r)$ from which they deduced the shear rate profile:

$$\dot{\gamma}(r) = r \frac{\partial \frac{v(r)}{r}}{\partial r} . \quad (5.7)$$

Since they know the shear stress $\tau(r)$ in the gap such that:

$$\tau = \frac{\Gamma}{2\pi r^2 L} \quad (5.8)$$

with L being the cylinder length, and Γ the applied torque, they obtain the viscosity throughout the gap. Then, they compute the particle volume fraction profile from the relation between the viscosity and the particle concentration.

Thus, the way they used to measure the concentration profiles is indirect and likely to introduce errors. Indeed, the authors do not measure themselves the relation between the viscosity and the particle volume fraction. They adopt arbitrarily the Krieger-Dougherty relation:

$$\eta_s(\phi) = \left(1 - \frac{\phi}{\phi_m}\right)^{-1.82} \quad \text{with } \phi_m = 0.68 \quad (5.9)$$

This value of the packing volume fraction ($\phi_m = 0.68$) is very elevated compared to the values usually obtained for nonbrownian suspensions ([Ovarlez et al. 2006] $\phi_m = 0.615$, [Boyer et al. 2011 a] $\phi_m = 0.58$, present study [Dbouk et al. 2011] $\phi_m = 0.58$).

Thus, to compare our numerical simulations with the [Shapley et al. 2002, Shapley et al. 2004] experimental data, we first re-calculate the ϕ -profiles data with our measured relative suspension viscosity of the form:

$$\eta_r(\phi) = \left(1 - \frac{\phi}{\phi_m}\right)^{-2} \quad \text{with } \phi_m = 0.58 \quad (5.10)$$

After correcting their original experimental concentration profiles ϕ with our measured relative viscosity of equation (5.10), we present in the following Figures for three different bulk suspensions, the predictions of the “Modified **SBM**”

5.4. THE MODIFIED SBM IMPLEMENTED IN OPENFOAM®

for their steady volume fraction of particles at variables $\frac{a}{R_{out}} = 0.0015847$, $\alpha = 4$, $\phi_m = 0.58$, $f(\phi) = \left(1 - \frac{\phi}{\phi_m}\right) (1 - \phi)^{\alpha-1}$, and $\frac{\eta_s}{\eta_0} = \left(1 - \frac{\phi}{\phi_m}\right)^{-2}$:

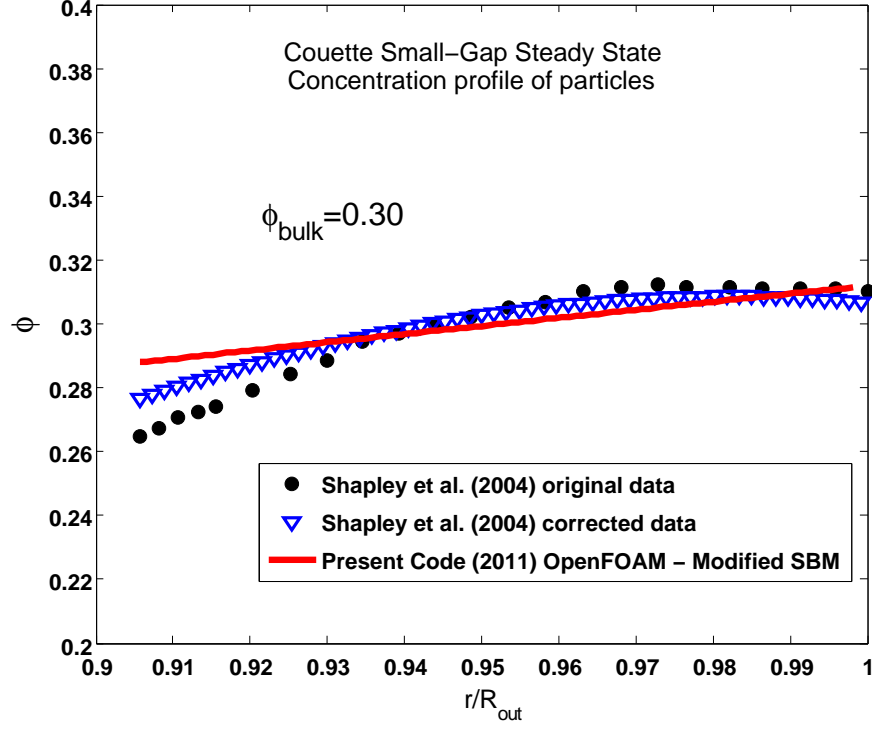


Figure 5.3: Steady State Concentration Profiles of 30% initial suspension

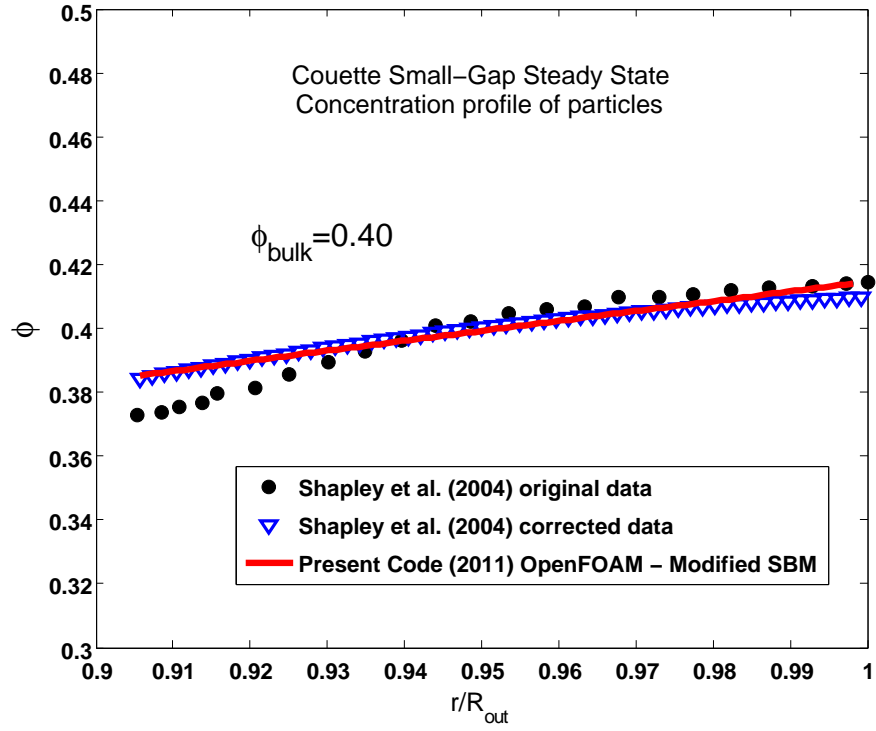


Figure 5.4: Steady State Concentration Profiles of 40% initial suspension

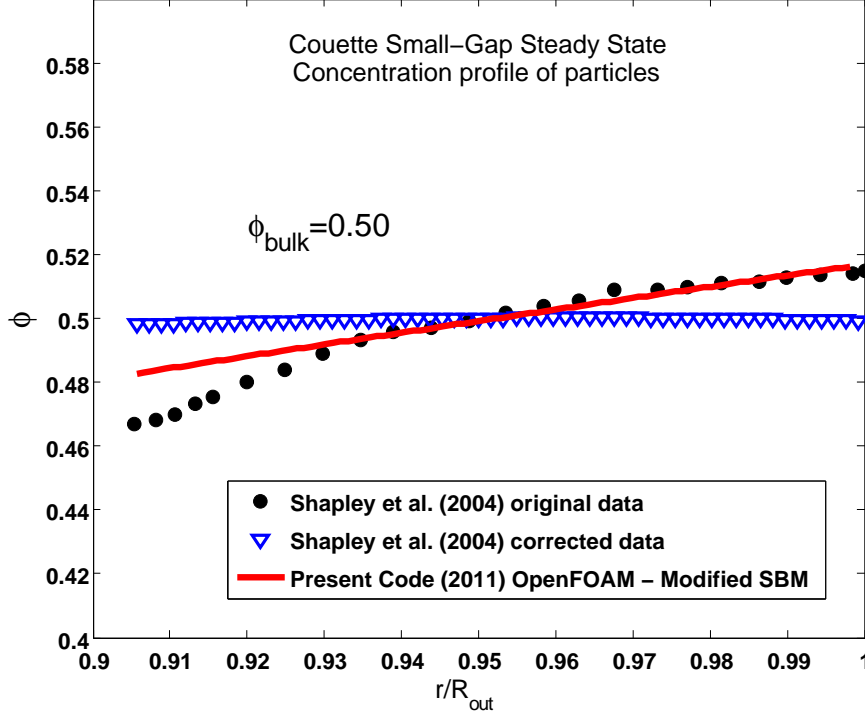


Figure 5.5: Steady State Concentration Profiles of 50% initial suspension

We observe good agreements between the “Modified **SBM**” steady concentrations predictions, and the corrected experimental data of [Shapley et al. 2002, Shapley et al. 2004] specifically for the moderate particle volume fractions of 30 & 40 % (Figures (5.3) & (5.4)). However, it is clearly observed in Figure (5.5) that the numerical profile deviates well away from the corrected experimental one. This may be due to the fact that we have measured the particle stress tensor Σ^p only for particle concentrations lower than 47%. The extrapolated laws for higher concentrations may not be correct and additional measurements of Σ^p should be necessary to predict the shear-induced migration in so concentrated suspensions.

5.5 THE SBM AND THE MODIFIED-SBM

One can wonder about the consequences of having modified the particle stress tensor Σ^p on the shear-induced migration. We start by presenting in Figure (5.6) an example for the simulation of the latter experiment of [Shapley et al. 2002, Shapley et al. 2004] at $\phi = 40\%$ using both model versions.

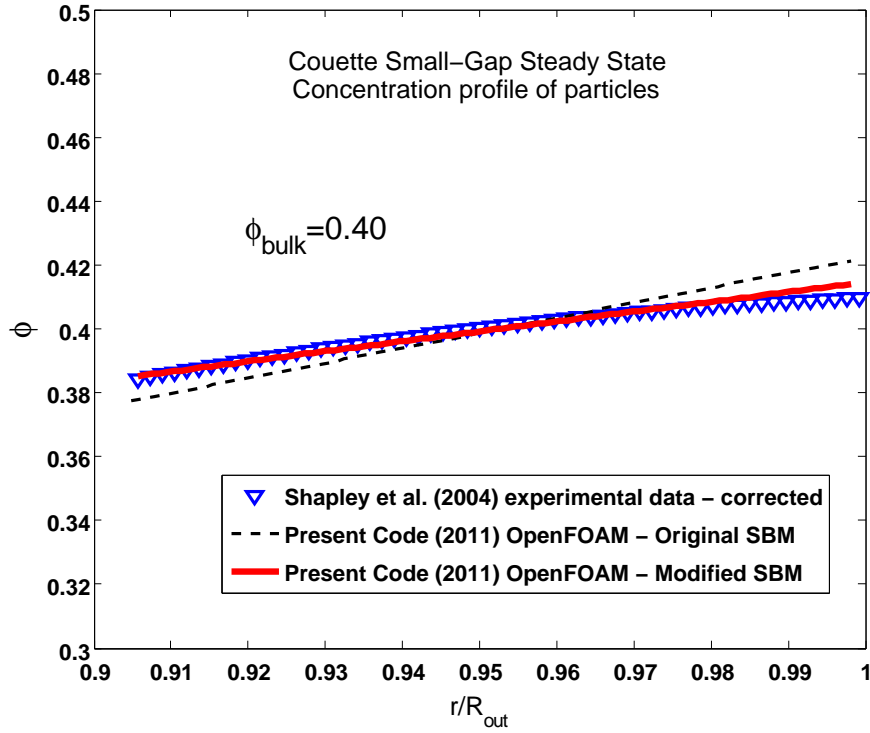


Figure 5.6: Steady State Concentration Profiles of 40% initial suspension

It is clearly observed from Figure (5.6), that the modified **SBM** captures the steady concentration profile better than as it was predicted by the original **SBM** for the 40% bulk suspension flow in a narrow gap Couette cell.

Moreover, we present in Figure (5.7) the results of simulations for the square cross sectional conduit case at bulk volume fraction of 40% and at different ϕ_m values.

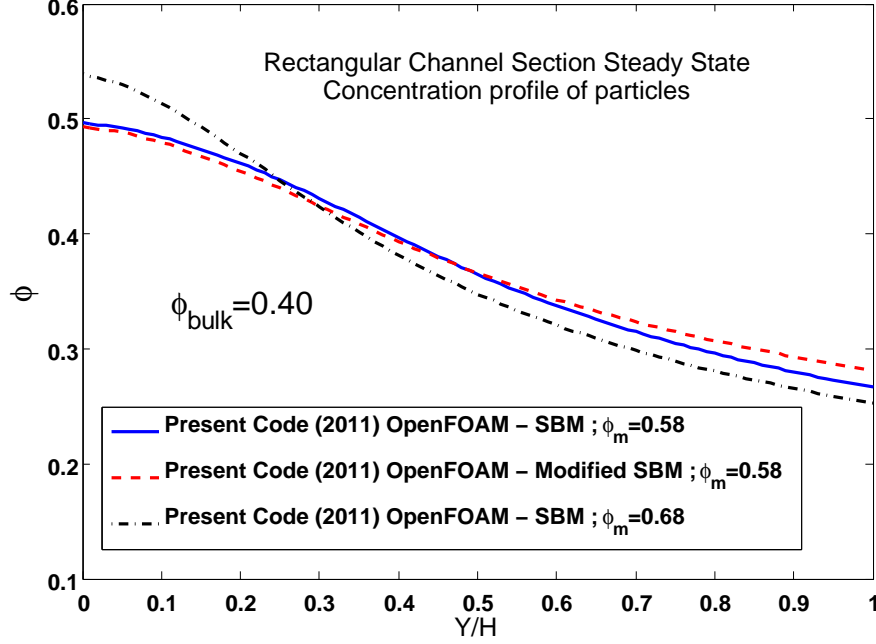


Figure 5.7: Steady State Concentration Profiles of 40% initial suspension

One observes clearly, that ϕ_m plays an important role in the predictions of the concentration profiles at steady state. Thus, the particle concentration profiles depend more on the value of ϕ_m than on the form of the particle stress tensor Σ^p . In other words, it is necessary to know the material functions including the particle stress tensor to explain or predict the shear induced particles migration.

5.6 CLOSURE

In this chapter (5), we have presented the “Modified SBM” , as an update to the original SBM. The modifications were done according to experimental measurements we obtained for the particle stress tensor used inside the model. The modified version “The Modified SBM” is implemented in [OpenFOAM®]. Since the SBM depends on the suspension material functions, it would be of interest to perform, in

5.6. CLOSURE

the near future, direct migration experiments on a suspension whose all material functions had already been determined. Moreover, it is necessary to carry out further experiments on the measurements of the particle normal stresses to verify the validity of the expressions obtained for η_N , η_s , λ_2 , and λ_3 in the zone where $\phi < 0.20$ and $\phi > 0.47$. In the next chapter (6) we will present and discuss the extended version of this model here “The modified SBM”, into a 2D general version which is “Frame-Invariant” that can account for the general 2D flow of non-Brownian suspensions.

Chapter 6

ADVANCED SUSPENSION MODELING

6.1 OVERVIEW

This chapter (6) covers the advanced suspension modeling techniques that exist in literature. In section (6.2) we give and discuss the extension of the “Modified SBM” of chapter (5) into a new version which is “Frame-Invariant” that considers the suspension local kinematics and which accounts for the 2D general flows of non-Brownian monodispersed suspensions. Section (6.3) reveals how can one update the SBM to account for Buoyancy problems.

6.2 THE 2D FRAME-INVARIANT MODIFIED Suspension Balance Model

6.2.1 Introduction

We have seen in the previous chapters of the thesis, the original and the modified versions of the **SBM**, and their validation through the implementation in the

6.2. THE 2D FRAME-INVARIANT MODIFIED SUSPENSION BALANCE MODEL

[OpenFOAM®] environment. The previous model until now was just limited to the cases of simple shear flows of non-Brownian suspensions, and if one wants to use it in the general case of a flow that is not necessarily a simple shear one, it requires modifications.

So, here we will describe the process of developing a Frame-invariant version of our “modified **SBM**” that we have seen previously in chapter (5).

We will present here, the framework for suspension flow modeling in general geometries, where two-dimensional (2D) flows are considered. The work done here follows the previous efforts of [Miller and Morris 2009] where we re-extend the “modified **SBM**” by formulating its frame-invariant form.

It is known that in a general flow field, the local kinematics can vary between pure extension and solid-body rotation, with simple shear representing an equal balance between them. Due to that fact, it is essential to relate the particle stress Σ^p to the local kinematics of the flow since, as it was previously shown by [Brady and Morris 1997, Morris and Katyal 2002], that the existence of shear-induced normal stresses in suspensions was going back to the breaking of fore-aft symmetry of the pair-particle microstructure, and since that the particle stress Σ^p drives the particle phase migration.

Basically, an anisotropic particle normal stress $\Sigma_{nn,3}^p$ will be represented here using the local kinematics for the development of the framework in general flows of suspensions in 2D situations.

6.2.2 Frame-Invariant Suspension Kinematics

The suspension flow kinematics represent the local motion or behavior that a micro-zone (micro-structure-zone) of the suspension (fluid-particles) may undergo. It is the zone where the particles inside the fluid may be going away from each other, approaching each other, colliding, or even rolling over each other aligning in a preferred position by the flow between both the compression, and the tension axes as schematically depicted in Figure (6.1).

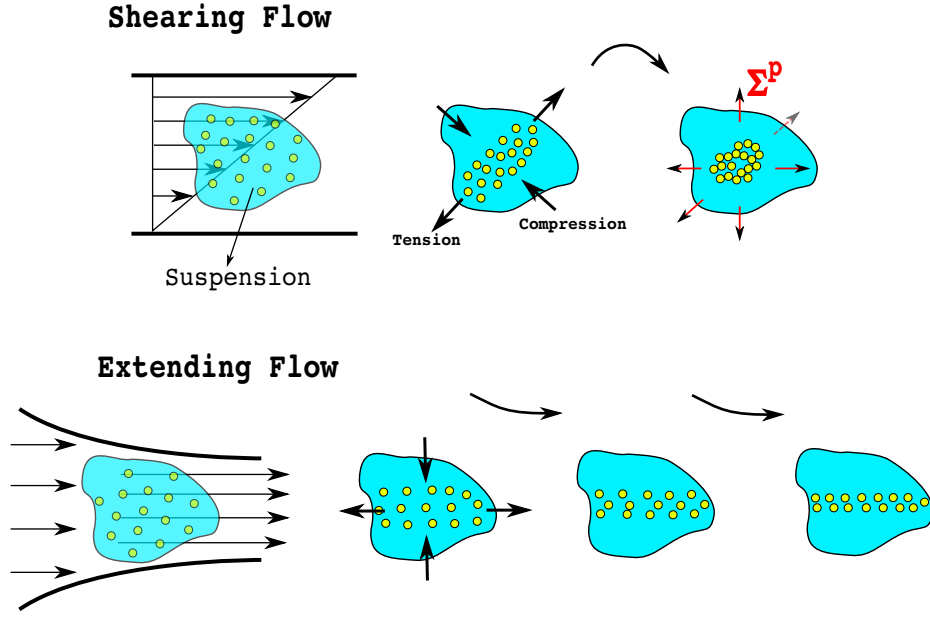


Figure 6.1: Suspension flow between shearing and extending

We represent this local kinematics between shearing and extending suspension flows, in the spirit of the previous works of [Miller and Morris 2009] for suspensions, and whom their work was based on that of [Schunk and Scriven 1990, Bird et al. 1987] for polymers.

6.2.2.1 Kinematic Ratio

The local kinematics of the suspension is characterized by:

1. The local material deformation rate defined as:

$$\dot{\gamma} = \sqrt{2\mathbf{E} : \mathbf{E}} \quad (6.1)$$

where \mathbf{E} is the rate of strain tensor.

2. The relative rotation $\boldsymbol{\omega}_{rel}$ defined as:

$$\boldsymbol{\omega}_{rel} = \frac{\boldsymbol{\omega}}{2} - \mathbf{W} \quad (6.2)$$

where $\boldsymbol{\omega}$ is the local vorticity given by the curl of the velocity \mathbf{U} :

6.2. THE 2D FRAME-INVARIANT MODIFIED SUSPENSION BALANCE MODEL

$$\boldsymbol{\omega} = \nabla \times \mathbf{U} \quad (6.3)$$

\mathbf{W} is the local rotation of the axes of the rate of strain given by:

$$\mathbf{W} = \mathbf{e}_i \times \left[\frac{\partial \mathbf{e}_i}{\partial t} + \mathbf{U} \cdot \nabla \mathbf{e}_i \right] \quad (6.4)$$

with \mathbf{e}_i being an eigenVector corresponding to an eigenValue Λ_i of \mathbf{E} satisfying the following equation

$$(\mathbf{E} - \Lambda_i) \cdot \mathbf{e}_i = \mathbf{0} \quad (6.5)$$

"This representation of $\boldsymbol{\omega}_{rel}$ in equation (6.2) sets the rotation relative to a stationary rate of strain and since each rotation quantity ($\boldsymbol{\omega}/2$, \mathbf{W}) is calculated in the same Cartesian frame of reference, taking the difference produces a frame invariant measure of rotation [Miller 2004]". **Note** that in our work the term $\frac{\partial \mathbf{e}_i}{\partial t}$ of equation (6.4) is neglected since we are interested in a quasi-stationary flow.

In order to account for the two effects of local kinematics, ($\dot{\gamma}$ & $\boldsymbol{\omega}_{rel}$), we follow [Ryssel and Brunn 1999] to introduce the following ratio known as the "kinematic ratio $\hat{\rho}_k$ " defined as:

$$\hat{\rho}_k = \frac{2|\boldsymbol{\omega}_{rel}|}{(\dot{\gamma}/2) + |\boldsymbol{\omega}_{rel}|} \quad (6.6)$$

$\hat{\rho}_k$ varies between 0 and 2 according to the flow local kinematic state. In pure extension $\hat{\rho}_k = 0$ ($|\boldsymbol{\omega}_{rel}| = 0$), in simple shear $\hat{\rho}_k = 1$ ($|\boldsymbol{\omega}_{rel}| = \frac{\dot{\gamma}}{2}$), and in solid body rotation $\hat{\rho}_k = 2$ ($\dot{\gamma} = 0$).

6.2.2.2 Compression-Tension Coordinates and Transition Matrix

In the 2D situation, the \mathbf{e}_i vectors are defined as the principal axes of the rate of strain tensor, where the subscript $i = "t"$ stands for the **t**ension axis corresponding to the positive eigenValue of $\Lambda_{i=t} > 0$, and $i = "c"$ for the

6.2. THE 2D FRAME-INVARIANT MODIFIED SUSPENSION BALANCE MODEL

compression axis corresponding to the negative eigenValue of $\Lambda_{i=c} < 0$ as you can see in the following Figure (6.2).

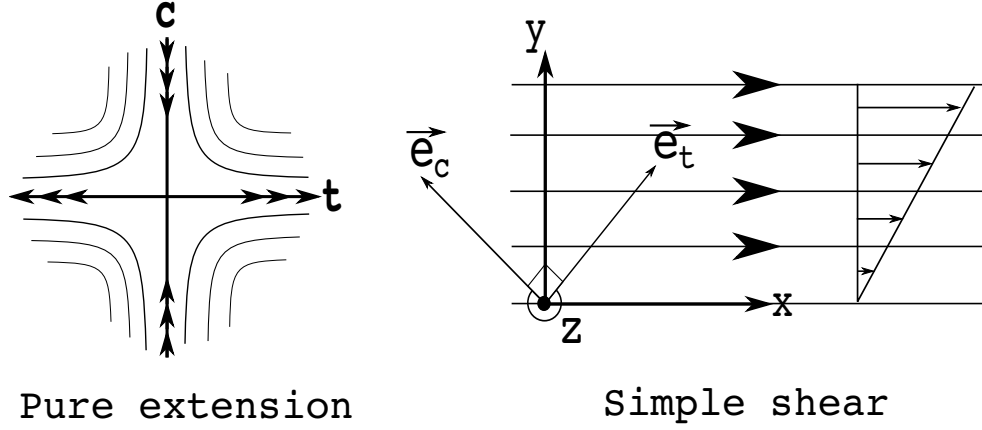


Figure 6.2: compression-tension axes

So, now the 2D transformation that can transport one from the general cartesian system $(\vec{e}_x, \vec{e}_y, \vec{e}_z)$ to the local frame of reference $(\vec{e}_t, \vec{e}_c, \vec{e}_z)$ can be defined as the 2D transition Matrix \mathbf{T}_m :

$$\mathbf{T}_m = \left[\vec{e}_t \begin{pmatrix} e_{t1} \\ e_{t2} \\ 0 \end{pmatrix} \mid \vec{e}_c \begin{pmatrix} e_{c1} \\ e_{c2} \\ 0 \end{pmatrix} \mid \vec{e}_z \begin{pmatrix} 0 \\ 0 \\ 1 \end{pmatrix} \right] \quad (6.7)$$

where its inverse matrix $(\mathbf{T}_m)^{-1}$ (equal to its transpose $(\mathbf{T}_m)^T$ due to the symmetry of \mathbf{E}) transports one from $(\vec{e}_x, \vec{e}_y, \vec{e}_z)$ to $(\vec{e}_t, \vec{e}_c, \vec{e}_z)$.

6.2.3 Anisotropic Particle Stress in the SBM

The $\Sigma_{nn,2}^p$ tensor of modified Suspension Balance Model of chapter (5) valid for simple shear flows only, is set up in the 2D compression-tension coordinates $(\vec{e}_t, \vec{e}_c, \vec{e}_z)$ (6.2.2.2), and extended to a new tensor $\Sigma_{nn,3}^p$ which is valid for general flow types that are defined by $\hat{\rho}_k$. This extension provides a frame of reference independent of the 2D geometry of the flow, but strongly depends on the local kinematic state of the flow of the suspension. The extension of $\Sigma_{nn,2}^p$

6.2. THE 2D FRAME-INVARIANT MODIFIED SUSPENSION BALANCE MODEL

to $\Sigma_{nn,3}^p$ is as the following:

$$\Sigma_{nn,2}^p = \begin{bmatrix} \Sigma_{nn,2}^{p,11} & 0 & 0 \\ 0 & \Sigma_{nn,2}^{p,22} & 0 \\ 0 & 0 & \Sigma_{nn,2}^{p,33} \end{bmatrix} = \eta_0 \eta_N(\phi) \dot{\gamma} \begin{bmatrix} 1 & 0 & 0 \\ 0 & \lambda_2(\phi) & 0 \\ 0 & 0 & \lambda_3(\phi) \end{bmatrix} \quad (6.8)$$

$$\Sigma_{nn,2}^p = \begin{bmatrix} \left(\frac{\Sigma_{nn,2}^{p,11} + \Sigma_{nn,2}^{p,22}}{2} \right) & \frac{N_1}{2} & 0 \\ \frac{N_1}{2} & \left(\frac{\Sigma_{nn,2}^{p,11} + \Sigma_{nn,2}^{p,22}}{2} \right) & 0 \\ 0 & 0 & \Sigma_{nn,2}^{p,33} \end{bmatrix} \quad (6.9)$$

$$\Sigma_{nn,3}^p = \begin{bmatrix} \left(\frac{\Sigma_{nn,2}^{p,11} + \Sigma_{nn,2}^{p,22}}{2} \right) \cdot B_t(\hat{\rho}_k) & \frac{N_1}{2} \cdot C(\hat{\rho}_k) & 0 \\ \frac{N_1}{2} \cdot C(\hat{\rho}_k) & \left(\frac{\Sigma_{nn,2}^{p,11} + \Sigma_{nn,2}^{p,22}}{2} \right) \cdot B_c(\hat{\rho}_k) & 0 \\ 0 & 0 & \Sigma_{nn,2}^{p,33} \end{bmatrix} \quad (6.10)$$

$\Sigma_{nn,3}^p$ constitutes the modified particle normal stress anisotropic tensor.

$B_t(\hat{\rho}_k)$, and $B_c(\hat{\rho}_k)$ are the functions that weight the particle normal stress in the tension, and compression directions respectively, with $\Sigma_{nn,2}^{p,33}$ being the one in the out-of-plane direction. $C(\hat{\rho}_k)$ corresponds to the tangential stress weighting function. We take the same weighting functions as [Miller and Morris 2009] where the different possible cases of B_t , B_c , and C are presented in the following Figure (6.3). We can try to provide some explanation about the choice of the values of B_t , B_c , and C and their variation with $\hat{\rho}_k$.

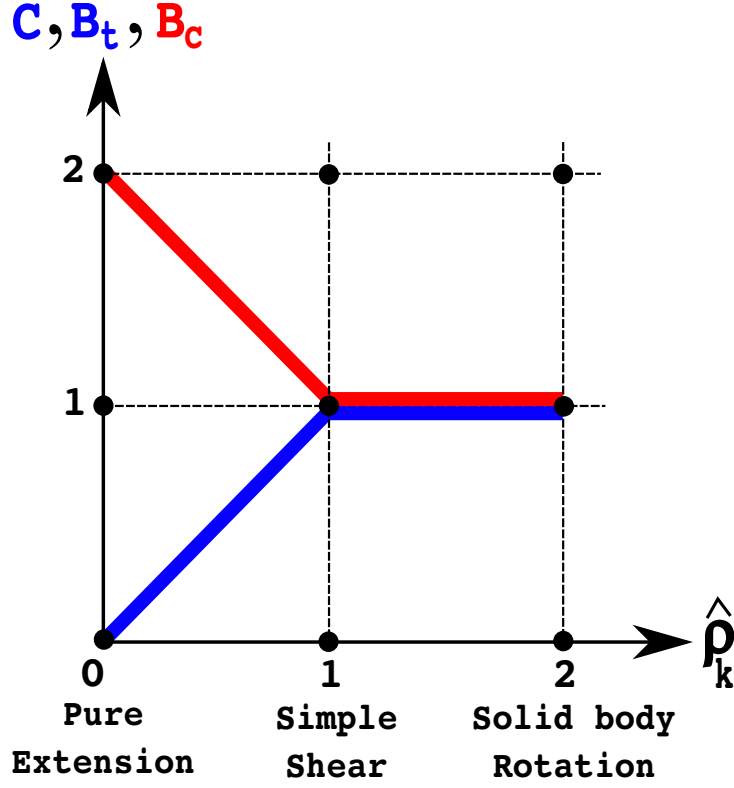


Figure 6.3: B_t , B_c , and C as function of $\hat{\rho}_k$

- **Simple shear flow:** In a **simple shear** situation, $\hat{\rho}_k = 1$ and we have $B_t = B_c = C = 1$ such that the tensor $\Sigma_{nn,3}^p$ after transformation in equation (6.11) goes back to be equal to $\Sigma_{nn,2}^p$.
- **Pure extension:** Taking $B_t = 0$ is quite natural since, during a **pure extension** (Figure (6.2)), along the extensional axis, the particles are far away from each other and the normal stress in that direction should be almost zero. Of course C that represents the tangential stress is also to be zero.
- **Rotation:** When $\hat{\rho}_k > 1$ we suppose that the rotation plays no role where we take unity for $B_t = B_c = C = 1$.
- At last, when $0 < \hat{\rho}_k < 1$ we interpolate linearly the “weighting” functions B_t , B_c , and C to account for the local kinematics between the compression

6.2. THE 2D FRAME-INVARIANT MODIFIED SUSPENSION BALANCE MODEL

and tension axes.

Note that, the tensor $\Sigma_{nn,3}^p$ is retransformed back from the local axes to the general ones through the transformation matrix \mathbf{T}_m such that:

$$\Sigma_{nn,3}^p \leftarrow \left(\mathbf{T}_m \cdot \Sigma_{nn,3}^p \cdot \mathbf{T}_m^{-1} \right) \quad (6.11)$$

$\angle(\vec{e}_x, \vec{e}_y, \vec{e}_z)$ $\angle(\vec{e}_t, \vec{e}_c, \vec{e}_z)$

6.2.4 Validation

The last General “Frame-Invariant” 2D **SBM** was also implemented in the [OpenFOAM®] with its new equation for Σ^p including the tensor $\Sigma_{nn,3}^p$. The results using this general extended version (Frame-Invariant) for the suspension flow in both, a wide gap Couette cell of [Phillips et al. 1992], and in a rectangular-cross-section channel of [Lyon and Leal I 1998], were compared to the previous version of the **SBM** (Frame-dependent).

Note that, nevertheless the flow of the suspensions in such geometries is a simple shear flow, we intend to do these comparisons. That’s in order to validate our new code for the transformation of Σ^p (see equation (6.11)) between the local and the general frame references, $(\vec{e}_t, \vec{e}_c, \vec{e}_z)$ and $(\vec{e}_x, \vec{e}_y, \vec{e}_z)$, respectively.

6.2.4.1 2D Frame-Invariant Suspension Flow in a Channel and in a Couette cell

As you can see in Figures (6.4) & (6.5) for the suspension flow in a channel, and Figures (6.6) & (6.7) for the flow of a suspension in a Couette cell of large gap, the last 2D “Frame-invariant **SBM**” captures well the concentration profiles of particles that had been computed using the “Frame-dependent” one.

6.2. THE 2D FRAME-INVARIANT MODIFIED SUSPENSION BALANCE MODEL

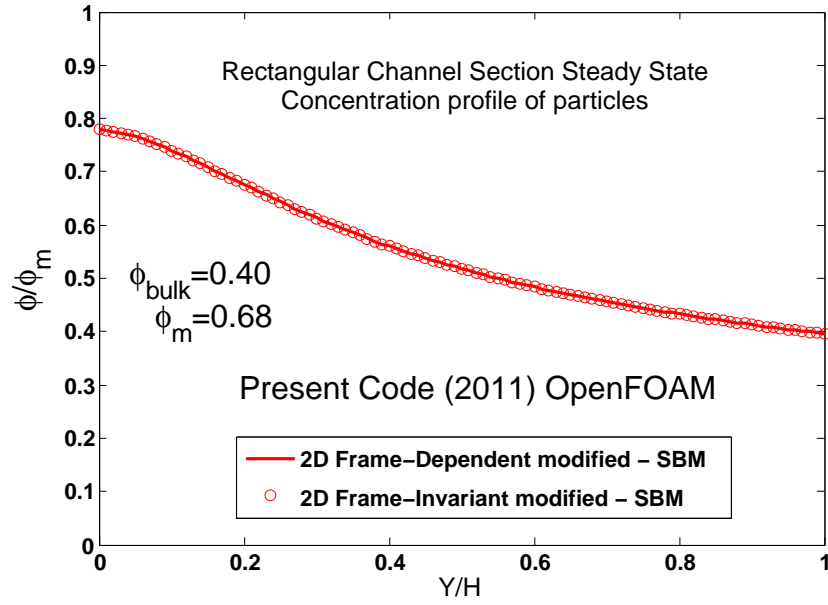


Figure 6.4: Steady State Concentration Profiles of 40% initial suspension

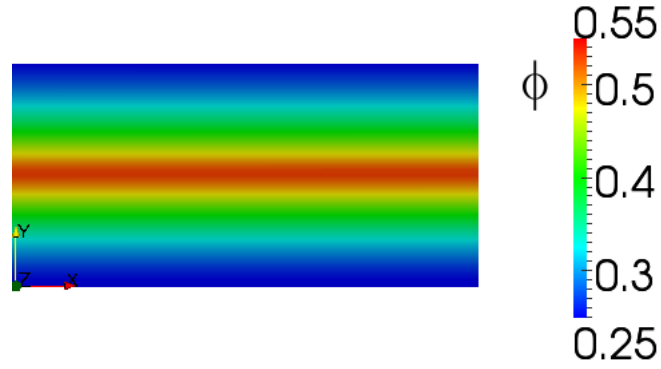


Figure 6.5: The “Frame-Invariant” **SBM** 2D Steady State ϕ

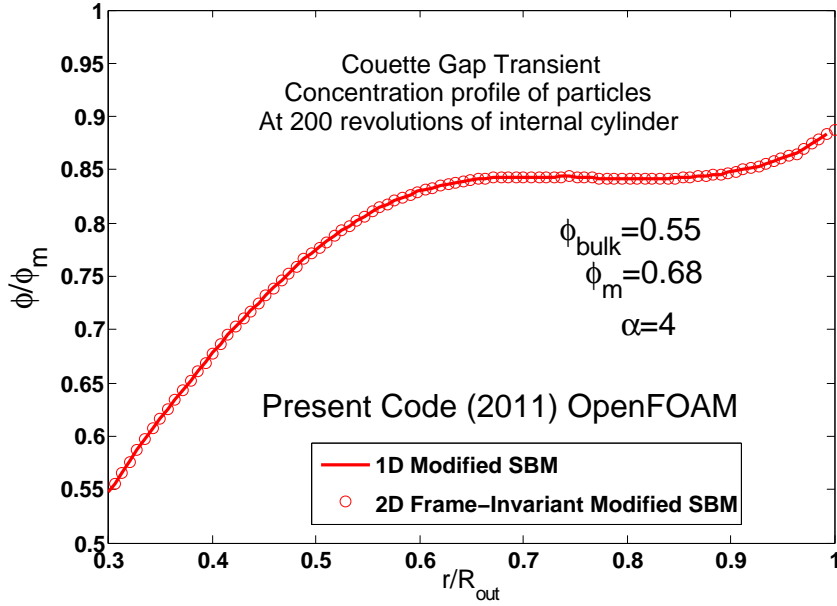


Figure 6.6: Transient Concentration Profiles of 55% initial suspension

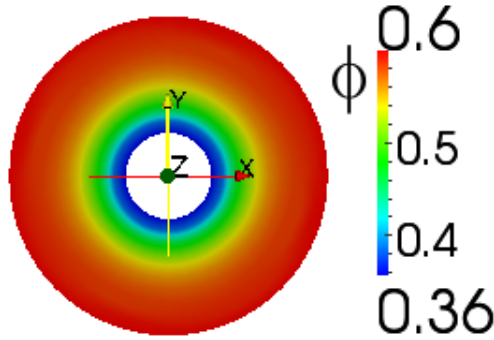


Figure 6.7: The “Frame-Invariant” SBM 2D concentration at 200 revolutions

6.2.4.2 Oscillating shear of a suspension cloud

In this section, we apply our last 2D general code of the **SBM** to an experimental configuration used by [Metzger et al. 2011] to observe the behavior of a suspension cloud in an oscillatory high amplitude shear strain.

The clouds were composed of spherical PMMA particles ($2a = 450 \mu m$) dispersed in a newtonian liquid of viscosity $\eta_0 = 3 Pa \cdot s$. The particle concentration in the cloud is either 30% or 40%. The suspension droplet is placed, far away

6.2. THE 2D FRAME-INVARIANT MODIFIED SUSPENSION BALANCE MODEL

from the walls, in a shear cell filled with the same suspending liquid (see Figure (6.8)).

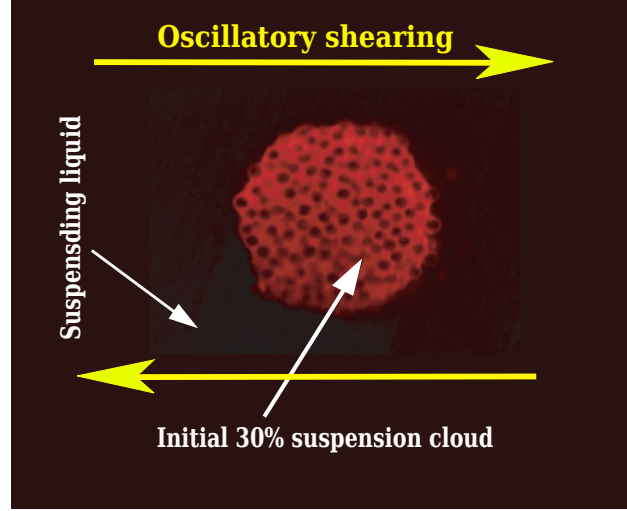


Figure 6.8: Experimental [Metzger et al. 2011] initial 30% suspension cloud in an oscillatory shearing between two parallel plates.

Upon reversal of the shear flow, [Metzger et al. 2011] showed that the cloud does not reconstitute identically by the end of each cycle of shear, but expands progressively in the flow direction. They show that the strength of the extension E depends mainly on the applied strain amplitude γ_0 and the number of cycles N (see Figure (6.9)). **Note** that one cycle of shear corresponds to a whole deformation that is two times the strain amplitude.

6.2. THE 2D FRAME-INVARIANT MODIFIED SUSPENSION BALANCE MODEL

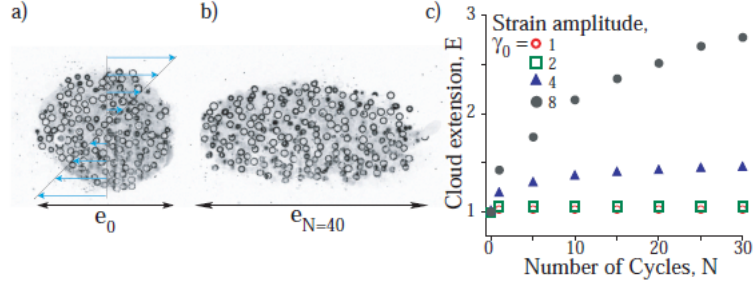


FIG. 2. Evolution of clouds composed of particles with $d = 450 \mu\text{m}$ at an initial volume fraction 30%. Images were taken a) initially and b) after 40 cycles at a strain amplitude of $\gamma_0 = 6$. c) Evolution of the cloud extension, $E(N) = e_N/e_0$, in the flow direction.

Figure 6.9: Taken From [Metzger et al. 2011]

The xy-2D mesh of 30% suspension cloud case is presented in the following Figure (6.10):

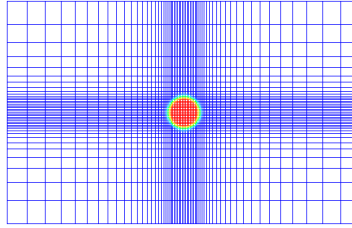


Figure 6.10: 2D-Mesh of the 30% suspension cloud

During $N = 30$ cycles of shear at an amplitude of $\gamma_0 = 8$, the numerical evolution of the cloud extension $E(N)$ in the flow direction (x-axis) was measured and compared to the experimental one obtained by [Metzger et al. 2011].

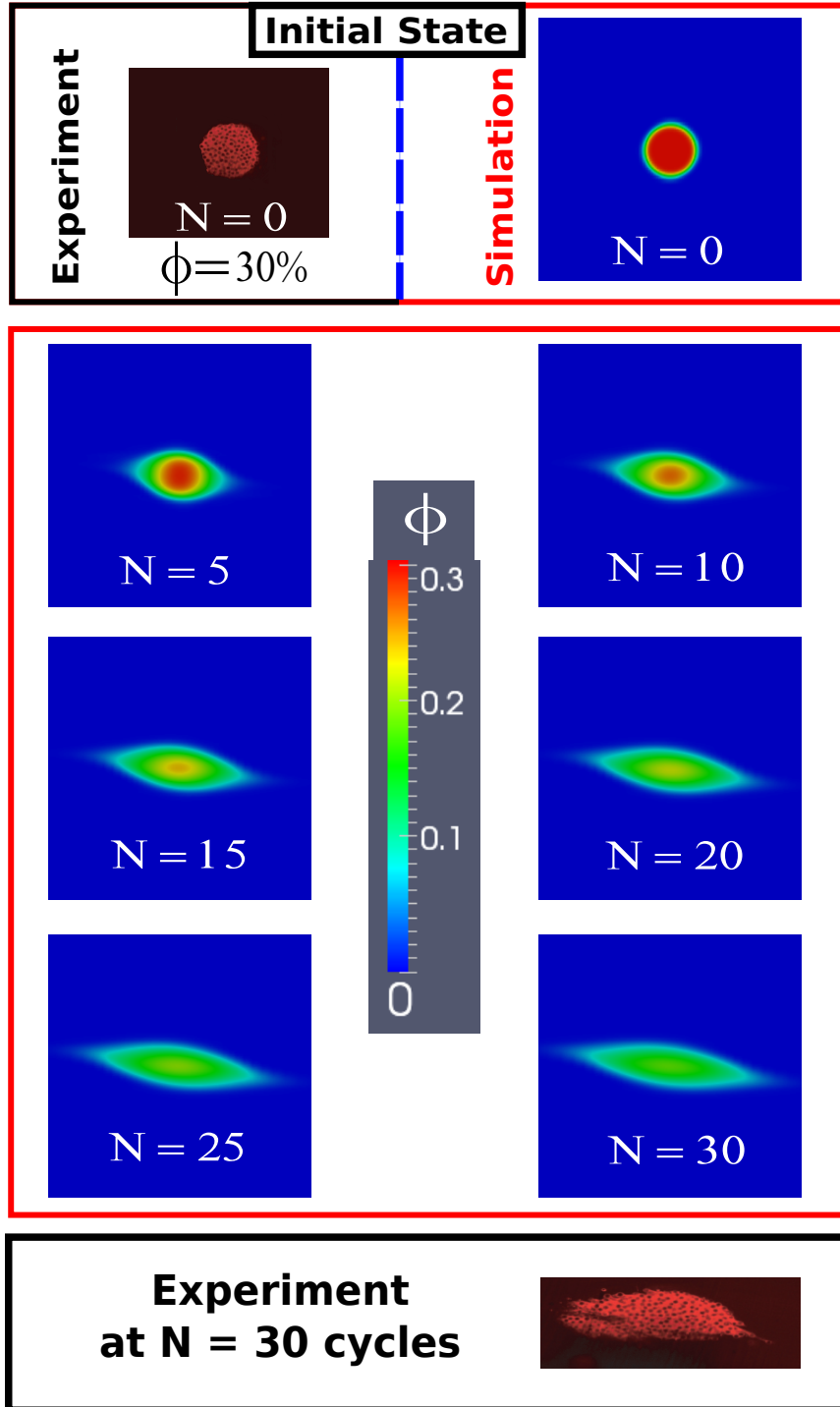


Figure 6.11: 30% suspension cloud extension in the flow direction at a strain amplitude $\gamma_0 = 8$.

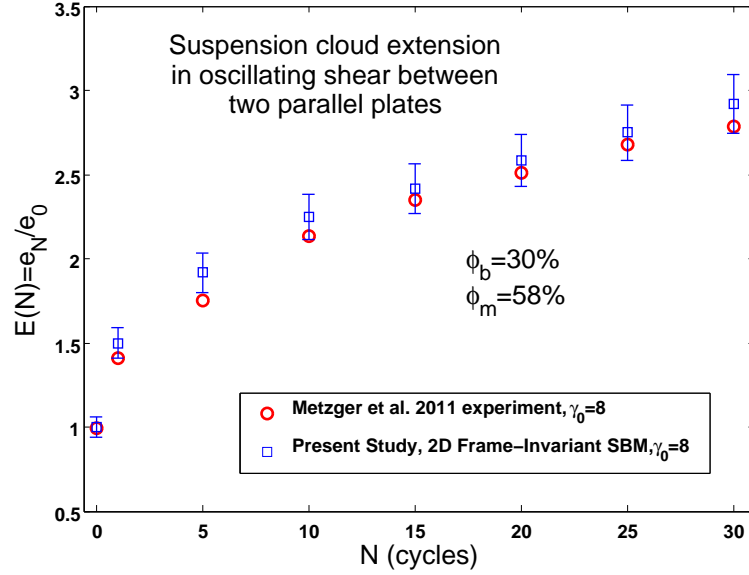


Figure 6.12: 30% suspension cloud extension in the flow direction

Figures (6.11) & (6.12) show that the simulation gives the same type of behavior with a good agreement between the experimental data and the numerical ones obtained by using the 2D “Frame-invariant” **SBM**.

Nevertheless, the comparison can be only qualitative since the numerical calculations have been done in a 2D case while the experiments are of course 3D. Furthermore, we know from [Kolli et al. 2002, Narumi et al. 2002] that upon shear reversal, the normal stresses exhibit a transient behavior over a deformation of about unity. This transient behavior had never been introduced in the **SBM** and thus the calculations are valid only for high strain amplitudes where the transient behaviors upon shear reversal could be neglected.

6.3 THE SBM EXTENDED TO BUOYANCY

All the previous contents of the thesis covered the RheoPhysics of “**neutrally buoyant Suspensions**” only. What happens now, if the suspensions are no more neutrally buoyant?

Another more properties happen in these “dense” suspensions of “unmatched

6.3. THE SBM EXTENDED TO BUOYANCY

particles-fluid densities” ($\rho_p \neq \rho_f$) like sedimentation, and viscous resuspension. The latter is when a fluid flows past an initially settled bed of heavy particles, to disturb and resuspend the sediment layer. It was first reported by [Gadala-Maria 1979] and investigated well experimentally and numerically later by [Leighton and Acrivos 1986, Leighton and Acrivos 1987, Schaffinger et al. 1990, Rao et al. 2002 b]. To account for that phenomenon which is the true general case in nature where many suspensions are dense, buoyancy should be included in our previous **SBM**.

So here we will repass over the three basic governing equations of the **SBM** which are the mass, Stokes momentum and transport conservation equations in a manner of trying to update them to account for unmatched particles-fluid densities in the non-Brownian suspensions of hard spheres.

Let ρ_p^i and ρ_f^i be the densities of the particle and fluid phases, respectively. According to the total suspension mixture concentration ϕ , and the mixture density ρ as a whole, one can write the following:

$$\rho = \phi \rho_p^i + (1 - \phi) \rho_f^i \quad (6.12)$$

with

$$\rho_p = \phi \rho_p^i \quad (6.13)$$

$$\rho_f = (1 - \phi) \rho_f^i \quad (6.14)$$

where ρ_p and ρ_f are the mass fraction concentrations of the particles and of the fluid, respectively.

The suspension mass and momentum balances become:

$$\nabla \bullet \mathbf{U} = 0 \quad (6.15)$$

$$\nabla \bullet \Sigma + \Delta \rho^i \mathbf{g} \phi = \mathbf{0} \quad (6.16)$$

respectively, where $\Delta \rho^i = \rho_p^i - \rho_f^i$ is difference in pure densities, \mathbf{U} is the suspension mean velocity, \mathbf{g} is the gravitational acceleration, and Σ is the suspension stress tensor as it was defined in the previous chapters of the thesis.

The transport equation of the particles phase in the mixture becomes as following:

$$\frac{\partial \phi}{\partial t} + \mathbf{U} \cdot \nabla \phi = -\nabla \bullet \vec{j}_t \quad \text{with} \quad \vec{j}_t = \vec{j}_\perp + \vec{j}_\mathbf{g} \quad (6.17)$$

where \vec{j}_\perp is the migration flux defined previously in section (1.7.4) as:

$$\vec{j}_\perp = \frac{2a^2}{9\eta_0} f(\phi) [\nabla \bullet \Sigma^p] \quad (6.18)$$

and $\vec{j}_\mathbf{g}$ is the defined as:

$$\vec{j}_\mathbf{g} = \frac{2a^2}{9\eta_0} f(\phi) [\Delta \rho^i \mathbf{g} \phi] \quad (6.19)$$

In this form the **SBM** is extended to a new version which accounts for buoyancy, that is also implemented in the [OpenFOAM®] environment.

6.3.1 Validation

6.3.1.1 Viscous resuspension and 2D mixing

We present here the recent validation results of the modified-to-buoyancy 2D code of the **SBM**. That's through the simulation of 2D resuspension and mixing in a horizontal Couette cell which goes back to the works of [Rao et al. 2002 b]. In their experiment, [Rao et al. 2002 b] used PMMA particles ($a = 397 \mu m$) of density $\rho_p^i = 1.18 g \cdot cm^{-3}$, suspended in a newtonian liquid (glycerol/water solution) of density $\rho_f^i = 1.253 g \cdot cm^{-3}$ and of viscosity $\eta_0 = 0.588 Pa \cdot s$. They used the **NMR** imaging to measure the concentration profile during the demixing

6.3. THE SBM EXTENDED TO BUOYANCY

of an initially 20% well-mixed suspension. The suspension was placed between two concentric horizontal cylinders (wide-gap Couette cell $R_i = 0.64\text{ cm}$ $R_{out} = 2.54\text{ cm}$) where the gravity, before rotating the inner cylinder, acted on the suspension causing the particles to float toward the upper surface of the larger cylinder. Then, the suspension is sheared in the Couette cell by rotating the inner cylinder where the concentration profiles were measured through **NMR**. The xy-2D mesh of this case is presented in the following Figure (6.13).

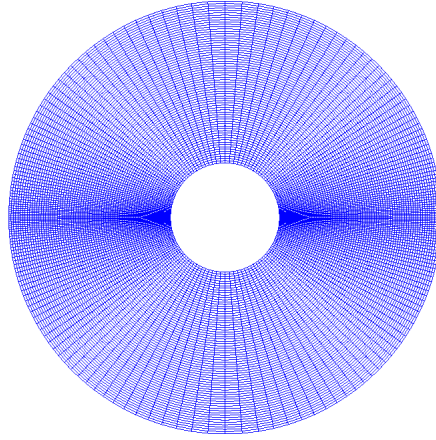


Figure 6.13: xy-2D mesh of the wide-gap Couette cell

The initial conditions on ϕ before the rotation of the inner cylinder are presented in Figure (6.14).

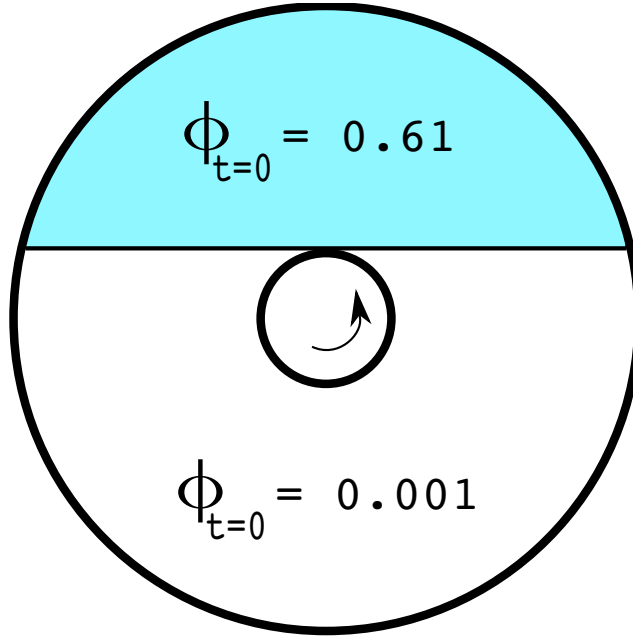


Figure 6.14: Initial conditions on ϕ at $t = 0$

The transient concentration profiles results (after 45 turns of the internal cylinder) of the numerical simulations using the 2D frame-invariant-buoyancy-included **SBM** are compared with those obtained by [\[Rao et al. 2002 b\]](#) as you can see in Figure [\(6.15\)](#).

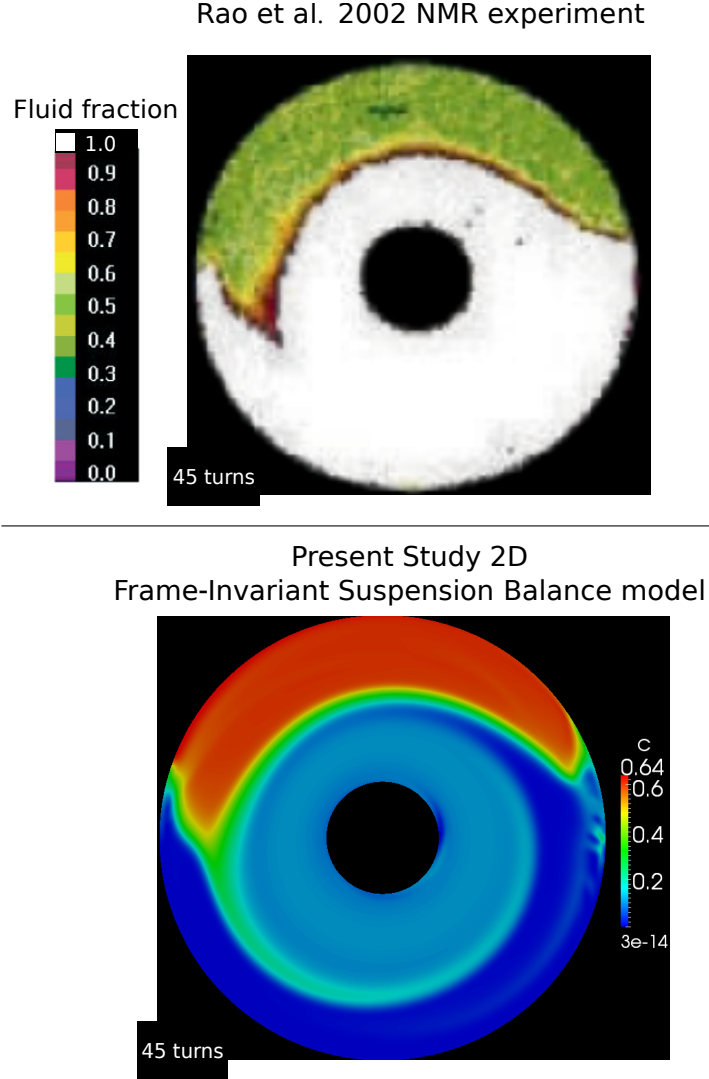


Figure 6.15: Concentration profile at 45 turns of the inner cylinder ($\phi \equiv c$), $\phi_m = 0.64$.

The predictions of the model are quantitatively good compared to the **NMR** experimental data obtained by [Rao et al. 2002 b].

Thus, the “Frame-Invariant” **SBM** implemented in [OpenFOAM®] seems to capture well the physical features involved in the shear-induced particle migration even in quite complex geometries. Nevertheless, the normal stresses are known to be very sensitive to the shear-induced microstructure in the suspension [Brady and Morris 1997] that itself depends on the flow. An improvement

in the model proposed by [Miller and Morris 2009] would consist in introducing this coupling between the flow and the microstructure.

6.4 CLOSURE

We have seen here in this chapter (6) an extended 2D version of the SBM which is general “Frame-Invariant” and that takes into account the local kinematics of the suspension. The new version was validated after the implementation in [OpenFOAM®] by simulating the 2D flow of neutrally buoyant monodispersed non-Brownian suspensions in both geometries, a wide-gap Couette cell, and a rectangular-cross-section channel. The simulation of a suspension cloud undergoing an alternative shear gives results that are very close to the recent experimental results of [Metzger et al. 2011]. Moreover, the possibility of the SBM to account for Buoyancy problems, where unmatched particles-fluid densities may be present, was also presented including the governing equations and has been validated for the suspension mixing in a horizontal wide-gap Couette cell.

Chapter 7

SUMMARY, CONCLUSIONS & PERSPECTIVES

7.1 SUMMARY AND CONCLUSIONS

This thesis covers the RheoPhysics (Experiments and Simulations) of Non-brownian Suspensions of particles immersed in a Newtonian Liquid at very low Reynolds Number. It is composed of two main topics.

The first branch covers the Mathematical Modeling of the kinematics of these suspensions as a continuum modeling approach and by using the Finite Volume Method as the numerical technique to solve the problem.

The second branch is the experimental part for the measurements of the suspension Material functions (the viscosity η_s and the first and second Normal Stress Differences N_1 and N_2) and of the particle stress tensor Σ^p .

The central point in this thesis is the phenomenon of shear-induced migration of particles and its predictions upon using the Suspension Balance Model (**SBM**). Thus, according to the need for the different measurable variables in this Model, experiments were developed in order to measure well those variables, which can complete and modify the **SBM** to be capable of predicting

7.1. SUMMARY AND CONCLUSIONS

well the suspension Kinematics.

Finally, after the completeness of the Model with all of its measurable variables being measured, it was implemented numerically and validated in the [OpenFOAM®] environment for the tracking process of the Kinematics of these suspensions.

A **detailed summary** of this thesis can be achieved now by grouping all the closures of the chapters as the following:

- We have seen in the first chapter (1) an introduction to Rheology Science since its inception in 1929. Suspensions were classified, and their Rheophysics were presented, in addition to the shear-induced migration of particles. After the presentation of the different Models in literature that modelize the migration phenomenon, we adopted the **SBM** of [Nott and Brady 1994, Morris and Boulay 1999].
- The conservative Finite Volume Method for incompressible flows had been described globally in chapter (2) in a simplified clear manner. However, an extension of this method for compressible flows can be found in literature well explained by [Moukalled and Darwish 2009].
- In chapter (3), we explained the implementation of the original Suspension Balance Model (as it was presented previously in Literature by [Nott and Brady 1994, Morris and Boulay 1999]) in the [OpenFOAM®] environment, and its validity for suspension flows inside channels of two different cross-sectional areas, and for suspension flows inside Couette cell geometry.
- The fourth chapter (4) is the heart of this manuscript. Using a single experiment, this chapter has proposed a determination methodology of the three material functions (the viscosity, and the two normal stress differences) in non-brownian suspensions of hard spheres for a wide zone of concentrations $\phi = 0.2 \leftrightarrow 0.46$. The measurement of the radial profile of Σ_{22} in a torsional flow between two parallel disks, provides us with the two

7.1. SUMMARY AND CONCLUSIONS

linear combinations of α_1 and α_2 : The slope of Σ_{22} gives $-(\alpha_1 + 2\alpha_2)$, and the ordinate at the origin returns $(\alpha_1 + \alpha_2)$. Simultaneously, we measure the viscosity of the suspension. It is so well surprising, we measure a positive N_1 . For that reason, we did a chain of tests to show that the sign of N_1 does not depend neither on the particles size, nor on the gap size between the two disks. The behavior of $[(\alpha_1 + 2\alpha_2)/\eta_s]$ as a function of the volume fraction of particles ϕ is very close to that measured recently by [Boyer et al. 2011 a] in a rotating rod experiment. When ϕ is less than 0.47, α_1/η_s and α_2/η_s seemed to vary linearly with the volume fraction with threshold of orders 0.25 for α_1/η_s , and 0.2 for α_2/η_s .

The pore pressure measurements permit us to have an access to the values of the particle normal stress in the direction of velocity-gradient ($\Sigma_{22}^p = \Sigma_{22} + P_f$), and to deduce from Σ_{22}^p , α_1 and α_2 the two other particle normal stresses Σ_{11}^p and Σ_{33}^p . The particle normal stresses are of the same order of magnitude of N_2 . Generally, our obtained results for the particle normal stresses are in good agreements with those presented in the literature, which were obtained numerically [Sierou and Brady 2002, Yeo and Maxey 2010a], theoretically [Mills and Snabre 2009], and experimentally [Deboeuf 2008, Deboeuf et al. 2009, Zarraga et al. 2000]. We observe, as [Sierou and Brady 2002] showed numerically, that the three particle normal stresses (Σ_{11}^p , Σ_{22}^p , and Σ_{33}^p) do not vary exactly in the same manner with the variation of the volume fraction of particles ϕ . This is in a difference with the particle normal stresses used by [Morris and Boulay 1999] in the Suspension Balance Model that explains and predicts the shear-induced migration of particles. Nevertheless, the values of Σ_{11}^p , Σ_{22}^p and Σ_{33}^p that we have measured are not very different from that proposed by [Morris and Boulay 1999]. As they found, we obtain $\lambda_3 = \frac{\Sigma_{33}^p}{\Sigma_{11}^p} \approx 0.5$, and a quadratic variation of $q(\phi) = \frac{\eta_N(\phi)}{\eta_s(\phi)} = \frac{-\Sigma_{11}^p}{\Sigma_{12}^p}$ such that ($q(\phi) = 3.2\phi^2$) for us, and ($q(\phi) = 2.2\phi^2$) for them. At last, while they suppose that $\lambda_2 = \frac{\Sigma_{22}^p}{\Sigma_{11}^p}$ is independent of ϕ , we measured a slight increase of λ_2 when ϕ

7.1. SUMMARY AND CONCLUSIONS

increases from 0.2 ($\lambda_2 \approx 1$) to 0.46 ($\lambda_2 \approx 1.3$).

Above $\phi = 0.47$, we have not been able to measure neither the material functions (η_s , α_1 and α_2) nor the particle normal stresses (Σ_{11}^p , Σ_{22}^p , and Σ_{33}^p). In particular we have observed that the Σ_{22} profile deviated from its predicted expression. We suppose that for high ϕ , the flow between the disks is no more a simple shear flow in the central region. Further rheo-optics experiments should be performed to measure the velocity profile between the disks and to verify that a jammed zone is present.

At last we have studied the secondary flow that is present in the torsional between two parallel plates. It has been used to validate the pressure measurements. The secondary flow velocity has been measured both in a simple liquid and in a suspension, and its influence on the shear induced particles migration has been estimated.

- Chapter (5), has presented the “Modified **SBM**” , as an update to the original **SBM**. The modifications were done according to our last experimental measurements we obtained for the particle stress tensor Σ^p used inside the model. The updated version “The Modified **SBM**” is implemented also in [OpenFOAM®], where the simulation results are compared to those obtained previously upon using the model before its update.
- The final chapter (6) provides an extended 2D version of the SBM which is general “Frame-Invariant” and that takes into account the local kinematics of the suspension. The new version was validated after the implementation in [OpenFOAM®] by simulating the 2D flow of neutrally buoyant monodispersed non-Brownian suspensions in both geometries, a wide-gap Couette cell, and a rectangular-cross-section channel. The simulation of a suspension cloud undergoing an alternative shear gives results that are very close to the recent experimental results of [Metzger et al. 2011]. Moreover, the possibility of the **SBM** to account for Buoyancy problems, where unmatched particles-fluid densities may be present, was also pre-

sented including the governing equations and has been validated for the suspension mixing in a horizontal wide-gap Couette cell.

7.2 PERSPECTIVES

- **Experimentally:** Since the **SBM** depends on the suspension material functions, it would be of interest to perform in the near future, direct migration experiments on a suspension whose all material functions had already been determined. Moreover, it is necessary to carry out further experiments on the measurements of the particle normal stresses to verify the validity of the expressions obtained in chapter (4) for η_N , η_s , λ_2 , and λ_3 especially in the zones where $\phi < 0.20$ and $\phi > 0.47$.
- **Numerically:** It will be so interesting in the near future to continue the simulations to better test and validate the new 2D general “Frame-Invariant” **SBM** in more complex suspension flows, where the flow is no more a simple shear one. It will be also vital to study to what limit, the model can predict and quantify well the migration of particles in such flows.
- **Further Missions:** The **SBM** using the continuum modeling approach of non-brownian suspensions of hard spheres, can not capture the suspension relaxation effects that go back to the changes in suspension microstructure during the flow. These effects have been seen and proved well through different experimental evidences in the literature [Blanc et al. 2011]. Soon, it is possible or not, it will be quite interesting to include these effects of the suspension microstructure in the modeling of these suspensions.

APPENDICES

Appendix A

WEDGE TYPE MESH

A.1 Wedge type mesh description

The simulation domain is a cylindrical pipe with diameter D and length L . To reduce computational effort, mesh is created as 2D axi-symmetrical. Schematically the drawing of the mesh with very small angle α is shown on the Figure (A.1) in the "X", "Y", and "Z" - coordinates. Thus, only variations in the "X"-"Z" 2D plane are considered [openfoamwiki.net].

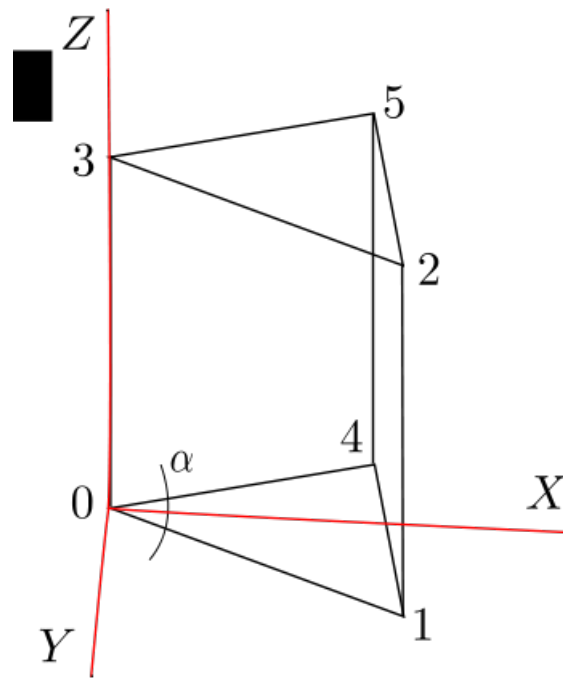


Figure A.1: **Wedge type Schematic**

Appendix B

NUMERICAL SCHEMES AND SOLUTION SOLVERS IN OpenFOAM®

B.1 Numerical Schemes & Solution Solvers

[[Numerical Schemes](#)] AND [[Solution Solvers](#)] IN OpenFOAM®

Printed from the website documentation of [[OpenFOAM®](#)] under the
3rd permission rule of:

Copyright © 2004-2011 OpenCFD Limited.

“This website and its content (including without limitation the text, computer code, artwork, photographs, images, music, audio material, video material and audio-visual material on this website) is owned by OpenCFD Limited.

Any redistribution or reproduction of part or all of the contents in any form is prohibited other than the following:

B.1. NUMERICAL SCHEMES & SOLUTION SOLVERS

1. you may view this website and the material on this website on a computer or mobile device via a web browser;
2. you may copy and store this website and the material on this website in your web browser cache memory;
3. **you may print pages from this website for your own use.**

You may not distribute or commercially exploit the content. Nor may you transmit it or store it in any other website or other form of electronic retrieval system. The automated and/or systematic collection of data from this website is prohibited”.

Appendix C

IN OpenFOAM®

C.1 The convection term (precisely in OpenFOAM®)

Concerning the flux term, the convection term (precisely in OpenFOAM®) is expressed as:

$$\sum_f \mathbf{U}_f (\mathbf{U} \cdot \mathbf{n})_f S_f = \sum_f \mathbf{U}_f \Phi_f \quad (\text{C.1})$$

where Φ is always the kinematic mass flux defined on each cell face, and \mathbf{U} must be interpolated onto the cell faces using different interpolation schemes. The convection based terms in the matrix \mathbf{A} are found by using the Upwind interpolation scheme for \mathbf{U} . In other words \mathbf{U} -values are adopted from the cell that is located on the Upwind side of the surface. If, anyway, some other interpolation scheme is used for \mathbf{U} , the terms that differ from the Upwind-scheme are included in **src**. The discretization practise of interpolating the velocity values onto the cell faces can be expressed ganerally as:

$$\mathbf{U}_{f,HS} = \mathbf{U}_{f,UW} - (\mathbf{U}_{f,HS} - \mathbf{U}_{f,UW}) = \mathbf{U}_{f,UW} - \mathbf{U}_{f,\Delta} \quad (\text{C.2})$$

with HS standing for “Higher order Scheme”, UW for “Upwind Scheme”, and Δ for the “difference between both”. In this general case the Upwind based

C.3. IMPLEMENTATION OF THE SIMPLE ALGORITHM IN OPENFOAM®

term multiplying $\mathbf{U}_{f,UW}$ is included in \mathbf{A} , and $\mathbf{U}_{f,\Delta}$ in \mathbf{src} along with the term multiplying it. The Upwind scheme fabricates an easily solvable matrix and is therefore used as the basic Scheme on which other schemes are built[Jasak 1996].

C.2 The flux term in OpenFOAM®

In reality, the flux Φ can be written in two different ways:

1. It can be the inner product of the velocity interpolated onto the cell surface with the cell surface vector, $(\mathbf{U}_f \cdot \mathbf{n}_f S_f)$, or
2. It can be an older corrected flux field such that $\Phi = (\mathbf{U}_f^* \cdot \mathbf{n}_f) S_f + \Phi_{corr}$,

where Φ_{corr} corrects the interpolated velocity based flux by comparing an older flux, Φ , and an older velocity interpolated onto the cell surface.

C.3 Implementation of the SIMPLE algorithm in OpenFOAM®

The SIMPLE algorithm can be implemented in OpenFOAM as follows (The complete implementation of the algorithm can be seen in the source code of the simpleFoam solver provided with OpenFOAM):

- Store the pressure calculated at the previous iteration, because it is required to apply under-relaxation

```
p.storePrevIter();
```

- Define the equation for U

```
tmp<fvVectorMatrix> UEqn  
(  
    fvm::div(phi, U) - laplacian(nu, U)  
);
```

“tmp< > is used to reduce peak memory.”

C.3. IMPLEMENTATION OF THE SIMPLE ALGORITHM IN OPENFOAM®

- Under-relax the equation for U

```
UEqn.relax();
```

- Solve the momentum predictor

```
solve (UEqn == -fvc::grad(p));
```

- Update the boundary conditions for p

```
p.boundaryField().updateCoeffs();
```

- Calculate the a_P coefficient and calculate U

```
volScalarField AU = UEqn().A();
```

```
U = UEqn().H()/AU;
```

```
UEqn.clear();
```

- Calculate the flux

```
phi = fvc::interpolate(U) & mesh.Sf(); adjustPhi(phi, U, p);
```

- Define and solve the pressure equation and repeat for the prescribed number of non-orthogonal corrector steps

```
fvScalarMatrix pEqn (
```

```
    fvm::laplacian(1.0/AU, p) == fvc::div(phi)
```

```
);
```

```
pEqn.setReference(pRefcell, pRefValue);
```

```
pEqn.solve();
```

- Correct the flux

```
phi -= pEqn.flux();
```

- Calculate continuity errors

```
# include "continuityErrs.H"
```

- Under-relax the pressure for the momentum corrector and apply the correction


```
p.relax();
```

```
U -= fvc::grad(p)/AU;
```

```
U.correctBoundaryConditions();
```

- Check for convergence and repeat from the beginning until convergence criteria are satisfied.

Note: In OpenFOAM 1.6. and 1.6.x the convergence check has been implemented in `simpleFoam` by defining

eqnResidual: Initial residual of the equation

maxResidual: Maximum residual of the equations after one solution step

convergenceCriterion: Convergence criterion specified by the user

- The value of the initial residual can be obtained when solving the corresponding equation using the `initialResidual()` method. Two syntax are possible:

```
eqnResidual = solve
```

```
(  
  UEqn() == -fvc::grad(p)  
) .initialResidual();
```

or, equivalently, for the pressure equation, since it has been already defined,

```
eqnResidual = pEqn.solve().initialResidual();
```

C.4 References

1. [openfoamwiki.net]
2. J. H. Ferziger, M. Peric, Computational Methods for Fluid Dynamics, Springer, 3rd Ed., 2001.
3. H. Jasak, Error Analysis and Estimation for the Finite Volume Method with Applications to Fluid Flows, Ph.D. Thesis, Imperial College, London, 1996.

Appendix D

SCHEMES USED IN OpenFOAM® FOR THE DIFFERENT SIMULATION CASES

D.1 The schemes used in OPENFOAM® in this work for different simulation cases

ddtSchemes

```
{  
  default CrankNicholson 1;  
}
```

gradSchemes

```
{  
  default Gauss linear;  
}
```

D.2. SOLVERS SETTINGS USED IN OPENFOAM® IN THIS WORK FOR DIFFERENT SIMULATION CASES

divSchemes

```
{  
  default Gauss linear;  
}
```

laplacianSchemes

```
{  
  default Gauss linear corrected;  
}
```

interpolationSchemes

```
{  
  default linear;  
}
```

snGradSchemes

```
{  
  default corrected;  
}
```

D.2 Solvers settings used in OpenFOAM® in this work for different simulation cases

solvers

```
{  
  p  
  {  
    solver PCG;  
    preconditioner DIC;
```

D.2. SOLVERS SETTINGS USED IN OPENFOAM® IN THIS WORK FOR DIFFERENT SIMULATION CASES

```
tolerance 1e-10;  
relTol 0.05;  
}
```

```
U  
{  
solver PCG;  
preconditioner DIC;  
tolerance 1e-09;  
relTol 0.1;  
}
```

```
c ( $c \equiv \phi$ ) (concentration of particles)  
{  
solver PBiCG;  
preconditioner DILU;  
tolerance 1e-09;  
relTol 0.1;  
}  
}
```

```
SIMPLE  
{  
nCorrectors 2; //minimum 2  
nNonOrthogonalCorrectors 0;  
pRefcell 0;  
pRefValue 0;  
}
```

```
relaxationFactors
```

D.2. SOLVERS SETTINGS USED IN OPENFOAM® IN THIS WORK FOR DIFFERENT SIMULATION CASES

```
{  
p 0.3;  
U 0.7;  
}
```

Bibliography

- [Abbott et al. 1991] J. R. Abbott, N. Tetlow, A. L. Graham, S. A. Altobelli, E. Fukushima, L. A. Mondy, and T. S. Stephens, “Experimental observations of particle migration in concentrated suspensions: Couette flow”, *J. Rheol.* 35, 773–797, (1991). [1.6](#), [1.6.1](#)
- [Acrivos et al. 1993] A. Acrivos, R. Mauri and X. Fan, “Shear-induced resuspension in a Couette device”, *Int. J. Multiphase Flow*, 19, Issue 5, 797-802, (1993). [4.2](#), [4.6.2](#)
- [Acrivos et al. 1994] A. Acrivos, X. Fan and R. Mauri, “On the measurement of the relative viscosity of suspensions,” *J. Rheol.* 38, 1285–1296, (1994). [4.5.1.1](#)
- [Adrian 1980] R. J. Adrian, “Laser Velocimetry”, University of Illinois, Urbana-Champaign, (1980).
- [Aalcoutabli et al. 2009] M. Aalcoutabli, S. G. Baek, J. J. Magda, Xiangfu Shi, S. A. Hutcheson, and G. B. McKenna, “A comparison of three different methods for measuring both normal stress differences of viscoelastic liquids in torsional rheometers”, *Rheol. Acta*, 48, 191–200, (2009). [2](#)
- [Altobelli et al. 1991] S. A. Altobelli and R. C. Givler, “Velocity and concentration measurements of suspensions by nuclear magnetic resonance imaging”, *J. Rheol.* 35, 721–734, (1991). [1.6](#)

BIBLIOGRAPHY

- [Altobelli et al. 1997] S. A. Altobelli, E. Fukushima, and L. A. Mondy, “Nuclear magnetic resonance imaging of particle migration in suspensions undergoing extrusion”, *J. Rheol.* 415, 1105–1115, (1997). [1.6.1](#)
- [Arp and Mason 1977] P. A. Arp and S. G. Mason, “The kinetics of flowing dispersions. IX. Doublets of rigid spheres”, *J. Colloid Interface Sci.* 61, 44–61, (1977). [1.6](#)
- [Assinck 1995] F. H. Assinck, “An Introduction To Suspensions”, A Literature Study, report number 95.054, Technical University Eindhoven, Departement of Mechanical Engineering, (1995).
- [Auvinen et al. 2010] M. Auvinen, J. Ala-Juusela, N. Pedersen, and T. Siikonen, "Time-Accurate Turbomachinery Simulations with Open-Source® CFD: Flow Analysis of a Single-Channel Pump with OpenFOAM®", "ECCOMAS CFD 2010", Fifth European Conference on Computational Fluid Dynamics, J. C. F. Pereira and others, (2010). [2.6.1](#)
- [Averbakh 1997] A. Averbakh, A. Shauly, A. Nir, and R. Semiat, "Slow viscous flows of highly concentrated suspensions – Part I: Laser-Doppler velocimetry in rectangular ducts", *Intl J. Multiphase Flow* 23, 409–424, (1997).
- [Barakat and Clark 1966] H. Z. Barakat and J. A. Clark 1966, “Analytical and experimental study of transient laminar natural convection flows in partially filled containers”, In *Third Int. Heat Transfer Conf.*, volume II, paper 57, (1966). [1](#)
- [Barnes 1989] H. A. Barnes, "Shear-thickening ("dilatancy") in suspensions of nonaggregating solid particles dispersed in Newtonian liquids", *J. Rheol.*, 33(2), 329-366, (1989).

BIBLIOGRAPHY

- [Barnes et al. 1989] H. A. Barnes, J. E. Hutton, and K. Walters F. R. S., “AN INTRODUCTION TO RHEOLOGY”, © Elsevier Science Publishers B.V., (1989). [1.4.1](#)
- [Batchelor 1951] G. K. Batchelor, “Note on a class of solutions of the navier-Stokes equations representing steady rotationally-symmetric flow”, Quart. J. Mech. and Applied Math, vol. IV, Pt. 1, (1951).
- [Batchelor and Green 1972a] G. K. Batchelor & J. T. Green, “The hydrodynamic interactions of two small freely-moving spheres in a linear flow field”. J. Fluid Mech. 56, 375, (1972).
- [Batchelor and Green 1972b] G. K. Batchelor & J. T. Green, “The determination of the bulk stress in a suspension of spherical particles to order c^2 ”. J. Fluid Mech. 56, 401, (1972).
- [Batchelor 1977] G. K. Batchelor, “The effect of Brownian motion on the bulk stress in a suspension of spherical particles”. J. Fluid Mech. 83, 97, (1977). [1.4.2.1](#)
- [Bernoulli 1738] D. Bernoulli, “Hydrodynamica”, Dulsecker, Strasbourg, (1738). [1.2.1](#)
- [Bingham 1922] E. C. Bingham, "Fluidity and Plasticity," McGraw-Hill Book Co., New York, (1922). [1.2.1](#)
- [Bingham 1944] E. C. Bingham, "The History of the Society of Rheology from 1924- 1944," January, (1944). [1.2.2](#)
- [Bird et al. 1977] R. B. Bird, R. C. Armstrong, and O. Hassager, “Dynamics of polymeric liquids”, Copyright © John Wiley & sons Inc., p 176-179, (1977). ([document](#)), [1.4.1](#), [1.5.3](#), [4.2](#)
- [Bird et al. 1987] R. B. Bird, R. C. Armstrong, and O. Hassager, “Dynamics of polymeric liquids, vol.1 Fluid Mechanics, vol.2 Kinetic Theory”, Copyright © John Wiley & sons, Inc. (1987). [1.4.1](#), [1.5.3](#), [6.2.2](#)

BIBLIOGRAPHY

- [Blanc et al. 2011] F. Blanc, F. Peters, and E. Lemaire, “Particle Image Velocimetry in concentrated suspensions : Application to local rheometry”, *Appl. Rheol.* 21:2, 23735, (2011).
- [Blanc et al. 2011] F. Blanc, F. Peters, and E. Lemaire, “Experimental Signature of the Pair-Trajectories of Rough Spheres in the Pair Distribution Function of Dilute Sheared Non-Colloidal Suspensions”, *PRL, Pyhsical Review Letters*, Oct. (2011). [7.2](#)
- [Metzger et al. 2011] Bloen Metzger and Jason E. Butler, ”Clouds of particles in a periodic shear flow”, in press, (2011). ([document](#)), [6.2.4.2](#), [6.8](#), [6.2.4.2](#), [6.9](#), [6.2.4.2](#), [6.4](#), [7.1](#)
- [Boltzmann 1878] L. Boltzmann, *Wied. Ann.*, 5, 430, (1878). [1.2.1](#)
- [Boyer et al. 2011 a] Boyer F., Pouliquen O., and Guazzelli E., “Dense suspensions in rotating-rod flows: normal stresses and particle migration”, *J. Fluid Mech.*, 272, (2011). ([document](#)), [3](#), [1](#), [1.6](#), [4.2](#), [4.5.3.4](#), [4.5.3.4](#), [4.6.1](#), [4.9](#), [5.4.1](#), [5.4.2](#), [7.1](#)
- [Boyer et al. 2011 b] Boyer F., Pouliquen O., and Guazzelli E., “Unifying suspension and granular rheology”, *PRL*, preprint, (2011). ([document](#)), [1.7.4.5](#)
- [Boyle 1660] R. Boyle, “New experiments physico-mechanicall, touching the spring of air and its effects”, London, (1660). [1.2.1](#)
- [Brady and Bossis 1988] J. Brady, and G. Bossis, "Stokesian Dynamics". *Ann. Rev. Fluid Mech.* 20: 111–157, (1988).
- [Brady and Morris 1997] J. F. Brady and J. F. Morris, “Microstructure of strongly sheared suspensions and its impact on rheology and diffusion”, *J. Fluid Mech.* 348, 103– 139, (1997). [1.7.3.3](#), [1.7.3.4](#), [4.6.2](#), [6.2.1](#), [6.3.1.1](#)

BIBLIOGRAPHY

- [Brady and Vivic 1995] J. F. Brady and M. A. Vicic, “Normal stresses in colloidal dispersions”. *J. Rheol.* 39, 545, (1995).
- [Breedveld et al. 1998] V. Breedveld, D. van den Ende, A. Tripathi, and A. Acrivos, “The measurement of the shear-induced particle and fluid tracer diffusivities in concentrated suspensions by a novel method”, *J. Fluid Mech.* 375, 297–318, (1998). [1.6](#), [1.6.1](#)
- [Bricker and Butler 2006] Bricker J. M., Butler J. E., “Oscillatory shear of suspensions of noncolloidal particles“. *J Rheol* 50(5), (2006). [4.3](#)
- [Brinkman 1952] H. C. Brinkman, *J.Chem.Phys.* 20, 571 (1952). [1.4.2.1](#)
- [Fletcher 1991] C. A. J. Fletcher, “Computational Techniques for Fluid Dynamics, Springer Series in Computational Physics Vols. I and II, 2nd ed.”, Springer, Berlin, (1991).
- [Caretto et al. 1972] L. Caretto, R. M. Curr, and D. B. Spalding, “Two numerical methods for three-dimensional boundary layers”, *Comp. Methods Appl. Mech. Eng.*, 1-39, (1972).
- [Cauchy 1827] A. L. Cauchy, “Ex.de Math”, 2, 42, (1827). [1.2.1](#)
- [Chan and Powell 1984] Chan D., and R. L. Powell, “Rheology of suspensions of spherical particles in a Newtonian and a non-Newtonian fluid”, *J. Non-Newtonian Fluid Mech.* 15, 165–179, (1984). [1.6.1](#)
- [Chapman 1990] B. Chapman, “shear-induced migration phenomena in concentrated suspensions”. PhD thesis, University of Notre Dame, (1990). ([document](#)), [1.6](#), [1.6.1](#), [1.7.3.1](#), [3.4.1.1](#), [4.3](#), [4.4.7](#), [4.8.3](#)
- [Chow et al. 1994] Chow A. W., S. W. Sinton, J. H. Iwamiya, and T. S. Stephens, “Shear-induced migration in Couette and parallel-plate viscometers: **NMR** imaging and stress measurements”, *Phys. Fluids* 6, 2561–2576, (1994). ([document](#)), [1.6](#), [1.6.1](#), [1.7.3.1](#), [4.3](#), [4.4.7](#)

BIBLIOGRAPHY

- [Chow et al. 1995] Chow A. W., J. H. Iwayima, S. W. Sinton and D. T. Leighton, “Particle migration of non-Brownian, concentrated suspensions in a truncated cone-and-plate”, Society of Rheology Meeting, Sacramento, CA, (1995). ([document](#))
- [Chung 1980] E. Y.-C. Chung, ”Experimental investigations of the transport properties of flow suspensions”. PhD thesis, California Institute of Technology, (1980).
- [Corbett and Phillips 1995] A. M. Corbett, R. J. Phillips, “Magnetic resonance imaging of concentration and velocity profiles of pure fluids and solid suspensions in rotating geometries”, J. Rheol. 39, 907–924, (1995). [1.6.1](#)
- [Courant et al. 1952] R. Courant, E. Isaacson and M. Rees, “On the solution of non-linear hyperbolic differential equations by finite differences”, Comm. Pure Appl. Math. 5:243, (1952). [1](#)
- [Couturier et al. 2011] E. Couturier, F. Boyer, O. Pouliquen, and E. Guazelli, “Suspensions in a tilted trough: second normal stress difference”, J. Fluid Mech. 686, 26-39 (2011). ([document](#)), [3](#), [2](#), [4.2](#), [4.5.3](#), [4.5.3.1](#), [4.5.3.4](#)
- [C++] Programming languages - C++. ISO/IEC Standard 14822:1998, (1998). [3.1](#), [3.3.1](#)
- [Cramers Rule] http://en.wikipedia.org/wiki/Cramer%27s_rule [2.4.4](#)
- [Crank-Nicolson] http://en.wikipedia.org/wiki/Crank%E2%80%93Nicolson_method [3](#), [2.4.3](#)
- [Davis and Acrivos 1985] R. H. Davis and A. Acrivos, “Sedimentation of non-colloidal particles at low Reynolds numbers”, Annu. Rev. Fluid Mech. 17, 91-118 , (1985). [1.7.4.2](#)

BIBLIOGRAPHY

- [Dbouk et al. 2011] T. Dbouk, E. Lemaire and L. Lobry, “Normal Stress Differences In Concentrated non-Brownian Suspensions”, J. Fluid Mechanics,..... in press. [4.2](#), [5.4.2](#)
- [Deboeuf 2008] A. Deboeuf, “Interactions Hydrodynamiques Dans Les Suspensions Macroscopiques”, PhD thesis, Pierre and Marie Curie University, (2008). ([document](#)), [1.7.4.5](#), [4.6.2](#), [4.9](#), [7.1](#)
- [Deboeuf et al. 2009] A. Deboeuf, G. Gauthier, J. Martin, Y. Yurkovetsky and J. Morris, “Particle Pressure in a Sheared Suspension: A Bridge from Osmosis to Granular Dilatancy”, Phys. Rev. Lett. 102, 108301, (2009). ([document](#)), [1.7.4.5](#), [4.2](#), [4.3.1](#), [4.6.1](#), [4.6.2](#), [4.9](#), [7.1](#)
- [Deepak Doraiswamy] Deepak Doraiswamy, “The Origins of Rheology: A Short Historical Excursion”, DuPont iTechnologies, Experimental Station, Wilmington, DE 19880-0334. [1.2.1](#)
- [Deshpande and Shapley 2010] K. V. Deshpande and N. C. Shapley, “Particle migration in oscillatory torsional flows of concentrated suspensions”, J. Rheol. 54(3), 663-686, (2010). [1.6](#)
- [Drew and Lahey 1993] D. A. Drew and R. T. Lahey, “Analytical modeling of multiphase flow”, in Particulate Two-Phase Flows, edited by M. C. Roco (Butterworth-Heinemann, Boston), (1993). [1.7.4.2](#)
- [Eckstein et al. 1977] E. C. Eckstein, D. G. Bailey, and A. H. Shapiro, “Self-diffusion in shear flow of a suspension”, J. Fluid Mech. 79, 191-208, (1977).
- [Einstein 1906] A. Einstein, Ann. Physik, 19, 289, (1906). [1.2.1](#), [1.4.2.1](#)
- [Euler 1755] L. Euler, “Memoires de Academie de Science”, Berlin, 11, 217, (1755). [1.2.1](#)
- [Eulers Method] http://en.wikipedia.org/wiki/Euler_method [2.2](#)

BIBLIOGRAPHY

- [Fang et al. 2002] Z. Fang, A. Mammoli, J. F. Brady, M. S. Ingber, L. A. Mondy, and A. L. Graham, “Flow-aligned tensor models for suspension flows”, *Int. J. Multiphase flow* 28 (1),137–166, (2002). [1.7.3.4](#)
- [Gadala-Maria 1979] F. A. Gadala-Maria, “The rheology of concentrated suspension”, Ph.D. thesis, Stanford University, (1979). ([document](#)), [3](#), [1.6](#), [1.6.1](#), [4.2](#), [6.3](#)
- [Gadala-Maria and Acrivos 1980] F. Gadala-Maria and A. Acrivos, ”A. Shear-Induced Structure in a Concentrated Suspension of Solid Spheres”, *J. Rheol.* 24,799, (1980). [1.6](#), [4.5.1.3](#), [4.5.1.3](#)
- [Galerkin Method] http://en.wikipedia.org/wiki/Galerkin_method [2.2](#)
- [Gaussian elimination] http://en.wikipedia.org/wiki/Gaussian_elimination [2.4.4](#)
- [Gentry et al. 1952] R. A. Gentry, R. E. Martin and B. J. Daly., “An Eulerian differencing method for unsteady compressible flow problems”, *J. Comp. Phys.* 5:243, (1952). [1](#)
- [GISEC06 2010] [http://www.pmmh.espci.fr/~mephy/wiki/doku.php?id=rencontres:2010-3&s\[\]=gisec06](http://www.pmmh.espci.fr/~mephy/wiki/doku.php?id=rencontres:2010-3&s[]=gisec06) [4.2](#)
- [Goldsmith et al. 1967] H. L. Goldsmith and S. G. Mason, “The microrheology of dispersions. In *Rheology Theory and Applications*” (ed. F. R. Eirich), vol. 4, pp. 86–246. Academic, (1967). [3.4.1.1](#)
- [Goto and Kuno 1982] H. Goto and H. Kuno, “Flow of Suspensions Containing Particles of Two Different Sizes through a Capillary Tube “, *J. Rheol.* 26,387, (1982).
- [Graham et al. 1991] A. L. Graham and S. A. Altobelli, “**NMR** imaging of shear-induced diffusion and structure in concentrated suspensions”, *J. Rheol.* 35, 191–201, (1991). [1.6](#)

BIBLIOGRAPHY

- [Graham et al. 1998] A. L. Graham, A. A. Mammoli, and M. B. Busch, “Effects of demixing on suspension rheometry”, *Rheol. Acta* **37**, 139–150, (1998). [1.7.3.3](#)
- [Guyon et al. 2001] E. Guyon, J-P. Hulin, and L. petit, “Hydrodynamique physique”, EDP Sciences, (2001). [4.4.4](#)
- [Versteeg 1995] H. K. Versteeg and W. Malalasekera, “An Introduction to Computational Fluid Dynamics: The Finite Volume Method”, Longman Scientific and Technical, (1995). [2.4.4](#)
- [Hampton et al. 1997] R. E. Hampton, A. A. Mammoli, A. L. Graham, N. Tetlow, and S.A. Altobelli, “Migration of particles undergoing pressure driven flow in a circular conduit”, *J. Rheol.* **41**, 621–640, (1997). [1.6](#), [1.6.1](#), [3.4.1.2](#)
- [Han et al. 1999] Han M., C. Kim, M. Kim, and S. Lee, “Particle migration in tube flow of suspensions”, *J. Rheol.* **43**, 1157–1174, (1999). [1.6.1](#)
- [Herschel and Bulkley 1926] W. Herschel and R. Bulkley, *Koll. Z.*, **39**, 291, (1926). [1.2.1](#)
- [Hestens and Steifel 1952] M. R. Hestens and E. L. Steifel, “Method of conjugate gradients for solving linear systems”, *Journal of Research*, **29**:409–436, (1952). [2.4.4](#)
- [Hirsch 1991] C. Hirsch, “Numerical computation of internal and external flows”, John Wiley & Sons, (1991). [2.4.3](#)
- [Jasak 2006] H. Jasak, “Multi-Physics Simulations in Continuum Mechanics” *Proceedings of 5th International Conference of Croatian Society of Mechanics*, Trogir (2006).
- [Hoffman 1972] RL. Hoffman, “Discontinuous and dilatant viscosity behavior in concentrated suspensions. I. Observation of flow instability”, *Trans. Soc. Rheol.* **16**, 155-173, (1972). ([document](#)), [1.4](#)

BIBLIOGRAPHY

- [Hooke 1678] R. J. Hooke, “De potentia restitutuva”, J.Martyn, London, (1678). [1.2.1](#)
- [Hookham 1986] P. A. Hookham, “Concentration and velocity measurements in suspensions flowing through a rectangular channel”, PhD thesis, California Institute of Technology, (1986). [1.6](#)
- [Ingber et al. 2009] M. S. Ingber, A. L. Graham, L. A. Mondy, and Z. Fang, “An improved constitutive model for concentrated suspensions accounting for shear-induced particle migration rate dependence on particle radius,” *Int. J. Multiphase Flow* 35, 270–276, (2009). [1.6.1](#)
- [Issa 1986] R. I. Issa, “Solution of the implicitly discretized fluid flow equations by operator-splitting”, *J. Comp. Physics*, 62:40–65, (1986).
- [Iwamiya et al. 1994] J. H. Iwamiya, A. W. Chow, and S. W. Sinton, “NMR flow imaging of Newtonian liquids and a concentrated suspension through an axisymmetrical sudden contraction”, *Rheol. Acta* 33, 267–282, (1994). [1.6.1](#)
- [Jacobs 1980] D. A. H. Jacobs: “Preconditioned Conjugate Gradient methods for solving systems of algebraic equations”: Central Electricity Research Laboratories Report, RD/L/N193/80, (1980). [2.4.4](#)
- [Jana et al. 1995] S. C. Jana, B. Kapoor, and A. Acrivos, “Apparent wall slip velocity coefficients in concentrated suspensions of noncolloidal particles”, *J. Rheol.* 39, 1123, (1995). [4.4.6](#), [4.4.6](#)
- [Jarny et al. 2006] S. Jarny, P. Monnet and L. David. “Rhéométrie locale par vélocimétrie laser”, Congrès Francophone de Techniques Laser (CFTL), Toulouse, 19 – 22 septembre (2006). ([document](#)), [4.7](#), [4.39](#)

BIBLIOGRAPHY

- [Jasak 1996] H. Jasak, “Error Analysis and Estimation for the Finite Volume Method with Applications to Fluid Flows”, PhD thesis, Imperial College, University of London, (1996). [2.4.2.2](#), [2.5](#), [C.1](#)
- [Jeffrey 1922] G. B. Jeffrey, Proc. Roy. Soc. Lond., A102, 161, (1922). [1.2.1](#)
- [Ferziger 1996] J. H. Ferziger and M. Peric, “Computational Methods for Fluid Dynamics”, Springer, Berlin, (1996). [2](#), [2.4.2.2](#), [2](#), [2.6.2](#), [2.6.2.2](#)
- [Jung et al. 2008] Jung Gun nam, Kyu Hyun, Kyung Hyun Ahn, Seung Jong Lee, “Prediction of normal stresses under large amplitude oscillatory shear flow”, J. Non-Newtonian Fluid Mech., 150, 1-10, (2008). [2](#)
- [Karnis et al. 1966] A. Karnis, H. L. Goldsmith and S. G. Mason, J. Colloid Interface Sci. 23, 531, (1966). [1.6](#)
- [Kaye et al. 1968] A. Kaye, A. S. Lodge, and D. G. Vale, “Determination of normal stress differences in steady shear flow. II. Flow birefringence, viscosity, and normal stress data for a polyisobutene liquid”, Rheol. Acta, Band 7, Heft 4, (1968). [2](#)
- [Keentok and Xue 1999] M. Keentok and SC Xue, “Edge fracture in cone-plate and parallel plate flows”. Rheol. Acta 38:321–348, (1999). [4.4.2](#)
- [Kim et al. 2008] J. M. Kim, S. G. Lee, and C. Kim, “Numerical simulations of particle migration in suspension flows: Frame-invariant formulation of curvature-induced migration”, J. Non-Newtonian Fluid Mech. 150, 162–176, (2008). [1.6](#), [1.6.1](#), [1.7.2](#)
- [Koh et al. 1994] C. J. Koh and P. Hookham, “An experimental investigation of concentrated suspension flows in a rectangular channel”, J. Fluid Mech. 266, 1–32, (1994). [1.6](#), [1.6.1](#)
- [Koh 1991] C. J. Koh, “Experimental and theoretical studies on two-phase flows”. PhD thesis, California Institute of Technology, (1991).

BIBLIOGRAPHY

- [Kolli et al. 2002] V. G. Kolli, E. J. Pollauf and F. Gadala-Maria, “Transient Normal Force Response in a Concentrated Suspension of Spherical Particles,” *Journal of Rheology* 46, 321-334 (2002) [4.5.1.3](#), [6.2.4.2](#)
- [Kotaka 1959] T. Kotaka, M. Kurata, and M. Tamura, “Normal Stress Effect in Polymer Solutions”, *J. Appl. Phys.* ,30, 1705, (1959). [2](#)
- [Krieger 1972] I. M. Krieger, “Rheology of monodisperse latices,” *Adv. Colloid Interface Sci.* 3, 111–136, (1972).
- [Krieger and Dougherty 1959] I. M. Krieger and T. Dougherty , “A mechanism for non-Newtonian flow in suspensions of rigid spheres” *Trans Soc Rheol* 3, 137, (1959). [1.4.2.1](#)
- [Krishnan et al. 1996] G. P. Krishnan, S. Beimfohr, and D. Leighton, “Shear-induced radial segregation in bidisperse suspensions”, *J. Fluid Mech.* 321, 371–393, (1996). [1.7.3.2](#)
- [Leighton and Acrivos 1986] D. Leighton and A. Acrivos, “Viscous Resuspension”, *Chemical Engineering Science*, 41, 1377-1384, (1986). [1.4.2.1](#), [6.3](#)
- [Leighton and Acrivos 1987] D. Leighton and A. Acrivos, “Measurement of self-diffusion in concentrated suspensions of spheres”, *J. Fluid Mech.* 177, 109–131, (1987). [1.7.3.1](#), [6.3](#)
- [Leighton and Acrivos 1987] D. Leighton and A. Acrivos, “The shear-induced migration of particles in concentrated suspensions”, *J. Fluid Mech.* 181, 415–439, (1987). [1.6](#), [1.7.3.1](#), [3.4.1.1](#)
- [Leonard 1991] B. P. Leonard, “The ULTIMATE conservative difference scheme applied to unsteady one-dimensional advection”, *Comp. Meth. Appl. Mech. Engineering*, 88:17–74, (1991).

BIBLIOGRAPHY

- [Lilek and Peric 1995] Ž. Lilek and M. Perić, “A fourth-order Finite Volume method with colocated variable arrangement”, *Computers and Fluids*, 24(3):239–252, (1995).
- [Lipson and Lodge 1968] J. M. Lipson and A. S. Lodge, “Determination of normal stress differences in steady shear flow. I. Stability of a polyisobutene liquid”, *Rheol. Acta*, Band 7, Heft 4, (1968). [2](#)
- [Lodge and Hou 1980] A. S. Lodge and T. H. Hou, “On the measurement of normal stress differences in steady shear flow, IV. A new truncated-cone and plate ("TCP") apparatus”, *Rheol. Acta*, Vol. 20, No. 3, (1980). [2](#)
- [Lyon and Leal I 1998] M. K. Lyon and L. G. Leal, “An experimental study of the motion of concentrated suspensions in two-dimensional channel flow, Part 1. Monodisperse systems”, *J. Fluid Mech.* 363, 25–56, (1998). [1.6](#), [1.6.1](#), [3.4.1.1](#), [6.2.4](#)
- [Lyon 1997] M. K. Lyon, “Experimental studies of noncolloidal suspensions undergoing two-dimensional flow”. PhD thesis, University of California, Santa Barbara, (1997).
- [Lyon and Leal II 1998] | M. K. Lyon and L. G. Leal, “An experimental study of the motion of concentrated suspensions in two-dimensional channel flow. Part 2. Bidisperse systems”, *J. Fluid Mech.* 363, 57–77, (1998). [1.6.1](#)
- [Macosko 1994] Christopher W. Macosko, “RHEOLOGY Principles, Measurements and Applications”, Copyright ©Wiley-VCH Inc., (1994). [\(document\)](#), [1.5](#), [1.7](#)
- [Maron and Pierce 1956] S. H. Maron and P. E. Pierce, *J. Colloid Sci.* 11, 80 (1956). [1.4.2.1](#)

BIBLIOGRAPHY

- [Marsh and Pearson 1968] B. D. Marsh and J. R. A. Pearson, “The Measurement of Normal-Stress Differences Using A Cone-and-Plate Total Thrust Apparatus”, *Rheol. Acta*, Band 7, Heft 4, (1968). [2](#)
- [Maxwell 1867] J. C. Maxwell, *Phil Trans. Roy. Soc. Lond.*, 157, 49-88, (1867). [1.2.1](#)
- [McCoy and Denn 1971] D. H. McCoy and M. M. Denn, “Secondary flow in a parallel plate rheometer”, *Rheol. Acta* 10, 408–411, (1971). [4.8](#)
- [Merhi et al. 2005] D. Merhi, E. Lemaire, G. Bossis, and F. Moukalled, “Particle migration in a concentrated suspension flowing between rotating parallel plates: Investigation of diffusion flux coefficient”, *J. Rheol.* 49, 1429–1448, (2005). [1.6](#), [1.6.1](#), [1.7.3.1](#), [4.3](#), [4.8.3](#)
- [Mewis 1979] J. Mewis, "Thixotropy-A general review", *Journal of Non-Newtonian Fluid Mechanics*, 6, 1-20, (1979).
- [Miller and Morris 2006] R. M. Miller and J. F. Morris, “Normal stress-driven migration and axial development in pressure-driven flow of concentrated suspensions”, *J. Non-Newtonian Fluid Mech.* 135, 149–165, (2006). [1.6.1](#), [3.4.1.1](#), [3.4.1.1](#), [3.4.1.1](#), [3.4.1.2](#)
- [Miller and Morris 2009] R. M. Miller, J. P. Singh, and J. F. Morris, “Suspension flow modeling for general geometries”, *Chemical Engineering Science*, 64, 4597-4610, (2009). [\(document\)](#), [6.2.1](#), [6.2.2](#), [6.2.3](#), [6.3.1.1](#)
- [Miller 2004] R. M. Miller, “Continuum Modeling of Liquid-Solid Suspensions for Nonviscometric Flows”. PhD thesis, School of Chemical & Biomolecular Engineering, Georgia Institute of Technology, (2004). [3.4.1.1](#), [2](#)
- [Mills and Snabre 2009] P. Mills and P. Snabre, “Apparent viscosity and particle pressure of a concentrated suspension of non-Brownian hard

BIBLIOGRAPHY

- spheres near the jamming transition”, *Eur. Phys. J. E* 30, 3, 309-316, (2009). [4.6.2](#), [4.9](#), [7.1](#)
- [Moraczewski and Shapley 2006] T. Moraczewski and N. C. Shapley, “The effect of inlet conditions on concentrated suspension flows in abrupt expansions”, *Phys. Fluids* 18, 123-303, (2006). [1.6.1](#)
- [Moraczewski and Shapley 2007] T. Moraczewski and N. C. Shapley, “Pressure drop enhancement in a concentrated suspension flowing through an abrupt axisymmetric contraction-expansion”, *Phys. Fluids* 19, 103-304, (2007). [1.6.1](#)
- [Moraczewski et al. 2005] T. Moraczewski, H. Tang, and N. C. Shapley, “Flow of a concentrated suspension through an abrupt axisymmetric expansion measured by nuclear magnetic resonance imaging”, *J. Rheol.* 49, 1409–1428, (2005). [1.6.1](#)
- [Morris and Brady 1996] J. F. Morris and J. F. Brady, “Self-diffusion in sheared suspensions”. *J. Fluid Mech.* 312, 223, (1996).
- [Morris and Brady 1998] J. F. Morris and J. F. Brady, “Pressure-driven flow of a suspension: Buoyancy effects”, *International Journal of Multiphase Flow*, 24, 1, 105-130, (1998). [4.3.1](#)
- [Morris and Katyal 2002] J. F. Morris and B. Katyal, “Microstructure from simulated Brownian suspension flows at large shear rate”. *Phys. Fluids* 14, 1920, (2002). [6.2.1](#)
- [Morris and Boulay 1999] J. F. Morris and F. Boulay, “Curvilinear flows of non-colloidal suspensions: the role of normal stresses”, *J. Rheol.* 43 (5), 1213-1237, (1999). [\(document\)](#), [1.4.2.1](#), [1.7.4](#), [1.7.4.2](#), [1.7.4.4](#), [1.7.4.4](#), [1.7.4.5](#), [3.1](#), [3.4.2](#), [3.4.2](#), [3.4.2](#), [3.4.2](#), [3.5](#), [4.2](#), [4.6.2](#), [4.6.2](#), [4.9](#), [5.1](#), [5.3](#), [7.1](#)

BIBLIOGRAPHY

- [Moukalled and Darwish 2009] F. Moukalled and M. Darwish, “Pressure-Based Algorithms for Single-Fluid and Multifluid Flows”, in *Handbook of Numerical Heat Transfer, Second Edition* (eds W. J. Minkowycz, E. M. Sparrow and J. Y. Murthy), John Wiley & Sons, Inc., Hoboken, NJ, USA, (2009). [2.4](#), [2.7](#), [7.1](#)
- [Muzaferija 1994] S. Muzaferija, “Adaptive Finite Volume method for flow prediction using un- structured meshes and multigrid approach”, PhD thesis, Imperial College, University of London, (1994). [2.4.4](#)
- [Narumi et al. 2002] T. Narumi, H. See, Y. Honma, T. Hasegawa, T. Takahashi and N. Phan-Thien, “Transient response of concentrated suspension after shear reversal”, *J. Rheol.*, 46, 295–305, (2002). [4.5.1.3](#), [6.2.4.2](#)
- [Navier 1823] C. L. M. H. Navier, *Bull. Soc. Philomath.*, 75, (1823). [1.2.1](#), [1.5.2](#)
- [Newton 1687] I. S. Newton, “*Philosophiae Naturalis Principia Mathematica*”, 1st Ed., Bk 2, Sect. IX, (1687). [1.2.1](#)
- [Nott, Guazzelli, and Pouliquen 2011] P. R. Nott, E. Guazzelli, and Olivier Pouliquen, “The Suspension Balance Model revisited”, *Phys. Fluids* 23, 043304, (2011). [4.6.1](#)
- [Nott and Brady 1994] P. R. Nott and J. F. Brady, “Pressure-driven flow of suspensions: simulation and theory”, *J. Fluid Mech.* 275, 157–199, (1994). ([document](#)), [1.7.4](#), [1.7.4.2](#), [3.1](#), [3.4.1.1](#), [3.4.1.1](#), [3.5](#), [4.2](#), [4.3.1](#), [5.1](#), [7.1](#)
- [Numerical Schemes] <http://www.openfoam.com/docs/user/fvSchemes.php#x20-1070004.4> [3.4.1.1](#), [B.1](#)
- [OpenFOAM®] OpenFOAM® project web pages, <http://www.openfoam.com>. ([document](#)), [2.2](#), [2](#), [2.4.4](#), [2.5](#),

BIBLIOGRAPHY

2.6, 2.6.1, 2.6.2, 2.6.2.2, 3.1, 3.3.1, 3.4.1.1, 3.4.1.1, 3.4.1.1,
3.4.1.2, 3.4.1.2, 3.4.2, 3.4.2, 3.4.2, 3.4.2, 3.5, 5.1, 5.4, 5.6, 6.2.1,
6.2.4, 6.3, 6.3.1.1, 6.4, 7.1, B.1

[openfoamwiki.net] <http://openfoamwiki.net> A.1, 1

[OpenSource®] Open Source initiative web pages,
<http://www.opensource.org>.

[Ovarlez et al. 2006] G. Ovarlez, F. Bertrand, and S. Rodts, “Local determination of the constitutive law of a dense suspension of noncolloidal particles through magnetic resonance imaging”, *J. Rheol.*, 50(3), 259-292, (2006). 1.4.2.1, 1.6, 1.6.1, 4.5.1.3, 5.4.2

[ParaView®] <http://www.paraview.org>

[Parsi and Gadala Maria 1987] F. Parsi and F. Gadala-Maria, “Fore-and-Aft Asymmetry in a Concentrated Suspension of Solid Spheres”, *J. Rheol.* 31, 725, (1987). 4.6.2

[Pascal 1663] B. Pascal, “Traites de l’équilibre des liqueres et de la pesanteur de la masse de l’air, Paris, (1663). 1.2.1

[Patankar 1978] S. V. Patankar and B. R. Baliga, “A new Finite-Difference scheme for parabolic differential equations”, *Numerical Heat Transfer*, 1:27, (1978). 2

[Patankar 1981] S. V. Patankar, “Numerical Heat Transfer and Fluid Flow”, Hemisphere, New York, (1981). 2.4.1, 2, 2.4.2.2, 2.4.2.3, 2.4.2.3, 2.6.2, 2.6.2.1, 2.6.2.2, 2.6.2.2

[Phillips et al. 1992] R. J. Phillips, R. C. Armstrong, R. A. Brown, A. Graham, and J. R. Abbott, “A constitutive model for concentrated suspensions that accounts for shear-induced particle migration”, *Phys. Fluids A* 4, 30-40, (1992). (document), 1.6, 1.6.1, 1.7.3.1, 1.7.4.4, 3.4.2, 3.4.2, 4.6.2, 5.4.1, 5.4.1, 6.2.4

BIBLIOGRAPHY

- [Phung et al. 1996] T. N. Phung, J. F. Brady, and G. Bossis, “Stokesian dynamics simulations of Brownian suspensions,” *J. Fluid Mech.* 313, 181–207, (1996). [4.6.2](#)
- [Poiseuille 1841] J. L. Poiseuille, “Comptes Rendus”, 12, 112, (1841). [1.2.1](#)
- [Rao et al. 2002 a] R. R. Rao, L. A. Mondy, T. A. Baer, S. A. Altobelli, and T. S. Stephens, “**NMR** measurements and simulations of particle migration in non-Newtonian fluids”, *Chem. Eng. Commun.* 189, 1–22, (2002). [1.6.1](#)
- [Rao et al. 2002 b] R. Rao, L. Mondy, A. Sun, and S. Altobelli, “A numerical and experimental study of batch sedimentation and viscous resuspension”, *Int. J. Numer. Meth. Fluids*, 39, 465–483, (2002). [\(document\)](#), [6.3](#), [6.3.1.1](#), [6.3.1.1](#), [6.3.1.1](#)
- [Rao et al. 2007] R. R Rao., L. A. Mondy, and S. A. Altobelli, “Instabilities during batch sedimentation in geometries containing obstacles: A numerical and experimental study”, *Int. J. Numer. Methods Fluids* 55, 723–735, (2007). [1.6.1](#)
- [Rhie and Chow 1982] C. M. Rhie and W. L. Chow: “A numerical study of the turbulent flow past an isolated airfoil with trailing edge separation”: AIAA-82-0998, AIAA/ASME 3rd Joint Thermophysics, Fluids, Plasma and Heat Transfer Conference, St. Louis, Missouri, (1982).
- [Rhie and Chow 1983] C. M. Rhie and W. L. Chow, “A numerical study of the turbulent flow past and airfoil with trailing edge separation”: *AIAA J.*, 21, 1525–1532, (1983). [2](#)
- [Richardson and Zaki 1954] J. F. Richardson and W. N. Zaki, “Sedimentation and fluidization: Part I”, *Trans. Inst. Chem. Eng.* 32, 35–47, (1954). [1.7.4.2](#), [5.4.1](#)

BIBLIOGRAPHY

- [Roscoe 1952] R. Roscoe, Brit. J. Appl. Phys. 3, 267 (1952). [1.4.2.1](#)
- [Runge-Kutta Method] http://en.wikipedia.org/wiki/Runge%E2%80%93Kutta_methods
[2.2](#)
- [Ryssel and Brunn 1999] E. Ryssel and P. O. Brunn, "Comparison of a quasi-Newtonian fluid with a viscoelastic fluid in planar contraction flow," J. Non-Newt. Fluid Mech., vol. 86, pp. 309-335, (1999).
[6.2.2.1](#)
- [Schaffinger et al. 1990] U. Schaffinger, A. Acrivos, and K. Zhang, "Viscous resuspension of a sediment within a laminar and stratified flow", Int. J. Multiphase Flow, 16, 567-578, (1990). [6.3](#)
- [Shapley et al. 2002] N. C. Shapley, R. C. Armstrong, and R. A. Brown, "Laser Doppler velocimetry measurements of particle velocity fluctuations in a concentrated suspension", J. Rheol. 46, 241-272, (2002). [1.6](#), [1.6.1](#), [5.4.2](#), [5.4.2](#), [5.4.2](#), [5.5](#)
- [Shapley et al. 2004] N. C. Shapley, R. A. Brown, and R. C. Armstrong, "Evaluation of particle migration models based on laser Doppler velocimetry measurements in concentrated suspensions", J. Rheol. 48, 255-279, (2004). [1.6](#), [1.6.1](#), [5.4.2](#), [5.4.2](#), [5.4.2](#), [5.5](#)
- [Schunk and Scriven 1990] P. R. Schunk and L. E. Scriven, "Constitutive equation for modeling mixed extension and shear in polymer solution processing", J. Rheol 34(7), (1990). [6.2.2](#)
- [Sierou and Brady 2002] A. Sierou and J. F. Brady, "Rheology and microstructure in concentrated noncolloidal suspensions", J. Rheol. 46, 1031, (2002). ([document](#)), [3](#), [1.4](#), [3](#), [1.7.4.5](#), [4.5.1.3](#), [4.5.3.4](#), [4.6.2](#), [4.9](#), [5.3](#), [7.1](#)
- [Simha 1952] R. Simha, J. Appl. Phys. 23, 1020 (1952). [1.4.2.1](#)

BIBLIOGRAPHY

- [Singh and Nott 2003] A. Singh and P. R. Nott, “Experimental measurements of the normal stresses in sheared Stokesian suspensions”, *J. Fluid Mech.* 490, 293–320, (2003). ([document](#)), [3](#), [4](#), [5](#), [4.2](#), [4.5.3](#), [4.5.3.1](#), [4.5.3.3](#), [4.5.3.3](#), [4.5.3.3](#), [4.26](#), [4.6](#), [4.5.3.3](#), [4.5.4](#)
- [Sinton et al. 1991] S. W. Sinton and A. W. Chow, “**NMR** flow imaging of fluids and solid suspensions in Poiseuille flow”, *J. Rheol.* 35, 735–772, (1991). [1.6.1](#)
- [Solution Solvers] <http://www.openfoam.com/docs/user/fvSolution.php#x21-1170004.5> [3.4.1.1](#), [B.1](#)
- [Stickel and Powell 2005] J. J. Stickel and R. L. Powell, “Fluid mechanics and rheology of dense suspensions,” *Annu. Rev. Fluid Mech.* 37, 129–149, (2005). ([document](#)), [1.3.2.2](#), [1.4.2.1](#), [1.5](#), [4.5.1.1](#)
- [Stickel et al. 2007] J. J. Stickel, R. J. Phillips, and R. L. Powell, “Application of a constitutive model for particulate suspensions: Time-dependent viscometric flows”, *J. Rheol.* 51, 1271–1302, (2007). [1.6.1](#)
- [Stokes 1845] G. G. Stokes, *Trans.Camb. Phil. Soc.*, 8, 287, (1845). [1.2.1](#), [1.5.2](#)
- [Tadros 1988] T. F. Tadros, "Viscoelastic properties of concentrated suspensions", *Materials Science Forum*, 25-26, 87-110, (1988).
- [Tanner 1970] R. I. Tanner, “Some methods for estimating the Normal Stress Functions in Viscometric Flows”, *Trans. Soc. Rheol* 14:4, 403–507, (1970). [2](#)
- [Tanner 2009] R. I. Tanner, “The changing face of rheology”, *Journal of Non-Newtonian Fluid Mech.* 157, 141-144, (2009). [1.2.4](#)
- [Tetlow et al. 1998] N. Tetlow, A. L. Graham, M. S. Ingber, S. R. Subia, L. A. Mondy, and S. A. Altobelli, “Particle migration in a Couette

BIBLIOGRAPHY

- apparatus: experiment and modeling”, J. Rheol. 42, 307–327, (1998). [1.7.3.3](#)
- [Turunen T. 2011] Tuomas Turunen, “PISO vs. transient SIMPLE: A Comparison of Two Different Transient Solution Algorithms in Incompressible CFD with OpenFOAM® and Python®”, Bachelor Thesis, Aalto University, School of Mechanical Engineering, 18 April, (2011).
- [Van Der Vorst 1992] H. A. Van Der Vorst, “Bi-CGSTAB: A fast and smoothly converging variant of Bi-CG for the solution of nonsymmetric linear systems”, SIAM J. Scientific Computing, 13(2):631–644, (1992). [2.4.4](#)
- [Van Doormal et al. 1984] J. P. Van Doormal and G. D. Raithby, “Enhancements of the SIMPLE method for predicting incompressible fluid flows, Numer. Heat Transfer, Vol. 7, pp. 147-163, (1984).
- [Vanka 1986] S. P. Vanka, “Block-implicit multigrid solution of Navier-Stokes equations in primitive variables”, J. Comp. Physics, 65:138–158, (1986).
- [Versteeg and Malalasekera 1995] H. K. Versteeg and W. Malalasekera, “An Introduction to Computational Fluid Dynamics: The Finite Volume Method”, John Wiley & Sons Inc., ©Longman Group Ltd., (1995). [2.4.1](#), [2.6.2](#)
- [Weissenberg 1946] K. Weissenberg, “Rep. Gen Conf. Brit. Rheol. Club”, p. 36, Edinburgh, (1946). [2](#)
- [Weller et al. 1998] H. G. Weller, G. Tabor, H. Jasak, and C. Fureby, “A Tensorial Approach to CFD using Object Orientated Techniques”, Computers in Physics, v 12 n 6, pp 620-631, (1998).
- [Wikipedia®] http://en.wikipedia.org/wiki/Main_Page [1.2.2](#)

BIBLIOGRAPHY

- [Xi and Shapley 2008] C. Xi and N. C. Shapley, “Flows of concentrated suspensions through an asymmetric bifurcation”, *J. Rheol.* 52, 625–647, (2008). [1.6.1](#)
- [Yapici et al. 2009] K. Yapici, L. Powell, and R. J. Phillips, “Particle migration and suspension structure in steady and oscillatory plane poiseuille flow”, *Physics of fluids* 21, 053302, (2009).
- [Yeo and Maxey 2010a] K. Yeo and M. R. Maxey, “Simulation of concentrated suspensions using the force-coupling method”. *J. Comput. Phys.* 229, 2401-2421, (2010). ([document](#)), [3](#), [1.7.4.5](#), [4.5.3.4](#), [4.6.2](#), [4.6.2](#), [4.9](#), [7.1](#)
- [Yeo and Maxey 2010b] K. Yeo and M. R. Maxey, “Dynamics of concentrated suspensions of non-colloidal particles in Couette flow”, *J. Fluid Mech.* 649, 205–231, (2010). [3](#)
- [Zarraga et al. 2000] I. E. Zarraga, D. A. Hill, and D. T. Leighton, “The characterization of the total stress of concentrated suspensions of noncolloidal spheres in Newtonian fluids”. *J. Rheol.* 44, 185-220, (2000). ([document](#)), [1.4.2.1](#), [3](#), [1](#), [5](#), [1.7.4.5](#), [4.2](#), [4.5.1.1](#), [4.5.1.3](#), [4.5.3](#), [4.5.3.1](#), [4.5.3.4](#), [4.5.3.4](#), [4.6.2](#), [4.9](#), [7.1](#)
- [Zienkiewicz et al. 1989] O. C. Zienkiewicz and R. L. Taylor, “The Finite Element method, vol 1: Basic formulation and linear problems”, McGraw-Hill, 4th edition, (1989).

[2.5.1](#)